4th Numerical Towing Tank Symposium

23-25. September 2001

Hamburg/Germany

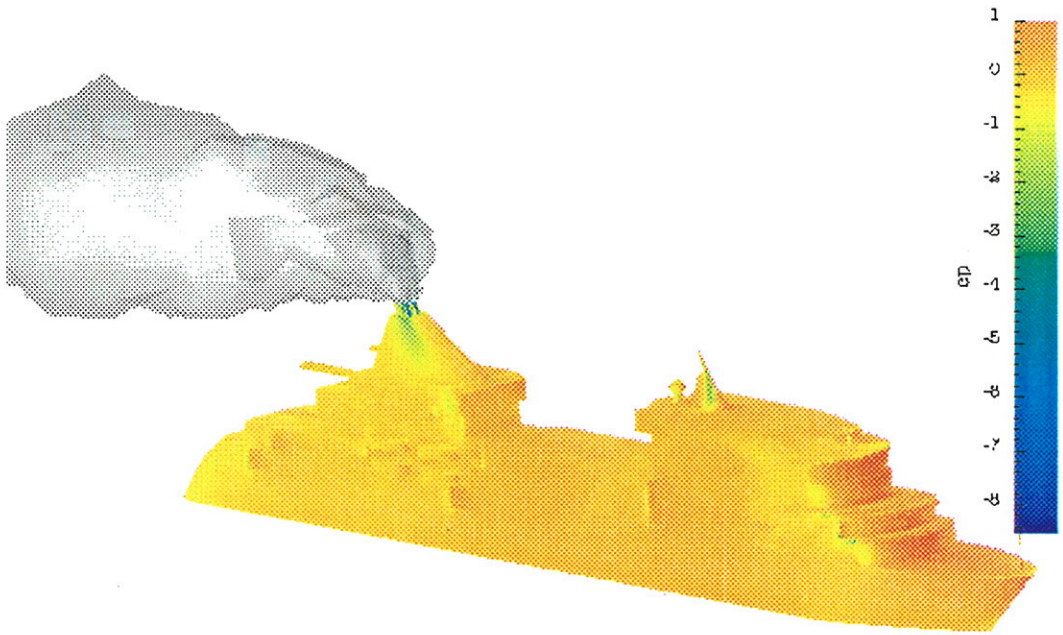

Volker Bertram (Ed.)

Dedicated to Professor Heinrich Söding, the "Master"

Sponsored by

VOITH

LÜRSSEN

FR. LÜRSSEN WERFT

AEA TECHNOLOGY

ENGINEERING SOFTWARE

ICEM CFD ENGINEERING

Storck Verlag, Hamburg

JAFO Technologie

The Master - Der Meister

(assorted Söding sagas compiled by his former colleagues and PhD students)

Söding's wife complained: "They fly to the moon, but still have not managed to make coffee pots that don't drop on the tablecloth!"
Sö: "Hmmm, that is quite simple. All we need is a sharp edge for flow separation. Let me quickly..."
He was on the verge of getting a hammer to improve (hydrodynamically) the coffee pot design, but this was vetoed by his wife.

The family car broke down. Sö launches his project to repair the carburetor.
Question: "Do you know how to repair a car engine?"
Answer: "Well, I never did it before. But everybody knows the purpose of a carburetor and then we have physics to help us understanding the individual parts. Can't be all that difficult."
Indeed, the car was fixed.

Back in the 1970s and 1980s, Sö worked on routing of ships. The meteorological department was slow in getting the input data for his routing optimization. Finally Sö was at the end of his patience: "Oh well, then we make our own weather!" - And programmed a working prediction program.

I was a rookie in Söding's team, starting work on my Ph.D. After one month of studying assorted publications on wave resistance, I wrote down how I intended to solve the problem. I went optimistically with my brilliant idea to Sö.
Bertram: "Do you have some time now?"
Sö: "No, why? But please come in and have a seat."
Bertram: "I have written down how..."
Sö: "Oh, very good. But it will take some time before I get to reading it. How urgent is it?"
Bertram: "Oh, well, ..."
Next day he was in the door to my office.
Sö: "You have done that already quite well. I have added a few comments."
The "few comments" filled all space and margins and also the other side was filled with scribbled remarks. My hair roots started tingling and the foreign legion appeared suddenly as serious plan B for my future career. Before I could choose the only honorable way out (i.e. jumping from my window to a premature, but well-deserved death) salvation came in the form of two older colleagues. Cheerfully grinning they asked if I had received my first feedback from the "master". My shameful nods drew salvos of laughter and they commented that this was quite normal. The master was just one or two orders of magnitudes more intelligent than us mere mortals. One would have joined the highest levels of the knighthood of scientists if Sö could scribble all his comments on just the front page. I have reached this status now. Alas, I learned to leave extra big margins and use double line spacing...

I was in my third year working on my PhD for the master. I was in my office, realizing yet again that I was dumb and he was good. But I was much smarter than I had been 3 years ago, and sometimes I did a few things right. And others were even dumber than me! Or so I thought. I was about to make yet another of my award-winning dumb mistakes...
Bertram: "Aren't you ever frustrated that we are so much dumber than you are?"
I don't know until this day what made me ask this question or what I expected as a reply. Perhaps a "Oh no, not you, you are sooooo smart." Or a "Oh well, Herr X is sometimes pretty frustrating, but you and Herr ..." Anyway, something along those line pampering the ego. Little did I count on the master's sincerity and love of truth. Sö tilted his head slightly, supporting it with on hand on his brow which wrinkled due to the intensive thought processes my question had provoked. His head nodded slightly, then it shook left and right, perhaps in irritation, perhaps in dissent. Seconds of silence felt like little eternities. Then his final judgement, clear and precise: "No...no, I am used to that."

The unfashionable concept of moral integrity is the most natural thing for the master. His attitude has always served as an example for his disciples. In many decisions, small or big, we have thought not

only what our parents would have done, but "what would Sö do in such a situation". Then things became often clear and we would know what was the right thing to do.

Sö never cared for professorial arrogance or a fixation on titles and positions. For a long time, there was a small piece of paper attached to his office door: "Herr ist Ehre genug" ('Mister' is honor enough.)

Sö's brain must be somewhat different. He reads a paper of Professor Grim while watching the news on TV. The information density of the news is simply not enough to keep his brain busy.

Sö has a unique style to use the copy machine. If he wants to copy 25 pages from a book, he selects 25 copies and then - with lightning speed and artistic skill - turns pages and flops the book getting in the end 25 perfectly copied pages in record time. All attempts of his disciples to copy this feat have failed miserably.

Sö was inspired by a PhD thesis on expanded complex 3-d shapes. Of course, he had some ideas of how to do things much better in much shorter time and wrote his own little program ABWIK based on finite elements. It was more by coincidence that we heard that this was used in the German aerospace industry for difficult shapes. Sö's programs were drifting around probably long before the terms "public domain" and "open source" were invented.

Prof. Wendel "held court" in Hanover at the university, sherry on and the collaborators around the table. Like Frederick the Great, he liked to discuss this and that, often topics far from naval architecture. One day the finer points of a rare plant were discussed and Wendel asked Sö for his comments. Afterwards, Wendel said with a mixture of his hanseatic, ever so distinguished way of speaking and a mischievous boyish grin: "You can ask Söding anything at all - and he will have to say something profound on the topic."

Sö developed a brilliant paper management system: put assorted papers, copies, files etc in a drawer or box and put a note with the today's date on it. If you ever come across these papers again, look at the note with the date. If it has exceeded n years (n being a personal constant) throw it away without looking at it again.

Institute council meeting: Students complain that some professors check out books from the library and never ever return these.
Söding: "I don't understand this. If I check out a book I read it in one or two days. Then I know what's in the book and give it back to the library. Why keep it any longer?!"
Widespread laughter in the non-professor faction and sour-dough faces among the professors.

Students feared him. Not because of his personality, but because of his 'casual' math which showed everybody quickly the limits of their minds. Also most professorial colleagues avoided discussions, knowing that they could only lose.

Sö has a special relationship with shoes. In winter he comes sometimes to work in sandals as he not always follows weather conditions too closely. Once he went shopping for shoes. He tried several pairs, none to his satisfaction. Finally he slipped into one pair and said immediately: "These fit superbly!" Alas, it was his old pair...

Sö is a master of systematic deduction and intense concentration. Once Sö went to Bonn for a meeting. While waiting in the corridors of the ministry, a colleague noticed: "Didn't you wear a coat, Professor Söding?"
Sö concentrates. You can almost hear the master machinery at work:
Söding: "Yes, I had coat! - Yes, in Hamburg I stepped on the train with a coat. - Did I leave with a coat in Bonn? - Yes, in Bonn on the platform I still had my coat. - Did I have it still in the taxi? - Yes,

I put it on the seat. - Did I exit the taxi with it? - No, there I no longer had the coat. - Yes, I left it in the taxi. - Yes, it must be lying on the back seat of the taxi."
Call at taxi central yields information that coat has been found. Request: Bring coat to train station 18:15h. Return to Hamburg with coat.

I was the only exam candidate that year in ship manoeuvring. I started writing the exam in the seminar room of the IfS. Sö wanted to work, of course, and went out saying he had something to do. Some time later, Professor Keil (director of the IfS) entered the room.
Keil: "What are you doing here?"
Muxfeldt: "I am writing an exam."
Keil: "But where is the supervision?!"
Muxfeldt: "Prof. Söding went away."
Keil: "This is impossible! An exam without supervision!"
Immediately Prof. Keil took the task of supervision on himself. After a while Sö returned to look after me. Prof. Keil immediately confronted him with several accusations, including that I could have asked anybody about the exam problems.
Söding: "Yes, he could have asked anybody...but nobody could have given him an answer - except me."
Keil stayed only a short time after that. Then he also went away.

My doctoral thesis (supervised by Sö) was to appear as IfS report as usual. The new procedure involved filling out a form to get permission to print which had to signed by Sö. The form asked also for the weight of the report. Sö thought this funny and I told him that I had not filled out that part as I still needed to weigh the report.
Söding: "Ahh, you don't need to do this."
El Moctar: "I think I have to. Otherwise the printers may reject the report."
Söding: "Shall I estimate the weight then?"
El Moctar: "Oh yes, please."
Söding did some mental acrobatics mumbling: "0.28 times 0.2...yes, plastic cover, say 9 gram..." etc. Then he says: "390 gram."
I went to the person in charge of accepting the printing orders ad told him: "As I did not have a scale, Söding estimated the weight."
The man said that this was not necessary as he had a precise scale. He weighed the report and - it was exactly 390 gram.

Söding was asked why he did not comment on a point in a discussion: "I only wanted to intervene when he would say complete nonsense...and he said only major nonsense!"
Note: If Sö does not react, maybe you are just producing major nonsense...

Contributions listed in alphabetical order of author(s)

Landrini, M.; Colagrossi, A.; Tulin, M.
Numerical studies of wave breaking compared to experimental observations

Laurens, J.M.; Leconte, T.; Grosjean, F.
Numerical study of the wave breaking generated by a submerged hydrofoil

Li, T.; Matusiak, J.
A refinement study of grid for turbulent ship free-surface flows

Lungu, A.
Vortical structures in a 3d unsteady viscous flow

Lungu, A.; Alexandru, G.
Numerical experiment for hull form improvement

Muscari, R.; Di Mascio, A.
A model for the simulation of spilling breaking waves

Nielsen, K.B.; Mayer, S.
VOF simulation of green water load problems

Salas, M.
Hydroelastic simulation of slamming loads

Simonsen, C.; Cross-Whiter, J.
RANS simulations for the flow around a manoeuvring tanker

Söding, H.
How to integrate free motions of solids in fluids

Starke, B.
A validation study of wake-field predictions at model and full-scale Reynolds numbers

Streckwall, H.; El Moctar, O.M.
Towards RANSE simulations for hull, propeller and rudder interaction

Xing, Y.; Hadzic, I.; Peric, M.
Predictions of floating-body motions in viscous flow

Calculation of the pressure reduction in the tip vortex core of a skew propeller in model and full-scale

Moustafa Abdel-Maksoud[1], Karsten Rieck[2], Potsdam Model Basin

Introduction

The prediction of the details of the tip vortex flow is important to understand the scale effect on propellers. High skew propellers have many advantages especially the reduction of cavitation and pressure pulses on the ship stern. On the other side, increasing the skew angle of the propeller leads to extend the length of the wall streamlines on the propeller blade. Therefore, an accurate prediction of the viscous effects on the performance of the skew propeller is important, especially for off-design conditions.

Numerical computations

The numerical computations of the viscous flow were carried out for a five blade propeller in homogeneous flow. Only one propeller blade is considered in the computation. The influence of the other blades is considered by appling of periodic boundary condition in the space. The calculation domain is a 72 degree segment of a cylinder.

The calculation domain is divided into a stationary part and a rotating part. A sliding boundary condition is applied between them. The propeller blade and part of the propeller shaft are included in the rotating part of the calculation domain. In this part, a rotating co-ordinate system is applied to calculate the flow around the propeller.

The RANS equations in a rotating co-ordinate system involve additional terms compared to those in an inertial system. The computations were carried out with the commercial CFD software package CFX-TASCflow of AEA Technology. CFX-TASCflow uses a Finite Element based Finite Volume method. It uses block-structured non-orthogonal grids. CFX-TASCflow models the equations for the conservation of mass, momentum and energy in terms of the dependent variables velocity and pressure in their Reynolds averaged form. The variables are discretised on a co-located grid with a second order fully conservative vertex based scheme. In the computations the "Linear Profile" scheme with "Physical Advection Correction" of Schneider and Raw [1] was applied. The resulting linear equation system is solved with an Algebraic Multi-Grid (AMG) solver, which shows a linear scalability of the code with the number of grid cells. The equations are solved fully coupled.

The standard k-ε-model with scalable wall function has been applied in the present study. The scalable near wall treatment allows a consistent grid refinement near the wall, Grotjans and Menter [2].

The diameter of the investigated propeller in model scale is 0.25 m. The scale ratio is $\lambda = 12$. Pitch ratio and blade area ratio are 1.635 and 0.779 respectively. The skew angle equals 18.8 degrees.

A block structured grid is applied. The numerical grid contains 11 blocks. Two numerical grids have been employed, the number of control volumes are 339.000 and 712.000. Figure 1 shows the topology of the numerical grid. The size of the tip vortex is very small in comparison to the size of the calculation domain. To determine the pressure distribution in the tip vortex a local refinement study was carried out in two steps. The number of control volumes after the first and the second grid refinement were 719.000 and 1.310.000 respectively, which means that about 1 million control volumes were located in the tip vortex region near the tip of the propeller blade. The reasults of the local refinement study are presented in Rieck and Abdel-Maksoud [3]

Calculations were carried out for five advance coefficients. The calculated and measured thrust and torque coefficients are shown in Figure 2. The calculated thrust coefficient in full-scale is higher than in model scale. At the design point $J = 1.245$, the difference is about 2%. The difference in thrust coefficient between model and full-scale decreases with increasing the propeller loading. The calculated torque coefficient of full-scale is 3% lower than the model one at the design point. With increasing the propeller loading, the difference between the torque coefficient of model and of full-scale becomes smaller.

Detailed velocity measurements of the propeller flow were made in the cavitation tunnel of the Potsdam Model Basin. The measurements were carried out using non-coincident Laser Doppler Velocimeter.

A comparison between the calculated and measured

[1] maksoud@sva-potsdam.de
[2] rieck@sva-potsdam.de

velocity components near the tip of the propeller blade at the station $0.1D$ behind the propeller is shown in Figures 4 and 5. The velocity components were normalised by the inflow velocity. A good agreement was achieved between the measured and the calculated values of the axial and radial velocity components. This fact is valid not only for the flow between the propeller blades but also for the flow behind it. The calculated tangential velocity component is a little bit higher than the measured values.

The calculation of the minimum pressure is more difficult than the calculation of the thrust and the torque coefficients. The size of the tip vortex is very small in comparison to the size of the calculation domain. The calculation of the pressure distribution in the centre of the tip vortex requires a high grid resolution in this region to resolve the high gradients.

The de-attachment location of the tip vortex on the propeller blade is depending on the Reynolds number and the loading coefficients. The axial location of centre of the tip vortex moves toward the leading edge of the propeller blade with increasing propeller loading. This effect is much stronger in model than in full-scale, see Figure 3. The change of the radial location of centre of the tip vortex is shown in Figure 6. With increasing propeller loading the centre of the tip vortex moves towards the rotation axis of the propeller, see Figure 6. This tendency is stronger at high Reynolds numbers.

Figure 7 shows the velocity distribution through the tip vortex at $J = 1.245$. The data are considered along a circular segment at radius $r/R = 0.995$ in the plan $x/D = 0.07$ behind the propeller, at which the minimum pressure of the tip vortex takes place. The tip of the propeller blade is located between the angular positions $111 < \Theta < 111.5$ degree. The pressure side is located at 111 degree and the suction side at 111.5 degree. The unsteadiness of the results in the region of 115 degree is due to the difference of resolution of the numerical grid between the refined and non-refined regions.

The acceleration of the flow is higher on the suction side than on the pressure side. The pressure differences between the pressure and the suction sides is the reason for the tip vortex. In this region, the flow is directed from the pressure side to the suction one. Therefore, the radial velocity component on the pressure side is positive and directed away from the rotation axis of the propeller. On the suction side, the radial velocity component is positive close to the wall surface and negative in a certain distance from the wall. In this case, the radial velocity becomes negative and is directed to the rotation axis of the propeller, see Figure 7. The change of the radial velocity component is proportional to the vorticity of the tip vortex.

The same results for full-scale are included in Figure 8. The comparison with the results for model-scale shows that the minimum and the maximum values of the radial velocity component are higher in full-scale than in model scale. The change of the pressure coefficient is shown in Figure 9. The reduction of the pressure coefficient in the core of the tip vortex in full scale is higher than in model scale. Similar results for $J = 0.871$ are presented in Figures 10, 11 and 12. The comparison between the results for $J = 1.245$ and $J = 0.871$ shows that the minimum and maximum values of the radial velocity component are higher at $J = 0.871$. The reason is the high propeller loading, which leads to strong tip vortex. The pressure distribution shows also a high pressure reduction in the centre of the tip vortex. Figure 12 shows a reduction of the pressure coefficient in full-scale. The location of the centre of the location of the minimum pressure at $J = 1.245$ is more away from the propeller blade than at $J = 0.871$. The reason is the earlier de-attachment of the tip vortex at high thrust loading coefficients.

The numerical results show that the reduction of the pressure in full scale is much higher than in model scale, which means that the cavitation will take place earlier in full-scale than in model-scale. The pressure reduction in full-scale is lower than expected according to the known observations of the cavitation on model and full-scale propellers. According to the numerical results, the earlier cavitation of the full-scale propeller may be not only a matter of high Reynolds numbers. The difference between the water quality in cavitation tanks and open sea may play an important role in this case.

Acknowledgement

The authors would like to express their gratitude to the Federal Office of Defense, Technology and Procurements, Department Ships and Naval Equipment for the support of the study (Prediction of tip vortex cavitation of marine propellers / numerical investigation of the velocity fields and pressure reduction in the core of the tip vortex of the marine propellers VP 1304) and the permission to publish this paper.

References

[1] SCHNEIDER, G. E., RAW, M. J., Control Volume Finite Element Method for Heat Transfer and Fluid Flow using Co-located Variables, Numerical Heat Transfer, Vol. 11, pp. 363-390, 1987

[2] GROTJANS, H., MENTER F. R.,Wall Functions for Industrial Applications, In Papailiou, K. D. Editor, Computational Fluid Dynamics 98, Volume 1, Part 2, pp.1112-1117, Chichester, 1998, ECCOMAS, John Wiley & Sons

[3] RIECK, K., ABDEL-MAKSOUD, M., Scale Effect on the Tip Vortex Flow of a Skew Propeller, Ship Technology Research, Vol. 49, 2002

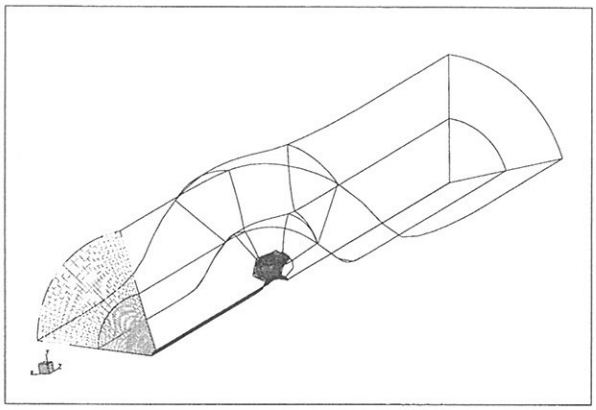

Figure 1: Topology of the numerical grid

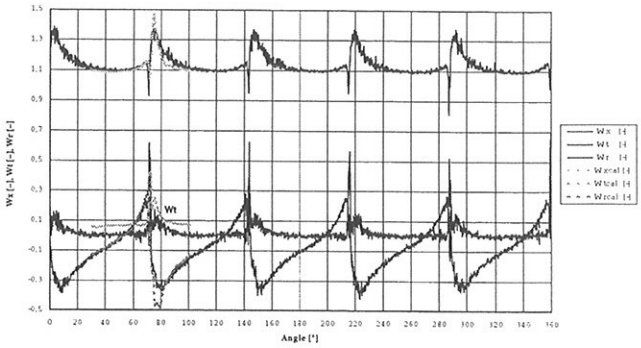

Figure 4: Measured and calculated velocity components, $x/D = 0.1,\ r/R = 0.95$

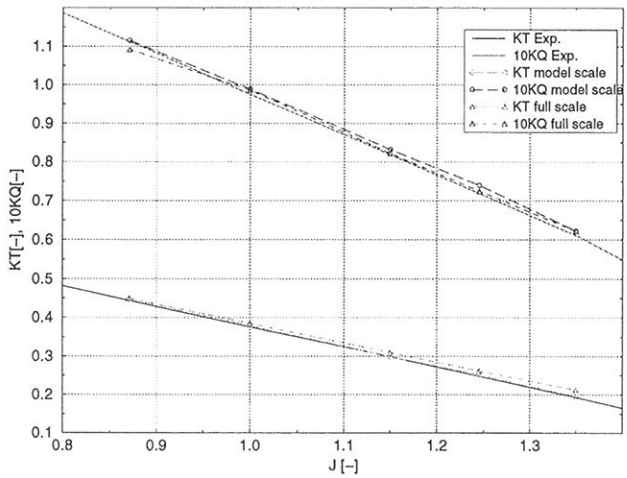

Figure 2: Thrust and torque coefficients

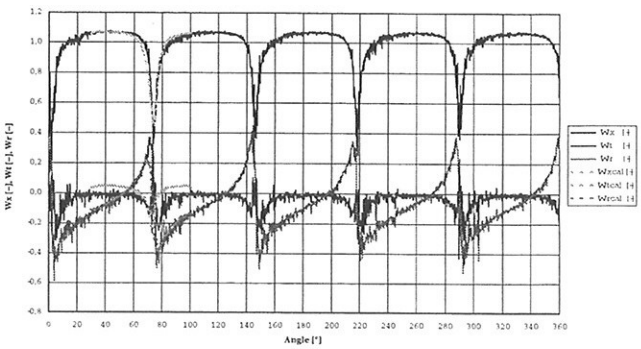

Figure 5: Measured and calculated velocity components, $x/D = 0.1,\ r/R = 1.0$

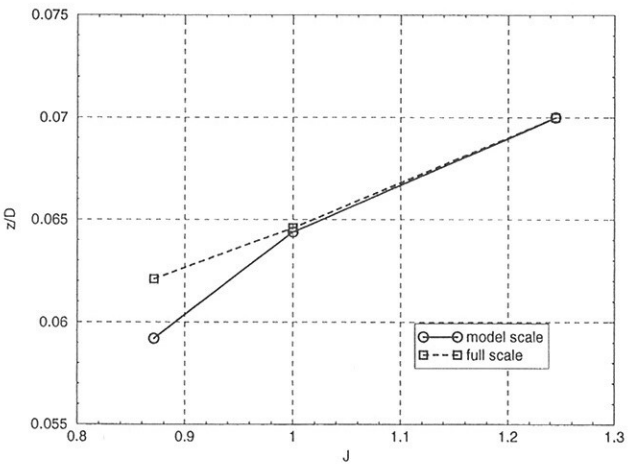

Figure 3: Axial location centre of tip vortex

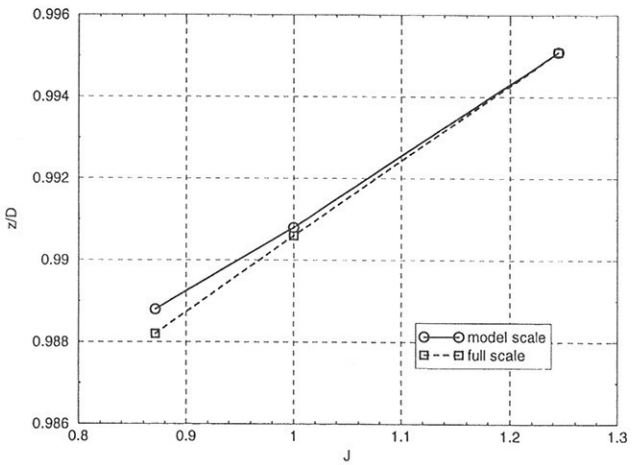

Figure 6: Radial location centre of the tip vortex

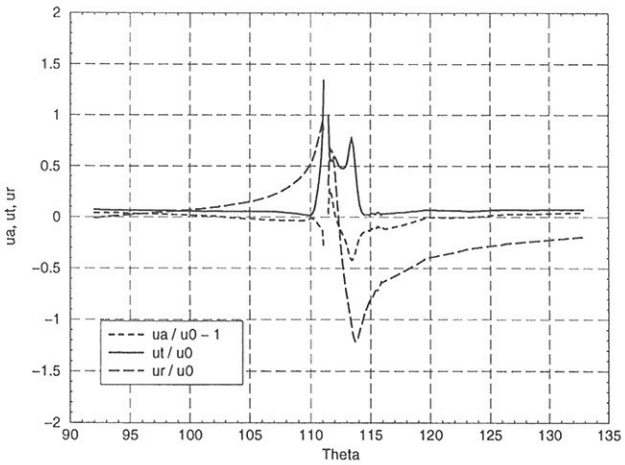

Figure 7: Velocity distribution in the tip vortex, $J = 1.245$, model scale

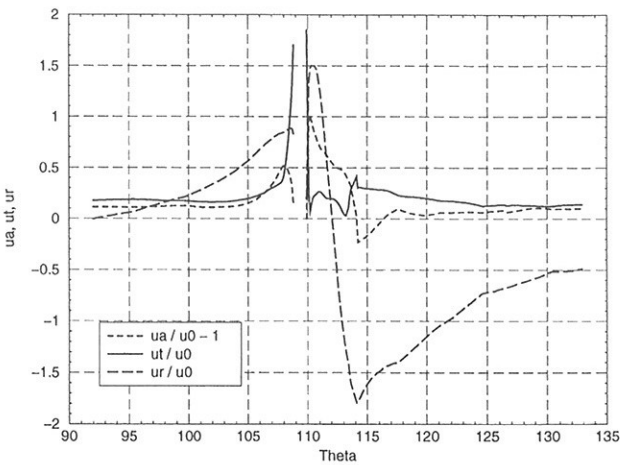

Figure 10: Velocity distribution in the tip vortex, $J = 0.871$, model scale

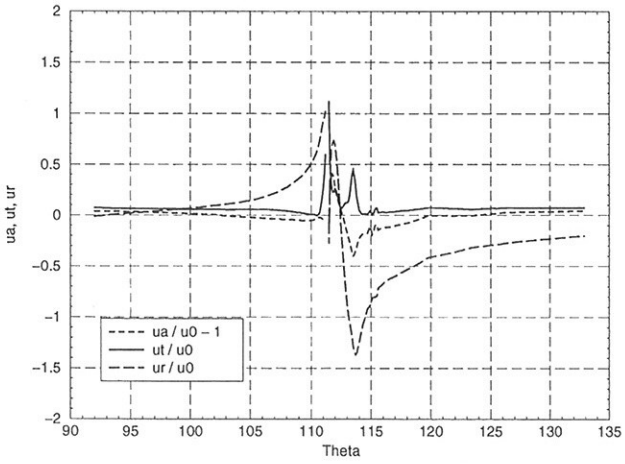

Figure 8: Velocity distribution in the tip vortex, $J = 1.245$, full scale

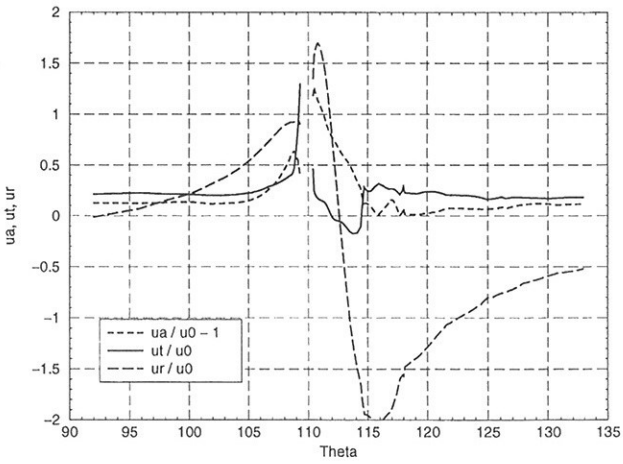

Figure 11: Velocity distribution in the tip vortex, $J = 0.871$, full scale

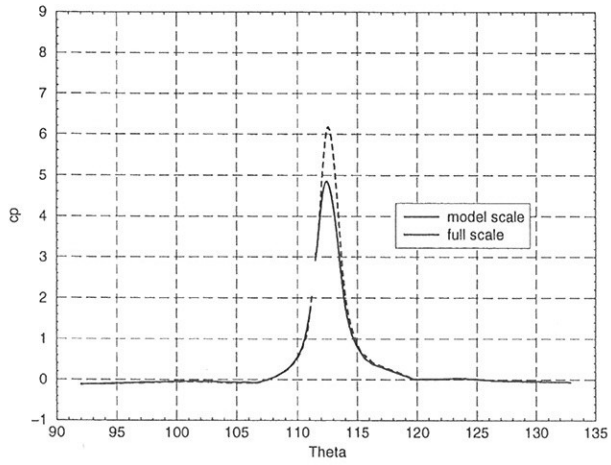

Figure 9: Pressure distribution in the tip vortex, $J = 1.245$, model and full scale

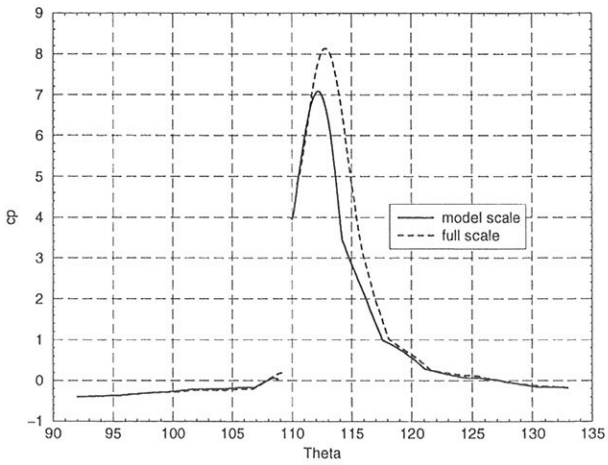

Figure 12: Pressure distribution in the tip vortex, $J = 0.871$, model and full scale

Effects of Hull Geometry and Irregular Frequencies on Three-dimensional Seakeeping Predictions

Tamer M. Ahmed, Dominic A. Hudson, Penny Temarel
Ship Science, School of Engineering Sciences, Univ. of Southampton, UK, tamer77@soton.ac.uk

Recently, seakeeping problems have become more crucial, particularly for the design of high-speed ocean going vessels –comparatively small in size- whose performance is drastically affected by ocean waves. In this paper, various techniques are applied to three-dimensional singularity distribution methods to eliminate deficiencies, such as flow behind the transom and occurrence of irregular frequencies, and thus, improve predictions. It should be noted that in these applications, singularities are distributed over the mean wetted surface of the vessel.

Virtual Appendage Method

It has been noted that above a Froude number of approximately 0.4 the flow separates from the transom stern. Potential flow based numerical methods do not adequately account for this. An attempt to remedy this problem is through the virtual appendage method, which involves the smooth extension of the hull at the transom stern such that it encloses the separated flow. It has been found that the streamline re-attachment length of the flow behind the transom step can be approximately taken as six times the step height, i.e. the transom's half breadth. In this manner, the transom stern body is closed by the addition of an extra point down stream of the transom, for each waterline [1].

The above method has been applied for a NPL5b hull form (C_B=0.4, B/T=1.99, $L/\nabla^{1/3}$=8.45) travelling in regular head waves at Fn.=0.53. NPL hull-forms are representative of modern high-speed crafts. The hull is of a fine form but having a relatively large transom stern, as shown in Fig. (1a) where 500 panels are used to discretise the mean wetted surface. The virtual appendage was panelled ensuring that the aspect ratio of the original hull's panelling is maintained. The resultant idealisation, shown in Fig. (1b) consists of 670 panels. Values for basic parameters of the actual hull (i.e. length (L), LCG, displacement, VCG, and moments of inertia) were all maintained the same in both sets of calculations. On the other hand, fluid-structure interaction parameters (i.e. added masses, damping coefficients, hydrostatic restoring coefficients and total exciting forces) for the hull with the virtual appendage, correspond to the relevant mean wetted surface. This is particularly important for the restoring coefficients, which were evaluated using the waterline properties of Fig. (1b). Results were obtained using both, pulsating and translating-pulsating source formulations, (the latter used for a more accurate representation of forward speed effects).

The variation of non-dimensional pitch added mass and heave damping coefficients is shown in Fig. (2). Comparisons with experimental data, shown in Fig. (3), indicate that the addition of the virtual appendage improved predictions for heave and pitch RAOs in head waves. Although, translating-pulsating source formulation gives better prediction for where resonance occurs (for both sets of calculations), the pulsating source one appears to be better for predicting the magnitudes of the RAOs. It is thought that predicted hydrodynamic coefficients and RAOs, may vary with the re-attachment length of the flow, depending on Froude number.

Irregular Frequencies

In adopting boundary integral techniques for calculation of hydrodynamic coefficients of an arbitrary shaped body oscillating in the free surface, it has been observed that there are certain frequencies at which, the integral equation fails to give a unique solution or this solution doesn't exist. These are the so-called irregular frequencies. Their presence can be seen when using a pulsating source distribution, see Figs. (2), (4) and (5).

One of the methods for overcoming this deficiency is modifying the Green's Function by adding terms corresponding to singularities in the interior of the hull at the free surface. The new Green's function is represented by the combination of the classical Green's function and terms derived by a succession of

linear operations on the classical Green's function (additional Green's function). Therefore, the method can be referred to as a **Multiple Green's Function Expression** [2], given by

$$G^{*}(p, q, n_1, n_2, n_3, \ldots.) = G_o(p, q) + \sum_{J=1}^{N} G'(p, q, n_J)$$

where

$$G'(p, q, n_J) = C\, G_o(n_J, q)\{[\partial/\partial x\, G_o(p, n_J)] + \mathrm{sgn}(y - y_J)[\partial/\partial y\, G_o(p, n_J)] + [\partial/\partial z\, G_o(p, n_J)]\}.$$

In these equations, $G_o(p, q)$ is the classical Green's function, $C = -\alpha\,(1- i) / \nu$, ν is the wave number, p and q are the external singularities distributed over the hull surface and taken as field and source points respectively and n_J denotes the singularities (up to a total number N) in the interior of the hull at the free surface.

Physically, the idea of the internal singularities is to function as a damping device absorbing or cancelling the interior resonant wave modes due to the presence of the free surface. Mathematically, at an irregular frequency of one of the integral equations (corresponding to either the classical or additional Green's function), only one of the solutions will satisfy the integral equation for the multiple Green's function; thus, uniquely defining the solution for all frequencies.
The multiple Green's function has been applied to a Rectangular box and a NPL5b form, using 76 and 500 panels respectively to idealise the mean wetted surface. Variation of non-dimensional hydrodynamic coefficients, shown in Figs. (4) and (5), reveal that this method has succeeded in the elimination of the discontinuities observed in the vicinity of the irregular frequencies. However, it has adversely affected the magnitudes of the hydrodynamic coefficients at low frequencies. This is still under investigation. Errors in the second derivatives of Green's function may be amongst the possible sources of observed discrepancies. The results shown in Figs. (4) and (5), where obtained using α=1. Sensitivity of results to the variation of α and number of internal singularities N has been investigated. It has been noted that the predictions are independent of α as it increases. It has also been noted that the best results with the multiple Green's function expression method are obtained when there is an internal singularity distribution along the centre line with approximately, one to one correspondence for each slice of panels. Furthermore, comparisons will be made, for the NPL5b hull form, with predictions obtained from a method which extends the hull surface idealization to include a lid placed, just below the free surface.

References

1. Couser, P.R., Wellicome, J.F. and Molland, A.F. An improved method for the theoretical prediction of the wave resistance of transom-stern hulls using a slender body approach. International Shipbuilding Progress, 45, pp.331-349, 1998.
2. Wu, X.J. and Price, W.G. A multiple Green's function expression for the hydrodynamic analysis of multi-hull structures. Applied Ocean Research, 9, pp.58-66, 1987.

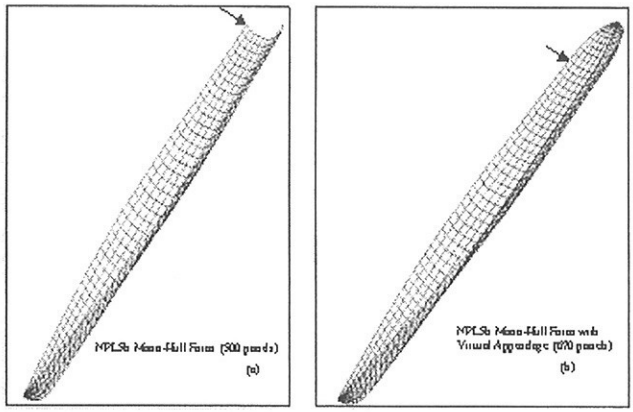

Fig. (1) Mean Wetted Surface Idealisation of NPL5b mono-hull
(a) original hull form (500 panels), (b) with virtual appendage (670 panels)

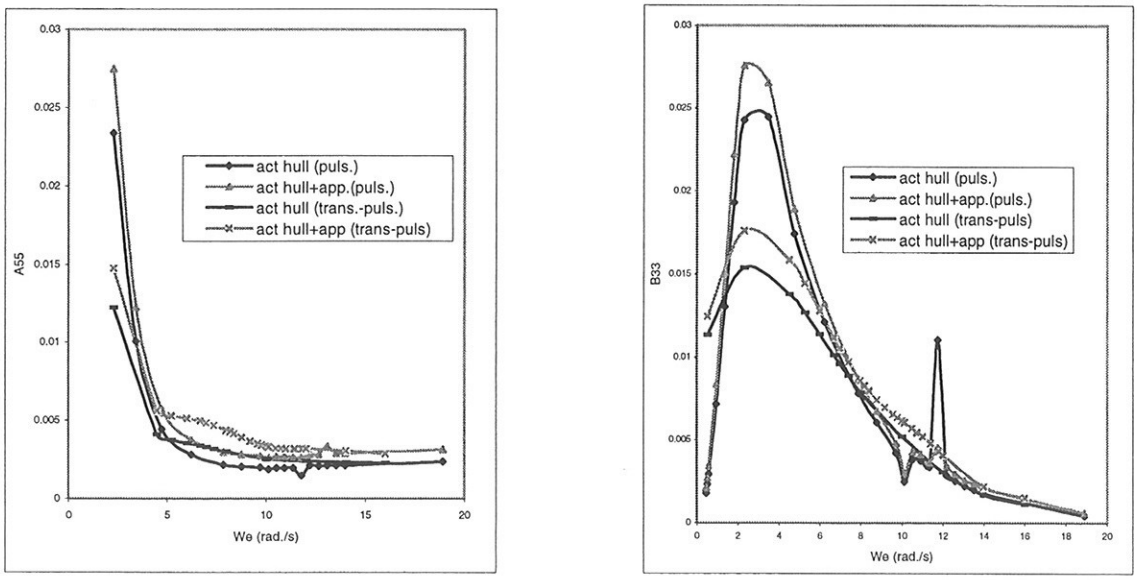

Fig. (2) Influence of Virtual Appendage on Non-dimensional Hydrodynamic Coefficients [A55=A'55/ρ(L/2)^5] of pitch added mass and [B33=B'33/ρ(L/2)^3(g/L)$^{1/2}$] of pitch damping for the NPL5b mono-hull travelling at Fn.=0.53

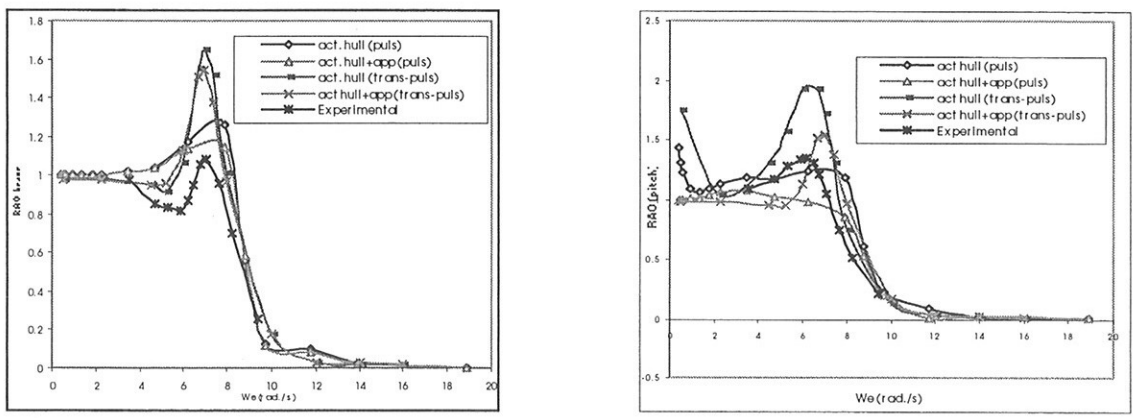

RAO (heave) RAO (pitch)

Fig. (3) Influence of Virtual Appendage on heave and pitch RAOs for the NPL5b mono-hull travelling at Fn.=0.53

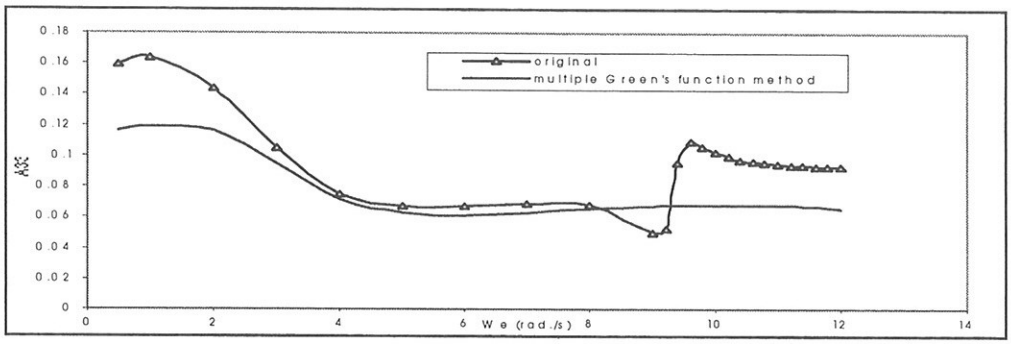

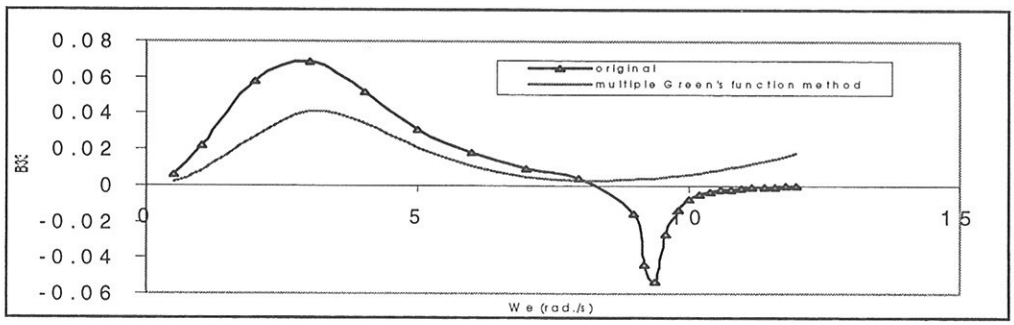

Fig.4 Influence of Irregular Frequencies on Non-dimensional Hydrodynamic Coefficients [A33=A'33/ρ(L/2)^3] of heave added mass and [B33=B'33/ρ(L/2)^3(g/L)$^{1/2}$] of heave damping for a Rectangular Box Vessel (76 panels), at Fn.=0.53

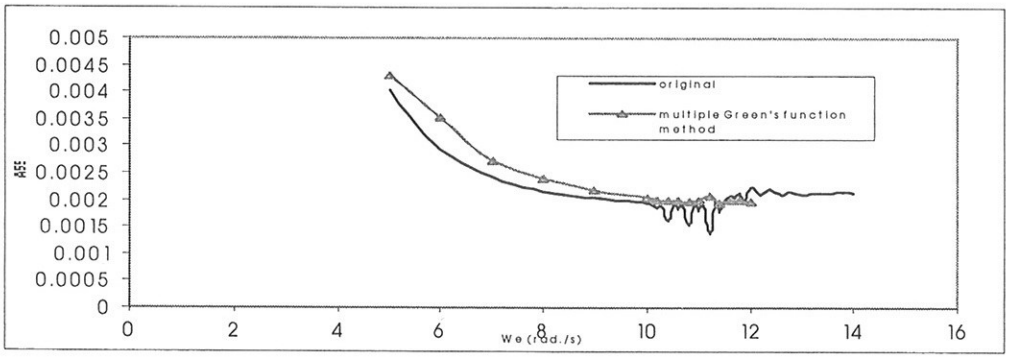

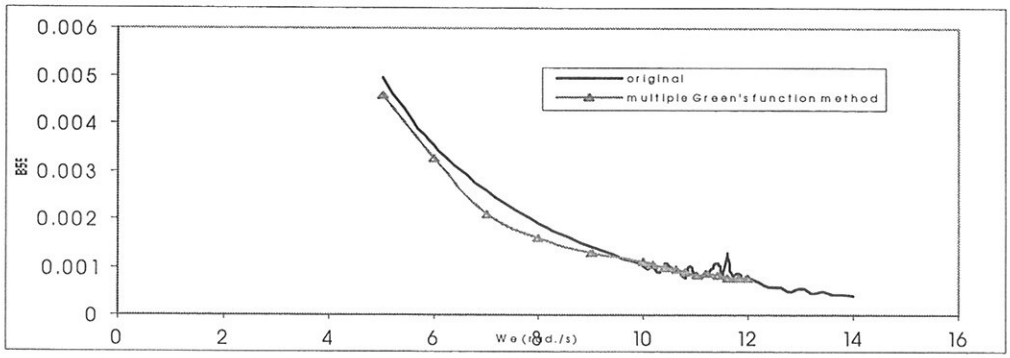

Fig. (5) Influence of Irregular Frequencies on Non-dimensional Hydrodynamic Coefficients [A55=A'55/ρ(L/2)^5] of pitch added mass and [B55=B'55/ρ(L/2)^5(g/L)$^{1/2}$] of pitch damping for a NPL5b mono-hull (500 panels), at Fn.=0.53

Free-surface RANSE simulations for steady and unsteady ship flows

Rodrigo Azcueta, MTG Marinetechnik GmbH[1]

1 INTRODUCTION: In this work the RANSE solver COMET was extended to both include the ship's running attitude in the calculations, and to simulate the motions of ships floating at the free surface. The work was presented as a PhD thesis, (*Azcueta* (2001), pdf file can be sent on request). This paper is a brief summary of it. RANSE computations are increasingly being used to predict the ship resistance. In recent years the deformation of the free-surface and hence the wave-making resistance have been successfully implemented and validated. But to date the ship's running attitude, i.e. the dynamic sinkage and trim of the ship underway, has been neglected, even in research applications. All viscous flow computations known to me are to date in the *model-fixed* condition, either at the floating attitude at rest or at the running attitude measured in the towing tank. To improve the resistance predictions further, the ship's running attitude has to be included in the computations (*model-free* condition), since its effect is usually significant. This was the first aim of this work. The second was to extend the numerical method to simulate the motions of bodies floating freely at the free surface in the 6 DOF. An important requirement was to implement the coupling of the body motions and the fluid flow in such a way that both types of simulations – steady and unsteady – could be performed with the same program, and that the method be extensible to still more complex tasks, such as for ship manoeuvring and ships in waves.

2 NUMERICAL METHOD: The flow solver used is based on a Finite Volume Method with unstructured meshes and an *interface-capturing scheme* to determine the shape of the free surface, *COMET* (2000). The method was extended with an *user-programmed rigid-body* module to couple the body motions in the 6 DOF with the fluid flow. A *single-grid* strategy was used, where a rigid, body-fixed grid moves relative to an inertial frame of reference and the ficticious flow forces are automatically taken into account in the flow equations. The rigid body module is linked and run simultaneously with the flow solver and can thus operate and update all flow variables, boundary conditions and parameters of the numerical method.

3 EXTRAPOLATION TO GRID-INDEPENDENT SOLUTION: Prior to extending the method to simulate body motions, the RANSE solver was extensively tested to assess the accuracy of the resistance prediction. Turbulence modelling, time integration, and the discretisation scheme used for the momentum equations were systematically investigated, see *Azcueta* (2001) for details. Here, only the latter aspect will be briefly addressed. Blending central-differencing (CDS) with upwind-differencing (UDS) is a widely used method to obtain an accurate flow prediction free from oscillations. However, for each discretisation scheme resulting from the different UDS/CDS ratios, the computed pressure distribution changes substantially. Figure 1 shows the behaviour of C_P for three systematically refined grids as an idealised sketch and Figure 2 for a real flow around a submerged hydrofoil. The strong dependency of C_P on the UDS-CDS ratio has been made used of to propose an alternative extrapolation method to the well known *Richardson extrapolation*, which attains the same accuracy computing only on the first two coarse grids. The grid-independent solution is found at the intersection of the two (basically straight) lines from the coarse and medium grid results. The time saving for not computing on the finest grid is at least a factor 10.

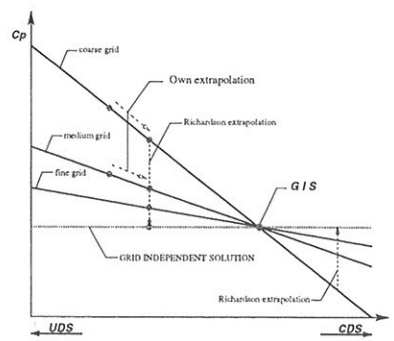

Figure 1: Idealised dependence of C_p on UDS-CDS ratio.

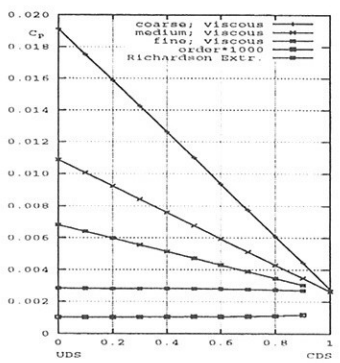

Figure 2: Dependence of C_p on UDS-CDS ratio for a real case.

[1]Wandsbeker Königstr. 62, D-22041 Hamburg, Azcueta@MTG-Marinetechnik.de

Series 60 Hull: Calculations at $F_n = 0.316$ for the straight-ahead condition and for the smallest measured drift angle ($\beta = 2.5\,°$) were performed and compared with measurements from the University of IOWA by *Longo and Stern* (1996). A coarse grid with 38,912 CVs was used. In the following, only the $0\,°$–drift case will be presented. Table 1 shows the comparison of computed results with experimental data. As shown before, the amount of CDS in UDS influences the computed pressure distribution. The results of the table are for 80% CDS. The computation under-predicts the measured total resistance coefficients by 14.6% in the model-fixed and by 5.9% in the model-free case. Thus, the inclusion of the running attitude in the calculations improves the agreement with the experiments by 10%. The computed wetted surface for the model-free condition grows by 4.7%. The computed sinkage and trim angle under-predict the measurements by about 8% and 6%, respectively. All computed resistance coefficients include the air resistance, which accounts on average for $1.5\% - 2.0\%$ of the total resistance. The CPU-time needed per time step for the model-free calculations increases by about 50% compared to the model-fixed case. The convergence history of forces and motions for the model-free condition is shown in Figure 3. These calculations were performed varying the ratio of UDS-CDS. Until 50 s, pure UDS was used. From there on, UDS was blended with CDS in 10% and 10 s steps. In the diagram, we can clearly see the dependence of the pressure resistance coefficient and the trim angle on the UDS-CDS mixing ratio. At 12.5 s the heave motion was released. The heave force (normalised for 1 m model) increases from 38.3 N to 41.5 N and balances exactly the model displacement. At 25 s the pitch motion was also released. In the converged final position (with 80% CDS) the hull is trimmed $0.1\,°$ by the bow, and the sinkage accounts for 0.36% of L. The trim moment is in balance with the trim moment caused by the towing force. The convergence histories for the $2.5\,°$–drift condition (model also free to heel) show the same behaviour as for the $0\,°$–drift condition. The heel moment and side force also show a strong dependence on the UDS-CDS ratio.

	C_T $[\times 10^{-3}]$	sinkage $[\times L]$	trim $[°]$	S_{wet} $[\times L^2]$
A: exp. (free)	5.96	−0.00392	−0.100	0.1699
B: comp. (fixed)	5.09	0.00000	0.000	0.1701
C: comp. (free)	5.61	−0.00360	−0.094	0.1779
$(B-A)/A$	−14.6%	–	–	0.1%
$(C-A)/A$	−5.9%	−8.2%	−6.0%	+4.7%
$(C-B)/B$	+10.2%	–	–	+4.6%

Table 1: Comparison of measured and calculated values ($0\,°$–drift condition)

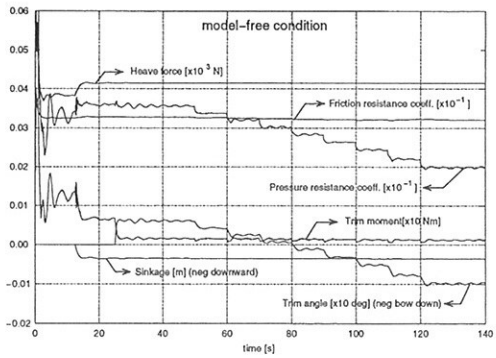

Figure 3: Convergence history (model-free)

Blunt-Bow Ship Model (Breaking Waves): The next computations are for the model of a very fat ship with a blunt bow. In this case the emphasis was on the large change in running attitude and thus resistance, as well as on the bow-wave breaking pattern and its comparison with model tests from the Ship Research Institute in Tokyo. Figure 4 shows a sketch of the used model. The Froude number based on the hull draft was $F_n = 0.7$ and the Reynolds number around $3.4 \cdot 10^6$. Three grids with substantially different fineness in the free-surface region (up to 2,147,628 CVs) were used in order to assess the grid-dependence of the computed wave patterns. Figure 5 shows the average position of the model and the contour of the free surface for the *model-fixed, sinkage-only* and *model-free* conditions. While the wave profile does not

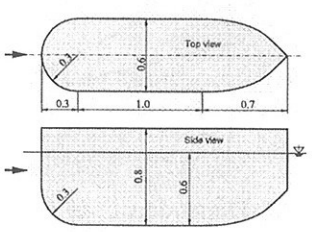

Figure 4: Sketch of the used model.

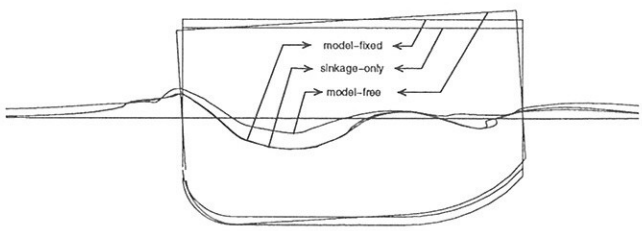

Figure 5: Model position and wave profile for the model-fixed, sinkage-only and model-free conditions.

change much for the sinkage-only condition, it looks quite different for the final trimmed attitude. The difference in free-surface shape is associated with large changes in force coefficients. The wetted surface underway increases by about 9%, the total resistance coefficient by 26%, mostly due to the predominant C_P values. Unfortunately, only measurements for the sinkage-only condition were available for validation. The computed resistance and sinkage were predicted with an accuracy of 6% and 9%, respectively. The agreement is thus quite satisfactory.

5 FREELY-FLOATING BODIES

In addition to the computation of the ship's running attitude (steady-state flow), simulations of the unsteady response of bodies released from a position out of equilibrium were performed.

Drop Tests (Plane Motion): The first example are simulations of 2-D drop tests with a prismatic wedge of 20 ° deadrise and a high aspect ratio (0.61 m × 2.44 m). Such drop tests are of relevance for investigating slamming problems. This test case was useful to validate the method with existing experimental data from *Peterson et al.* (1997). For an accurate simulation of water-entry phenomena and the associated ship responses and slamming forces, strong deformation of the free surface including jets, sprays, splashing, air trapping, and breaking waves have to be considered. The free-surface feature of the flow solver COMET has proven to be well suited for this task, *Azcueta et al.* (1999). In the present simulations the body trajectory, velocity and forces (in the planar 3-DOF) are obtained from the flow forces acting on the body, starting from the initial condition, without the need for prescribing the body motion. Unlike the experimental drop tests, the simulations do not only yield the vertical and angular accelerations, but also the transverse acceleration, as well as the water impact forces at each point of the model as a function of time. The physical model was dropped from different heights, with different weights, and with initial zero or non-zero heel angles. The numerical mesh used was relatively coarse with less than 15,000 CVs. It extended 2 m to the sides, 1 m from the keel upwards, and 1.5 m from the keel downwards. The drop height was 0.61 m. Figure 6 compares the simulated vertical and angular acceleration, vertical or impact velocity and angle of heel for an asymmetric drop tests (5 ° heel) in the medium-weight condition ($W = 293$ kg, $I_{xx} = 10.95$ kgm^2), with the corresponding experimental data. The experimental results contain mechanical vibrations associated with structural resonances, making a precise quantitative comparison between simulation and experiment difficult. Nevertheless, the comparison shows a surprisingly good agreement both for the magnitude and timing of the maximum accelerations and velocities.

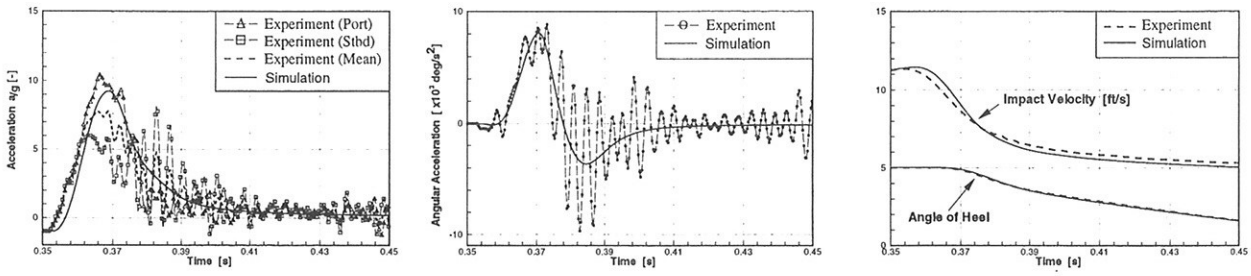

Figure 6: Comparison of measured and simulated results for an asymmetric drop test.

Boat Section (Plane Motion): The next application case is a roll extinction test (roll, heave and sway) with the midship section of a sailing boat with and without the keel. With these simulations the differences in roll damping due to the keel were quantified. Furthermore, the robustness of the numerical method for simulating large amplitude motions was addressed. The boat is a modern sailing yacht of 10 m length and 3 m beam (Dehler 33'). The numerical mesh was relatively coarse with 5,192 CVs. It was extended by a block above deck to allow large roll angles. Figure 7 on the left shows one half of the computational domain and on the right a close-up view of the hull/keel region. To induce a roll motion, the boat was initially inclined 30 ° in calm water to one side, and then suddenly let to roll freely. Figure 8 shows the time history of sway, heave and roll motion for the simulations with and without the keel for the first roll periods. The section without the keel completes the first period in 2.9 s and the roll angle decreases by 6.4 ° in this period of time, while the section with the keel needs 4.3 s to reduce the roll angle by 18.8 °. The logarithmic decrement together with the roll period were calculated for both cases. They characterise the roll damping coefficient. They are much larger for the case with the keel ($\delta_{keel} = 2.9$ to $\delta_{no-keel} = 4.2$). Another big difference

induced by the keel is in the sway response. As the hull section rights up, the keel acts like a lever pushing the hull to the left side (dotted line in the negative area in Figure 8). Without the keel the hull presses the water to the left, and gets an impulse to the right (dotted line in the positive area).

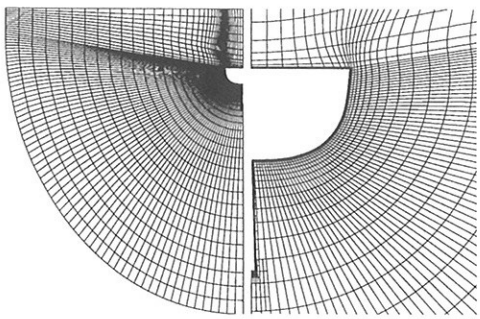

Figure 7: Numerical mesh.

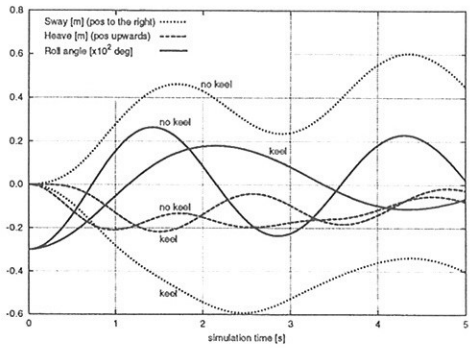

Figure 8: Time history of motions.

Sailing Boat in Planing Condition (3-D Case): The last application case is the 3-D coupled roll, pitch, sway and heave motion of the sailing boat of the example above at full speed ($v_o = 7$ m/s; $F_n = 0.7$, bare hull). The aim of this application was to show how both steady-state and transient problems can be simulated with the same computer program by simply adjusting the appropriate parameters of the numerical method. These simulations are performed for the full scale boat using the standard k-ϵ turbulence model with wall functions ($R_n = 7 \cdot 10^7$). The numerical mesh had a total of 280,000 CVs. Figure 9 shows the time history of the motions for the computation optimised to converge to the steady-state final sailing attitude. Figure 10 is for the time-accurate simulation of the boat motions. The boat was initially constrained in an inclined position (15 °) until the steady-state flow was reached. Then the 4 DOF were released simultaneously. The pitch angle converges to about 5 °. While in the first case the roll angle directly converges to near cero, in the real motion it takes many roll periods. Without the keel and rudder, the roll motion is slightly damped, but due to the forward speed more than in the 2-D case without the appendages. Due to the lack of experiments, this simulation could not be validated so far.

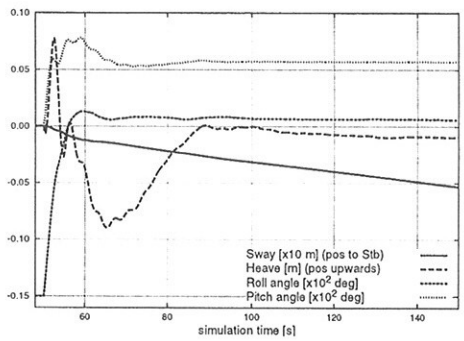

Figure 9: Motion history accelerated for convergence to steady-state sailing attitude.

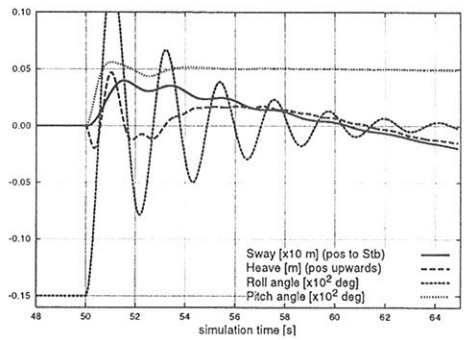

Figure 10: Motion history of the transient motion.

6 REFERENCES

Azcueta, R., 2001. *Computation of Turbulent Free-Surface Flows Around Ships and Floating Bodies.* PhD. thesis, Technical University Hamburg-Harburg (pdf file on request at rodrigo@azcueta.de).

Azcueta, R., Muzaferija, S., and Perić, M., *Computation of Breaking Bow Waves For A Very Fat Hull Ship*,7th International Conference on Numerical Ship Hydrodynamics, Nantes, 1999.

COMET, *Version 2.000 – User Manual*, ICCM GmbH, 2000.

Longo, J. and Stern, F., *Yaw Effects on Model-Scale Ship Flows*, Proceedings of the 21st Symposium on Naval Hydrodynamics, Trondheim, 1996.

Peterson, R. and Wyman, D. and Frank, C., 1997, *Drop tests to support water-impact and planing boat dynamics theory*, CSS Technical Report, Coastal Systems Station, Panama City.

Benchmarking CFD Flows - A Personal Interpretation of the G'2000 Workshop

Volker Bertram, HSVA, bertram@waves.insean.it

1. History of the validation workshops

You can compute many things and generally publications show "good" agreement or "plausible" results. The right selection of the tackled problem and the shown results help the individual author to paint a somewhat optimistic picture. Dedicated validation and benchmark projects reflect much better the true state of the art, particularly if the CFD simulation has to precede the experiments (blind test). There have been several such tests in the past where the way of displaying the results was prescribed or where the organizers did the post-processing for all submitted raw data allowing an optimal comparison. Such international benchmark comparisons give regularly a push in development activity and yield a good snapshot of the current state of the art in a particular field of CFD. The identified short-comings indicate further need for research.

The benchmark workshops show the state of the art in research, i.e. what can be achieved with great care, time and effort. In practice, results are generally worse as allowances for time and man-hours are considerably more limited.

In 1980, the SSPA-ITTC Ship Boundary Layer Workshop was held in Gothenburg. A major finding of this workshop was that integral boundary layer methods could not capture the flow in around the aftbody of ships. Research for RANSE solvers for this purpose was stimulated. In 1990, the SSPA-CTH-IIHR Workshop on Ship Viscous Flow was held in Gothenburg. A major finding was that the computations could not reproduce the 'hook' in the wake of a tanker. This indicated shortcomings in the numerical schemes and turbulence modelling. In 1994 the SRI-CFD Workshop was held in Tokyo introducing for the first time also a free-surface case. Shortcomings in turbulence modelling persisted and the RANSE solvers suffered from strong numerical dissipation which prevented the formation of a typical Kelvin wave pattern. In September 2000, the Gothenburg 2000 (G'2000) Workshop was held in Gothenburg, Larsson et al. (2000). The G'2000 workshop focussed on 'steady' free-surface flows. For the first time, the organizers asked for quantification of errors ('validation & verification') in experiments and CFD. As of now, it is undecided when and where the next workshop will be held, but it was decided that this should not be before 2005 and the next workshop shall focus on a ship in (regular) waves or a manoeuvring ship (probably in steady drift or turning rate)

2. Test cases of the G'2000 workshop

2.1. KVLCC

As in earlier workshops, a tanker was again selected for benchmarking flows without free surface. This test case was intended to evaluate CFD methods in terms of capturing the wake of ships. Wind tunnel tests measured in high resolution the flow at various cross sections in the aftbody of the tanker double-body model. Participants at the workshop were asked to compute also the flow for full-scale Reynolds number, although there are of course no experimental validation data available for this case. www.iihr.uiowa/gothenburg2000/KVLCC/tanker.html gives geometry and further parameters.

Computed total resistance values differed from the mean value between minimum and maximum by ±10% for model scale and ±12% for full scale. This was a larger fluctuation than for the free-surface cases. The derived form factors differed by ±40% while the flow patterns are quite "similar" at first glance. Thus we have massive error propagation in computing the resistance and form factors.

The KVLCC features (as the HSVA tanker of earlier workshops) a pronounced 'hook' in the axial velocity distribution at the propeller plane. This 'hook' is created by a strong bilge vortex drifting upwards as it moves downstream. The hook is qualitatively reproduced by most computations, but generally underpredicted in strength. The turbulence model influences how well the hook is captured. This was clearly demonstrated by a study of the Ecole Centrale Nantes which implemented 3 different turbulence models keeping grid and all other numerical details constant. Reynolds stress models yielded good results on relatively coarse grids (400,000 cells for Ecole Centrale Nantes, 193,000 cells for Fluent). On the other hand, computations of the Mississippi State University with almost 8 million cells and the standard k-ε model yielded just 'satisfactory' agreement with experiments. The largest differences in results appeared near the location of the propeller shaft. This can be attributed in part to

differences in the geometric modelling of this region, and in part to the sensitivity of the turbulence models to the flow in this region. Turbulence models employing wall functions were generally not capable to capture details of the streamlines near the hub (recirculation area).

The quality of the results was widely perceived as still not really satisfactory. Further research on turbulence models seems necessary.

2.2. KCS

The KRISO container ship (KCS) was selected as test case to evaluate the ability of RANSE solvers to capture wave making and ship-propeller interaction. The KCS can be considered as a typical representative of a modern, slender cargo vessel. The specified benchmark scenarios encompassed the unpropelled condition (resistance test) and the propelled condition (propulsion test), but most research groups treated only the unpropelled condition. www.iihr.uiowa/gothenburg2000/KCS/container.html gives geometry and other parameters. Two participants which did not have free-surface RANSE capabilities were still accepted for comparison. In one case the RANSE code prescribed a rigid plane surface (SVA Potsdam), in the other case the RANSE code prescribed a rigid wavy surface derived from potential flow computations (MARIN).

The total resistance was predicted higher than measured by most computations. Differences between computations and measurements for the total resistance varied between -0,3% and 11%.

Most participants captured the wave profile at the ship well except for the first steep wave crest at the bow. All RANSE computations showed a higher wave crest at the stern than measured by KRISO. This could be due to the measurement. More recent experiments of the Ship Research Institute in Tokyo found a higher wave crest which then agreed quite well with the RANSE simulations. MARIN's potential flow computations yielded a lower wave crest at the stern fitting well the older measurements of KRISO. There is so far no satisfactory explanation why inviscid computations should yield lower stern waves contrary to common expectation.

The agreement between experiments and CFD deteriorates for a wave cut further away from the ship. Modulations in the wave profile, probably due to breaking waves directly at the bow, were not captured by the RANSE simulations. Inviscid boundary element methods (as MARIN's RAPID) capture the wave pattern better, simply because (so far) RANSE solvers have to employ grids with too coarse resolution at the free surface. Downstream numerical dissipation becomes increasingly evident.

Dr. Cura of HSVA produced the best results for this the KCS using his in-house Neptun code, Fig.1. This is certainly in part due to great care and experience, but could also indicate a superiority of the level-set approach to free-surface capturing. More research is needed for a final evaluation of this matter.

The wake distribution in the propeller plane was predicted with considerable differences particularly near the propeller shaft. It is difficult to draw conclusions with respect to the methods as sometimes the propeller boss cap was included in the grid model, sometimes not. Apart from the differences in geometric modelling, different turbulence modelling will again have contributed to the differences in results.

Unfortunately only 3 participants computed the KCS in propelled condition including SVA Potsdam without free surface. Generally the agreement for the computed wake distributions is better in this case than for the unpropelled condition. Differences in turbulence modelling are largely hidden by the propeller action. As expected, the propeller action has hardly any influence of the wave formation.

2.3. Model 5415

The model 5415 of the David Taylor Research Center was investigated within a preliminary design study of the Office of Naval Research (ONR). Although never actually built, the hull form is considered as representative of a modern combatant with transom stern, flared forward sections, and sonar dome. http://www50.dt.navy.mil/5415/geomn.html gives geometry and other parameters. Since 1996 the model 5415 has been recommended as CFD validation test case by the ITTC "resistance and propulsion committee". IIHR and INSEAN have supplied extensive test data for the model 5415. This test case again focussed on free-surface capabilities of RANSE simulations.

The computed total resistance values varied around the measured total resistance (at model scale) between -7% and +6%. The errors for the residual resistance, the quantity of actual interest, are then 3 times as high. Thus the numerical resistance prediction is still plagued by considerable inaccuracy and margins of uncertainty.

The computed wave profiles at the hull agreed well with each other, but underestimated all the wave crest at the bow compared to experiments. One possible explanation was that the experiments may not have been corrected for trim, but may have given values in a ship-fixed coordinate system. This suspicion is subject to clarification. This potential source of error in interpreting the results is eliminated when comparing longitudinal wave cuts near the hull. Most CFD simulations failed to capture here the first wave crest, but the best computations (by INSEAN) showed good agreement, Fig.2. All computations underestimated the free-surface elevations further downstream which was attributed to numerical damping due to grids that are still too coarse. At least, most computations now managed to reproduce a typical Kelvin wave pattern over at least one ship length. Generally, the wave pattern was better captured than for the KCS test case. The best CFD simulations also resolved the sharp wave crest at the bow and a similar wave crest at the stern.

The wake distribution for this ship is relatively good-natured without any easy discernible vortices. Many CFD simulations reproduced the main characteristics of this 'easy' wake distribution with good agreement with the experiments.

3. Conclusions

Main conclusions and recommendations based on the workshop are:

- Validation and verification of CFD are increasingly used and have been substantially promoted due to the G'2000 workshop. Due to Fred Stern's efforts, ITTC now also recommends his procedures to quantify uncertainty. Even if these procedures are viewed with some reservation within the CFD community ("Uncertainty analysis is uncertain." The very rigorous error analyses did not remove uncertainties in evaluating methods to the extent desired by some.), there is consensus that grid refinement and convergence studies should simply be standard in scientific CFD analyses by now.
- The errors in experiments are larger than estimated by experimental facilities. The experimental results of KRISO and SRI differed for the same case by more than the sum of error margins given by the individual institutes. Obviously, the experimentalists were too optimistic.
- There has been considerable progress in free-surface RANSE simulations since the SRI workshop in Tokyo, SRI (1994). We employ now much finer grids, but these are still not fine enough. In the future, adaptive grid techniques may allow to capture the free-surface finely while not exceeding our available computer resources.
- We employ increasingly more sophisticated turbulence models, namely Reynolds stress models (RSM). There is visible progress compared to SRI (1994), but the progress is less than many in the CFD community hoped or expected.
- All G'2000 test cases are recommended by ITTC and further experiments shall extend the test data base for these hull forms.

These conclusions are the product of extensive discussions at and after the G'2000 workshop. In addition, I may add a few personal remarks:

- There are no standards for CFD plots. It was difficult for most research groups to conform with the requirements for plot formats at the G'2000 workshop. Several scientists spent more time with fulfilling the plot requirements than the actual computations needed. If ITTC would pass recommendations for CFD plots we would once and for all write macros for such plots and resort to them as far as possible for future validation workshops. Industry would benefit from such recommendations as e.g. we could more easily compare reports between various consultants. Unfortunately there are no activities towards such an overdue standardization visible at ITTC.

- Europe has by now gained a leadership position in marine CFD. Europe accounted for more submissions at the G'2000 workshop than the USA and the Far-East taken together. Also in terms of quality of the results, the Europeans were 'test winners' in most cases.
- Most validation data came from the USA and the Far-East. It is difficult to find at present funding for extensive systematic tests in Europe. Many validation tests performed in Europe suffer from an insufficient data density and/or confidentiality restrictions preventing them to become international standard test cases.

Acknowledgement

The Gothenburg 2000 Workshop was organised jointly by Lars Larsson, Fred Stern, and myself. While we discussed results and conclusions, the interpretation here is mine and does not represent an official conclusion of the workshop which is still to be published.

BERTRAM, V. (2001), *Stand der Technik CFD*, Jahrbuch der Schiffbautechn. Gesellschaft, Springer

LARSSON, L.; STERN, F.; BERTRAM, V. (2000), *Gothenburg 2000: A Workshop on Numerical Ship Hydrodynamics*, Chalmers Univ. of Technology

SRI (1994), *CFD Workshop Tokyo - An International Workshop for Improvement of Hull Form Designs*, Ship Research Institute, Tokyo

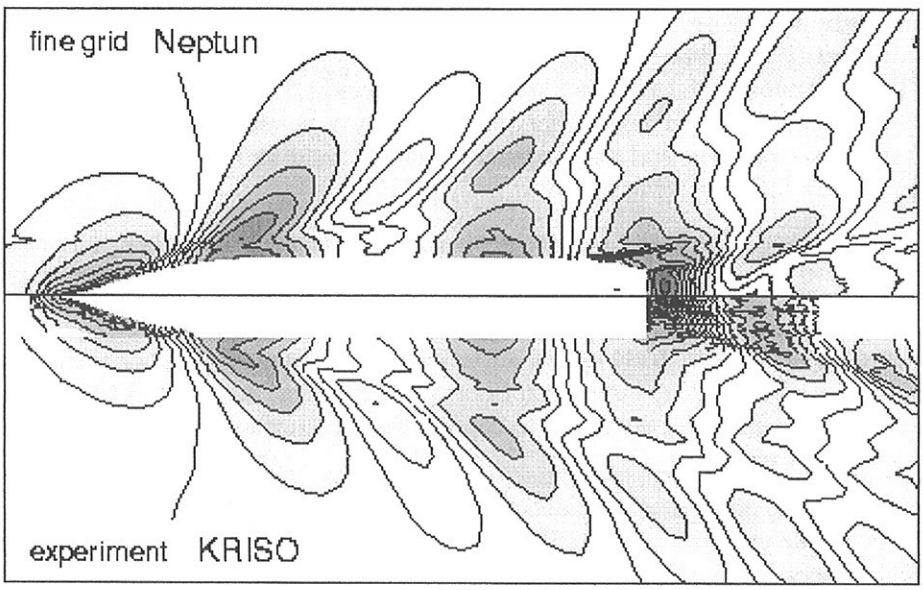

Fig.1: KCS without propeller: wave pattern measured (bottom) and Neptun code of HSVA (top)

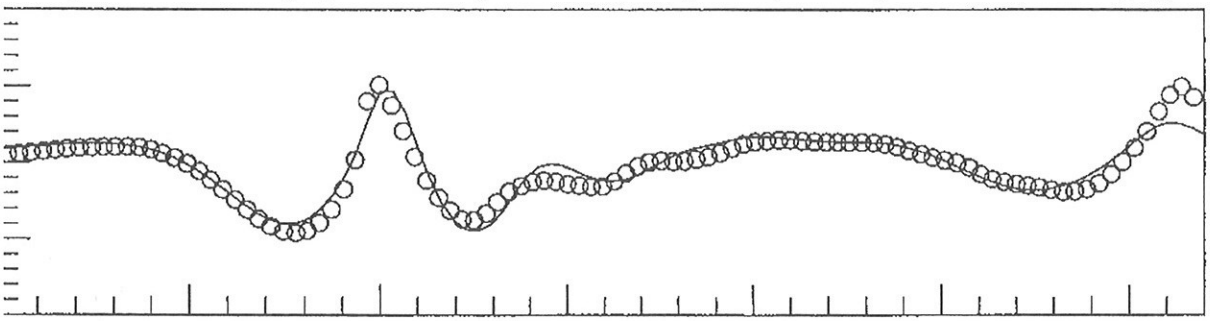

Fig.2: Comparison of CFD (---) and exp. (o) for wave cut at model 5415, both results of INSEAN

3-D CFD Preprocessors for a Nonlinear Strip Method

Volker BERTRAM, HSVA, Hamburg/Germany, bertram@waves.insean.it
Ricardo PEREIRA, MTG, Hamburg/Germany, pereira@mtg-marinetechnik.de
Ould M. EL MOCTAR, HSVA, Hamburg/Germany, elmoctar@hsva.de

Methods for calculating motions, shear forces and bending moments of a ship in waves are usually based on linear (small wave amplitude) theory. However, for dimensioning ship structures the loads in extreme waves are needed. Also for ship safety in sea waves, we need to consider extreme motions, particularly extreme roll motions up to capsize angles.

The computational effort for a three-dimensional field method or even boundary element method simulating the motions and loads on a ship at each time instant over a long time appears still beyond our current and near future computational capabilities. Thus we try to introduce simplifications that reduce the computational effort drastically without losing too much of the physical significance of the model. The tool of choice appears then to be a nonlinear strip method of some sort. The nonlinear strip method SIMBEL has been extended over the past two decades to include internal forces, propulsion system dynamics and manoeuvring. A long-term goal is to have a tool which can simulate also broaching and capsizing of vessels, i.e. a combination of extreme manoeuvring and seakeeping motions.

The method is a simulation in which large-amplitude rigid-body motions of the ship in 6 degrees of freedom, shear forces and bending moments are determined under the influence of forces and moments due to weight, Froude-Krylov pressure, radiation and diffraction pressure, speed effects (resistance and manoeuvring forces and moments due to oblique forward motion) and propeller and rudder actions. For large amplitude motions, the diffraction and radiation forces cannot be determined independently. But in principle we still couple forces $\underline{F}$ and (derivatives of) motions $\underline{u}$ using basic differential equations.

The forces can be determined by integrating the pressure over the instantaneously wetted surface of the ship. Unfortunately, the pressure distribution does not depend only on instantaneous position, velocity and acceleration of the ship, but also on the history of the motion (memory effects). This affects particularly heave and pitch motions. For linear computations in regular waves, this memory effect results in the frequency dependence of added mass and damping. For nonlinear simulations this is not quite as simple as many frequencies are present at the same time and the superposition principle no longer applies. The memory effects can be expressed in terms of convolution integrals, alternatively one considers 0 to n time derivatives of the force $\underline{F}$ and 1 to $n+1$ time derivatives of the motion $\underline{u}$:

$$B_0\underline{F}(t) + B_1\dot{\underline{F}} + B_2\ddot{\underline{F}} + ... = A_0\dot{\underline{u}}(t) + A_1\ddot{\underline{u}}(t) + ...A_2\,\dddot{\underline{u}}\,(t) + ... \tag{1}$$

The matrices A_i and B_i are determined in a preprocessing step for various drafts and inclination angles for each section. This procedure is called state space model. It is far more efficient than approaches using convolution integrals. Typical values for n (terms on left and right side) are 2 to 4. We chose 3. With increasing n problems appear with numerically induced oscillations which grow and make the simulation instable.

Stability and prediction accuracy of SIMBEL shall be improved by using some more advanced numerical methods to derive coefficients in the preprocessing stage. The added mass and damping coefficients for the linear radiation problem are now derived for each section by a 3-d Green-function method without forward speed. The forward speed effects are kept as before in the framework of the strip method. We currently validate to what extent the 3-d method improves accuracy at the ship ends and whether it improves the stability of the nonlinear strip method procedures. A standard Green function method is used to define the hydrodynamic coefficients. This was validated for a Series-60 $C_B = 0.7$ against experiments, Vugts (1971), and a standard

close-fit strip method. Heave added mass for sections are improved especially at the ship ends, as presented recently in Bertram et al. (2001). However, roll is predicted badly by both potential flow approaches as expected, Fig.1. We encountered some problems with irregular frequencies and also numerical deterioration of the code for extreme wave lengths due to insufficient grid resolution. Some problems disappeared or became acceptably small when we refined the grid, but the irregular frequency problem is fundamental. Again, we can take a pragmatic approach smoothing the curves for hydrodynamic coefficients before interpolating values for SIMBEL.

Another enhancement involves RANSE simulations using Comet for the drift force coefficients on the hull for various drafts and inclinations, El Moctar (2001). These are computed for the 3-d hull at forward speed as a preprocessing step. It is crucial to include the speed effect here as the separation characteristics and thus drift force coefficients change drastically with speed and forward speed.

The computations used 1.1 million cells for model Reynolds numbers. The drift angle is realized by changing the inflow velocity at the boundary of the domain. Thus the same grid can be used for all drift angles. The C-Box (FSG shipyard) was computed at model Reynolds numbers for drift angles between $\pm 20°$ in steps of $5°$. Appendages were not included in the computational model.

Conventional modular manoeuvring algorithms employ slender-body theories to compute the distribution of the transverse forces over the ship length. These slender-body methods assume that T/L and the change in cross sections in longitudinal direction are small. This assumption is violated at the ship ends. Viscosity is considered only by empirical corrections.

There are few experimental data on the longitudinal distribution of the transverse forces. These usually are obtained using segmented models, but it is difficult to have sufficiently thin segments at the ship ends where the gradients of the transverse forces are large. Fig.2 shows the transverse force distribution over the ship length for various drift angles for design draft. (The distribution was found to be nearly independent from draft.) The major part of the transverse force is generated near the bow. Three-dimensional separation and vortex generation create low-pressure regions in the aftbody which are responsible for the change of sign in the transverse force. These regions of negative transverse forces decrease the total transverse force and increase the yaw moment. RANSE computations of Takada and El Moctar (2000) for the ESSO OSAKA tanker and some experiments published in the literature also gave similar transverse force distributions. These contradict the usually employed asssumptions for the transverse force distributions in manoeuvring simulations, following semi-empirical formulae, or slender-body theory. A positive heel angle ϕ is towards starboard and refers to the x-axis. Positive drift angle means the ship drifts to port. The integral influence of heel on the transverse forces is small to moderate for $\pm\beta < 10°$, Fig.3. For $\beta = -10°$, the absolute value of the nondimensional side force $|Y'_H|$ for $\phi = 15°$ is 13% larger than for $\phi = 0°$. For $\beta = 10°$, $|Y'_H|$ for $\phi = 15°$ is 21% smaller than for $\phi = 0°$. Drift angle and heel angle of same sign increase the absolute value of the transverse force, opposite signs decrease the absolute value. The influence of heel on the longitudinal force is small for drift angles $\pm\beta < 10°$, Fig.3. Fig.4 shows the nondimensional yaw moment N'_H as function of drift angle and heel angle. For positive heel angle, $|N'_H|$ increases for positive drift angle and decreases for negative drift angle (opposite trend as for Y'_H). For $\phi > 0$, the yaw moment has a shallow characteristic for negative drift angles.

The method has been recently presented with more details, Pereira et al. (2001). We also started work on using virtual reality as postprocessing tools for seakeeping simulations as envisioned in Barcellona and Bertram (2000). The VRML models shall be made public such that other research groups can easily copy and adapt them as a suitable postprocessing tool.

References

BARCELLONA, M.; BERTRAM, V. (2000), *Virtual Reality for CFD postprocessing*, 1. Conf. Computer and IT Appl. in Mar. Techn., COMPIT, Potsdam

BERTRAM, V.; PEREIRA, R.; LANDRINI, M. (2001), *An enhanced nonlinear strip method for seakeeping analysis*, 16th Workshop Water Waves and Floating Bodies, Hiroshima

EL MOCTAR, O. (2001), *Numerical computations of flow forces in ship manoeuvring*, Ship Technology Research 48, pp.98-123

PEREIRA, R.; BERTRAM, V.; PUNTIGLIANO, F. (2001), *Nonlinear simulation of capsizing of undamaged ships in seaways*, to appear in Jahrbuch der Schiffbautechnischen Gesellschaft, Springer

TAKADA, N.; EL MOCTAR, O.M. (2000), *Simulation of viscous flow about ESSO OSAKA in manoeuvring motions*, 3rd Numerical towing Tank Symposium, Tjärnö

VUGTS, J.H. (1971), *The hydrodynamic forces and ship motions in oblique waves*, TNO report 150S, NSRC, Delft

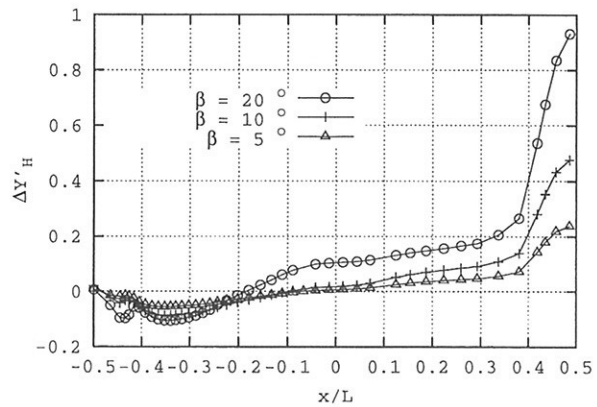

Fig.2: Transverse force distribution at design draft T

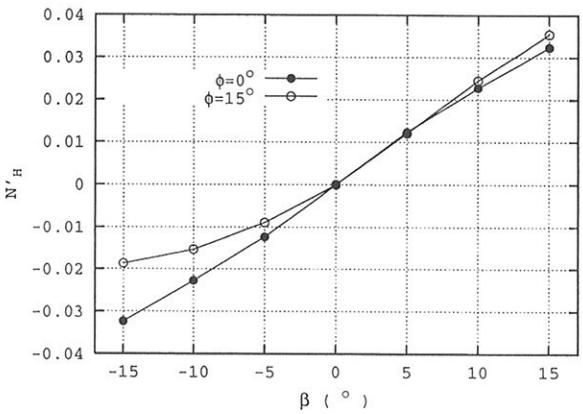

Fig.4: Yaw moment N'_H as function of drift angle and heel angle

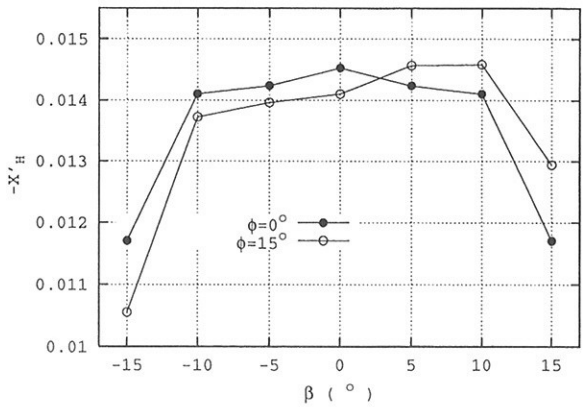

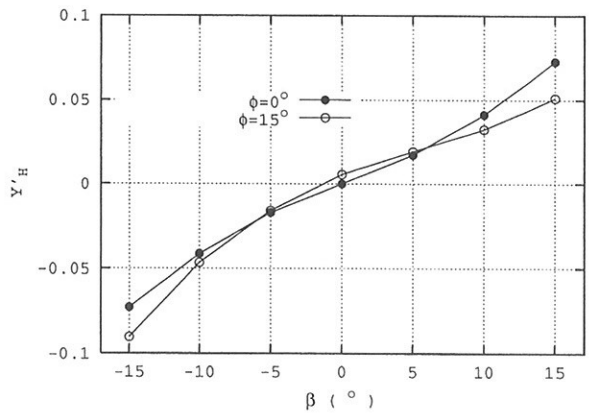

Fig.3: X'_H and Y'_H as functions of drift angle and heel angle

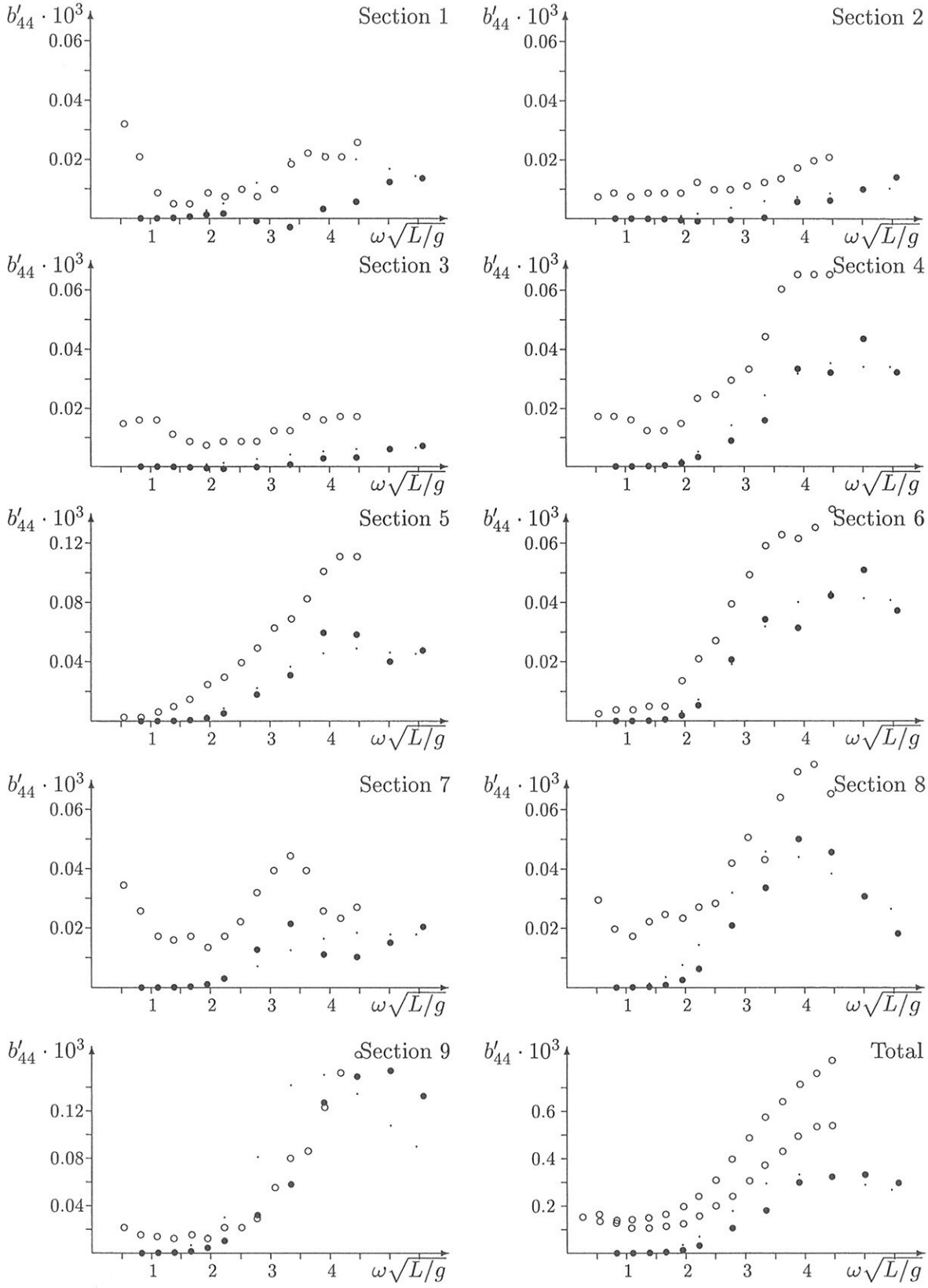

Fig.1: Series-60, $C_B = 0.7$, $F_n = 0$; hydrodynamic damping
$b'_{44} = b_{44}/(L^2 \cdot m \cdot \sqrt{g/L})$ for roll moment due to roll motion for strips and total ship;
$\circ$ Exp., $\bullet$ GFM, $\cdot$ strip method

Computation of Free-Surface Ship Flow at Full-Scale and Model-Scale Reynolds Number Using VOF Method

Yen-Jen Chen* <clive_chen@yahoo.com> Jen-Shiang Kouh* <kouhjsh@ccms.ntu.edu.tw> Shiu-Wu Chau** <chausw@cycu.edu.tw>

* *Institute of Naval Architecture and Ocean Engineering, National Taiwan University, Taiwan, R.O.C.*

** *Department of Mechanical Engineering, Chung Yuan Christian University, Taiwan, R.O.C*

Introduction

Predicting ship flow at full-scale Reynolds number is an important topic in numerical towing tank. It is also one of the advantages when comparing with a real towing tank. In the Gothenburg 2000 workshop, a VLCC hull form is used to be a test case of this topic. Reynolds number of this ship at model-scale and full-scale is $4.6*10^6$ and $2.0*10^9$, respectively. With the double model assumption, the free-surface effect is not taken into account in this case. In this workshop, many calculated results at model-scale agree well with measured data. Due to lack of measured data, the full-scale predictions are hard to be validated. However, obvious differences between model-scale and full-scale predictions can be observed in many fluid properties. It shows that Reynolds number still plays an important role, especially for the near-ship properties.

Volume-of-fluid method (VOF) is a robust method when computing ship flow with free surface. Not only for the simplified ship hull but also for the practical hull form, many researches point out that the predicted results are in good agreements with the experimental ones.

Numerical Method

The numerical computation is performed using the commercial code **COMET** developed by *ICCM*. The applied numerical scheme is known as an interface-capturing method, combining 'finite volume method' (FVM) and VOF method. The steady flow solution is computed using an unsteady approach. The numerical computation is performed until a steady-state solution is obtained. An implicit first-order scheme in time domain is applied [8]. The SIMPLE algorithm [7] is adopted to update the pressure field. The process to decouple velocity and pressure starts from solving the linearized momentum equations by using an initial pressure field. Then the continuity equation is linearized to calculate the velocity correction at cell faces in order to satisfy the mass conservation for each cell. The computation of velocity correction at cell faces also involves the pressure interpolation at cell faces. To avoid the unrealistic pressure oscillations, the pressure interpolation at cell faces follows the method of [9]. After the algebraic equation system is solved using pressure correction as dependent variable, the velocity and mass flux at cell faces are then updated. Please see [5] for more details.

Case Description and Other Details

A practical naval combatant, US Navy Combatant DTMB 5415, is chosen as the test case for this paper. It is also one of the test cases in Gothenburg 2000 workshop. The side view of this hull form is shown in Fig.8. The geometry features a wedge-shaped bow, sonar dome, flat keel and transom stern. Its principal dimensions at full-scale are listed in Table 1. It was conceived as a preliminary design for a surface combatant ca. 1980. The model-scale test condition listed in Table 2 is corresponding to the experiments from *David Taylor Model Basin* (*DTMB*) [4] in *Washington D.C.* and the *Istituto Nazionale per Studi ed Esperienze di Architettura Navale* (*INSEAN*) [6] in *Rome*, *Italy*. The advanced velocity of full-scale under this condition is 20 knots corresponding to $Fn = 0.2755$. The sinkages at this speed are given by measured data in towing tank. Both computations and experiments are in bare hull condition, where appendages and propeller are not considered. This ship is never constructed. Therefore, no full-scale experimental data exist.

Table 1: Principal dimension of full-scale ship

Length	142.037 m
Beam	17.983 m
Draft	6.179 m
Wet Surface Area	2976.7 m^2
Water Plane Area	1987.2 m^2
Displacement	12901.6 m^3
Block Coefficient	0.506
Froude Number (*Fn*)	0.2755
Reynolds Number (*Re*)	$1.46*10^9$

Table 2: Condition for model-scale test

Scale Ratio	24.832
Length (L)	5.72 m
Draft (T)	0.248 m
Wet Surface Area (S)	4.861 m^2
Advance Velocity (U_0)	2.0637 m/s
Froude Number (Fn)	0.2755
Reynolds Number (Re)	$1.26*10^7$
Sinkage at FP	-0.0028L
Sinkage at AP	-0.0009L

Both model-scale and full-scale computations are performed with fixed sinkage and trim given by experimental result. Full flow speed, i.e. without accelerating the flow from rest is used as the initial condition. The standard k-ε turbulence model, a most widely used and quite stable eddy viscosity model, is chosen for these computations. More computational details can be found in [1][2].

Computational Results

At first, the numerical method mentioned above is validated by comparing the calculated result with the experimental data at model-scale Reynolds number. The computations are performed using four grids with systematic refinement listed in Table 3. The calculated wave system using the coarsest grid (Grid A) is shown in Fig.2. The ship hull is laid between x/L = -0.5 and +0.5. Comparing with the measured one in Fig.3, this predicted wave system seems reasonable. The calculated bow and stern wave systems near ship hull are similar to the experimental results. Nevertheless, waves away from ship diffuse due to insufficient grid density. The predicted total resistance coefficient C_T is about 6% smaller than the average of measured ones (C_T = $4.27*10^{-3}$ measured by *DTMB* and $4.23*10^{-3}$ measured by *INSEAN*). In the Fig.4 and Fig.5, some difference also exist between calculated and measured axial velocity at propeller plane (x/L = 0.435).

Table 3: Arrangement for grids at model-scale

	No. of Cells	I * J * K	Predicted C_T
Grid A	100,509	123 * 25 * 31	$3.99*10^{-3}$
Grid B	211,086	123 * 54 * 31	$4.12*10^{-3}$
Grid C	432,675	123 * 99 * 35	$4.24*10^{-3}$
Grid D	841,650	123 * 194 * 35	$4.28*10^{-3}$

Because the free-surface wave system is mainly dominated by Froude number, the wave prediction at full-scale is less important than near-ship ones, such as the total resistance coefficient and the axial velocity distribution at propeller plane. In order to get better prediction in these properties, the numerical grid is refined latitudinally suggested by [3]. After the latitudinal refinement, the predicted accuracy in C_T is obviously improved. The difference between prediction using finest grid (Grid D) and the average of two measure data is less than 1%. The calculated axial velocity distribution at propeller plane using Grid B, C and D are shown in Fig.6 ~ Fig.8, respectively. Generally speaking, the calculated results qualitatively match the experimental one.

After the flow properties at model-scale are well predicted, the computations are performed at full-scale Reynolds number. Two numerical grids, Grid E and Grid F, are used to calculate the ship flow at full-scale. The arrangements of these grids listed in Table 4 are the same as Grid A and Grid B, respectively. In order to reduce the $y+$ to a reasonable range, the grid points are more concentrated on the ship hull in Grid E and Grid F. The components of calculated resistance coefficient using finest grid (Grid D for model-scale, Grid F for full-scale) are compared in Table 5. Theoretically, the pressure component of resistance coefficient is mainly dominated by Froude number. So it's reasonable the major difference consists in the shear component. The C_{F0} from *ITTC* line are $2.88*10^{-3}$ and $1.46*10^{-3}$ for model-scale and full-scale Reynolds number, respectively. Fig.11 and Fig.12 are the predicted axial velocity distribution at propeller plane for full-scale Reynolds number using two different numerical grids. Compared with the calculated results at model-scale, the axial velocity distribution is more uniform except small region close to the ship hull. At full-scale computational case, the Reynolds number is larger and the viscous effect is smaller. This trend at velocity distribution is quite reasonable and consists with the calculated results of the VLCC in Gothenburg 2000 workshop.

Table 4: Arrangement for grids at full-scale

	No. of Cells	I * J * K	Predicted C_T
Grid E	100,509	123 * 25 * 31	$2.40*10^{-3}$
Grid F	211,086	123 * 54 * 31	$2.47*10^{-3}$

Table 5: Components of resistance coefficient for model-scale and full-scale

	Pressure	Shear	Total
Model-Scale	$1.33*10^{-3}$	$2.96*10^{-3}$	$4.28*10^{-3}$
Full-Scale	$1.39*10^{-3}$	$1.08*10^{-3}$	$2.47*10^{-3}$

Conclusions

By solving RANS equations using FVM and VOF method, the free-surface ship flow at model-scale and full-scale Reynolds number are compared in this paper. With sufficient grid density, the

calculated results agree well with measured one in near-ship properties at model-scale. According to the calculated results, the free-surface wave system and the pressure component of resistance coefficient are little influenced. Reynolds number plays a more important role at the shear component of resistance coefficient and the axial velocity distribution at propeller plane. A more uniform distribution is obtained at full-scale Reynolds number because of the smaller viscous effect.

References

[1] Chen, Y. J., Kouh, J. S., Chau, S. W., "Numerical Evaluation of Free Surface Wave and Resistance of DTMB 5415", Proceedings of the Gothenburg 2000 Workshop, 2000.

[2] Chen, Y. J., Kouh, J. S., Chau, S. W., "CFD for Predicting Free-Surface Wave and Resistance of a Practical Combatant Hull", Proceeding of the 9th National Conference on Science and Technology of National Defense, 2000.

[3] Chen, Y. J., Kouh, J. S., Chau, S. W., "Assessment of Efficient Grid Arrangement for Computing Free-Surface Ship Flow Using VOF Method", Proceeding of the 13th National Conference on Society of Naval Architecture and Marine Engineering, 2001.

[4] DTMB, http://www50.dt.navy.mil/5415/

[5] COMET User Manual, Institute of Computational Continuum Mechanics GmbH, Hamburg, Germany.

[6] INSEAN, http://www.insean.it

[7] Pantankar, S. V., "Numerical Heat Transfer and Fluid Flow", Hemisphere Publishing, 1980.

[8] Peri• , M., Ferziger, J. H., "Computational Methods for Fluid Dynamics", Springer Verlag, 1996.

[9] Rhie, C. M., Chow, W. L., "Numerical Study of the Turbulent Flow Past an Airfoil with Trailing Edge Separation", AIAA Journal, Vol. 21, No. 11, pp. 1525-1532, 1983.

Fig.1: Hull form of US Navy Combatant 5415

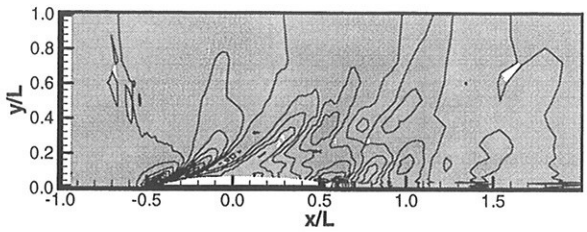

Fig.2: Predicted wave contours (model-scale, Grid A)

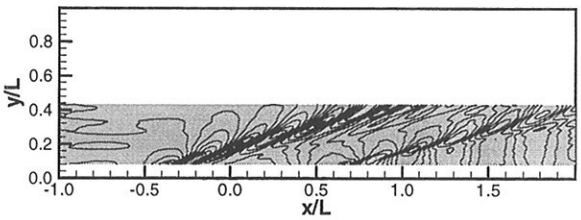

Fig.3: Measured wave contours

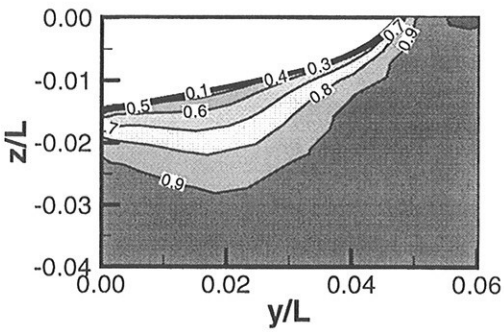

Fig.4: Predicted axial velocity distribution at propeller plane (model-scale, Grid A)

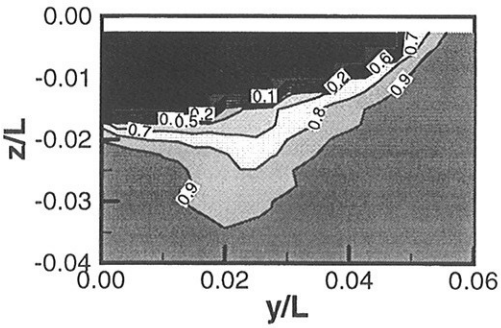

Fig.5: Measured axial velocity distribution at propeller plane

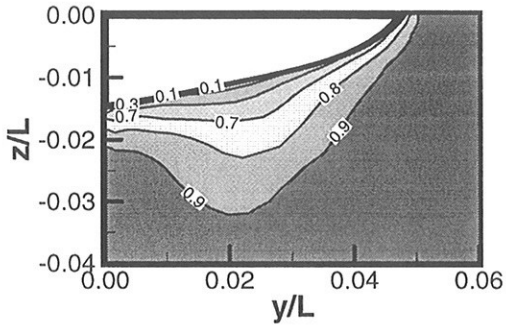

Fig.6: Predicted axial velocity distribution at propeller plane (model-scale, Grid B)

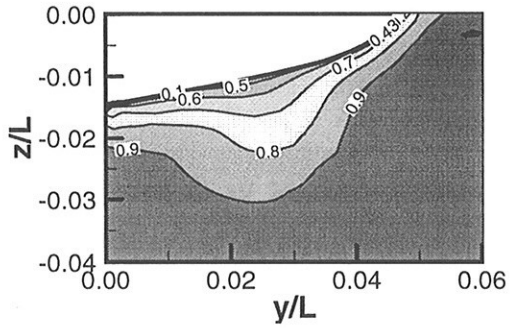

Fig.7: Predicted axial velocity distribution at propeller plane (model-scale, Grid C)

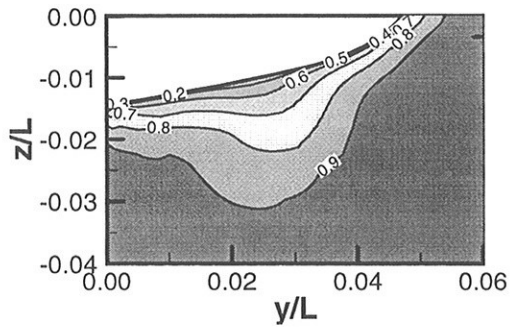

Fig.8: Predicted axial velocity distribution at propeller plane (model-scale, Grid D)

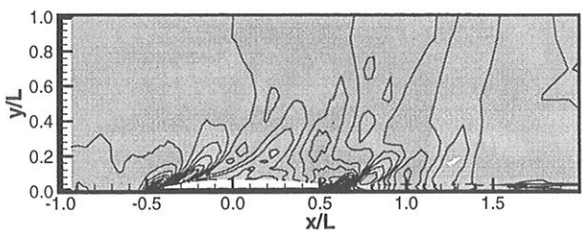

Fig.9: Predicted wave contours (full-scale, Grid E)

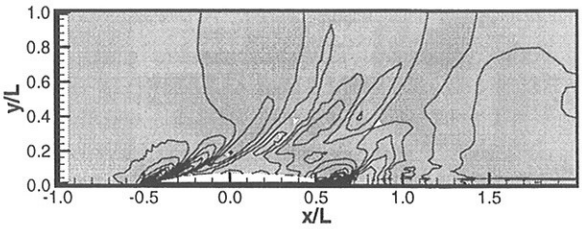

Fig.10: Predicted wave contours (full-scale, Grid F)

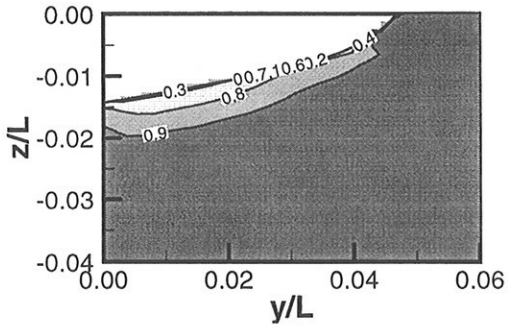

Fig.11: Predicted axial velocity distribution at propeller plane (full-scale, Grid E)

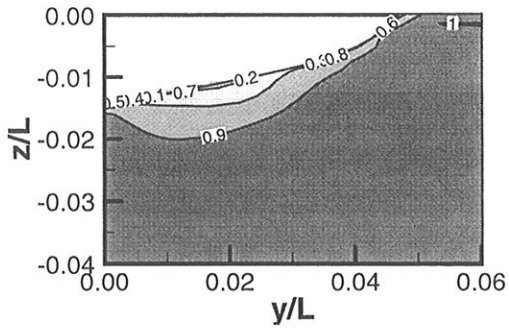

Fig.12: Predicted axial velocity distribution at propeller plane (full-scale, Grid F)

A Lagrangian Meshless Method for Free-surface Flows

Andrea Colagrossi [1], *Maurizio Landrini* [2] and *Marshall P. Tulin* [1]

1 *Ocean Engineering Laboratory*, UCSB. mpt@engineering.ucsb.edu
2 INSEAN, *The Italian Ship Model Basin*, Roma, Italy. maulan@waves.insean.it

Introduction A distinguishing feature of free-surface flows, and more in general of multi-phase flows, is that interfaces separating media can break and fragment. These circumstances are by no means rare, and are of rather great importance in engineering applications. Most of the CFD solvers proposed are usually based on the use of a grid (fixed or moving) to discretize the field equations, and then coupled to algorithms either to track or capture the interfaces.

Here, we describe a different strategy based on a mesh-less method, named Smoothed Particle Hydrodynamics (SPH) [7], where a number of fluid particles is tracked in a Lagrangian fashion to determine the evolution of the flow field. Intra- and boundary-particles interactions are modeled by discretizing the field equations and the boundary conditions through the interpolation integral technique. The method has been already used successfully to highlight some mechanisms of wave breaking [13]. See also the companion paper [6] in this Symposium. Scope of the present paper and of the presentation is summarizing our most recent experience aimed to further improve accuracy, efficiency, and applicability of the method.

Interpolation integral In meshless methods of the type here considered, the field of a generic quantity, say u, is represented through "interpolation integrals" of the form:

$$\tilde{u}(\boldsymbol{x}_P) \;=\; \int_\Omega u(\boldsymbol{x}^\star)\, W(\boldsymbol{x}_P \,-\, \boldsymbol{x}^\star; h)\, dV^\star \;, \qquad (1)$$

where $W(\boldsymbol{x}_P - \boldsymbol{x}^\star; h)$ is a weight function and h is a measure of the support of W, *i.e.* where W differs from zero. Physically, h is also representative of the domain of influence of $\boldsymbol{x}^\star$. In the SPH framework, $W(\boldsymbol{x}_P - \boldsymbol{x}^\star)$ is called *smoothing function* or *kernel*, and has the following properties:

- $W(\boldsymbol{x}_P - \boldsymbol{x}^\star) \geq 0$ for $\boldsymbol{x}_P \in \Omega_{x^\star} \subset \Omega$, and zero otherwise.
- $\int_\Omega W(\boldsymbol{x}_P - \boldsymbol{x}^\star, h) dV^\star \;=\; 1$
- $W(\boldsymbol{x}_P - x^\star, h)$ decreases monotonously as $\|\boldsymbol{x}_P \,-\, \boldsymbol{x}^\star\|$ increases.

In the limit for $h \to 0$, the kernel function W becomes a Dirac delta function, and therefore

$$\lim_{h \to 0} \int_\Omega u(\boldsymbol{x}^\star)\, W(\boldsymbol{x}_P \,-\, \boldsymbol{x}^\star; h)\, dV^\star \;\equiv\; u(\boldsymbol{x}_P) \;.$$

Formally, we can deduce approximations to any derivative of the field u by differentiating (1). For example:

$$\begin{aligned} \nabla u \simeq \nabla \tilde{u}(\boldsymbol{x}_P) \;&=\; \int_{\partial\Omega} u(\boldsymbol{x}^\star) W(\boldsymbol{x}_P - \boldsymbol{x}^\star; h)\, \boldsymbol{n}\, dS^\star \\ &+\; \int_\Omega u(\boldsymbol{x}^\star)\, \nabla W(\boldsymbol{x}_P - \boldsymbol{x}^\star; h)\, dV^\star \;. \end{aligned} \qquad (2)$$

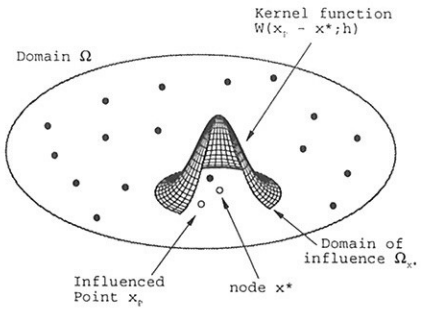

Fig. 1: Sketch of the kernel function

Kernel functions In practical computations the smoothing function affects both the CPU requirements and the stability properties of the algorithm. We have experienced b-spline kernels of third and fifth order, as well as the Gaussian kernel:

$$W(s,h) \;=\; \frac{1}{\pi h^2}\, e^{-s^2} \;, \qquad (3)$$

where $s = \|\boldsymbol{x}_P - \boldsymbol{x}^\star\|$. This kernel has not compact support. Therefore, we introduced a cut-off limit and renormalized the kernel to match the property of unit integral. The use of (3) resulted in a more efficient code.

Interpolation of scattered data If data samples u_j of the field u are known, a naive discrete approximation of (1) gives:

$$\tilde{u}(\boldsymbol{x}_P) \simeq \langle u(\boldsymbol{x}_P) \rangle \;=\; \sum_j u_j\, W(\boldsymbol{x}_P \,-\, \boldsymbol{x}_j; h)\, dV_j \;, \qquad (4)$$

and a discrete approximation to the gradient (2) is:

$$\langle \nabla u(\boldsymbol{x}_i) \rangle \;=\; \sum_j u_j \otimes \nabla W_j(\boldsymbol{x}_i)\, dV_j \;, \qquad (5)$$

where, for brevity, $W_j(\boldsymbol{x}_i) = W(\boldsymbol{x}_i - \boldsymbol{x}_j; h)$. The surface integral contribution in (2) is usually neglected.

We observe that the above approximations, when used on data arbitrarily scattered, do no allow to reproduce correctly very simple constant or bi-linear functions. In general, we have:

$$\textstyle\sum_j W_j(\boldsymbol{x}_i) dV_j \neq 1 \qquad \sum_j \boldsymbol{x}_j W_j(\boldsymbol{x}_i) dV_j \neq \boldsymbol{x}_i \qquad (6)$$

$$\textstyle\sum_j \nabla W_j(\boldsymbol{x}_i) dV_j \neq \boldsymbol{0} \quad \sum_j \boldsymbol{x}_j \otimes \nabla W_j(\boldsymbol{x}_i) dV_j \neq \boldsymbol{I} \qquad (7)$$

Therefore, a constant field will not be reproduced correctly and it will introduce a spurious gradient, etc. The capability of "reproducing" given functions is clearly related to the convergence

properties of the method [1]. Here, we summarize some of the techniques we have compared with (4). A first variant, based on the Shepard interpolation technique [10], consists in using:

$$\begin{aligned} \langle u_i \rangle &= \textstyle\sum_j u_j \, W_j^S(\boldsymbol{x}_i) \, dV_j \\ W_j^S(\boldsymbol{x}_i) &:= W_j(\boldsymbol{x}_i) \Big/ \textstyle\sum_k W_k(\boldsymbol{x}_i) \, dV_k \end{aligned} \tag{8}$$

which allows to reproduce exactly constant functions and gradients of constant functions. Compared with the basic discretization (4), the additional computational cost for (8) is rather small.

It is possible to correct to higher orders the SPH approximation. By introducing a linear operator $\boldsymbol{\beta}(\boldsymbol{x}_i)$ [4], we can require that the modified kernel

$$W_j^{MLS}(\boldsymbol{x}_i) = [\, \beta_0(\boldsymbol{x}_i) + \beta_1(\boldsymbol{x}_i) x_j + \beta_2(\boldsymbol{x}_i) y_j \,] \, W_j(\boldsymbol{x}_i) \tag{9}$$

reproduces linear functions. In this case, the computation of $\beta_k(x_i)$ needs the solution of a 3×3 linear algebraic problem for each computational point (*i.e.* for each particle).

Cheaper and effective corrections can be obtained simply by rewriting the basic approximation in the symmetric form:

$$\langle \nabla u_i \rangle = \sum_j (u_j - u_i) \otimes \nabla W_j(\boldsymbol{x}_i) \, dV_j \ , \tag{10}$$

which removes the spurious gradient of a constant field. Also, using symmetric forms as (10) improves the stability properties of the system.

The inequalities (7) can be corrected by using a linear operator $\boldsymbol{G}(\boldsymbol{x}_i)$ on ∇W^S and requiring that:

$$\sum_j \boldsymbol{x}_j \otimes \boldsymbol{G}(\boldsymbol{x}_i) \left[\nabla W_j^S(\boldsymbol{x}_i) \right] dV_j = \boldsymbol{I} \ . \tag{11}$$

It follows:

$$\boldsymbol{G}(\boldsymbol{x}_i) = \left[\sum_j \nabla W_j^S(\boldsymbol{x}_i) \otimes \boldsymbol{x}_j \, dV_j \right]^{-1} \ . \tag{12}$$

If the form (10) is adopted, the correction function reads:

$$\boldsymbol{H}(\boldsymbol{x}_i) = \left[\sum_j \nabla W_j(\boldsymbol{x}_i) \otimes (\boldsymbol{x}_j - \boldsymbol{x}_i) \, dV_j \right]^{-1} \ , \tag{13}$$

which has been renamed to be distinguished from (12).

Discretized fluid flow equations The field equations for fluid motions can be discretized following one of the two approaches: 1) *Galerkin Method.* The starting point is a weak form of the fluid-flow equations as for finite elements approaches, and then use is made of the interpolation integral techniques. This approach is usually Eulerian. Galerkin methods [1, 4] are usually built to "reproduce" correctly linear fields, and to conserve globally momentum and angular momentum. Mass is not necessarily conserved. The computational cost is by far larger than the collocation method.

2) *Collocation Method.* The (strong form of) fluid-dynamic equations are enforced in a finite number of points, which are also the points used to write the integral interpolations. The method is usually Lagrangian and the interpolation points can be physically interpreted as fluid particles.

The SPH approach belongs to last category. We will discuss different SPH approximations to the Euler Equations. The general form of the discrete equations is:

$$\langle \frac{D\rho}{Dt} \rangle_i = -\rho_i \sum_j \mathcal{M}_{ij} \qquad \langle \frac{D\boldsymbol{u}}{Dt} \rangle_i = -\frac{1}{\rho_i} \sum_j \boldsymbol{\mathcal{F}}_{ij} + \boldsymbol{f}_i \tag{14}$$

describing the evolution of density and momentum, respectively, of the i-th particle. $\mathcal{M}_{ij}$ and $\boldsymbol{\mathcal{F}}_{ij}$ are particle-to-particle interaction terms, discussed below, and $\boldsymbol{f}_i$ is a body force term. Because of the kernel properties, summations are extended only to those particles within the radius of interaction (proportional to h).

In the basic implementation, the interaction terms $\boldsymbol{\mathcal{F}}_{ij}$ models the pressure interactions and, therefore, contain the pressure p_i which, in the present implementation, is determined through the value of the density ρ_i and an equation of state of the form $p = p(\rho) + C$, in which the parameters are chosen to have maximum oscillations of the density of order 1% of a reference value ρ_0. In practice, this is accomplished by choosing the sound speed $c_s = dp/d\rho$ at least ten times larger than the highest fluid velocity expected in the simulation. The use of the actual sound speed in water would imply time-steps too small for being practical. By assuming the fluid *weakly compressible*, we avoid the solution of the Poisson equation for the pressure and, therefore, the method does not require the solution of an algebraic problem, thus reducing memory occupation and increasing the efficiency.

In practice, we have tested the following reproducing (or partially reproducing) forms:

$$\begin{aligned} A &\begin{cases} \mathcal{M}_{ij} &= (\boldsymbol{u}_j - \boldsymbol{u}_i) \cdot \nabla W_j(\boldsymbol{x}_i) dV_j \\ \boldsymbol{\mathcal{F}}_{ij} &= (p_j - p_i) \nabla W_j(\boldsymbol{x}_i) dV_j \end{cases} \\ B &\begin{cases} \mathcal{M}_{ij} &= \boldsymbol{u}_j \cdot \boldsymbol{G}(\boldsymbol{x}_i) \nabla W_j^S(\boldsymbol{x}_i) \, dV_j \\ \boldsymbol{\mathcal{F}}_{ij} &= p_j \, \boldsymbol{G}(\boldsymbol{x}_i) \nabla W_j^S(\boldsymbol{x}_i) \, dV_j \end{cases} \\ C &\begin{cases} \mathcal{M}_{ij} &= (\boldsymbol{u}_j - \boldsymbol{u}_i) \cdot \boldsymbol{H}(\boldsymbol{x}_i) \nabla W_j(\boldsymbol{x}_i) dV_j \\ \boldsymbol{\mathcal{F}}_{ij} &= (p_j - p_i) \boldsymbol{H}(\boldsymbol{x}_i) \nabla W_j(\boldsymbol{x}_i) dV_j \end{cases} \end{aligned} \tag{15}$$

The discrete volume element dV_j is computed by giving to the j-th particle the m_j, with a local value of the density

$$dV_j = m_j / \rho_j \ . \tag{16}$$

Mass conservation is therefore intrinsic in the method.

We observe that none of the forms (15)A–C satisfies the property:

$$\boldsymbol{\mathcal{F}}_{ij} + \boldsymbol{\mathcal{F}}_{ji} = 0 \ , \tag{17}$$

which guarantees the local conservation of momentum and angular momentum. Therefore, we used also the forms:

$$D-E\begin{cases}\mathcal{M}_{ij} &= (\boldsymbol{u}_j-\boldsymbol{u}_i)\cdot\nabla W_j(\boldsymbol{x}_i)dV_j\\ \boldsymbol{\mathcal{F}}_{ij} &= \begin{cases}(p_j+p_i)\nabla W_j(\boldsymbol{x}_i)dV_j\\ \rho_i\rho_j(\frac{p_j}{\rho_j^2}+\frac{p_i}{\rho_i^2})\nabla W_j(\boldsymbol{x}_i)dV_j\end{cases}\end{cases} \tag{18}$$

which satisfy (17) and imply a discretized pressure gradient in the forms:

$$\langle\nabla p\rangle_i = \begin{cases}\sum_j(p_j+p_i)\nabla W_j(\boldsymbol{x}_i)\,dV_j\\ \sum_j\rho_i\rho_j(\frac{p_j}{\rho_j^2}+\frac{p_i}{\rho_i^2})\nabla W_j(\boldsymbol{x}_i)\,dV_j\end{cases}, \tag{19}$$

respectively [3, 7]. Both forms in (19), when points are arbitrarily scattered, do not reproduce correctly a uniforms field of pressure. This is their main drawback, leading also to the so-called "tension instability" [2, 11], consisting in the formation of particle clumps which destroy the quality of the solution. On the other hand, the implementation of (18) results in a quite efficient code, in which the tension instability can be reduced and controlled by properly choosing the kernel function [9] or other corrections to the discrete equations [8].

Finally, the motion of the particles is described by:

$$\frac{d\boldsymbol{x}_i}{dt}=\boldsymbol{u}_i+\varepsilon\sum_j m_j\frac{\boldsymbol{u}_{ij}}{\hat{\rho}_{ij}}W_j(\boldsymbol{x}_i)\;, \tag{20}$$

where the latter term weakly ($\varepsilon=0{\cdot}5$) averages the velocity field around the particle and prevents particles inter-penetration [7].

Regardless the discrete form actually adopted, the characteristic discretization parameters are: (i) the ratio $h/\mathcal{L}$, where $\mathcal{L}$ is a typical length scale of the problem, and (ii) the number $\mathcal{N}$ of particles within the interaction radius. Roughly speaking, the ratio $\Delta x = h/\mathcal{N}$ is the equivalent of the grid spacing in mesh-based methods. It can be shown that the convergence of the method requires $N\to\infty$ as $h,\Delta x\to 0$. This theoretical result is computationally rather demanding. Usually, $\mathcal{N}=30-50$, while $h/\mathcal{L}$ is problem-dependent. The resulting total number of particles depends on the application considered, in some cases being of order of 10^5.

Artificial viscosity A term $\Pi_{ij}\nabla W_j(\boldsymbol{x}_i)dV_j$ is usually included in the discretized momentum equation with the purpose to increase the stability properties of the numerical algorithm. We adopted the general form

$$\Pi_{ij}=\frac{-\alpha\hat{c}_{s,ij}\mu_{ij}+\beta\mu_{ij}^2}{\hat{\rho}_{ij}}\qquad \boldsymbol{u}_{ij}\cdot\boldsymbol{P}_{ij}<0 \tag{21}$$

and zero otherwise [7]. In Eq. (21) the compact notation $f_{ij}:=f_i-f_j$, $\hat{f}_{ij}:=(f_i+f_j)/2$ is used, and c_s is the speed of sound, which follows from the state equation. In our simulations $\beta=0$ always, and the influence of α has been checked in the range 0·005-0·02.

Searching algorithm and time integration The number of particles interacting with, say, the i-th particle is finite because the kernel has a compact support. To compute the interaction terms $\mathcal{M}_{ij},\boldsymbol{\mathcal{F}}_{ij}$, we need a searching algorithm to find efficiently all the neighbors. We use a background Cartesian grid, larger than the fluid domain, with square cells of size equal to interaction radius. Therefore, a particle within a box will interact only with the particles within that box and the surrounding eight boxes, as shown in figure 2. The only operation needed is to build the list of particles within a given box and the list of indices pointing to the box containing a given particle. This operation is computationally rather cheap, and it is updated periodically.

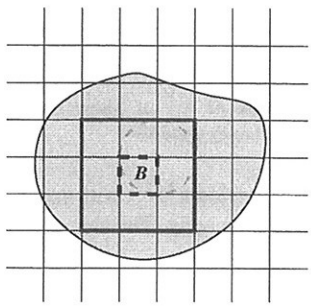

Fig. 2: Searching strategy. The particle within the dashed box B can, at most, interact with the particles within the thick frame. The dashed circle shows the radius of interaction. The network of boxes overlaps the fluid domain (grey shaded area).

Once the interaction terms have been computed, the evolution equations (14), (20) can be stepped forward in time by any ODE numerical-integration scheme. We presently use a second-order predictor-corrector scheme, with a dynamic choice of the time step δt according to stability constraints related (i) to the local speed of sound, and (ii) to the local value of the particle acceleration. The resulting stability requirements are quite stringent (a weak point of the pseudo-compressible SPH formulation) and the time step *locally* requested can be easily extremely small. To alleviate the problem, we employed an individual time-stepping algorithm [5]: the particles are sorted into $k=0,\ldots,L$ levels such that $\delta t_{max}/2^k$ is small enough for the particles of the k-th level. Then, the particles evolve hierarchically according their own time step and after 2^L sub-steps all the particles have reached the same physical time.

We remark that, although the evolution equations (14), (20) are coupled, the interaction terms $\mathcal{M}_{ij},\boldsymbol{\mathcal{F}}_{ij}$ can be evaluated independently of the others, and without the solution of an algebraic system. Therefore, the memory requirement is just proportional to the number N of the particles, and the algorithm is well suited for use on parallel computers.

Free-slip condition on solid boundaries The usual way to enforce the no-penetration boundary condition in SPH computations is by using "repellent" particles [7]. Differently, we propose to mimic the body by "ghost particles" with density, pressure and velocity deduced from the those of the physical particles adjacent to the solid boundary.

Let us consider a plane wall, as in figure 3. At each time step,

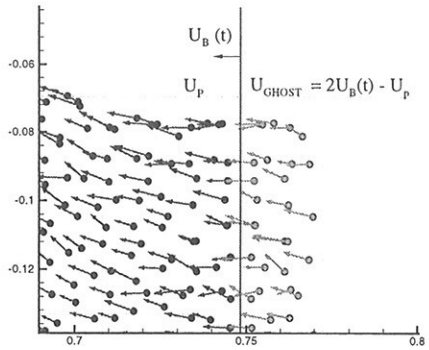

Fig. 3: Example of use of ghost particles to enforce the no-penetration boundary condition

all the particles within a layer with thickness h from the wall are mirrored within the body. The characteristics given to the ghost particles are:

$$\begin{array}{lll} \boldsymbol{x}_{i_G} = 2\boldsymbol{x}_w - \boldsymbol{x}_i & u_{n\,i_G} = 2U_{nw} - u_{n\,i} & p_{i_G} = p_i \\ & u_{t\,i_G} = u_{t\,i} & \end{array} , \tag{22}$$

where u_n and u_t are the tangential and normal velocity components to the boundary $\partial\Omega_w$, and U_{nw} is the local displacement velocity of the body. For plane boundaries, eqs. (22) allow to fulfill exactly the free-slip condition. For arbitrary shaped boundaries, the mirroring is performed point-wise by considering the local tangent plane. Corrections have to be enforced to avoid an excess of ghost-mass, so to speak. In the practice, comparison with BEM computations in case of surface piercing bodies gave very good results also in case of arbitrary shaped boundaries.

Free-surface conditions The free surface is a material boundary, and using a Lagrangian tracking of particles fulfills implicitly the kinematic free-surface boundary condition. Moreover, consistently with the dynamic free-surface boundary condition, the discretized pressure field for non-reproducing formulations, *e.g.* Eq. (19), falls to zero approaching the free surface, which can be considered spread over the support of the kernel. Therefore, also the dynamic free-surface boundary condition is implicitly verified, if other boundary conditions are not explicitly enforced. In practice, along the free-surface contour, small oscillations of the pressure are observed.

For the reproducing formulations (15)A-C, the pressure condition along the free surface has to be enforced explicitly by the concept of ghost particles. The method is more complex and requires (i) the explicit capturing of the particles on the free surface and (ii) the introduction of ghost particles according to

$$p_{i_G} = 0 \qquad u_{n\,i_G} = 0 \qquad u_{t\,i_G} = 0 \tag{23}$$

with a constant density ρ_0 such that $p(\rho_0) = 0$.

For non-reproducing formulations, a more strictly condition on the pressure can be obtained by the periodic re-initialization of the density distribution using the Shepard representation

$$\langle \rho_i \rangle = \sum_j W_j^S(\boldsymbol{x}_i) m_j \tag{24}$$

and enforcing $\rho = \rho_0$ for the free-surface particles. The re-initialization of the density field reduces also high-frequency oscillations due to the weak-compressibility (in practice sound waves) and helps in keeping ordered the particles field.

Practical details of the implementation and results from selected test cases will be presented at the Symposium.

Acknowledgement This work has been supported as part of a program for the simulation of ship breaking waves by the Ship Hydrodynamics Program of ONR, managed by Dr. Pat Purtell.

References

[1] Belytschko T., Krongauz Y., Dolbow J. and Gerlach C., On the completeness of meshfree particle method, *Int. J. Num. Meth. Engng,* **43**, pp. 785-819 (1998).

[2] Belytschko T., Guo Y., Liu W.K. and Xiao S.P., A unified stability of meshless particle method, *Int. J. Num. Meth. Engng,* **48**, pp. 1359-1400 (1999).

[3] Bonet J. and Lok T-SL., Variational and momentum preserving aspects of smoothed particle hydrodynamics (SPH) formulation, *Comp. Meth. Appl. Mech. Engng.* **180**(1-2), pp. 97-116 (1999).

[4] Dilts G.A., Moving least square particle hydrodynamics I: consistency and stability, *Int. J. Num. Meth. Engng,* **44**, pp. 1115-1155 (1999).

[5] Hernquist L. and Katz N., TREESPH - a unification of SPH with the hierarchical tree method, *The Astroph. J. Supp. Ser.* **70**, pp. 419-446 (1989).

[6] Landrini M., Colagrossi A. and Tulin M.P., Numerical Studies of Wave Breaking Compared to Experimental Observations, 4^{th} Num. Towing Tank Symp. (Ed. V. Bertram), Hamburg (2001).

[7] Monaghan J.J., Simulating Free-Surface Flows with SPH, *J. Comp. Phys.* **110**, pp. 399-406 (1994).

[8] Monaghan J.J., SPH without a Tensile Instability, *J. Comp. Phys.* **159**, pp. 290-311 (2000).

[9] Morris J., A study of the stability properties of smooth particle hydrodynamics, *Publ. Astron. Soc. Aust.* **13** (1996).

[10] Shepard D., A two-dimensional interpolation function for irregularly spaced data, Proc. of 23^{rd} *ACM Nat. Conf.*, pp. 517-524 (1968).

[11] Swegle J.W., Hicks D.L. and Attaway S.W., Smoothed Particle Hydrodynamics Stability Analysis, *J. Comp. Phys.* **116**, pp. 123-134 (1995).

[12] Randles P. and Libersky R., Smoothed Particle Hydrodynamics: Some recent improvement and applications, *Comput. Meth. Appl. Mech. Engng.* **139**, pp. 375-408 (1996).

[13] Tulin M.P. and Landrini M., Breaking Waves in the Ocean and around Ships, 23^{rd} Symp. on Naval Hydrod., Val de Reuil, France (2000).

Free-surface Flow After a Dam break: A Comparative Study

Giuseppina Colicchio [1,3], *Andrea Colagrossi* [2], *Marilena Greco* [3] and *Maurizio Landrini* [3]

1 *Department of Civil & Environmental Engineering*, Southampton University, UK
2 *Ocean Engineering Laboratory*, UCSB.
3 INSEAN, *The Italian Ship Model Basin*, Roma, Italy. maulan@waves.insean.it

Introduction

The water flow after the sudden break of a dam is schematically represented as an initially rectangular column of fluid supported by a horizontal bottom, limited by a wall on one side and free to evolve on the other one. The flow is characterized by the

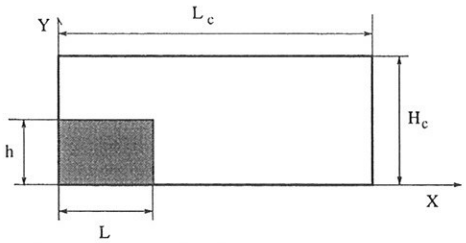

Fig. 1: Variables definition for the dam-break problem. The shaded area represents the initial configuration of the water domain.

development of a tongue of liquid quickly spreading along the horizontal boundary without any sign of free-surface breaking. This problem has been widely investigated numerically because, besides its practical meaning, it is a clean test case to verify and validate methods handling large deformations of the free surface. Here, we present a comparative study between 1) the Boundary-Element Method for potential-flow, 2) the Smoothed Particles Hydrodynamics method for the Euler equations, and 3) the direct solution of the Navier-Stokes equations coupled with the Level Set method for the capturing of the free surface.

Numerical modelling

Boundary-Element Method (BEM) This is a well known approach to deal with free-surface flows. In this method, the free surface is sharply defined and the problem is solved by integral equations which require discretization and tracking of the boundary only. The resulting method is quite efficient, relatively easy to implement, capable to deal with rather complex geometries. Within the underlying hypothesis, usually the potential-flow assumption, the results achievable are among the most accurate and reliable. On the other hand, any computation stops when free-surface breaking and fragmentation occur.

In our implementation [2], the free-surface motion is tracked in a Lagrangian way, with the dynamics following from the Bernoulli equation. The velocity potential at each time step is computed by a panel method with linear shape functions for the unknowns (the normal gradient on the free surface and the potential on solid boundaries). Local regriding is occasionally used to maintain high resolution, and the time step is adjusted dynamically according to the velocity of the boundary points.

Smoothed Particle Hydrodynamics (SPH) This method is presented in two companion papers in this Symposium [1, 4]. In short, the fluid is divided into a collection of particles interacting each other through suitable evolution equations. The method is rather robust, even for large free-surface fragmentation and folding, efficient, and relatively easy-to-code in its most naive implementation. Less obvious is dealing with no-slip body boundary conditions, and modelling turbulent flows. Stability of the method can be an issue. Finally, in the present implementation, only the flow in water has been modeled and, in principle, this limits the validity of the long-time post-splashing evolution.

Level-set method (LSM) The evolution both of the air and of the water is modeled. A single computational grid is used to discretized the two phases, and any fluid property, say f, is treated as a continuous field, defined as:

$$f = \chi f_{air} + (1 - \chi) f_{water} \tag{1}$$

where a rapid but smooth transition from one phase to another is guaranteed by the bridge function $\chi \in [0, 1]$. Clearly, most of the difficulties are shifted to the treatment of the function χ.

In the following, we will use a Level Set approach to define the transition from one phase to another, while the evolution of the flow field is described by the Navier Stokes equations for an incompressible fluid.

All the quantities entering the field equations are referred to air or water according to the value of the bridge function χ. A laminar flow is assumed. The field equations are discretized using a finite-difference scheme, with second-order accuracy both in time and space. The spatial discretization is based on an upwind ENO scheme [7]. The time discretization is based on the split time-step method [3] and on a varible density projection.

In the computations, two different boundary conditions are applied on solid boundaries: a free-slip condition enforcing just the no-penetration constraint, or a no-slip condition.

The air-water interface is not explicitly followed but its position is captured as the zero level of a scalar field ϕ, defined in the whole computational domain [6]. More specifically, ϕ has the meaning of a signed distance function (or level function) from the interface: we associate to each point its absolute distance from the interface taken with a positive sign if the point is in air and with a negative sign if the point is in water, so that the interface is the loci where $\phi = 0$. The level function evolves in time according to

$$\phi_t + \boldsymbol{u} \cdot \nabla\phi = 0 \tag{2}$$

where $\boldsymbol{u}$ is the fluid velocity. Therefore, the zero level move exactly with the velocity of the interface.

Clearly, the fluid velocity field does not preserve the meaning of ϕ and a reinitialization procedure is regularly applied. The reinitialization step is based on the distance-function property $|\nabla\phi| = 1$. A pseudo evolution in time according to the equation

$$\phi_\tau + \frac{\nabla\phi}{|\nabla\phi|}\nabla\phi = 1 \tag{3}$$

assures that this property is satisfied when stationary conditions are achieved. The direction of propagation of the signal is from the zero level towards regions with higher absolute values of the distance functions. The generally used upwind schemes could violate this direction of propagation in points next to the free surface, altering the position of the level zero. To avoid this error no upwind scheme is applied where ϕ changes sign, but it is modified preserving both the property $|\nabla\phi| = 1$ and the ratio of the function across the interface [8].

The bridge function χ used in (1) is here defined through the distance function ϕ. In practice, χ cannot be arbitrarily steep across the fluid interface to avoid difficulties in the solution of the field equations. Physically, this means that the interface is not sharply defined but rather it is smeared over a transition layer of thickness δ. On the other end, the actual shape of χ becomes

more important when the transition layer between the two media becomes larger. In our experience, the sinusoidal shape

$$\chi = (1 + \sin(\pi\phi/\delta))/2 \qquad -\delta/2 < \phi < \delta/2$$

works well for a broad range of δ. Also, from a practical point of view, the choice of the compound variable becomes important both to reduce δ and to maintain the quality of the solution for a given transition layer.

Discussion

Flow development after the dam break The first case considered reproduces one of the experiments in [5], with $L = h = 2.25''$ (about 5.7 cm). The following non-dimensional variables are used: $x = X/h$, $y = Y/h$, $p = P/(\rho g h)$, $f = F/(\rho g h L)$ and $\tau = t\sqrt{g/h}$.

Fig. 2 gives the propagation in time τ of the water-front toe, x_{max}, after the dam break. All the codes show the fluid accelerating smoothly and reaching an almost stationary value of the velocity. We note that, at $\tau = 0$, the inviscid solution is singular. Clearly, none of the methods capture this behaviour, which in any event has to be smoothed to be able to compute the solution. For small τ all the presented results are in reasonable

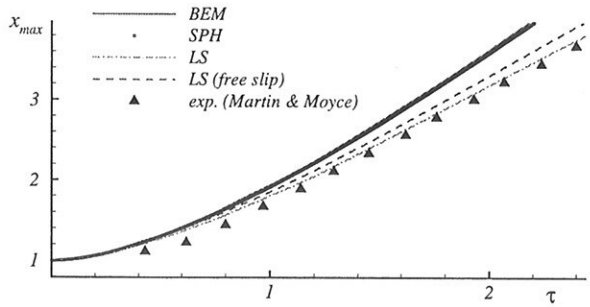

Fig. 2: Time evolution of the water-front toe. $\tau = 0$ is the dam break and x_{max} is the distance from the initial position of the dam.

agreement. On a longer time scale, BEM and SPH give practically the same results and predict a faster motion of the water front with respect to the Navier-Stokes simulation, regardless the boundary condition enforced along the horizontal boundary in the viscous computations.

When the no-slip condition is enforced, the LSM solution agrees reasonably well with the experimental data, □, reported in the same figure, characterized by the slowest water front velocity. For $\tau < 1$, the differences between measurements and (all) numerical results are more pronounced, and maybe are related to a not completely broken diaphragm in the experiments.

The free-surface profiles by the three methods are graphically superimposed, and are not shown. Differences can be detected only by a closer inspection of the water-front region, as reported in Fig. 3. LSM predicts a blunter shape: the tip is more rounded and slower. The deficit of mass in the front region is stored upwardly. This phenomenon is due to numerical approximations in the LSM calculations. There, we assume that the distance function is symmetric with respect to the bottom, so that the tip of the front is like a spike; this shape implies a discontinuity of $\partial\phi/\partial x_i$ in the coordinate direction that is smoothed in the numerical procedure altering the guess of the zero level. In this perspective, we believe that the better agreement of LSM with the experiments could be a coincidence.

Besides the imperfections in the numerics, several source of uncertainties hamper a clearer comparison against the experiments. In none of the codes surface-tension effects have been modeled. In the experiments, two different scales (L=5·7 and

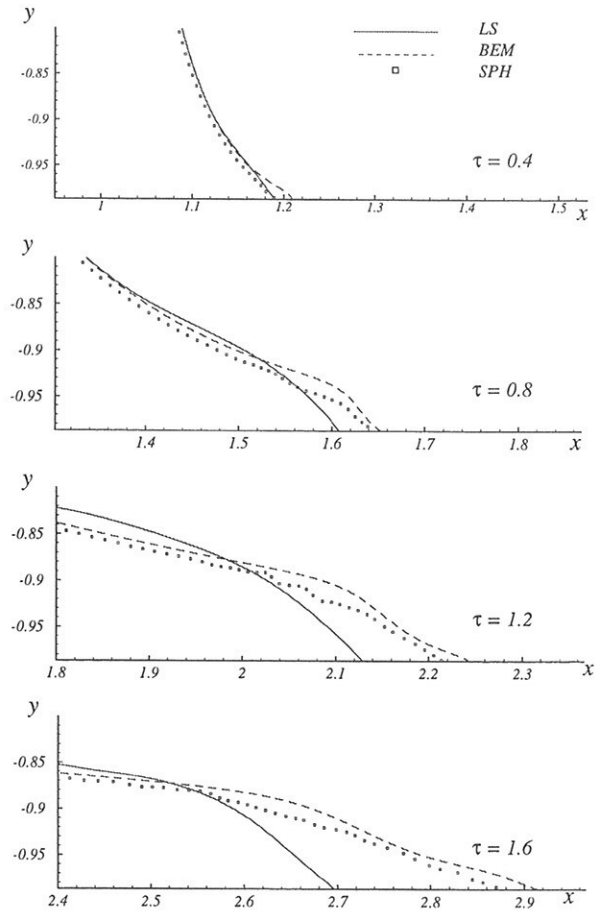

Fig. 3: Details of the water front. Time increases from top to bottom.

11·4 cm) have been considered to rule out significant surface-tension effects, though in both cases the radius of curvature at the water front is still rather small. In [2] it is shown that the comparison between Dressler large-scale experiments and BEM is much better than in the present case. Another source of uncertainty is related to the bottom roughness which alters the propagation velocity and trigger the development of turbulence at the water front (not modeled).

Pressure distribution Fig. 4 shows the comparison of the pressure along the bottom, as obtained by the three methods. With the exception of the tip area, where different free-surface profiles imply different pressure distributions, the comparison appears satisfactory. It is worth to mention that in SPH computa-

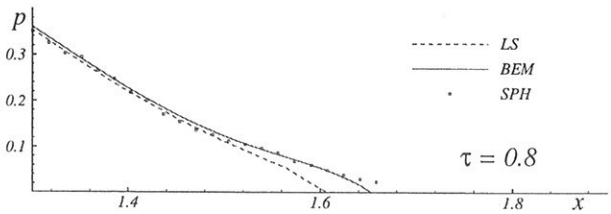

Fig. 4: Pressure distribution along the bottom.

tions we observed large high-frequency oscillations due to the "cold start" and related to acoustic waves bouncing back and forth within the boundary domain. We overcame the problem by initializing the pressure field with the $t = 0^+$ pressure distribution as obtained by BEM. The obtained pressure evolution is smooth, as reported above. In this respect, in spite of the positive comparison, the SPH method needs further improvement to allow an easier evaluation of the pressure distribution, often required in practical applications.

Impact with a vertical wall In many practical circumstances,

the water finds obstacles on its way and it becomes relevant to evaluate the impact flow, and the related loads. Figure 5 shows the forces acting on the bottom, f_b, and on the right wall, f_w, of a container whose dimensions are $L_c = 2{\cdot}1h$, $H_c = 1{\cdot}36h$. The flow is originated by a reservoir with $L/h = 1$. Rather small

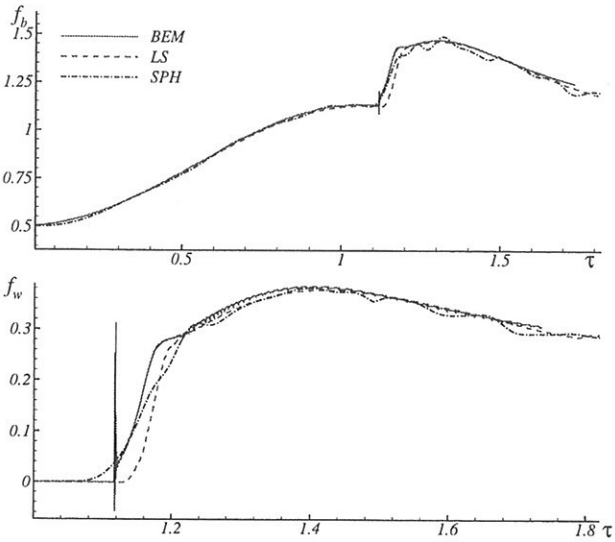

Fig. 5: Top: time evolution of the vertical load on the horizontal boundary after the dam break (L/h=1). The water propagation is stopped by a vertical wall, $L_c = 2{\cdot}1h$, and the bottom plot reports the the horizontal impact force.

oscillations in SPH computations are detectable, and the agreement of the average result with other methods is rather good. Even the jumps related to the impact of the fluid onto the right vertical wall are in reasonable agreement, with BEM and SPH always closer each other. The delay of the LSM data is related to the smaller velocity propagation of the front.

A high peak, with short duration, is found by the BEM method. Though surely affected by numerical noise, it is interesting a clearer interpretation of this result. In particular, at the impact time, the water front can be approximated by a wedge of about 60°, followed by a free surface with mean slope of about 25°. By using a similarity solution for the impact of a fluid wedge against the wall, we found the results reported in Fig. 5, suggesting that the first steep force peak is due to the impact of the blunter portion of the water front. The local refinement of

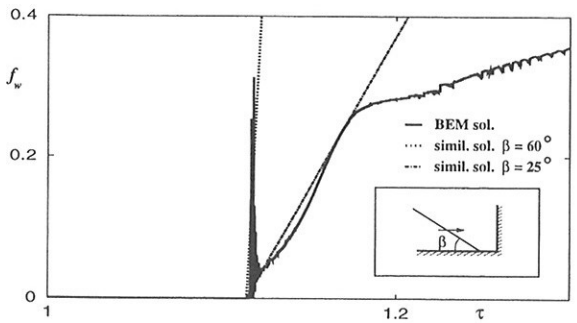

Fig. 6: Impact loads by a semi-analytical similarity solution and BEM results (*cf.* Fig. 5, bottom plot).

BEM is probably higher than in SPH and LSM computations, which do not capture the first "burst" in the horizontal load.

We now consider, Fig. 7, the experiments from [9], where a reservoir of water (height h and length $2h$) is placed at a distance $3{\cdot}366\,h$ from a vertical obstacle. Wave heights and pressure have been measured at the locations A,B and C, respectively. The following analysis is mainly due to the third author,

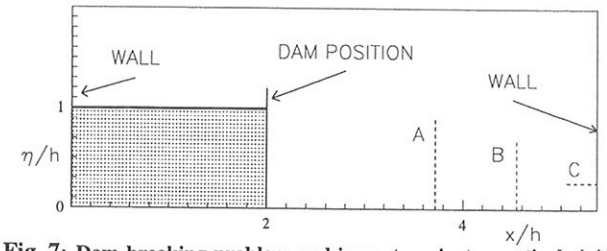

Fig. 7: Dam-breaking problem and impact against a vertical rigid wall. Sketch of the problem and of the experiment performed in [9] with $h = 0{\cdot}6$ m. A-B: wave-gauges. C: pressure-transducer.

[2]. The sequence in Fig. 8 shows the global development of the fluid flow. The different solutions are reported: for SPH only the free-surface layer of particles is plotted, and for LSM the dashed lines is the zero-level of the distance function ϕ. After the dam is removed, the flow develops along the deck, impacting against the vertical wall. The fluid is violently deviated upwards, rising

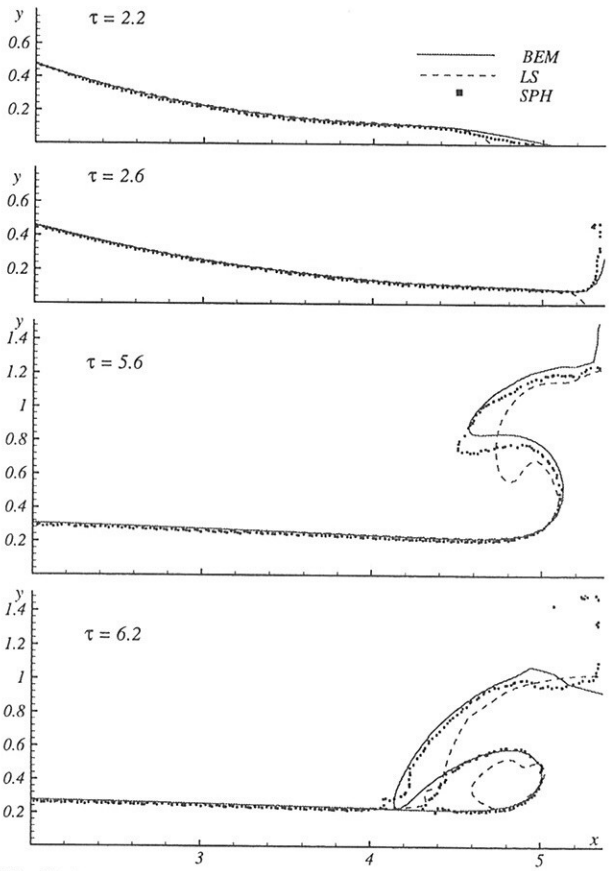

Fig. 8: Free-surface flow and impact against the vertical wall following the breaking of the dam (*cf.* Fig. 7).

along the wall. Formation of spray and fragmentation of the free surface may occur. BEM cannot handle these details and also LSM suffers a lack of resolution. SPH predicts high particle velocities, and some of them leave the main bulk of the fluid. We can not judge the accuracy of these details. Under the restoring action of gravity, the fluid acceleration decreases and the jet slows down. The motion of the water is reversed in a waterfall, overturning in the form of a wave plunging onto the deck. At this stage, BEM simulation has to be stopped, while both LSM and SPH continue further on.

From the impact on, the lack of resolution in our present LSM simulations leads to an increasingly poor agreement with the other two methods. Fig. 9 is an enlarged view for $\tau = 6{\cdot}2$. The agreement between SPH and BEM is quite good, considering the complexity of the flow field. Our LSM simulation is unsatisfac-

tory, with an excess of smoothing which prevents to capture correctly the overturning. Also, the smaller velocity at the impact could influence the mass involved in the overturning. Though no experimental data are available for the free-surface profile, we believe the agreement between BEM and SPH is rather convincing.

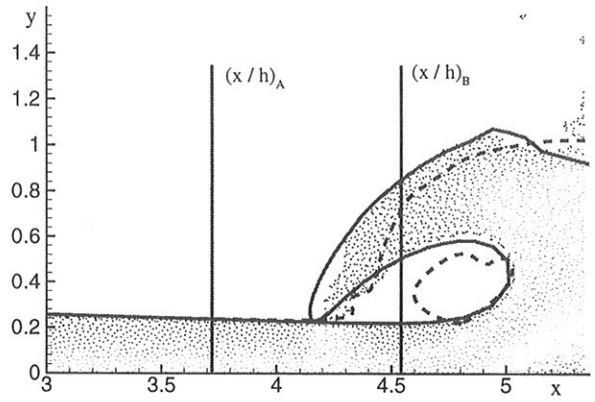

Fig. 9: Comparison of free-surface profiles as computed by BEM and SPH, $\tau = t\sqrt{g/h} = 6{\cdot}2$.

Fig. 10 gives the time evolution of the water height h_w at $(x/h)_A = 3{\cdot}721$ and $(x/h)_B = 4{\cdot}542$ along the deck. From the analysis of the numerical simulations and of the experiments we identify the three fundamental stages: 1) STAGE I is characterized by the sudden rise of the water level h_w, due to the transition from dry-deck conditions to wet-deck conditions. The shape of the water front determines the growth rate of h_w. Some differences can be detected between the numerical solution and the experimental measurements. 2) STAGE II is characterized by a much slower growth rate of the water level because of the almost flat free surface above the wave gauges. 3) STAGE III shows a new steep increase of h_w. This is due to the water overturning which gives an additional contribution to the wave height measured at the location B. Later on, also the signal recorded by the gauge located in A displays this phenomenon, which cannot be followed further on by BEM, while it is qualitatively captured by SPH.

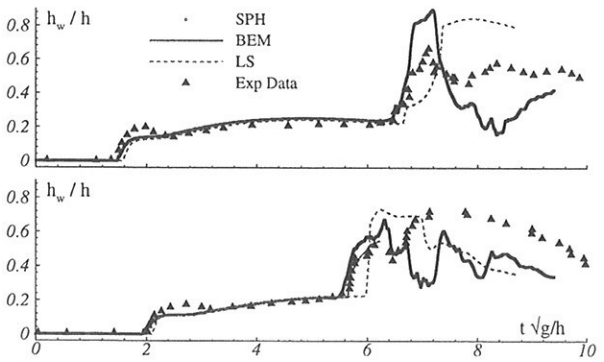

Fig. 10: Wave height measured at locations A (top) and B (bottom) (*cf.* Fig. 7) and comparison with BEM and SPH computations.

Though the experimental and numerical evolutions are in satisfactory agreement, in Fig. 10 the numerical solutions underpredict the measured data when the water level attains non-zero value, and the measured h_w has a maximum which is not present in the numerics. The temporal record can be converted to a spatial free-surface profile and suggests a hump in the free surface close to the contact point. This is not visible in the dam-breaking free-surface profiles by Dressler (see [2]) and could be due to a non perfectly dry deck before the breaking of the dam. This is consistent with other flow visualizations by Stansby *et al.* (see [2]). Unfortunately, the limited set of data available does not allow for a better verification of the present speculation.

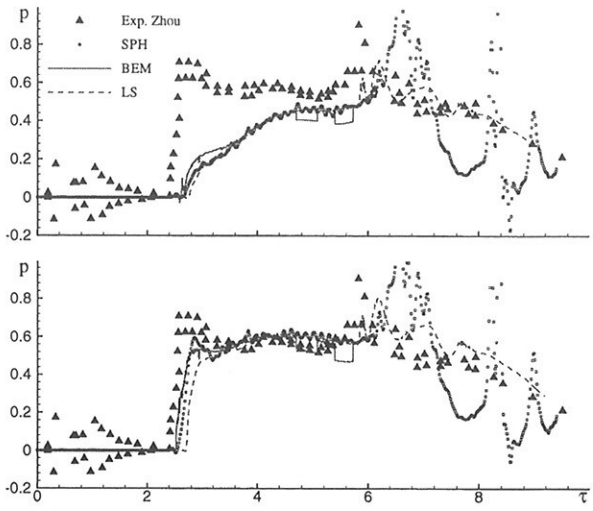

Fig. 11: Top: pressure measured at the centre of the circular transducer located in C (*cf.* Fig. 7) and comparison with BEM and SPH computations. Bottom: as above but the numerical results are evaluated at the bottom boundary of the circular transducer area.

The pressure measured on the vertical wall during the impact is presented in Fig. 11. In the experiments, a circular shaped gauge, with diameter 0·09 m centred in C, has been adopted. The top plot shows the measurements compared with the numerical values computed at that location. The initial rise is well synchronized with BEM and SPH while, LSM exhibits the already commented delay, related to the different propagation velocity of the water front. Other than that, we observe a rather limited agreement between computations and experiments. Actually, [9] reported difficulties to achieve repeatability of the measurements and no conclusive statement can be made. We observe that the pressure undergoes large variation within the area of the transducer, and indeed the experimental pressure curve is closer to the pressure computed at the bottom boundary of the transducer area, as we report in the bottom plot of Fig. 11.

Acknowledgements OEL work is supported as part of a program for the simulation of ship breaking waves by the Ship Hydrodynamics Program of ONR, managed by Dr. Pat Purtell. INSEAN research activity is supported by the Italian *Ministero dei Trasporti e della Navigazione* through INSEAN Research Program 2000-02.

References

[1] Colagrossi A., Landrini M. and Tulin M.P., A Lagrangian Meshless Method for Free-surface Flows, 4^{th} Numerical Towing Tank Symposium (Ed. V. Bertram), Hamburg (2001).

[2] Greco M., A two-dimensional study of green-water loading, Ph.D. Dissertation Thesis, Dept. Marine Hydrodynamics, NTNU, Trondheim, Norway (2001).

[3] Hirt C.W. and Nichols B.D., Volume of fluid (VOF) method for the dynamics of free boundaries. *J. Comp. Physics* **39**, pp. 201-225 (1981).

[4] Landrini M., Colagrossi A. and Tulin M.P., Numerical Studies of Wave Breaking Compared to Experimental Observations, 4^{th} Numerical Towing Tank Symposium (Ed. V. Bertram), Hamburg (2001).

[5] Martin J.C. and Moyce W.J., An experimental study of the collapse of liquid columns on a rigid horizontal plane. *Philos. Trans. Roy. Soc. London* **244A**, pp. 312-324 (1952).

[6] Sussman M., Smereka P. and Osher S., A Level Set Approach for Computing Solutions to Incompressible Two-Phase Flow. *J. Comp. Physics* **114**, pp. 146-159 (1994).

[7] Whu C.W. and Osher S., Higher-Order Essentially Nonoscillatory Schemes for Hamilton-Jacobi Equations. *SIAM J. Num. Anal.* **28**, pp. 907-922 (1991).

[8] Russo G. and Smereka P., A remark on computing distance functions. *J. Comp. Physics* **163**, pp. 51-67 (2000).

[9] Zhou Z.Q., De Kat J.O. and Buchner B., A nonlinear 3–D approach to simulate green water dynamics on deck. *Proc. 7^{th} Int. Conf. Num. Ship Hydrod., Nantes, Ed. Piquet, J.*, pp. 5.1–1, 15 (1999).

Influence of waterline integral and irregular frequencies in seakeeping computations

Gérard DELHOMMEAU[1], Christophe MAURY[1], Jean-Philippe BOIN[2], Michel GUILBAUD[2]

[1]Laboratoire de Mécanique des Fluides (UMR CNRS 6598), Division Hydrodynamique Navale, Ecole Centrale de Nantes BP 92101, 44321 Nantes Cedex 3, France
e-mail: Gerard.Delhommeau@ec-nantes.fr, tel. 33.240.74.25.95
[2]Laboratoire d'Etudes Aérodynamiques (UMR CNRS 6609), CEAT - Université de Poitiers, 43, rue de l'Aérodrome - 86036 Poitiers Cedex France
e-mail: Michel.Guilbaud@lea.univ-poitiers.fr, tel. 33.549.53.70.27

Introduction :

The linear problem of seakeeping with forward speed in perfect fluid is very difficult to solve and no fully satisfactory solution are available today. The most common method used to treat this problem is the boundary element method using either Rankine source which is the fundamental solution of the Laplace equation in infinite domain or Kelvin source with a Green function satisfying the linear free-surface equation and the radiation condition. The first method needs to solve big linear systems of equations and is not available for all speeds. This is not the case for the second method where there are no speed limitations, smaller system of equations to solve and no reflection of waves on the grid boundary on the free surface. The only drawback is the numerical difficulties of the Green function. Thanks to new algorithms of calculation of this Green function ([1] to [5]), and to the progress of computers such a method can be now developed and managed even on small workstation. Two very different algorithms have been developed and compared in LMF (Nantes) and LEA (Poitiers). Once this Green function accurately computed, it has been introduced in the corresponding seakeeping codes of Nantes (Aquaplus) and Poitiers (Poseidon). The results obtained are not still entirely satisfying in all cases. So we have to study the influence of other mathematical problems on the results. These problems are the quadrature on panels, waterline integral and the irregular frequencies. We present here the results of this study.

Mathematical problem

The irrotational flow of an inviscid and incompressible fluid around a ship hull with constant forward speed submitted to small harmonic motions or to regular waves is considered. We use the Cartesian system Oxyz moving with the hull, z=0 is the mean free surface and the axis of symmetry of the hull Ox is parallel to the velocity. We use the velocity potential in the frequency domain which satisfies the Laplace equation, the body and the free surface linear boundary condition and the radiation condition. The third Green's identity leads to an integral equation using G, the diffraction-radiation with forward speed Green function.

The body surface in divided into N_b panels where the source intensity is assumed to be constant and the waterline is divided into N_l segments where the density is equal to those of the adjacent panel. The body condition written at the centre of each panel leads to a linear system of equations where the R.H.S. c_i is given by the unit body motions or the diffraction potential.

$$\sum_{j=1}^{N_b} a_{ij}\sigma_j + \sum_{l=1}^{N_l} b_{il}\sigma_l = c_i \ , \ i = 1,...,N_b \ ; \ a_{ij} = \iint_{s_j} \frac{\partial G}{\partial n}(M_i, M')ds(M') \ ; \ b_{il} = \int_{C_l} \frac{\partial G}{\partial n}(M_i, M')dc(M') \qquad (1)$$

The solution of the linear system is the source distribution. The local velocities on each panel and the pressure distribution are then computed. By summation, added mass and damping coefficient are calculated. The wave pattern on the free surface around the body can be also calculated. The difficulty leads in the accuracy of the computation of the quadratures in (1).

Numerical methods

To check the accuracy of the computations, two very different codes have been developed in Nantes and Poitiers.

The Nantes code uses the steepest descent method [1] to compute both the Green function and its derivatives and their integration on an elementary panel or waterline segment with nodes Q_l for a field point P with S_l surface of the triangle (Q_l, Q_{l+1}, Q_{l-1}). This method needs to evaluate only one single complex integral and the path in the complex plane can be chosen to avoid strong oscillations of the integrands. Integration on panels can be performed either by numerical quadrature using Gauss points or by analytical formulas as given in [4]. The accuracy for the integration can be chosen. The steepest descent method is very efficient to compute the oscillating terms, but is difficult to program due to a great number of peculiar cases to take into account.

In the Poitiers calculations, the Froude dependant part of the Green function has been split in 2 terms G_1 and G_2 [2]. By use of the Stokes theorem, the surface integrals on an elementary planar panel with m nodes S_j are transformed into a contour one. Due the properties of the modified complex integral functions, analytical integration over panels or segments can be obtain [5]. Only a numerical integration of a real integral remains. This is done by a Simpson adaptative method with a given accuracy.

In both cases, we have tested the influence of waterline integral and also the influence of irregular frequencies on the results.

Results

The first test deals with the comparison of numerical and analytical integration over panels and segments. We have chosen a panel of coordinates M_1 (-0.43301,-0.25,0.), M_2 (-0.43301,-0.25,-0.5), M_3 (0.43301,0.25,-0.5), M_4 (0.43301,0.25,0.) for field points y=0., z=-0.25 and x varying from -10 to 10. The velocity is U=1 m/s and the pulsation $\omega = 2\pi$ rad/s. Figure 1 shows the results for the real part of the x-derivative of the Green function. We can see that numerical integration is not sufficiently accurate, even with 16 Gauss points where oscillations remain. The computation time of the analytical integration is approximately the same that for 4 Gauss points. For the computation of the line integral, we have chosen a line M_1 (0.43301,0.25,0.), M_2 (-0.43301,-0.25,0.) and the field points on the free surface y=2, z=0 and x varying. The results are given on figure 2. We see that at least 16 points are needed to obtain acceptable results while the computation time for analytical integration is approximately the same as for 2 Gauss points.

Figures 3 and 4 show added mass and damping coefficients for a modified Wigley hull in forced heave or pitch motions at Froude number=0.2. The equation of the Wigley hull is :

$$y_r = (1-x_r)^2(1-z_r{}^2)(1+0.2x_r{}^2)+z_r{}^2(1-z_r{}^8)(1-x_r{}^2)^4$$

$$x_r = \frac{2x}{L}, y_r = \frac{2y}{B}, z_r = \frac{z}{T}, L = 3., B = 0.3, T = 0.1875$$

Results obtained by the two different codes of Nantes and Poitiers are in very good agreement, except perhaps close to the singular value of the Brard parameter τ=1/4 for the coefficient ca33 at ω=1. The results, computed with waterline integral and irregular frequencies cancellation, have been compared also with the test measurements [6]. They show the validity of the two methods of computation of Green function and his integration over panels. The results obtained are closed to experiments and also to the encounter frequency hypothesis

Calculations have been also performed for a Series 60 C_B=0.6 hull at the same Froude number, figures 5 and 6. The existence of irregular frequencies is clearly show in the figures 5 and 6 by the dashed line with circles. The influence of taking into account the line integral is to damp these oscillations. The continuous lines are with waterline integral and suppression of these frequencies. The test measurements of [7] have been also plotted on these figures with a relatively good agreement. A method to suppress these irregular frequencies have been developed (with and without the waterline integral). A horizontal surface, slightly immersed have been added, also divided into panels where a zero normal velocity condition has been satisfied. Very good results have been then obtained with suppression of the irregular frequencies. It is surprising to observe that results obtained with the hypothesis of encounter frequency are not far from experiments and from the final results of the complete Green function analytically integrated over panels, with line integral and irregular frequencies elimination.

After these first results, the development of the methods will be pursued to improve their efficiency et performed other comparisons with local data such as the wave pattern around the hull. Further experiments are also needed for an accurate evaluation of these local quantities.

Bibliography

[1] Iwashita H. and Okhusu M., Hydrodynamic Forces on a Ship Moving at Forward Speed in Waves, J.S.N.A. Japan, Vol. 166 (1989), 87-109.

[2] Ba M. and Guilbaud M., A fast method of evaluation for the translating and pulsating Green's function, Ship Technology Research, Vol. 42 (1995), 68-80.

[3] Brument A. et Delhommeau G., Evaluation numérique de la fonction de Green de la tenue à la mer avec vitesse d'avance, Proc. of the 6èmes Jour. de l'Hydrodyn. (1997), 147-160.

[4] Iwashita H., Evaluation of the Added-Wave-Resistance Green Function Distributing on a Panel, Mem. Fac. Eng. Hiroshima Univ., Vol. 11, 2 (1992), 21-39.

[5] Guével P. and Bougis J., Ship motions with forward speed in infinite depth, Int. Ship. Progress, Vol. 29 (1982), 103-117.

[6] Gerritsma J., Motions, wave loads and added resistance in waves of two Wigley hull forms, Delft University of Technology, Shiphydromechanics laboratory, Report 804 (1988).

[7] J.P. Boin, M. Guilbaud et M. Ba, Frequency domain numerical and experimental investigation of forward speed radiation by ships, Proc. of the 22nd Symposium on Naval Hydrodynamics (2000).

Key words: Boundary element method, Green function, diffraction-radiation with forward speed, frequency domain, waterline integral, irregular frequencies

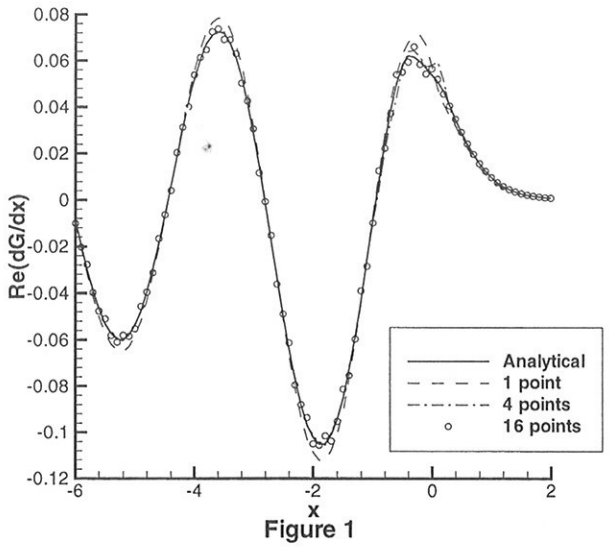

Figure 1

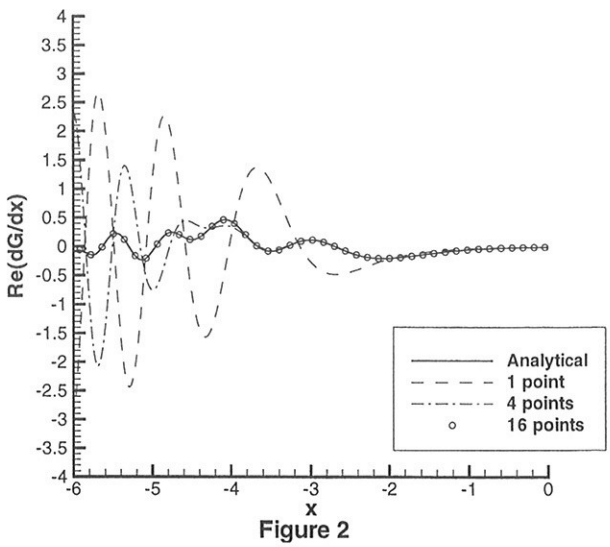

Figure 2

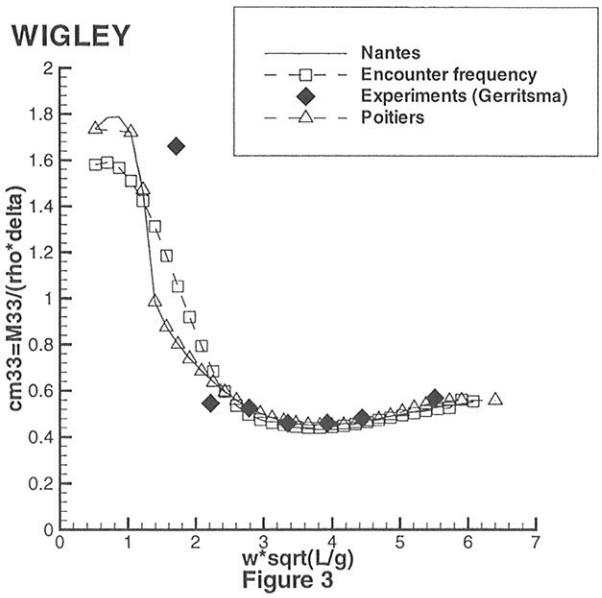

Figure 3

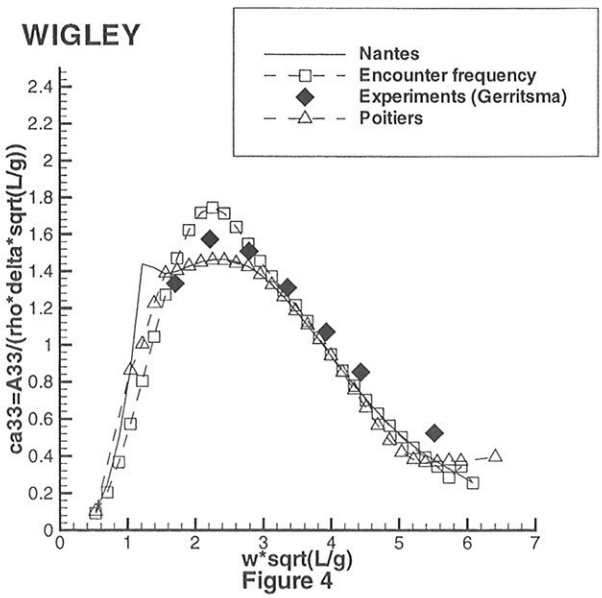

Figure 4

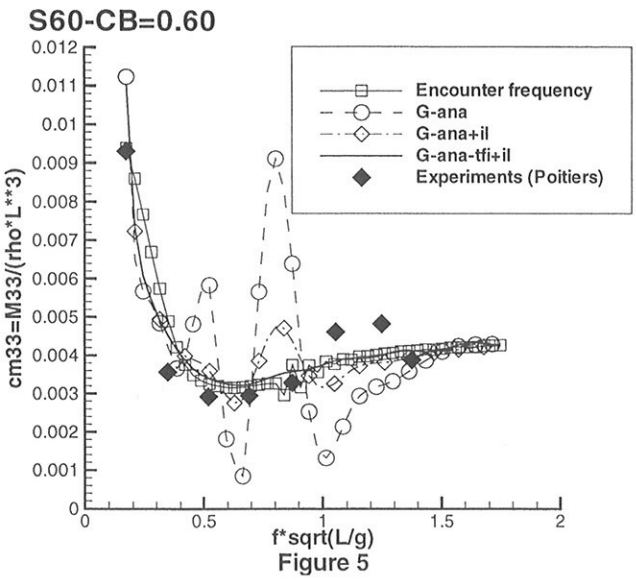

Figure 5

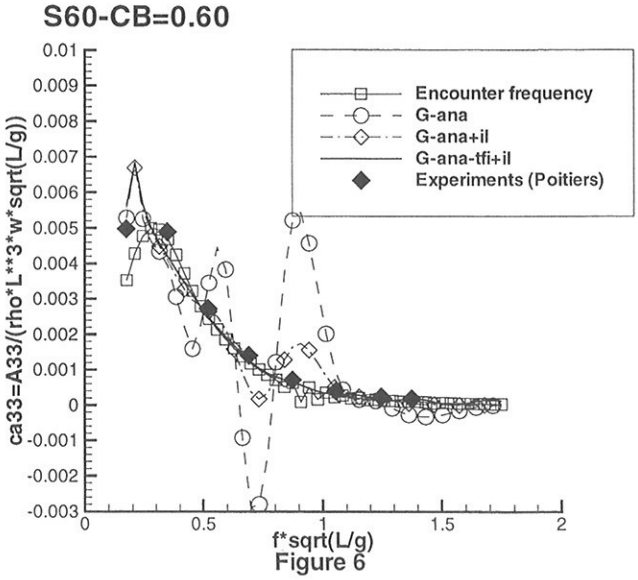

Figure 6

Towards a Practical Design Optimization Tool for Incompressible and Turbulent Flows

R. Duvigneau & M. Visonneau
Laboratoire de Mécanique des fluides CNRS UMR 6598
Ecole Centrale de Nantes, BP 92101, FR-44321 Nantes, France
Regis.Duvigneau@ec-nantes.fr Michel.Visonneau@ec-nantes.fr

Introduction

For the past decades, Computational Fluid Dynamics (CFD) solvers have became practical analysis tools in ship building to study the flows around tanks during the design process. Today, thanks to the progress in CFD and to the development of the calculation means, automated design optimization tools may be helpful to improve hull shapes. The aim of the present investigation is to develop a multi-purpose shape optimization tool for incompressible and turbulent flows. The necessity to deal with accurate forces on the bodies in the design procedure requires the use of a sophisticated flow solver. It should be able to take into account realistic geometries as well as complex phenomena, such as turbulence or free surface. Moreover, its robustness during the search of the optimum shape is obviously needed. The flow solver ISIS, developed in our laboratory, is employed to solve the incompressible Reynolds-Averaged Navier-Stokes Equations (RANSE) on unstructured grids. Several near-wall low-Reynolds number turbulence models are implemented. Free surface calculations are also treated using surface-tracking or surface-capturing methods. In order to facilitate the implementation of a such flow solver in the design procedure, a derivative-free approach for the optimizer is chosen. Thus, the flow solver is considered as a "black box", which provides a more robust and flexible tool than gradient-based algorithms. A comparison of two optimization methods is presented in this paper. The "down-hill" simplex method from Nelder & Mead is opposed to genetic algorithms to find the optimum shape in two practical design applications. First, the shape of the flap of a multi-element airfoil is optimized to increase the lift without increasing the drag. Then, the Serie 60 hull shape is modified in order to decrease the drag with a fixed hull volume.

Problem statement

Shape optimization consists in minimizing an objective function depending on the flow variables and the design variables. The governing equations of the flow are considered as constraints which must be satisfied at each step of the optimization loop. Some geometrical constraints must be added to the problem in order to find a realistic solution. Thus, the variation domain of the design variables is usually closed. Moreover, physical constraints depending on the problem may be taken into account. Gradient-based optimizers are often used since they require only a few cost function evaluations. However, the evaluation of the derivatives of the cost function is a difficult task, since the flow solver should be accurately differentiated[1]. Moreover, these algorithms are very sensitive to the noisy errors arising from the simulation process. Therefore, strongly converged state analysis are necessary. To overcome these limitations, a derivative-free approach is chosen, providing an easier implementation. Furthermore, this kind of algorithms is less sensitive to the noise and only partially converged solutions of the state equations may be used, decreasing the calculation costs.

Simplex algorithm

The simplex method[2] consists in moving a simplex of $n+1$ vertices $\mathbb{R}^n$ (a triangle in $\mathbb{R}^2$, a tetrahedron in $\mathbb{R}^3$, etc), for a problem of n parameters, each vertex representing a distinct shape. Displacements are performed in order to reduce at each move the cost function evaluated at the worst vertex. The vertex corresponding to the worst value is projected through the centroid of the remaining vertices, expecting a better shape. The simplex may then be expanded or contracted, depending on the performance of the previous move. The loop is repeated until a minimum of the objective function is reached. More details about the application of the simplex method to design optimization may be found in [3].

Genetic algorithms

Genetic algorithms belong to the evolutionary methods of optimization. They mimic the natu-

ral laws of evolution to improve the performance of a set of shapes. A binary-coding representation of the shapes provides chromosomes, which evolve from one generation to an other, through genetic operators. The selection operator consists in a two-point tournament, retaining the best individuals. A one-point crossover is then applied to create new offsprings shapes by swapping a part of the chromosomes between two parents. Finally, a mutation is realized to increase diversity, by permutation of some bits[4]. Contrary to the "downhill" methods, genetic algorithms are able to avoid local minima and can perform multi-objective optimizations. Some examples are given in [5].

Flow solver ISIS

The flow solver ISIS, included in the optimization process, solves the pseudo-steady incompressible Reynolds-averaged Navier-Stokes equations with a strongly conservative formulation. The discretization scheme uses a finite-volume method, generalized to unstructured meshes composed of arbitrary volume shapes. The flow variables are stored at the centers of the control volumes. Surface and volume integrals are evaluated using second-order accurate approximations. The pressure-velocity coupling is performed by a SIMPLE-like algorithm. The solver includes several near-wall low-Reynolds number turbulence models and multi-fluids calculation methods[6].

Parameterization and mesh update

For the two-dimensional cases, the shape may be easily described by a B-spline curve, whose control points represent the design variables during optimization. In that manner, only smooth shapes are considered and the number of design variables is small. For each new shape proposed by the optimizer, a mesh should be created automatically. Since the automatic grid generation is difficult for grids adapted to viscous flows, the initial mesh is deformed using an analogy with both lineal and torsional springs[7], which maintains the quality of the mesh near the wall during the update [3]. For the three-dimensional cases, the parameterization and the mesh deformation are particularly complex in the unstructured context. Therefore, a Free-Form Deformation (FFD) technique[8] is employed to control simultaneously the shape and the mesh modifications. It consists in embedding in a box the object to be deformed, and then modifying the shape of the box and the space inside by moving control points on the box, rather than modifying the object itself.

Multi-element airfoil

The flap of the multi-element airfoil AGARD 303 is optimized, for a Reynolds number $Re = 3.53 \times 10^6$ and an incidence of 4.01 degrees. The grid used is a hybrid mesh of 50 659 nodes, with a structured grid near the bodies and in the wakes, and an unstructured grid in the outer domain. The modelization of the turbulence is achieved by the SST $k - \omega$ model. The shape is parameterized using a third-order b-spline with 14 active control points, the trailing edge and the leading edge being kept fixed during the optimization process. For the first optimization test, the goal is the increase of the lift. The figure 1 shows the evolution of the cost function during the design process, for the simplex method and genetic algorithms involving 30 and 40 individuals at each generation. The shapes obtained are represented on figure 2. As seen, both algorithms find the same optimum, corresponding to an increase of 7% of the lift, but genetic algorithms need to use 40 individuals. When only 30 individuals are involved, a premature convergence occurs and a local minimum is found.

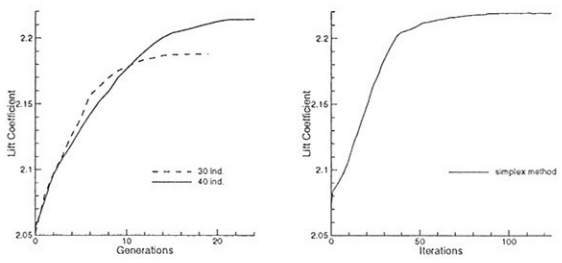

(a) Genetic algorithms (b) Simplex

Figure 1: Evolution of the lift

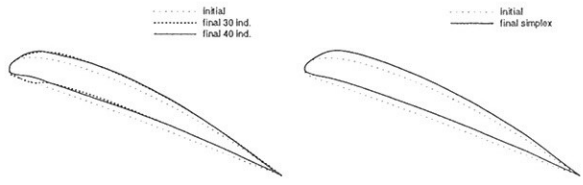

(a) Genetic algorithms (b) Simplex

Figure 2: Initial and final shapes

A second optimization is then performed, whose purpose is to increase the lift while maintaining the drag fixed, using a penalty function. The figures 3 and 4 show the evolution of the cost function,

including the constraint, and the final shapes. For all the tests, an optimum shape is found, with a performance of the same order of magnitude (increase of 4% of the lift with an increase of the drag less than 1%). The final shapes obtained by the simplex method and genetic algorithms with 30 individuals are the same. But the one found by genetic algorithms with 40 individuals differs and is slightly better. Therefore, the capability of genetic algorithms to avoid local minima or reach several optima is shown.

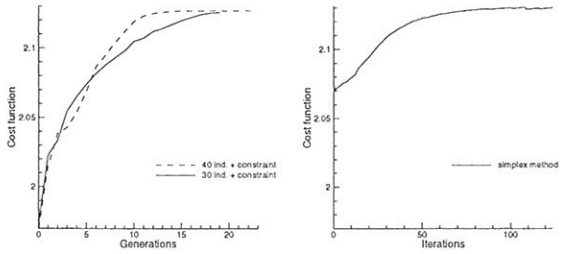

(a) Genetic algorithms (b) Simplex

Figure 3: Evolution of the cost function for the constrained case

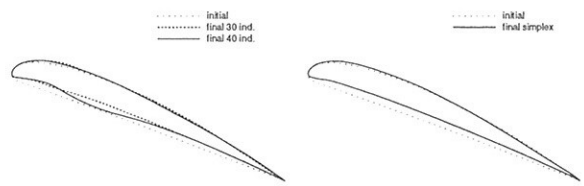

(a) Genetic algorithms (b) Simplex

Figure 4: Initial and final shapes for the constrained case

A comparison of the calculation costs is given in the table 1. Genetic algorithms require about four times more flow solver evaluations than the simplex method. However, they could be easily parallelized to reduce the costs. The number of evaluations is large, but each simulation is only partially converged. If the number of evaluations is transformed into the number of evaluations equivalent for the computational time to a reduction of 6 orders of the residuals (second row of the table 1), the costs for the simplex method become comparable to those of a gradient-based method.

	simplex	G.A.
number of eval.	250	1000
number of equiv. eval.	30	115
CPU time	380 h	75 h (20 proc.)

Table 1: Calculation costs

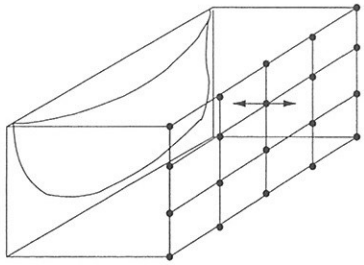

Figure 5: S60 parameterization

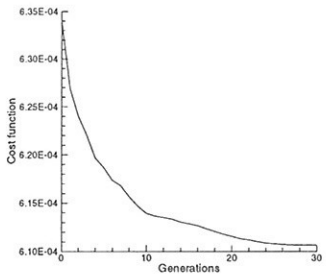

Figure 6: Evolution of the cost function

Serie 60

The Serie 60 hull shape is optimized to decrease the drag while maintaining the volume fixed, for a Reynolds number $Re = 1. \times 10^5$. A quite coarse mesh is used since the three-dimensional simulations are expensive. It is composed of a structured domain near the wall of 50×30×30 nodes, in the streamwise, radial and girthwise directions respectively, and an unstructured mesh around. The Spalart-Allmaras turbulence model is employed. The parameterization is achieved by FFD using a 5×4 active control points net, in a vertical plane and moved only horizontally (figure 5). The evolution of the cost function, including the constraint as a penalty term, is represented in figure 6 for genetic algorithms with 30 individuals. A reduction of 2% of the drag is observed, for a modification of 1% of the volume. Some slices in the shapes at the location x=0.25, x=0.5, x=0.75 and z=0.00 are shown on figure 7 and a comparison of the streamlines at the location $y^+ = 1$ for the initial and final hull shapes on figure 8. The modifications of the longitudinal vortex may be particularly noticed. This test case provides promising results, even if a quite small number of individuals is used and better results may be expected employing more computational means.

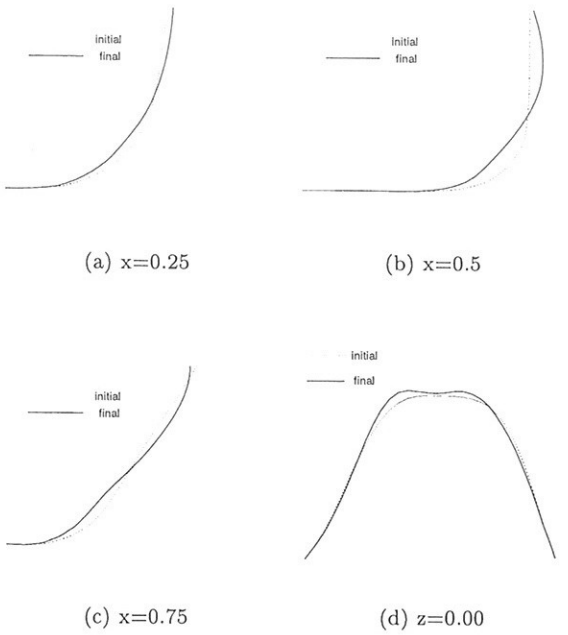

(a) x=0.25 (b) x=0.5

(c) x=0.75 (d) z=0.00

Figure 7: Slices in initial and final shapes

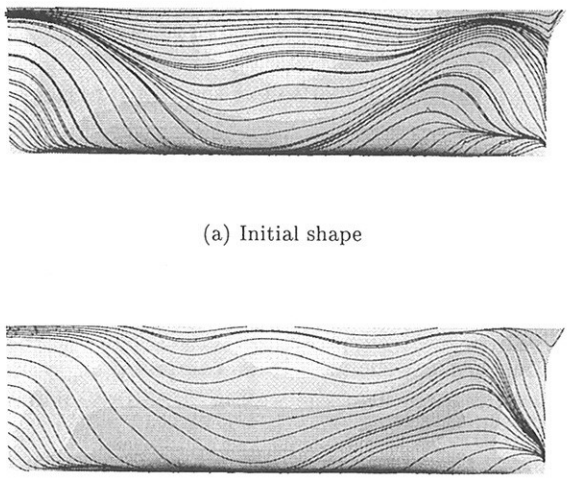

(a) Initial shape

(b) Final shape

Figure 8: Streamlines at $y^+ = 1$

Conclusion

Complex design optimization problems, involving three-dimensional viscous and turbulent flows, have been successfully studied using derivative-free optimizers. This pragmatic approach allows an easy implementation and is quite insensitive to noisy errors. Thus, only partially converged state solutions are used, reducing the computational costs, although a high number of function evaluations is required. The simplex method as well as genetic algorithms have shown a satisfactory behaviour. Genetic algorithms seem to have a more general approach, which allows to perform multi-criteria optimizations and to avoid local minima, contrary to "downhill" methods, such as simplex. But their efficiency requires high computational means and they may yield poor results if a too small number of individuals is used. Finally, these methods look complementary. Genetic algorithms are aimed to find interesting unexpected new shapes, while the simplex method is more adapted to slight modifications of existing shapes.

References

[1] W. K. Anderson and V. Venkatakrishnan, "Aerodynamic Design Optimization on Unstructured Grids with a Continuous Adjoint Formulation," *Computers and Fluids*, vol. 28, no. 4, pp. 443–480, 1999.

[2] J. A. Nelder and R. Mead, "A Simplex Method for Function Minimization," *Computer Journal*, vol. 7, pp. 308–313, 1965.

[3] R. Duvigneau and M. Visonneau, "Shape Optimization for Incompressible and Turbulent Flows using the Simplex Method." AIAA Paper 2001–2533, june 2001.

[4] D. Goldberg, *Genetic Algorithms in Search, Optimization and Machine Learning.* Addison Wesley Company Inc., 1989.

[5] R. Duvigneau and M. Visonneau, "Single- and Multi-Objective Optimization for High-Fidelity CFD using Genetic Algorithms," in *EUROGEN 2001 - Evolutionary Methods for Design, Optimisation and Control with Applications to Industrial Problems*, September 2001.

[6] G. Deng, E. Guilmineau, P. Queutey, and M. Visonneau, "Capture et Suivi d'Interfaces d'Ecoulements de Fluides Visqueux Incompressibles non Miscibles," in *8e Journées de l'Hydrodynamique, Ecole Centrale de Nantes*, pp. 17–30, Mars 2001.

[7] C. Farhat, C. Degand, B. Koobus, and M. Lesoinne, "Torsional Springs for Two Dimensional Dynamic Unstructured Fluid Meshes," *Computational Methods in Applied Mechanics and Engineering*, vol. 163, pp. 231–245, 1998.

[8] T. Sederberg and S. Parry, "Free-From Deformation of Solid Geometric Models," *Computer Graphics*, vol. 20, no. 4, pp. 151–160, 1986.

RANSE Simulations for High-Fn, High-Re Free-Surface Flows

Ould El Moctar, Volker Bertram
HSVA, Bramfelder Str 164, D-22305 Hamburg, elmoctar@hsva.de

The flow around surface-piercing profiles (snorkels and masts) on submarines features high Froude numbers, typically $F_n>2$. These high Froude numbers are often associated with steep, massively breaking waves which cause a significant acoustic signature. The wave making depends strongly on the shape of the profile. Similar flows appear for surface piercing struts in towing submerged bodies. We investigated recently the vortex generation on new airbus designs in deeply submerged condition in the small towing tank of HSVA observing strong wave breaking on the struts supplied by the customer. Subsequently, we performed CFD analyses for several profile shapes for high Froude numbers.

The wave breaking causes a mixing of water and air. The flow becomes highly unsteady. Potential flow codes still dominate practical applications for free-surface flows, but most of these boundary element methods are applicable only for slender bodies (like most ships) up Froude numbers of 0.3 to 0.4 and cannot handle breaking waves. In principle, field methods could also handle breaking waves even if based on potential flow. However, few such codes have been developed in research and none has progressed to being a practical tool. If we have to resort to field methods anyhow, we may as well employ RANSE solvers to achieve also a considerable improvement in applicability and sometimes also quality of prediction for free-surface flows.

We employed the commercial RANSE solver Comet, ICCM (2000), for our analyses. We modeled the flow for the strongly breaking waves as a two-phase flow computing both air and water flow simultaneously. The conservation equations for mass and momentum are solved in integral form using a finite volume method. The integrals are approximated using the midpoint rule. The variables respectively their gradients are determined using linear interpolation respectively central differences. The SIMPLE algorithm couples pressures and velocities. The Reynolds stress tensor (i.e. turbulence) is modelled using the RNG-k-ε turbulence model. Time is discretized using an implicit Euler scheme. Demirdzic et al. (1998) give more details of the method.

The interface between water and air is determined in a surface capturing method. We define a scalar function C ($0 \le C \le 1$) which describes the volume percentage of water in each cell. C=1 for cells filled completely with water, C=0 for cells filled completely with air. This scalar function allows us to model the two phases in our flow as one effective fluid with locally weighted material properties (viscosity μ_{eff}, ν_{eff}):

$$\mu_{eff} = C\,\mu_{water} + (1\text{-}C)\,\mu_{air}$$
$$\nu_{eff} = C\,\nu_{water} + (1\text{-}C)\,\nu_{air}$$

In addition to the RANSE and the turbulence transport equations, we solve one more convective transport equation to capture the convection of the water-air interface defined by C=0.5. The specially constructed high-resolution interface capturing (HRIC) scheme keeps the transition region from C=0 to C=1 relatively narrow and allows thus a quite sharp resolution of the water-air interface, Muzaferija and Peric (1998).

RANSE methods for free surface flows have been extensively validated in the Gothenburg 2000 workshop, Larsson et al. (2000), albeit only for moderate Froude numbers. As the Froude number increases, breaking of waves complicates the flow simulation. We computed the flow around surface-piercing profiles for Fn=2.04 and $Re=3.5\cdot10^6$. As the flow is highly unsteady, we model both port and starboard sides of the symmetrical profile. The computational domain extends 10 profile lengths upstream, downstream, and to each side of the profile, 8 profile lengths above and 4 below the calm-water line. The block-structured grid consisted of 1.7 million cells. The majority of the cells is clustered near the free-surface to ensure high resolution. The velocity components (u, v, w) and the turbulence quantities (k, ε) are specified at the inlet. At the outlet we enforce zero gradients in

longitudinal direction for all variables. On the profile surface we enforce a no-slip condition via a wall function. The free surface position is specified on the outer boundaries.

We reduced CPU times and storage requirements by accelerating the flow from 0 to the given speed using initially large time steps to obtain quickly an approximate solution. The rapid acceleration tends to produce an overshooting leading-edge wave if the usual number of outer iterations (SIMPLE scheme) is employed. This destroyed the convergence of the numerical scheme in the first tries. We found that this problem is removed by using a large number of outer iterations in the first time steps. The initial wave is then reduced to a reasonable size and the computation converges. In the course of the simulation the size of the time steps is reduced to keep discretization errors small and to better capture the free surface. At the end of the simulation, the time steps are one order of magnitude finer as at the beginning. The simulation is terminated when a quasi steady state has been reached in the flow taking the forces on the profile as criterion. The computations were performed on a parallel PC cluster using 6 nodes in parallel.

The pressure distribution on the body has a significant influence on the wave making, as expected. Profiles with rounded leading edges, particularly cylinders, feature areas with high pressure (near stagnation pressure) at the leading edge. As the leading edge radius increases, the wave height and spray formation increases. Doubling the profile thickness roughly doubles the wave height (for NACA profiles. The rounded profile is more wetted at the leading edge than at the trailing edge. The sharp profile features a parabolic wetted surface. For all profiles the water sheet above the water line is relatively thin. For a cylinder a thick breaking wave front appears.

The wave height may be limited and wave breaking largely suppressed by employing transverse plates on the profile. These prevent the rise of the thin water sheet at the profile. The width of the transverse plates is decisive for the prevention of spray. A similar transverse plate was less effective for the cylinder.

DEMIRDZIC, I.; MUZAFERIJA, S.; PERIC, M. (1999), *Computation of turbulent flows in complex geometries, calculation of complex turbulent flows,* WIT Press

ICCM (2000), *User Manual Comet Version 1.045*, ICCM GmbH, Hamburg

LARSSON, L.; STERN, F.; BERTRAM, V. (2000), *Gothenburg 2000 - A workshop on numerical ship hydrodynamics*, Chalmers Univ. of Technology, Göteborg

MUZAFERIJA, S.; PERIC, M. (1998*), Computation of free surface flows using interface-tracking and interface-capturing methods*, Nonlinear Water Wave Interaction, Comp. Mech. Publ., Southampton, pp.59-100

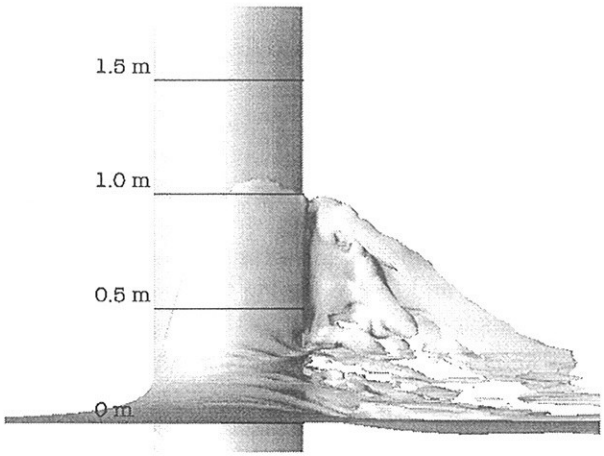

Fig.1: Parabolic strut with sharp edge, side view
F_n=2.03, R_e=3.35·10^6

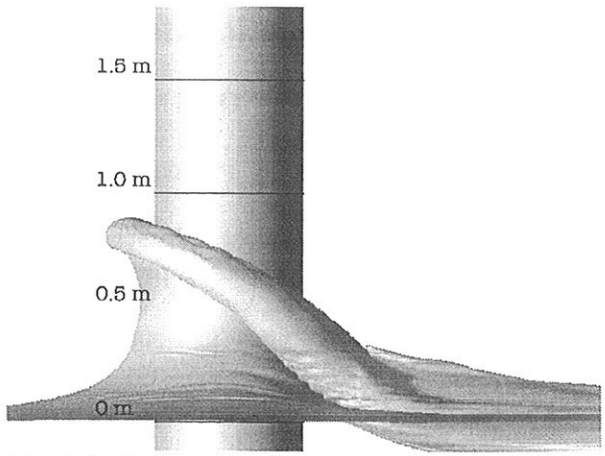

Fig.2: Cylinder, side view
F_n=2.03, R_e=3.35·10^6

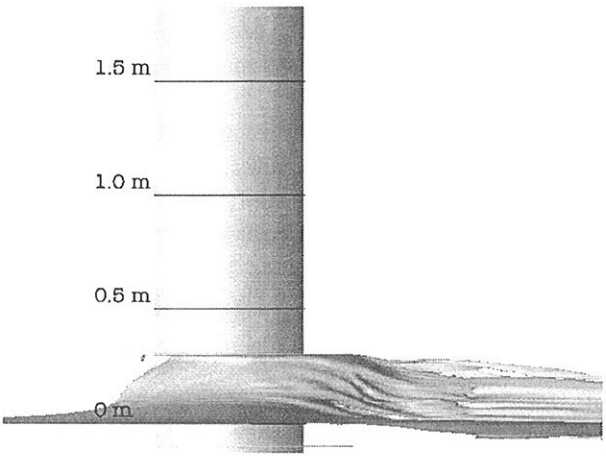

Fig.3: Parabolic strut with transverse plate
F_n=2.03, R_e=3.35·10^6

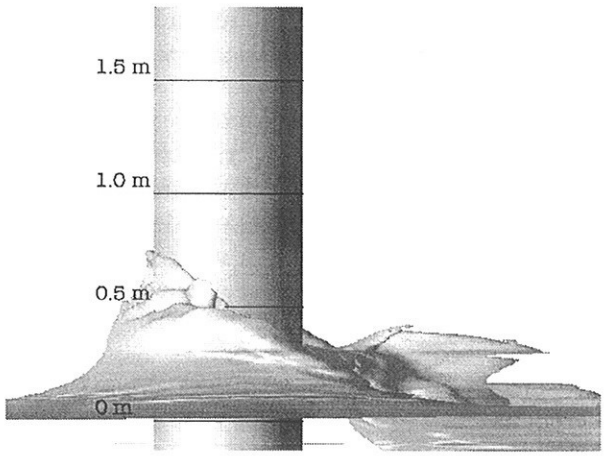

Fig.4: Cylinder with transverse plate
(plate hidden under overflowing wave)
F_n=2.03, R_e=3.35·10^6

RANSE Simulations for Aerodynamic Flows around Ship Superstructures

Ould M. El Moctar, Scott Gatchell, Volker Bertram

HSVA, Bramfelder Str 164, D 22305 Hamburg, Germany, elmoctar@hsva.de

Aerodynamic flows about ship superstructures are of increasing interest for the marine industries. A typical example is exhaust gas propagation in cruise vessels and ferries during the design stage to ensure passenger comfort on the top deck. Other applications concern safety of helicopter landing, wind resistance and drift forces (particularly for ferries and car-carriers), ventilation of internal rooms etc.

State-of-the-art for aerodynamic analysis of ship superstructures are experimental investigations in wind tunnels. These experiments are usually reasonably cheap and fast. As an alternative, CFD has some unique advantages over experiments in that it is easy to inspect all areas, including all those usually difficult to access physically. In addition, one can always come back to CFD and extract additional data, as all the results remain on file or are quickly reproduced. Still, CFD has so far not been accepted as an alternative for wind tunnel experiments due to the complex grid generation which prevented it from being competitive in terms of time and cost until most recently. Research partially sponsored by the German ministry for education and research (BMBF) has allowed us progress over the last year in this arena. We see now CFD as a potential alternative for wind tunnel experiments also for the maritime industry.

A fast and sufficiently accurate modeling of the ship geometry in a suitable grid is decisive for the success of CFD. Ship superstructures are geometrically much more complex than underwater bodies of ships. Ship superstructures feature many appendages like masts, winches, radar, etc. Railings stimulate turbulence and are usually considered to be essential in physical wind tunnel testing. Geometric modeling of all these appendages in a CFD grid is practically impossible, but fortunately also not necessary. It suffices to model the global effect of the filigree appendages and model only the larger appendages geometrically.

The aerodynamic flow around ships is turbulent and features massive separation. The appropriate numerical tool is thus a RANSE solver for turbulent flow. The flow is inherently fully turbulent and can be performed at the Reynolds numbers of the full-scale ship. Unlike in wind tunnel tests, there is no need for additional turbulence stimulators. The blockage effect of small appendages is captured by using so-called baffle elements, i.e. elements or cell faces with specified partial permeability, Fig.1. These baffle elements were incorporated by ICCM GmbH in their RANSE solver Comet. Preliminary studies for a railing structure showed that the partial blocking of the flow is much higher than intuitively assumed. This is partially due to the effect of the boundary layer, partially due to the local flow direction which is often far from being orthogonal to the railing's plane. The RANSE simulations were conducted for 2-d unsteady flow capturing vortex shedding at the railings. The geometry of the railing (diameter and spacing of rods) was taken from actual railing data. We assumed a vertical hull wall with a typical height of a deck over the design draft. The flow is then diverted steeply upwards hitting the railing at a small angle and forming a complex vortex structure downwind of the railing, Fig.2.

Based on these numerical studies, higher blockage values should be chosen for the baffle elements. More systematic tests are needed before we can give quantitative advise. Unfortunately there are no guidelines in the literature or the internet. We found extensive data an assorted forest configurations from flow simulations over land, but nothing on grill-type structures as railings.

The aerodynamic boundary layer is much thicker than the hydrodynamic boundary layer. This allows a coarser discretization of the fluid domain near the hull. Grids based on tetrahedral and prism elements become then feasible. These grids are much faster to generate than our usually employed grids based on hexahedral elements, as largely automatic grid generation procedures exist for tetrahedral elements. Figs.3a-b show grid details for the cruise ship. The grid consists of 10 layers of prism cells at the ship surface with the residual space of the computational domain being automatically meshed with tetraeder elements.

Combined, baffle elements and tetrahedral grids now allow to generate grids about ship superstructures within acceptable times based on a suitable CAD description. Often, such a CAD description is not available and has to be created as a first step preceding the actual CFD analysis. A reference application was recently produced for a typical generic cruise vessel created at HSVA from published deckplans of actual modern cruise vessels. The created CFD model is far more detailed than any other such aerodynamic CFD model for ships found in the literature. Several grids of increasing fineness were created with the largest having approximately 5 million cells. Ongoing research focuses on determining proper grid resolution, and we expect that 1-2 million cells may suffice for most practical applications.

The aerodynamic CFD analysis showed extensive recirculation regions at the upper deck of the cruise vessel. One of these recirculation areas appears directly behind the funnel structure, Fig.4.

For exhaust propagation we modeled the flow as two-phase flow in Comet. In addition to the usual transport equations we also solve an equation for the energy balance solving also the thermodynamic distribution in the air. We specify the exhaust temperature and velocity and then trace the development in an externally specified wind distribution, Fig.5. We use a uniform wind speed over height at the domain inlet.

We tested this procedure first for a funnel on a flat plate. This initial test gave plausible results. There were no validation data. We then performed a similar study for the cruise ship in wind direction coming from 30° ahead. The results are seen on the cover of the proceedings. The results look again plausible.

One of our problems is that there are no validation data in the open literature for ships where a 3-d CAD description of the ship structure is given. Either data are from commercial projects and confidential or data were obtained for physical models made from 2-d drawings with a certain amount of creativity on the side of the model maker involved. Usually, we have to resign ourselves for the foreseeable future to create a suitable 3-d description first ourselves before we can commence with grid generation.

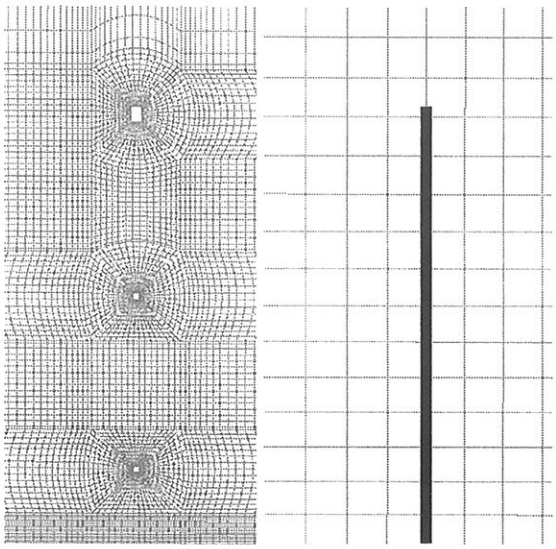

Fig.1: Principle of baffle elements;
22000 cells for direct resolution,
6000 cells using baffle elements

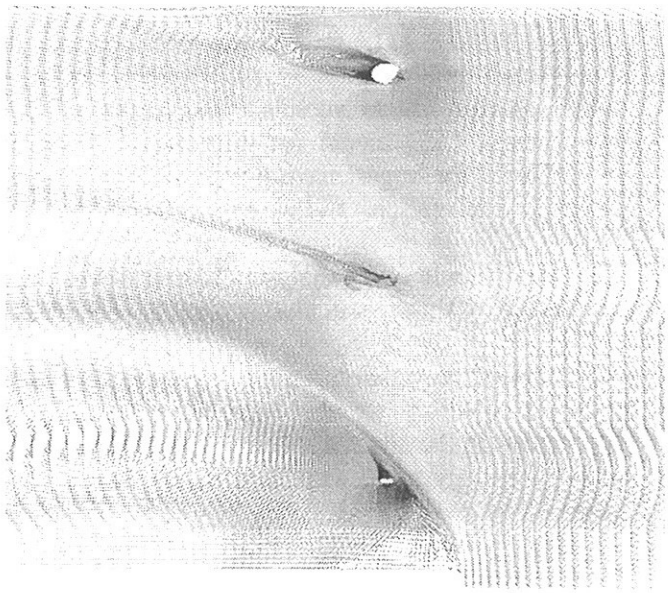

Fig.2: Detail 2-d study for railing at step (hull)

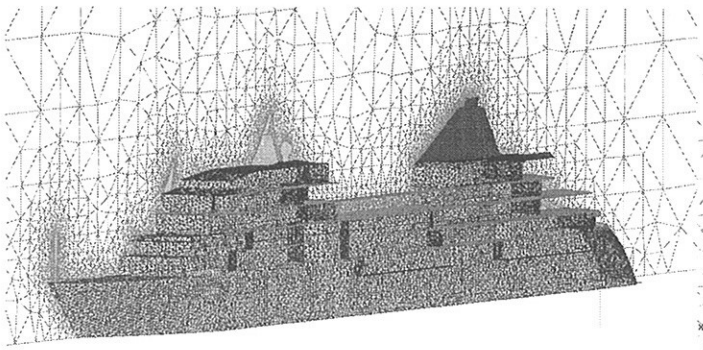

Fig.3a: Grid for cruise vessel

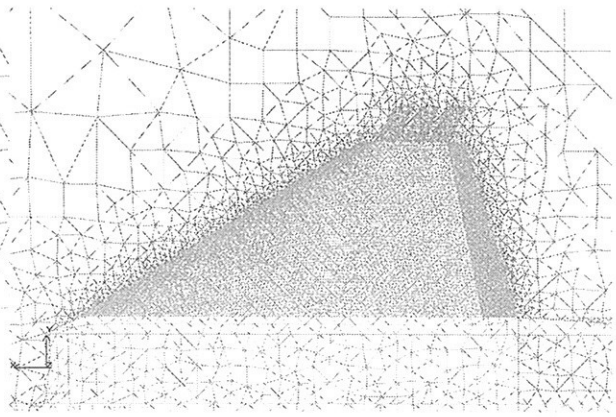

Fig.3b: Grid for cruise vessel, detail

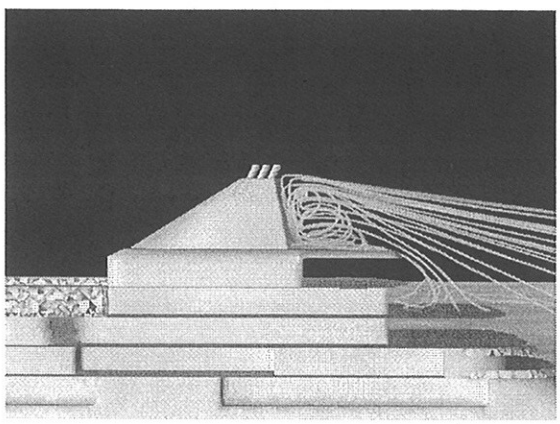

Fig.4: Streamlines after funnel

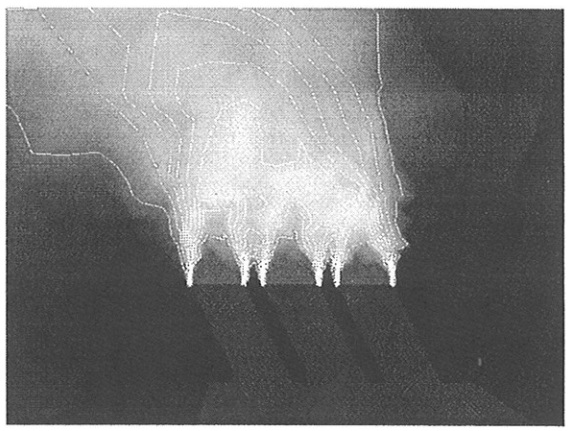

Fig.5: Thermic distribution

LES of flow around a sphere at subcritical Reynolds number

Ibrahim Hadžić and Milovan Perić
TU Hamburg-Harburg, AB Fluiddynamik und Schiffstheorie, Hamburg, Germany,
[hadzic,peric]@tu-harburg.de

The work presented in this paper is part of the ongoing DFG (German Research Foundation) project on Large Eddy Simulation(LES) of transitional flows with separation. The feasibility of LES of the transitional flows around a bluff body with separation from a smooth surface is investigated here. The specific case chosen is the flow around a sphere held by a stick with a diameter around 10% of sphere diameter, attached to it at the rear stagnation point. The bulk Reynolds number based on sphere diameter and undisturbed flow is Re = 50000. In the past flows around bluff bodies such as circular or square cylinder have been extensively studied, both experimentally and numerically, because of their importance in engineering practice. Although the flow around sphere is relevant for many technical problems, extensive numerical studies have been done in the past only for laminar regime; experimental data for turbulent flows is also scars and is mostly limited to integral parameters such as drag. Flow around sphere is a challenging case for turbulence modeling owing to the relatively complex physical phenomena and different flow regimes present. Downstream of stagnation point a very thin laminar boundary layer forms, which separates near equator and undergoes transition to turbulence. As the flow separates from a smooth surface, the separation line is not fixed. The wake is highly turbulent and includes a large recirculation region. It is known that most RANSE-models are not capable of handling this kind of flows with satisfactory accuracy; in the case of sphere, the predicted drag coefficient is often less than half the measured value.

The method used is an incompressible implicite second-order finite volume method with a collocated variable arrangement and cell-wise local grid refinement Demirdžić *et al.* (2000). The code used "Comet", is based on unstructured grids with arbitrary shape of control volumes. The SIMPLE algorithm is used for pressure-velocity coupling. The code is parallelized using grid decomposition and the message passing interface (MPI). Computations have been performed on a supercomputer on 64 processors.

Computations have been carried out on a mesh consisting of about 1.6 million control-volumes, with grid refinement applied in the region around the sphere, shear layer and the recirculation region. As the sub-grid scale (SGS) model the SmagorinskySmagorinsky (1963) model was used. Computations are preformed also with no model. To suppress unphysical oscillations, the first-order upwind scheme is used in front of the sphere, upstream of the transition point and in the free-stream far away from the recirculation region. In the edge region of turbulent flow it is gradually mixed with the central difference scheme (CDS). The non-dissipative CDS is applied in the turbulent region of the flow.

Computational results are compared with avaliable experimental results by Šain (2001). The hot-wire technique was used in experiments. The experimental data of the mean velocity and

averaged square root of the velocity fluctuation corelation are avaliable at several position downstream from the separation point. Figure 1 shows the computational domain with the numerical grid. Figure 2 shows the time history of the drag coeficient. The experimental data of the drag coeficient are not yet avaliable by Šain (2001) but comparison to other experiments show that it is overpredicted for about 10%. All complexity of this flow is shown in Figure 3. Figure 4 shows the mean velocity vectors and the stream-wise normal component of the Reynolds stress tensor, before averaging in the circumferential direction. High level of symmetry of computational results was obtained for these quantities. The predicted length of the recirculation region is close to that observed in the experiment. Rather good agreement between experiment and LES is obtained for the mean velocity, as can be seen from Fig. 5. The agreement is qualitatively satisfactory also for the mean square root of the correlation of velocity magnitude fluctuations u/U_o; the discrepancy may be due to the relatively coarse grid.

The paper will present details on the numerical method, turbulence models (RANSE and LES), as well as details of grid-dependence analysis and further comparisons of computed and measured mean velocity and turbulence properties. The performance of numerical methods and the possibility of their improvement will also be discussed.

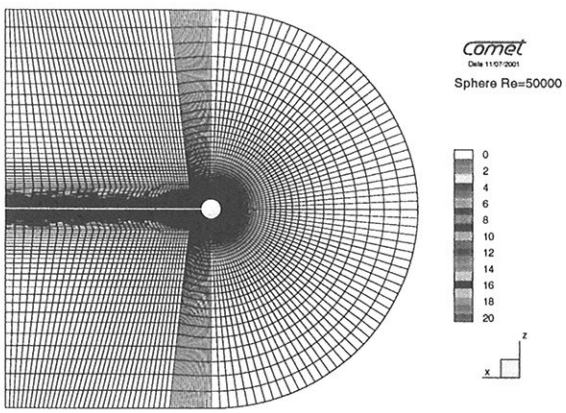

Figure 1: Computational domain with numerical grid.

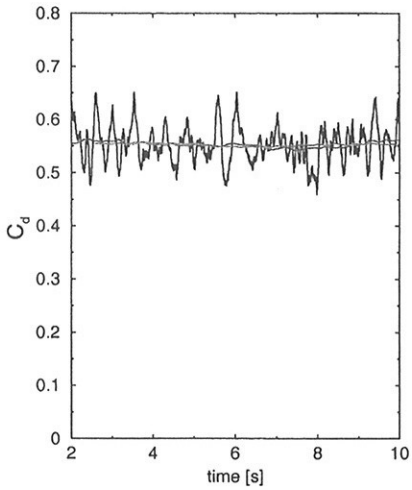

Figure 2: Time history of the drag coeficient.

Demirdžić, I., S. Muzaferija, and M. Perić (2000). General calculation experiments with the primitive equations. *Advances in Fluid Mechanics 27*, 249–300.

Smagorinsky, J. (1963). General calculation experiments with the primitive equations. *Mon. Weather Rev. 91*, 99,165.

Šain, V. (2001). Personal Communication.

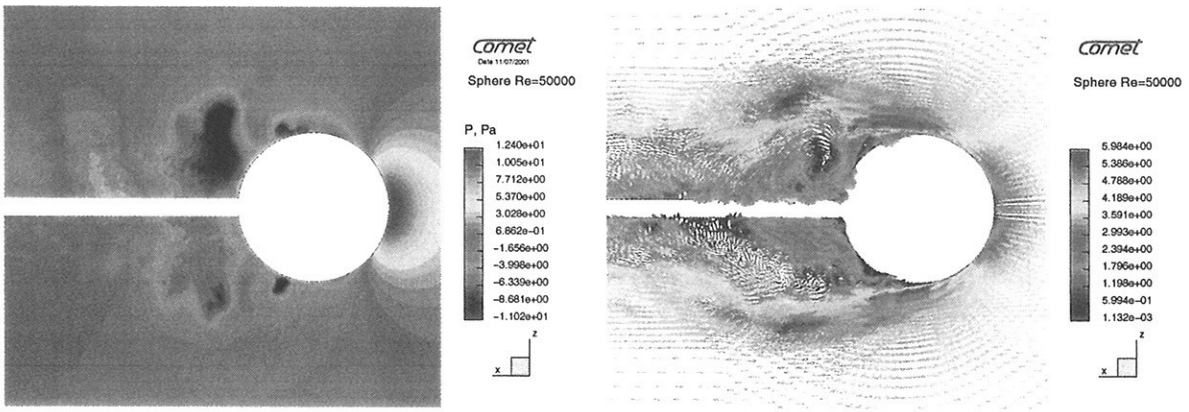

Figure 3: Instantaneous presure (a) and velocity vectors (b).

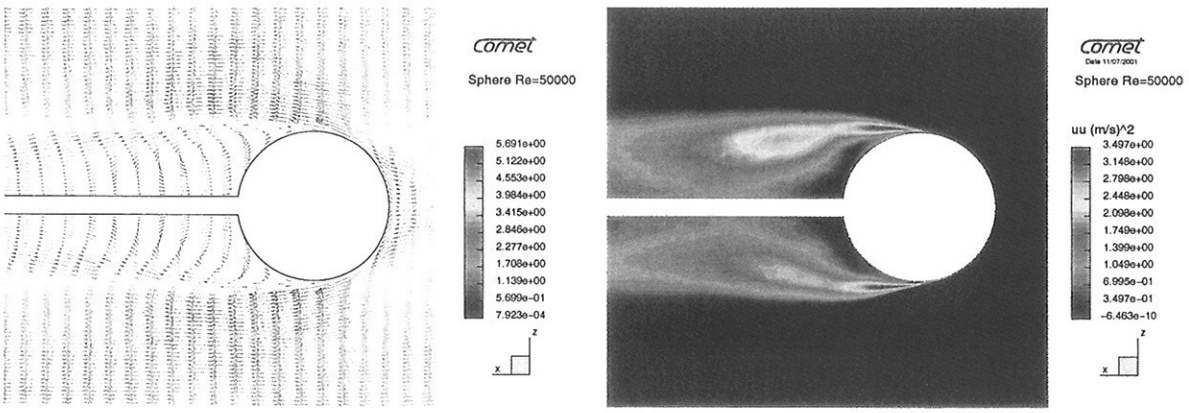

Figure 4: Mean velocity vectors (a) and streamwise component of the Reynolds stress tensor.

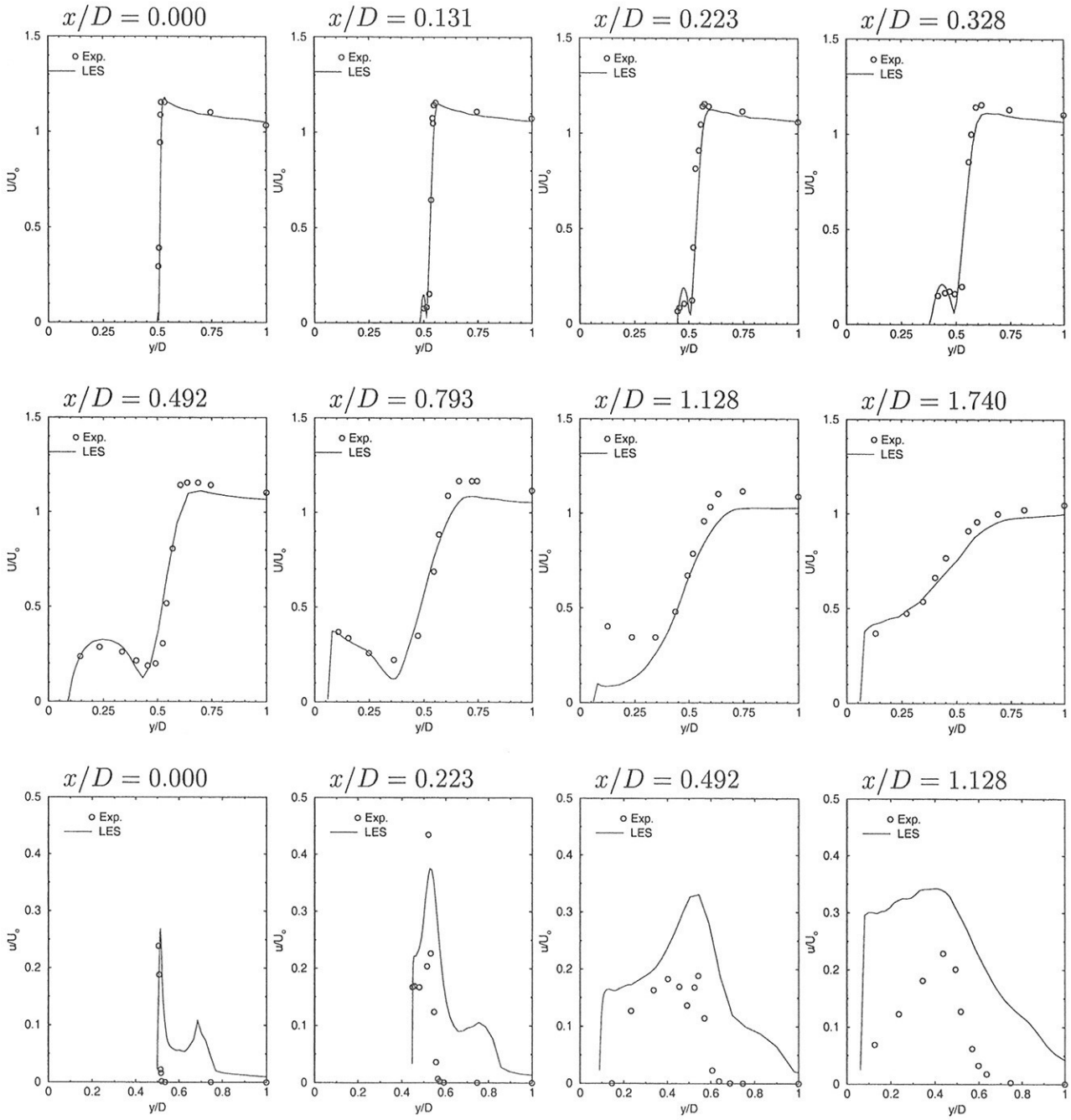

Figure 5: Comparison between experimental and numerical results. U/U_o is the mean of the absolute velocity and u/U_o the squer root of the corelation of the absolute velocity fluctuations.

Efficient Grid Generation for Maritime RANSE Simulations

Dieke Hafermann, HSVA, hafermann@hsva.de
Reimund Steberl, ICEM CFD Engineering, rst@icemcfd.com

When performing CFD simulations of complex maritime structures, like ships, grid generation is a time-consuming task representing the critical path in the simulation turnaround time. Applying advanced RANSE codes, HSVA has made significant progress in realistically modeling close-to-wall physics like viscosity, turbulence, and separation phenomena in the flow around ships. To use these new numerical methods efficiently, grid generation procedures have to be provided delivering quickly the required high-quality volume meshes for complex maritime structures.

To meet this objective HSVA and ICEM CFD Engineering have established an environment for "Efficient Grid Generation for Maritime RANSE Simulations" within a research project of the German ministry for education and research (BMBF). This grid generation environment is based on ICEM CFD, the worldwide most frequently used CFD preprocessor, and provides the user with a library of templates and tailored tools to quickly mesh maritime structures. The following are the key features and advantages of the developed maritime grid generation environment:

- Automated meshing of design variants

  For different types of ships (container ship, tanker, roro vessel, etc.) topology templates have been developed. The templates allow highly automatically mesh generation for similar ship geometries, and can account for different water level and trim and heel angles. As a result, the user can mesh a design variant of a certain type of ship in a fraction of the time needed to create a mesh from scratch.

  - Sub-topologies

    Sub-topologies are topologies/sub-meshes of parts that are referenced in a global topology/mesh. Sub-topologies are useful tools to model objects like propellers, rudders, etc., Fig.1. To account for instance in a flow model of a ship for a propeller the user activates a void cylindrical or conical space in the global topology and inserts the prefabricated propeller topology into the global topology applying sliding interfaces in between the propeller topology and the global ship topology, Figs.2 and 3. This procedure allows to quickly account for complex components and/or to quickly exchange components in maritime flow models.

    A propeller topology can be easily created by means of the sub-topology technique. First the block topology for a passage around a propeller blade is conventionally modeled by means of ICEM CFD Hexa. Then the passage topology is rotated and copied to model the entire propeller.

  - Navier-Stokes layers

    A special feature of the maritime grid generation environment allows to automatically redistribute and refine the boundary layers of an initial Euler grid to get Navier-Stokes layers near the boundary surfaces and a smooth transition to the farfield grid.

- Mesh smoothing

  The maritime grid generation environment provides smoothing functions to get well-conditioned meshes with good orthogonality normal to the boundary surfaces, resulting in good convergence behaviour of the RANSE codes, Fig.4.

The maritime grid generation environment has been proven as a useful tool to generate high-quality maritime CFD meshes for RANSE calculations in short time at HSVA. The described maritime grid generation environment will be enhanced by automatic tetrahedral/prism meshing capabilities to automatically create flow models for climate control in ship cabins or in container halls, for smoke propagation on/in ships and for similar applications.

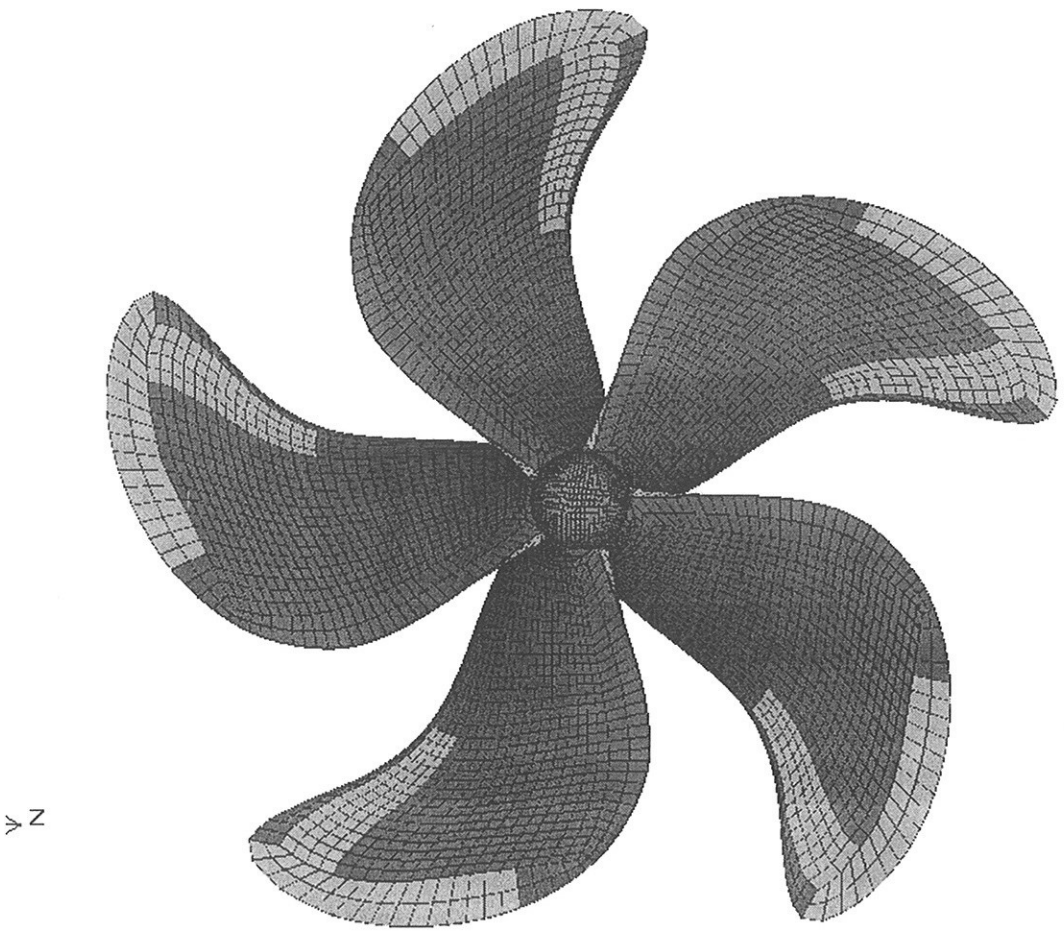

Figure 1: Grid of a propeller derived from a propeller subtopology

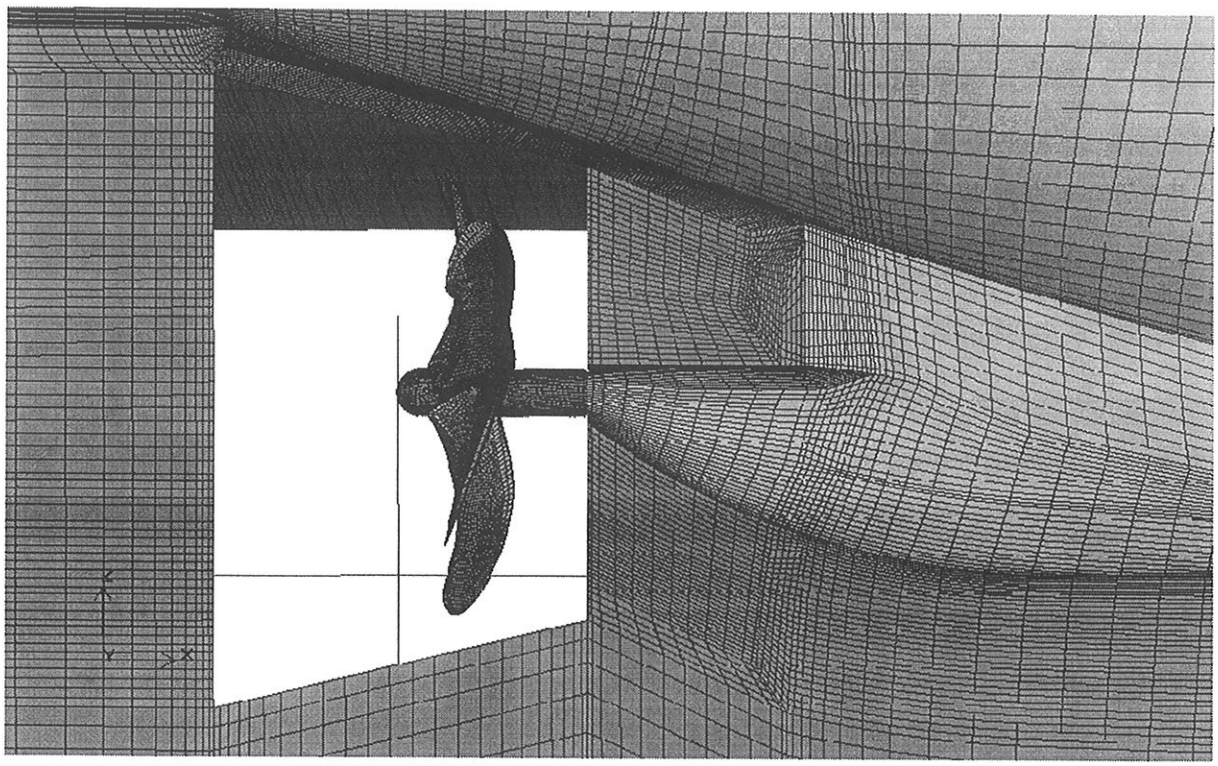

Figure 2: Aftbody detail: Grid of a propeller integrated into the global grid of a ship

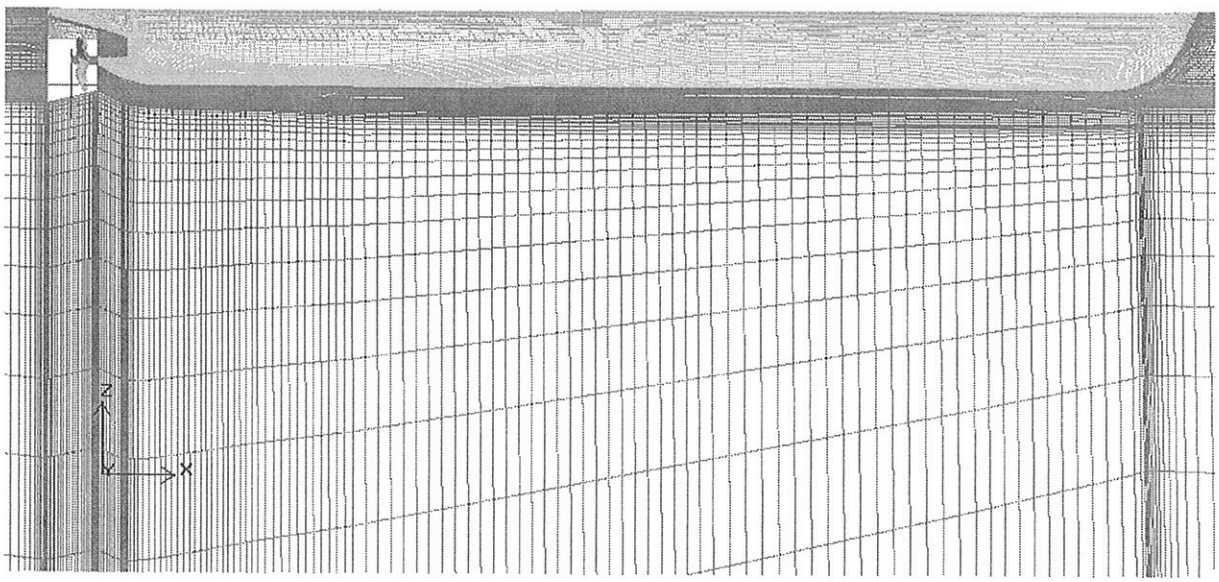

Figure 3: Global grid of a ship including integrated propeller

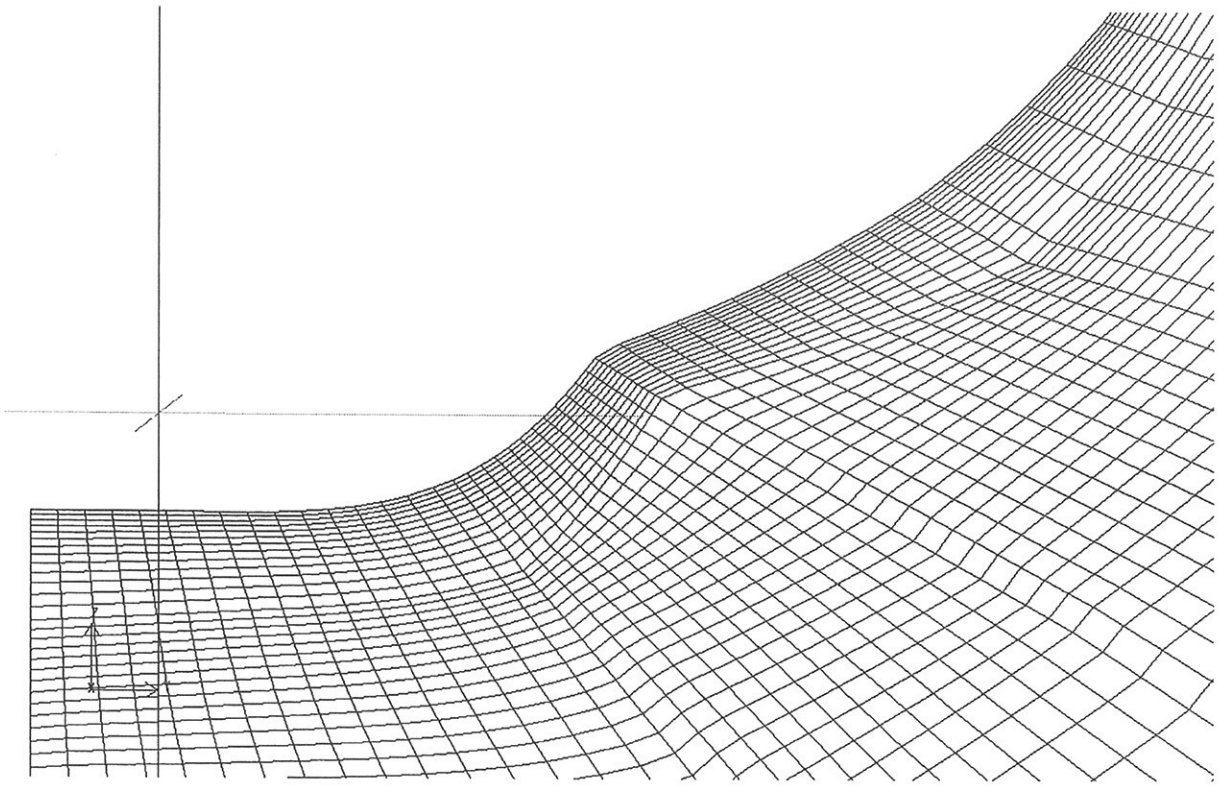

Figure 4: IJK-Plane of a smoothed grid

Multigrid Method for Ship Flow Computations on Unstructured Grids

Nobuyuki Hirata & Takanori Hino
National Maritime Research Institute, JAPAN

1. Introduction

Recently, computational fluid dynamics(CFD) has been demanded as the practical design tool in various fields of fluid engineering including naval architecture. Since most of real-world shapes are geometrically complex, grid generation procedures and flow solvers should be able to cope with complicated configurations. One of the possible solutions to overcome the difficulties, is an unstructured grid method in which computational grids are constructed by irregularly connected polyhedral cells. However, such computations take lots of CPU time in order to obtain the accurate solutions. Thus, the improvement of the computer efficiency is required.

The objective of this work is to develop an efficient and accurate unstructured grid code for simulating turbulent flows around a ship using cost-effective platforms. The artificial compressibility form of the three-dimensional incompressible Navier-Stokes equations is solved using an approximated Newton relaxation approach. In order to accelerate the convergence of the solutions, the multigrid method is applied. Computed results and convergence performance will be discussed at the meeting.

2. Numerical Procedure

2.1 Basic flow solver

The basic flow solver used in this work is called SURF[1]. The governing equations are the three-dimensional Reynolds averaged Navier-Stokes equations for incompressible flows. With the introduction of artificial compressibility, the system of equations becomes hyperbolic and is written in a non-dimensional form as

$$\frac{\partial \boldsymbol{q}}{\partial t} + \frac{\partial (\boldsymbol{e} - \boldsymbol{e^v})}{\partial x} + \frac{\partial (\boldsymbol{f} - \boldsymbol{f^v})}{\partial y} + \frac{\partial (\boldsymbol{g} - \boldsymbol{g^v})}{\partial z} = 0 \tag{1}$$

where $\boldsymbol{q} = [p, u, v, w]^T$ is the vector of flow variables. $(\boldsymbol{e}, \boldsymbol{f}, \boldsymbol{g})$ and $(\boldsymbol{e^v}, \boldsymbol{f^v}, \boldsymbol{g^v})$ are inviscid and viscous fluxes, respectively.

Spatial discretization is based on a finite-volume method for an unstructured grid. In the present approach, a cell centered layout is adopted in which flow variables are defined at the centroid of each cell and a control volume is a cell itself. As shown in Fig.1, cell shapes which the present solver can cope with, are tetrahedron, prism, pyramid or hexahedron and face shapes are either triangular or quadrilateral. These four types of cells give larger flexibility in handling complex geometries.

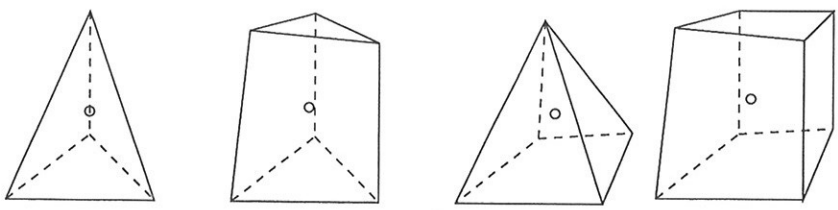

Fig.1 Computational cells (Tetrahedron, prism, pyramid and hexahedron).

Volume integration of the governing equations over a cell yields

$$\frac{\delta (V_i \boldsymbol{q}_i)}{\delta t} + \sum_j \boldsymbol{F}_{(i+j)/2} - \sum_j \boldsymbol{R}_{(i+j)/2} = 0 \tag{2}$$

where i is a cell index and j is the index of neighbor cells of the cell i. $(i+j)/2$ denotes the face between cells i and j as shown in Fig.2

$\boldsymbol{F}$ and $\boldsymbol{R}$ are the inviscid and viscous fluxes defined as

$$\boldsymbol{F} = eS_x + fS_y + gS_z, \quad \boldsymbol{R} = e^v S_x + f^v S_y + g^v S_z$$

(S_x, S_y, S_z) are the (x, y, z)-components of the area vector of a cell face in the direction from the cell i to the cell j.

The inviscid fluxes $\boldsymbol{F}$ are evaluated by the upwind scheme based on the flux-difference splitting of Roe. To maintain the second-order accuracy in space, the flow variables on the cell faces are computed from the cell centered values using the linear extrapolation.

The computation of viscous fluxes $\boldsymbol{R}_{(i+j)/2}$ requires velocity gradient on a cell face. These are computed by applying the divergence theorem to another control volume surrounding a cell face as shown in Fig.3.

The first-order accurate backward Euler scheme is used for the time integration. The linear equation system obtained by the linearization with respect to time is solved by the symmetric Gauss-Seidel (SGS) iteration. To achieve fast convergence, the cells are ordered from upstream to downstream. The Gauss-Seidel sweep is carried out from the upstream cell to the downstream first, then the second sweep follows the reverse order. The following sweeps change the direction alternately. Typically 10-20 SGS sweeps are performed at each time step.

A turbulence model used is a one equation model proposed by Spalart-Allmaras. The numerical method employed for the solution of turbulent equation is similar to the one for flow equations except that the advection terms are evaluated by the first-order upwind scheme.

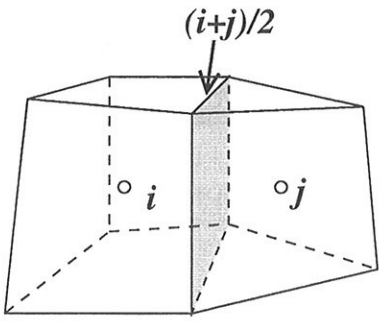

Fig.2 Definition sketch of cell and face index.

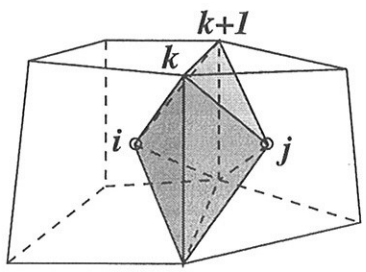

Fig.3 Control volume for the evaluation of velocity gradient.

2.2 Multigrid method

A multigrid method is known as the extremely efficient way to obtain fast convergence. The concept of the multigrid time stepping is to compute corrections to the solution on a fine grid by the time-stepping on a coarser grid. When operating the multigrid method on unstructured grids, the large difficulty lies in the generation of the coarser level grids. For structured grids, coarse level grids are generated by deleting every other points along grid lines of the finer grids, whereas the generation of coarse grids on unstructured grids, is not trivial. One way is the agglomeration method which coarse grids are constructed by fusing together neighboring fine grid cells to form a smaller number of larger and more complex cells on the coarse grid.

An agglomeration method used in this work is a global coarsening algorithm[2]. Since it is based on a global topological information of grids, the determination of the front advancing direction is not required. The algorithm is depicted in Fig.4 and constructed in the following way.

1. Calculate the aspect ratio $V/S^{1.5}$ of the two cells sharing each edge in Fig.4(a). Here, V and S are the volume and the surface area of a cell respectively.
2. Sort the edges in the descending order of the aspect ratios.
3. Add the largest aspect ratio edge to independent set of edges(ISE).
4. Add the next largest aspect ratio edge to ISE if the edge is not adjacent to any edges which are already in ISE. Repeat this procedure until all edges are checked. The dashed lines in Fig.4(b), show the elements in ISE.
5. For all the elements in ISE, agglomerate two cells sharing the edge into a coarse cell as shown in Fig.4(c). The cells in black are not agglomerated yet.
6. For unagglomerated cells, fuse the cell with the already generated neighboring coarse cells, so as to maximize the aspect ratio of the coarse cell. Repeat this procedure until all cells are agglomerated.(Fig.4(d)).
7. Repeat from step 1 until a specified number of cells are fused into a coarse cell.

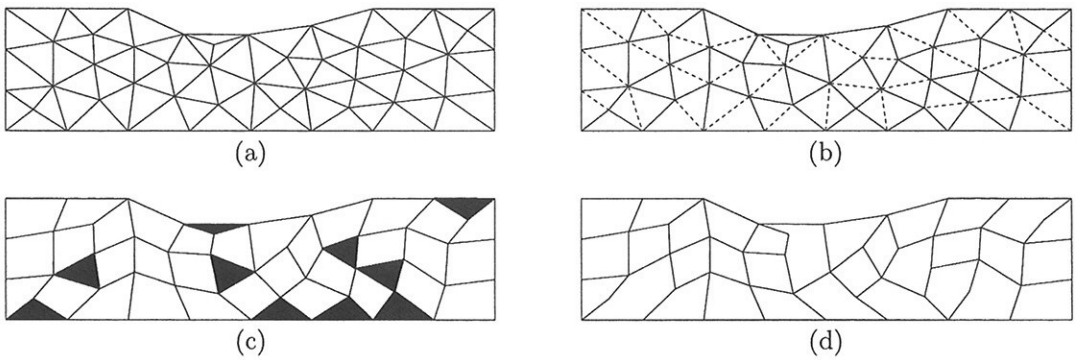

Fig.4 Agglomeration by the global coarsening algorithm

A multigrid cycle used in this work is V-cycle in which the equations are first solved at the finest grid and the solution moves down to the coarsest grid with an update of a solution at each grid and the interpolation is used in the transfer of correction from the coarsest grid to the finest one. As shown in Fig.4(d), the resulting coarse grids contain complicated polyhedral cells which are no longer simple geometries in Fig.1. Hence, the method for discretizing and solving the governing equations on these coarse grids must be devised.

Computed results and convergence performance will be discussed at the meeting.

References

[1] Hino, T., "A 3D Unstructured Grid Method for Incompressible Viscous Flows", J. of the Soc. Naval Archit. Japan, vol.182, pp.9-15, 1997.

[2] Okamoto, N., Nakahashi, K. and Obayashi, S., "A Coarse Grid Generation Algorithm for Agglomeration Multigrid Method on Unstructured Grids", *AIAA 98-0615*, 1998.

Numerical Studies of Wave Breaking Compared to Experimental Observations

Maurizio Landrini [1], *Andrea Colagrossi* [2] and *Marshall P. Tulin* [2]

2 *Ocean Engineering Laboratory*, UCSB. mpt@engineering.ucsb.edu
1 INSEAN, *The Italian Ship Model Basin*, Roma, Italy. maulan@waves.insean.it

We report our current investigation aimed to understand the fluid dynamics involved in bow-wave radiation, including wave breaking. The analysis is limited to practical slender ships, with a sharp stem, for which basic insight can be achieved by exploiting the idea that longitudinal gradients of relevant flow quantities are small compared with vertical and transverse gradients. On this ground, *cf.* Fig. 1, the steady inviscid three-dimensional problem can be simplified and shown to be mathematically equivalent to the unsteady two-dimensional free-surface flow in the plane vertical and transverse to the ship, as generated by a deformable body, the cross section of the passing through ship. Consistently, we call this approximation 2D+t model. See [3] for a review.

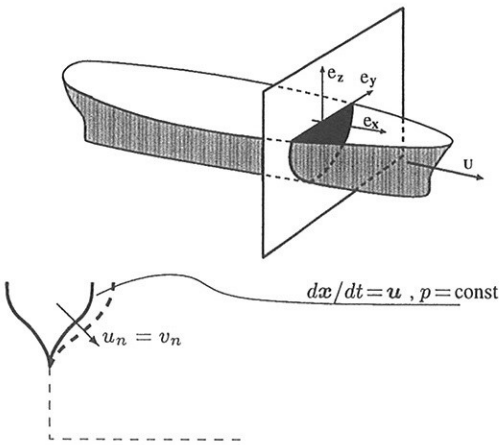

Fig. 1: Qualitative sketch of the 2D+t approximation to the steady three-dimensional flow around a ship.

Here, the nonlinearities due to free-surface and body motions are fully retained, and the problem is solved numerically by two different numerical tools:

a) For non-breaking flows, in the pre-breaking stage and up to the free surface overturns and plunges on itself, the flow field can be described efficiently and with high resolution by BEM. The method is well known and will not be described further.

b) For flows with wave breaking, a Lagrangian meshless method is applied, based on an improved SPH technique, and it is described in a companion paper in this Symposium.

Wigley hull The physics underlying the bow splash, the system of the radiated divergent waves and their pre-breaking evolution have been clarified in [6] by BEM computations. We briefly recall the key features of the wave pattern through Fig. 2: (i) the system of divergent waves radiated at the bow as a result of the collapse of the bow "splash", and (ii) the "rooster tail" just past the stern which is the source of another system of diverging waves. In this case, wave breaking does not appear. More in general, for this wall-sided hull, wave breaking has never been observed *at the hull*. In particular, through extensive computations, we determined that the radiated waves can be made steeper and steeper by increasing $Fr = U/\sqrt{gL}$, or reducing the draft D/L, or increasing the beam B/L. For suitable combinations of these parameters, the radiated waves eventually break, though relatively far from the hull.

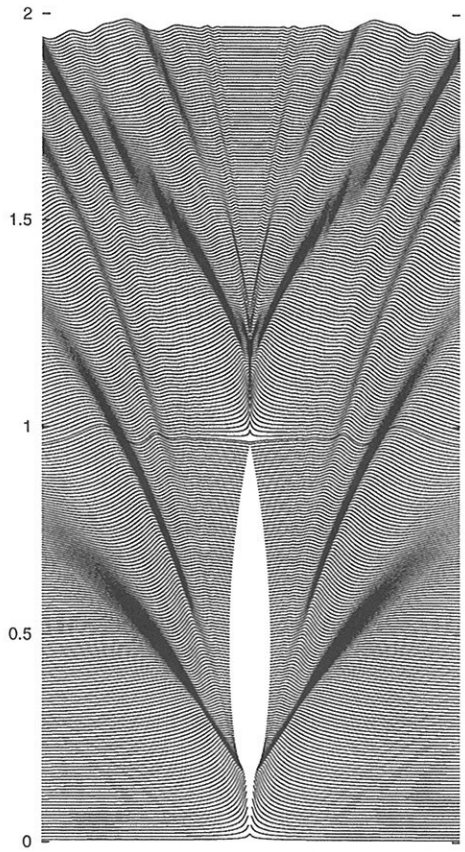

Fig. 2: Wave pattern past a Wigley hull ($B/L = 0{\cdot}1$, $D/L = 0.1$, $\mathbf{Fr} = 0{\cdot}3$).

One of these cases is described in Fig. 3 (top): the free-surface flow is not much decelerated before the stem, but upon reaching it, is deviated sharply upwards, rises on and eventually levels off and falls down. An entire thin sheet is formed in this process and appears as a splash on either side of the hull. The relaxation of these splashes is the prime source of diverging

waves. In this case, the radiated wave is large enough to break, following the typical evolution: crest-rising, front-steepening and jet formation. The breaking and post-breaking evolution

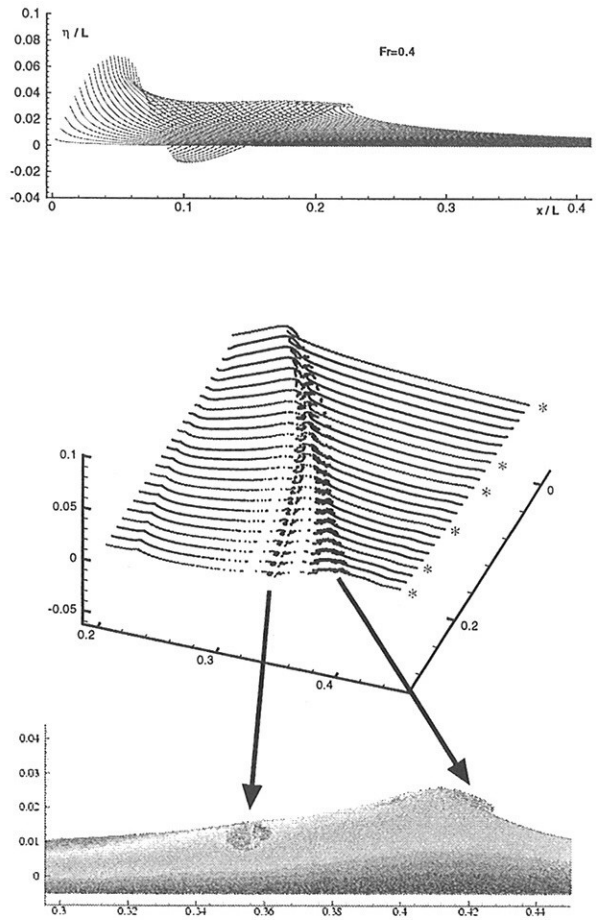

Fig. 3: Breaking of the bow wave radiated by a Wigley hull ($B/L = 0{\cdot}2$, $D/L = 0{\cdot}1$, Fr$= 0{\cdot}4$). Top: pre-breaking evolution by BEM, bow splash, wave radiation, steepening and overturning. Center: three-dimensional reconstruction of the breaking evolution by SPH, the initial conditions are given by the BEM computations. Bottom: last configuration in the post breaking evolution, vortex pairing past the broken crest and quasi-stationary eddy surfing the residual wave propagating rightward.

is analyzed by our SPH computations. The three-dimensional wave pattern is reconstructed in the center plot (only the upper layer of particles is represented), where the portion around the breaking is shown. The ship center plane located at $y = 0$, and the mid-ship cross section at $x = 0$. The impacting jet generates a splash-up, evolving into (i) a vortical structure left behind the crest, and (ii) remaining particles riding on the crest emerging after the breaking which resemble the steady eddy used by [2] to model two-dimensional steady spilling breakers. We named this behavior TYPE I breaking. This flow pattern is better visible in the two-dimensional bottom plot, and is remarkably similar to pictures of (two-dimensional) breaking waves shown in [4].

Frigate-type hull In practical cases, ship forms are often characterized by a substantial bow flare causing the ship-generated waves to break sooner, closer to the hull, if not *at the hull.* The picture in Figure 4, `http://www50.dt.navy.mil/5415/geomn.html`, is representative of such conditions: the water piles up against the curved hull, and then collapse down in the form of a rather thick jet. Intense bow breaking implies drag, noise (which

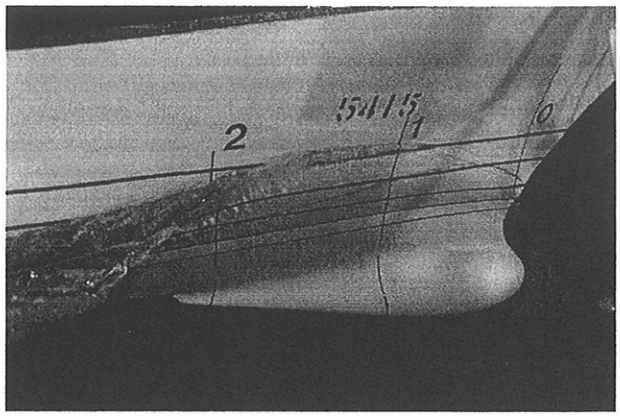

Fig. 4: Breaking bow splash for the Model 5415, Fr=0·41.

can be remotely detected or reduce the performances of the sonar), production of bubbly flows (which can have a significant acoustic backscatter). BEM can recover the initiation of this process and, by virtue of its great resolution and efficiency, can be effectively used (i) to capture the main features of the nascent breaking splash (*e.g.* plunge point, geometrical and dynamical characteristics of the breaker) and define the "quality" of bow geometry, and (ii) to develop improved bow forms with reduced or suppressed breaking, at least for some selected working conditions.

Fig. 5 shows systematic computations for the Model 5415 by 2D+t BEM. The actual geometry has been modified, reducing the volume of the bulb which is too blunt to be treated as slender. The speed decreases from top bottom. It can be seen the gradual transformation of the breaking bow splash: the strength decreases (mass and integrated momentum in the jet, maximum height reached by the splash) and the plunge point shifts upstream, approaching the bow section x_B, as in the following table:

Fr	0·41	0·35	0·315	0·28	0·24
$(x - x_B)/L$	0·179	0·1403	0·1266	0·118	0·0925

For the lower speeds, the outward radiation of the wave front is already started, although the plunge point is closer to the ship. Remarkably, for Fr$<$ 0·35, model-scale experiments do not show any significant breaking while full-scale observations reveal intense bow breaking waves even for the smallest Fr here considered. This is a clear example of the role of surface tension which, for the typical model scales adopted, is quite effective in suppressing the formation of plunging jets, if these are not energetic enough.

The breaking of the free surface prevents the BEM computations to proceed and further analysis relies on our meshless code. A three-dimensional reconstruction of the wave pattern

lapse, the jet impacts at the plunge point A, starting the cyclical splash-up B. For each event, two for the considered case, a vortical structure is created and left behind the breaking front, resulting in longitudinal wakes running almost parallel to the ship. A smooth plateau C is observed between the ship and the wake. Finally, the residual quasi-stationary eddy is observed.

These features have been recognized in a picture from INSEAN model tests. Fig. 9 shows the free surface around the bow for Fr= 0·41: the splash evolves into a jet plunging onto the free surface, point A, and creating the splash-up front, point B, and the scar D associated with the first vortical structure. The field of view in the picture is too narrow to observe the second breaking cycle. The effects of the latter are better seen in the stereoscopic picture from DTMB, Fig. 10. The air entrapped in the vortical regions created during the breaking process made visible the tracks of the longitudinal vortical structures, marked by the two black arrows in the picture, and clearly originating from the breaking front in the bow region upstream.

The fluid dynamics structure of breaking ship waves has been fully interpreted. Some fundamental features of the phenomenon (breaking with cyclical splash up, creation of rotational structures, air entrapment) have been detected and the analysis has been confirmed by experimental observations. Two stages of the breaking evolution have been identified. A TYPE I breaking results from less energetic breaking waves, and resembles the steady spilling breaking observed *e.g.* past hydrofoils at small incidence. TYPE I breaking appears also as the ending stage of the more vigorous TYPE II breaking, characterized by strong (possibly multiple) splash-up, causing larger air entrapment and vortex generation.

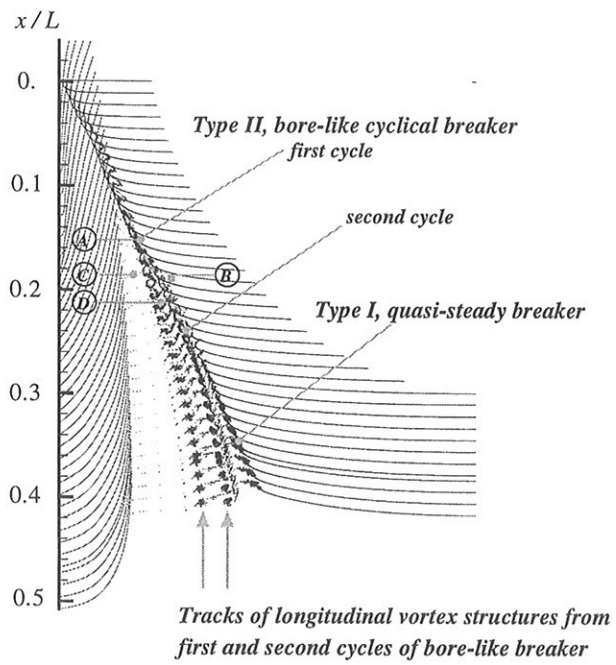

Fig. 8: Three-dimensional reconstruction and interpretation of the breaking wave pattern around the Model 5415. A= plunge point, B=splash-up front, C=plateau, D=origin of free surface scars.

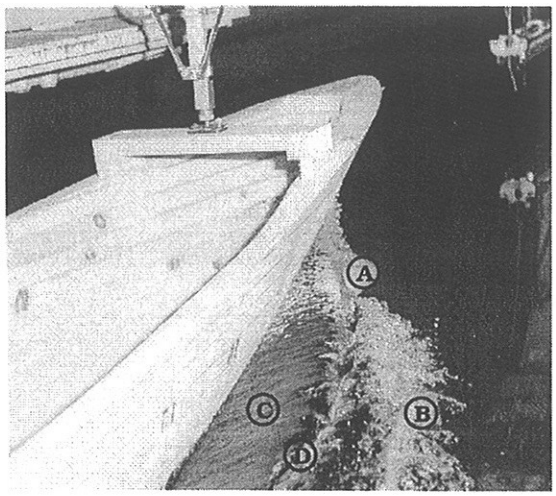

Fig. 9: Perspective view of breaking wave pattern in the bow region of the Model 5415 (INSEAN Model 2415). For labels see Fig. 8.

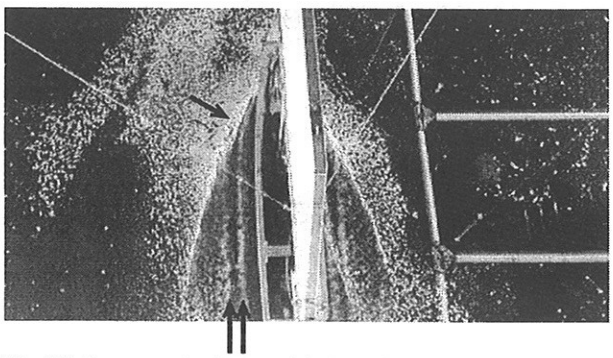

Fig. 10: Stereoscopic picture of the breaking wave pattern around the Model 5415 (DTMB). The ship is moving from bottom to top. The black arrows mark, respectively, the breaking front near the bow and the tracks of the vortical wakes generated.

Acknowledgement This work has been supported as part of a program for the simulation of ship breaking waves by the Ship Hydrodynamics Program of ONR, managed by Dr. Pat Purtell.

References

[1] Bonmarin P., Geometric properties of deep-water breaking waves, *J. Fluid Mech.*,**209**, pp. 405-433 (1989).

[2] Cointe R., Tulin M.P., A theory of steady breakers, *J. Fluid Mech.* **276** (1994).

[3] Fontaine E., Tulin M.P., On the prediction of free-surface flows past slender hulls using the 2D+t theory: the evolution of an idea, *Ship Tech. Res.* (2001).

[4] Melville W.K., The role of surface-wave breaking in air-sea interaction, *Ann. Rev. Fluid Mech.* **28**, pp. 279-321 (1996).

[5] Tulin M.P. and Landrini M., Breaking waves in the ocean and around ships, Proc. of the 23^{rd} *ONR Symp. on Naval Hydrodynamics*, Val de Reuil, France National Academy Press, Wash. D.C. (2000).

[6] Tulin M.P. and Wu M., Divergent bow waves, Proc. of the 21^{st} *ONR Symp. on Naval Hydrodynamics*, Trondheim, Norway, National Academy Press, Wash. D.C., pp. 99–117 (1996).

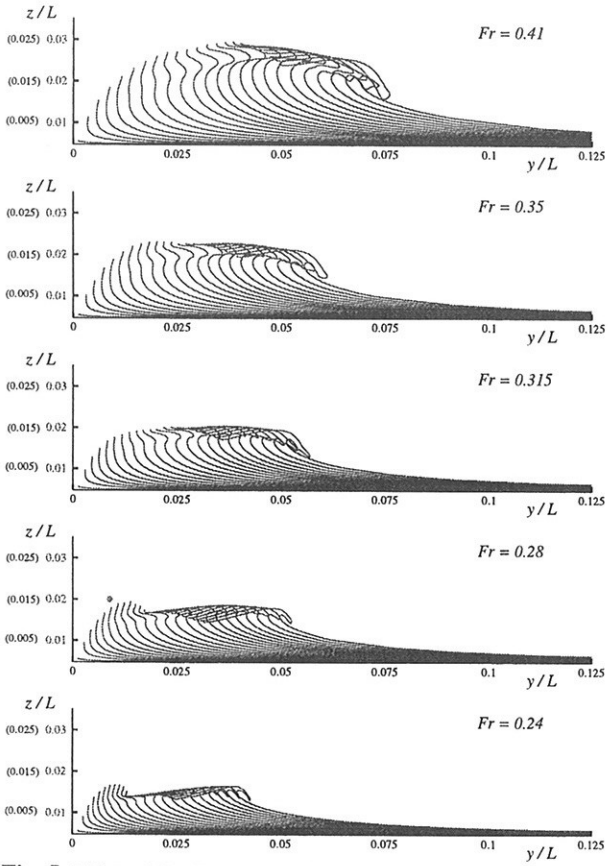

Fig. 5: Effect of the Froude number on the breaking bow splash of the Model 5415, as computed by BEM.

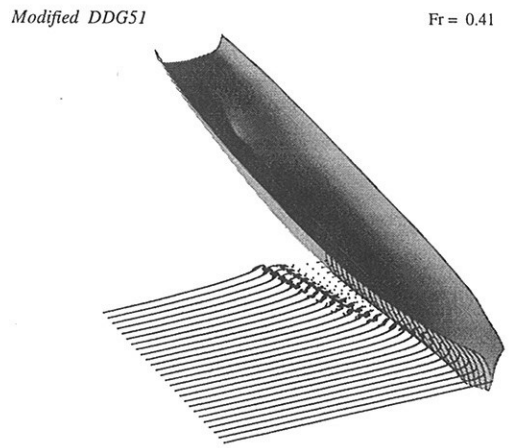

Fig. 6: Three-dimensional reconstruction of the breaking wave pattern around the Model 5415, Fr= 0·41, as computed by SPH.

is shown in figure 6. With the aid of Fig. 7, we can summarize the following observations: (i) when the jet impacts onto the free surface, a cavity is entrapped and circulation and vorticity suddenly are created (top plot). The origin of this vortical structure is "topological" and not connected to viscous effects, which on this short time scale can not play any significant role; (ii) a splash up is usually observed, with strength related to that of the impacting jet. The gravitational collapse of the splash up gives origin to a forward plunging jet and, therefore, vorticity is created with the same mechanism discussed above and with the same sign (middle plot). As observed in [1], the splash up can evolve also into a backward-facing plunging jet, creating a vortical structure of opposite sign, possible pairing with the ones previously created. We named this stage of the breaking process, TYPE II breaking and we found striking similarities with breaking bores in shallow water, discussed through numerical simulations in [5]; (iii) eventually, we observe a quasi-stationary eddy surfing the residual wave crest emerging after the more intense stage of the breaking process, similarly to that show for the Wigley hull (bottom plot). Clearly, the strength of the plunging

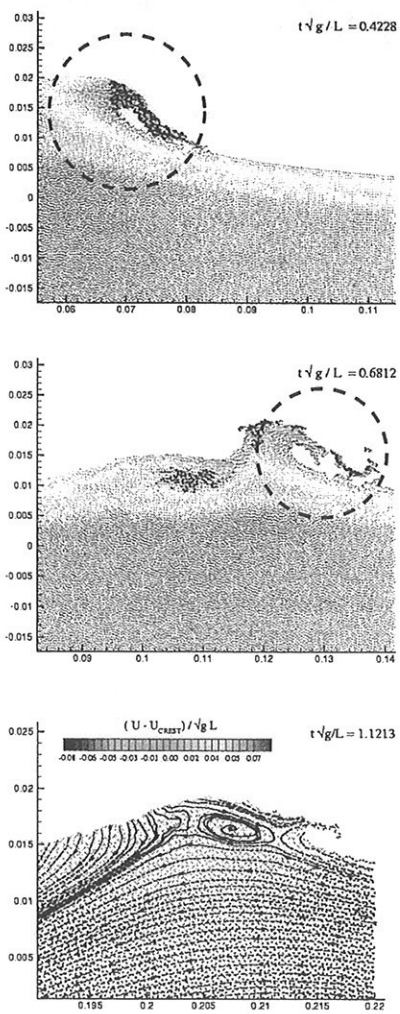

Fig. 7: Details of the breaking wave pattern past the Model 5415, as computed by SPH. Top: jet at the plunge point; Middle: second breaking cycle; Bottom: residual quasi-stationary eddy.

jet is crucial in determining that of the splash-up and the resulting process. For breaking bores we observed several splash-up cycles, [5].

This remarkable evolution is further clarified in the three-dimensional reconstruction of Fig. 8. After the bow splash col-

Numerical Study of the Wave Breaking Generated by a Submerged Hydrofoil

Jean-Marc Laurens, T. Leconte, Francois Grosjean

ENSIETA, Brest, Jean-Marc.Laurens@ensieta.fr

The Duncan (1983) experiment has been the subject of many consecutive studies. Duncan towed a fully submerged 2-d NACA0012 profile at a 5° angle of attack, nose up, in steady horizontal motion. At F_n= 0.567 (i.e. the wave length λ is equal to twice the chord length c), when the depth d dropped below the chord length c, the first wave in the train began to break. To enhance the short range of transition in terms of the submerged depth from a breaking to a non-breaking wavetrain, Duncan placed a cloth ahead of the foil and towed it at foil speed for a few seconds before removing it. At critical depth ($d \approx c$), disturbing the free surface resulted in a steady breaking wavetrain instead of the non-breaking wavetrain otherwise. This procedure and a more recent study, Miller (1999), confirmed the correction proposed by Banner and Phillips (1974) of the formula introduced by Stokes for the incipient breaking amplitude of a steady wave.

We used the Duncan case to assess the free-surface simulation capabilities of Fluent. The best we could achieve was to impose the free surface measured by Duncan in a non-breaking wavetrain case as a slip wall condition, Laurens et al. (1999), producing the expected foil hydrodynamic coefficients and pressure contours.

Fluent solves the RANS equations using a finite volume method. We model the flow as incompressible, two-phase flow using the Volume of Fluid (VOF) approach to capture the free surface. Water and air are explicitly represented. The option used were:

Solver : segregated, implicit, 2nd order, unsteady

Multiphase: VOF, implicit, implicit body force (gravity)

Surface tension: primary phase air, secondary phase water, 0.0735 N/m

Turbulence model: RNG k-ε two-layer zonal model, $y^+ \approx 1$

The VOF model theory relies on the fact that the two fluids are not interpenetrating. The two-phase flow interface is modelled by introducing the volume fraction variables α_w and α_a respectively for water and air. In each volume, the volume fractions of the two phases sum to unity. When the two phases are present within the same cell, the viscosity and the density are averaged according to volume fractions (i.e. $\rho = \alpha_w . \rho_w + \alpha_a . \rho_a$). To be consistent with the continuity equation for incompressible fluids, the substantial derivative of the volume fraction for each phase must equal zero. The momentum equation respects the physics as long as the velocities near the interface between the two phases do not present large differences. Again several schemes are available for volume fraction values computation. The most appropriate appears to be the implicit scheme, a finite difference interpolation method where the volume fraction rate of change at time step (t+dt) for each phase balances its flux :

$$\frac{\alpha_{t+dt} - \alpha_t}{dt} = -\frac{d(\Phi_{t+dt}\alpha_{t+dt})}{V}$$

where V is the cell volume and Φ_{t+dt} is the volume flux through the face. The surface tension model proposed by Brackbill et al. (1992) applies an additional source term when solving the water side of the interface. The computation is initialised by patching the respective volume fraction in each medium. Since the fluid is in motion and not the hydrofoil, both fluids and the horizontal walls are set to the same velocities. The last boundary condition is equivalent to a slip wall boundary condition.

The computation domain, Fig.1, was chosen large enough to be used within the range of the Froude numbers F_n. The largest Froude number (F_n=0.7) corresponds to a wave length of 0.62m ($\lambda = 2\pi F_n^2 c$ with c=203mm). To ensure a minimum of 2 wave lengths ahead of the hydrofoil and 4 wave lengths behind, the total length of the domain is 4.5m. To be consistent with Duncan's set-up the bottom wall

remains at a constant distance from the hydrofoil while the position of the free surface is moved to simulated the different water depths.

Fig. 1 Computation domain

To mesh the two dimensional domain, it was divided into several regions in order to control the free surface and the hydrofoil boundary layer and wake areas where structured meshes are used, whilst the rest of the domain is meshed using triangles, Fig.2. Hybrid meshes reduce the number of cells whilst respecting the relatively tough constrains of the solver regarding their aspect ratio and skewness.

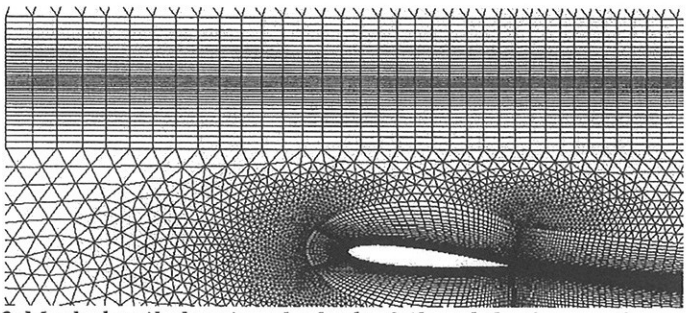

Fig.2 Mesh detail showing the hydrofoil and the free surface areas

We found 40 cells per wave length necessary to obtain an accurate representation of the free surface, Fig.2. Since Reynolds numbers are of the order of 10^5, a statistical model of turbulence was used. Lemaitre (2000) showed that best results are obtained using the two layer zonal model with RNG(k-ε) which implies values around 1 for y^+ within the hydrofoil boundary layer. Boundary condition parameters were set with 1% turbulent intensity for the upstream flow. Each computation corresponds therefore to a different mesh. Despite of all these constraints, the number of cells rarely exceeds 50,000 cells.

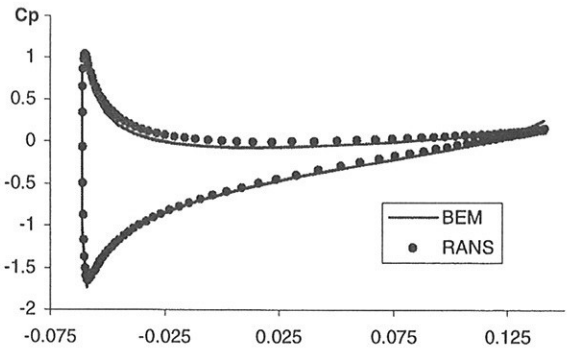

Fig.3 Comparison of Cp distribution results obtained by RANSE code and a boundary element code

If was first verified that Cp distribution, Fig.3, Cl and Cd were adequately computed when the free surface is not present. Since a problem with integration algorithm used by the code was identified, we built a procedure using the post-processor Fieldview to compute the hydrodynamic forces. Nominal Cd and Cl obtained were respectively 0.009 and 0.54 for angle of attack $\alpha=5°$. This is very much in agreement with all experimental data obtained for this case.

When using VOF model, the free surface is never clearly identified since between the two phases, a region of volume fraction exists as explained in the introduction. The fuzzy phase band produced by

our simulations is quite large, Fig.4, compared to other authors such as Deng et al. (2000), and this is independent from the mesh refinement. When we consider the line corresponding to a 0.5 water volume fraction, the free surface we obtain differs from Duncan's measurement from zero to 20%.

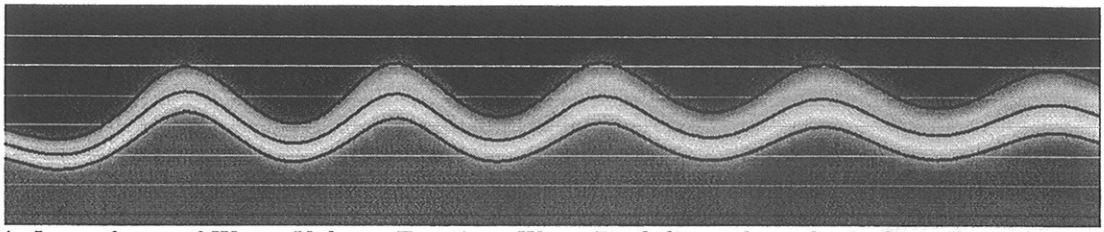

Fig.4: Isosurfaces of Water Volume Fraction: Wavy Dark lines show the isolines for water volume fractions of 0.1, 0.5 and 0.9 from top to bottom respectively. The horizontal lines are separated by 1 cm. (y-scale exaggeration x5). $\alpha = 5°$, *Immersion = 21 cm,* $F_n = 0.567$.

Although we are not fully satisfied with these results, we pursued the study to verify whether breaking waves can be simulated with the code. The free surface lines obtained from various immersions are presented in Fig.5.

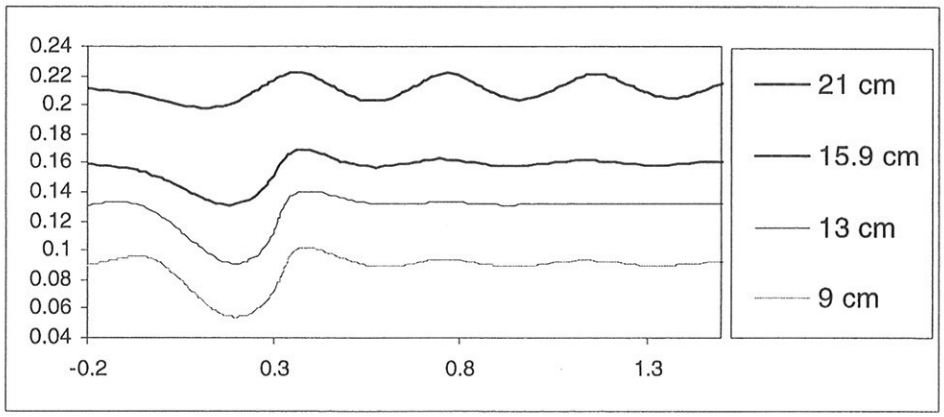

Fig.5: Numerical simulation results obtained for several immersions of the foil. $\alpha = 5°$, $F_n = 0.567$

These results and the analysis of the velocity field, Fig.6, comply with all previous studies. We can therefore consider that the code is capable to simulate breaking waves. Duncan's measurements showed that the breaking waves do not visibly modify the shape of the drag coefficient curve. On the other hand, the free-surface effect significantly affects the lift coefficient of a submerged foil and has to be taken into consideration at the design stage. Fig.7 shows lift and drag of the hydrofoil at $\alpha=5°$ versus immersion depth. As expected, the drag coefficient increases when the foil approaches the free surface because of the added wave resistance and as measured by Duncan, breaking waves do not appear to modify the curve. The lift curve behaviour is also as expected. Before breaking waves, lift increases as the free surface acts as a sliding wall which confine the flow. When waves are breaking, the combined actions of the vortex and the boundary layer attached to free surface produce the reverse effect which explains the shape of this curve. Unfortunately, experimental results of the Duncan case with lift measurement do not appear to exist. The existing experimental results of free surface effects on submerged hydrofoil lift are usually considering much higher Froude numbers. Without reaching these high values, we studied the effect of Froude number without finding significant effects. On the other hand, the angle of attack appears to be of great importance for the occurrence of breaking waves which appear at a larger depth of immersion when increased.

Although ample room for improvement still exists, we found that the latest version of Fluent is now capable of predicting some free surface effects with reasonable accuracy. The breaking waves effects numerically obtained on the submerged foil lift and drag are as expected but additional computations would be necessary to complete this study before considering 3D cases and wave piercing bodies.

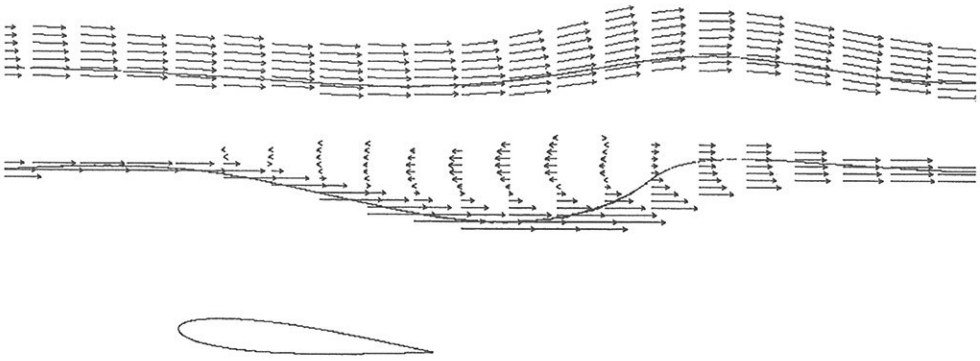

Fig.6: Velocity vectors in the fuzzy region at immersions 21 cm (non breaking) and 15.9 cm (breaking). The vortex, as suggested by the Cointe and Tulin (1994) model, accompanying the first wave is clearly identifiable.

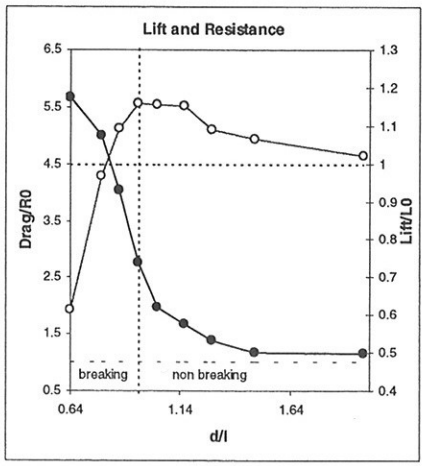

Fig.7: Lift (white dots) and Drag (black dots) results non-dimensionalised by their values without the presence of the free surface versus immersion depth non-dimensionalised by the profile chord.

Banner M. L. and Phillips O. M. 1974, *On the incipient breaking of small scale waves, J. Fluid Mech.,* vol. 65, 647-656.

Brackbill J.U. et al 1992, A continuum method for modelling surface tension. *J. Comput. Phys.,* vol.100, 335-354.

Cointe R. and Tulin M. P. 1994, A theory of steady breakers, *J. Fluid Mech.,* vol. 276, 1-20.

Duncan J.H. 1983, The breaking and non-breaking wave resistance of a two-dimensional hydrofoil, *J. Fluid Mech.,* vol. 126, 507-520.

Deng G.B. et al. 2000, Interface capturing and interface tracking of incompressible and immiscible viscous flows, $8^{ème}$ *Journées de l'Hydrodynamique, Nantes, France, March 5-7*

Laurens J.-M. et al. 1999, CFD en hydrodynamique navale, *RSTD* N°43,. 37-46.

Lemaitre D. 2000, Etude de Faisabilité de la Détermination Numérique du Coefficient de Forme, rapport de stage ENSIETA.

Miller et al. 1999, Incipient breaking of steady waves in the presence of surface wakes, *J. Fluid Mech.,* vol. 383, 285-305.

A Refinement Study of Grid for Turbulent Ship Free-Surface Flows

Tingqiu Li * Jerzy Matusiak

Helsinki University of Technology

Abstract

In this paper, a refinement study of grid for turbulent ship free-surface flows has been investigated using a FINFLO-SHIP solver. Test case is the KCS model from the KRISO container ship (Korea). A viscous steady free-surface flow around this ship is simulated in a numerical water tank. A cell-centred FV multigrid scheme is implemented for the resolution of the RANS equations with the artificial compressibility. The turbulent effect is considered with the Baldwin-Lomax turbulence model without a wall function. A free surface is tracked using a moving mesh, in which the exactly non-linear kinematic free-surface boundary condition is given on the actual location of the free surface. The calculated results on three consecutive grids are presented in terms of the free-surface waves and resistance. Furthermore, the convergence performance and the effects of the grid size on the wave systems are studied.

Introduction

A FINFLO-SHIP solver for application to viscous steady free-surface flows around transom stern ships has been developed by the CFD group at the Helsinki University of Technology (HUT) and Technical Research Center (VTT), Finland (see Li et al., 2000, and Li and Matusiak, 2001). This is an uncoupled approach between the bulk flow and a free surface. A moving mesh is implemented (Lehtimäki, 1998), including a second-order nonessential oscillation (ENO) scheme (Sussman, et al., 1994) and a high-order difference method. With a dry-transom model, a free-surface off a transom is treated. Based on our current study (Li, 2001), an approach for approximation of the contact line is proposed and incorporated to this solver. This provides the possibility for improvement of our previous results (Li, 2000). Its advantage lies that very stiff problems, such as a high aspect ratio within the boundary layer and a numerical singularity at the contact line, can be avoided.

Mathematical Models

We apply for the following 3-D RANS equations with the artificial compressibility in the Cartesian co-ordinate system:

$$\frac{\partial U}{\partial t} + \frac{\partial (F - F_v)}{\partial x} + \frac{\partial (G - G_v)}{\partial y} + \frac{\partial (H - H_v)}{\partial z} = 0 \tag{1}$$

where $U = (\rho, \rho u, \rho v, \rho w)^T$. ρ is the density of the fluid, and u, v and w are the velocity components in the x-, y- and z-directions, respectively. F, G, H and F_v, G_v, H_v are the inviscid fluxes and viscous fluxes, respectively (see Siikonen, 1998).

Initial and Boundary Conditions

An uniform flow and zero wave height are specified as the initial conditions.

*Correspondence to: Dr. Li Tingqiu, Ship Laboratory, Helsinki University of Technology, P.O. Box 4100 (otakaari 4) FIN-02015 HUT, Finland. Email:tli@nefer.hut.fi

On the wetted part of the hull surface, u = v = w = 0 are imposed. At the inlet, an uniform flow is specified. At the outlet, all variables are extrapolated with a zero-gradient approach. On the centerline boundary and the external boundary, the mirror conditions for all variables are implemented. On the free surface, the wave height h is given as

$$\frac{\partial h}{\partial t} + u\frac{\partial h}{\partial x} + v\frac{\partial h}{\partial y} = w \tag{2}$$

The following dynamic boundary conditions are employed for determination of the pressure and velocities (u, v, w) on the free surface:

$$n_i \sigma_{ij} n_j = 0 \qquad and \qquad n_i \sigma_{ij} t_j^{\alpha} = 0 \tag{3}$$

where n_i and t_i^{α} ($\alpha = 1, 2$) are the ith components of the normal and tangential vector on the free surface, respectively. σ_{ij} is the stress tensor.

Computational Conditions and Grids

Three grid levels with a grid refinement ratio of 2 are used for the computations. This is doubled mesh in each direction. The y^+ values for each of the respective grids are about 0.6, 1.2 and 2.4. The grid points with the finest mesh are about 1 million. The steady state solution on the coarse grid is used as an initial guess for the fine solution. An example is given at F_n=0.26 and $R_n = 1.4 \times 10^7$ due to the experimental data available.

Convergence Properties

Figure 1 illustrates the L_2 norm of residuals for the momentum (U, V, W) in the x-, y- and z-directions, the pressure (P) and the total resistance coefficient C_T. Solution change drops four (for P) and five orders (for U, V, W) of magnitude at the steady state. The variation in C_T converges to a certain value for these three grid levels.

The grid convergence study for the total resistance coefficient C_T, friction C_F and pressure coefficient C_P is assessed from varying levels (see Table 1, where S is the wetted-surface area of the hull surface). With grid refinement, C_T and C_P are decreasing, but C_F increases as expected. Moreover, these are closer to the experimental data at the fine mesh, especially for the finest mesh.

Table 1: Grid convergence study of C_T, C_F and C_P ($\times 10^{-3}$) for the KCS model.

Grids	S/L^2	C_T	C_P	C_F
the coarsest mesh (41 × 41 × 17)	0.1804	5.266	2.647	2.619
the fine mesh (81 × 81 × 33)	0.1804	4.091	1.353	2.738
the finest mesh (161 × 161 × 65)	0.1804	3.594	0.799	2.795
Experimental data	0.1781	3.561	0.731	2.83

Effects of Grid Refinement on Wave Systems

The effects of refined grid on the waves are studied on three consecutive grids. The results are presented in terms of the surface-wave profiles, the longitudinal wavecuts at y/L=0.1509 and the wave contours (see Fig. 2). It is observed that the results from two fine meshes are almost identical. The coarsest grid can not detect the wave motions well. This implies that no asymptotic grid convergence is attained for this mesh. As expected, the results are closer to the experimental data when the grid is refined systematically, as shown in Fig. 2. It is found that the essential details of the resolution can be captured with the relatively fine mesh. The maximum differences between two fine meshes occur at the bow (x/L=-0.5) for the surface-wave profiles and the trough (x/L=0.20) for the longitudinal wavecuts at y/L=0.1509.

For the wave contours, the amplitudes of the waves at the crest, the shoulder and the trough show closer agreement with the experimental data as the grid is refined. Furthermore, the detailed features of the wave systems are illustrated well at the fine mesh. Nevertheless, in the wake, numerical diffusion which leads to an artificial decrease in the wave elevation is obvious for the far-field waves. This is due to the effects of viscous or the grid size or the both.

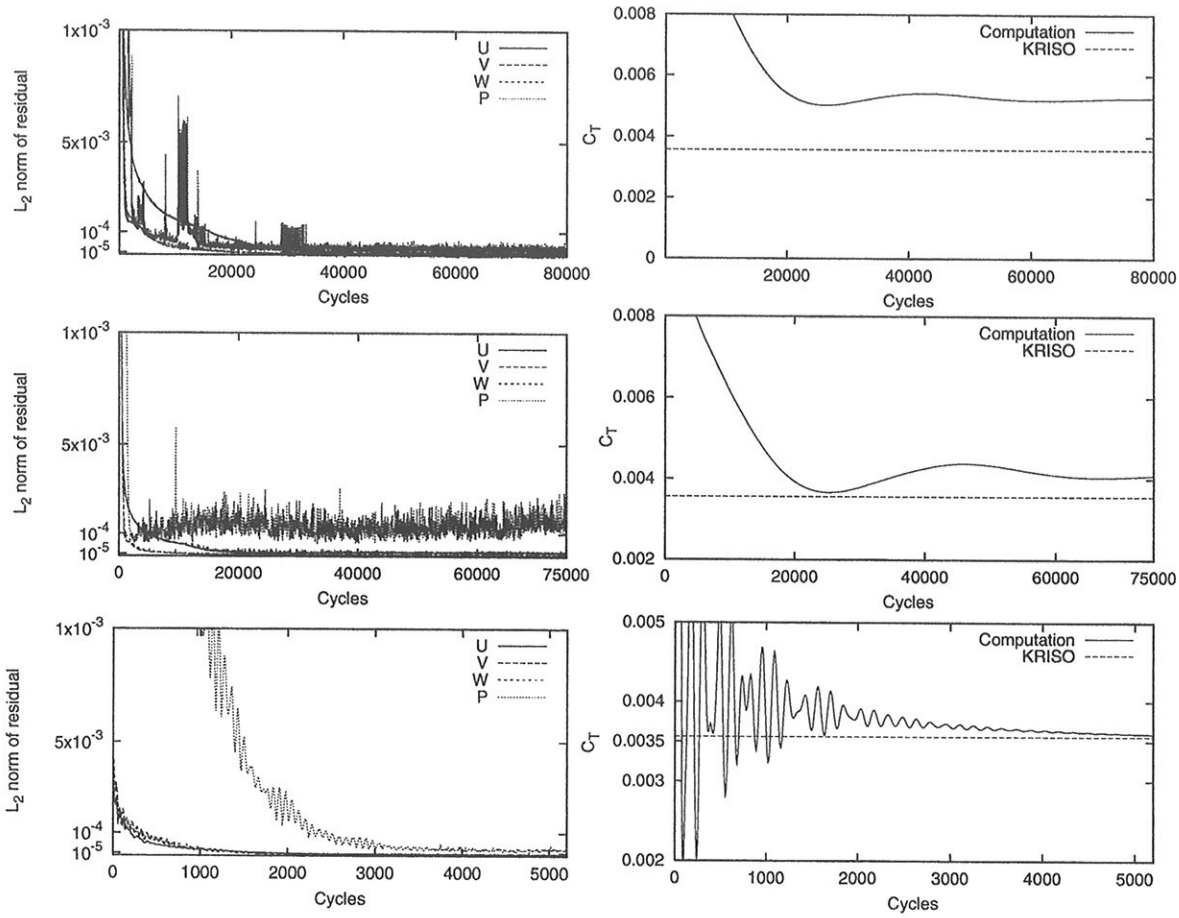

Figure 1: **Convergence histories of L_2 norm of residuals (U, V, W, P) and C_T, the KCS model (F_n=0.26 & R_n=1.4 × 10^7). Top: 41 × 41 × 17. Middle: 81 × 81 × 33. Bottom: 161 × 161 × 65.**

Conclusions

A FINFLO-SHIP solver can been applied to turbulent free-surface flows around modern surface ships. Good accuracy has been achieved in terms of the free-surface waves and the resistance.

Acknowledgements

The present work is sponsored by the Technology Development Center (Tekes) in Finland and Finnish Shipbuilding Industry.

Thanks are given to the members of the CFD group at Helsinki University of Technology for valuable help.

References

Lehtimäki R., 1998, "Grid Deformation Tools for Simulation of Free Surface Flows", In 6th International Conference on Numerical Field Simulation, London, UK.

Li, T., 2000, "Numerical Simulation of Viscous Steady Flow with Free Surface around Two Types of Modern Realistic Hull Forms: Hamburg Test Case and Tanker," Report M-247, Ship Laboratory, Helsinki University of Technology, Finland.

Li, T., Sanchez-Caja, A., Martio, J. and Matusiak, J., 2000, "Simulation of Free-Surface Viscous Flow around two Ship Hulls Using RANS Solver FINFLO", A Workshop on Numerical Ship Hydrodynamics, Editors by Lars Larsson, Fred Stern and Volker Bertram, Gothenburg.

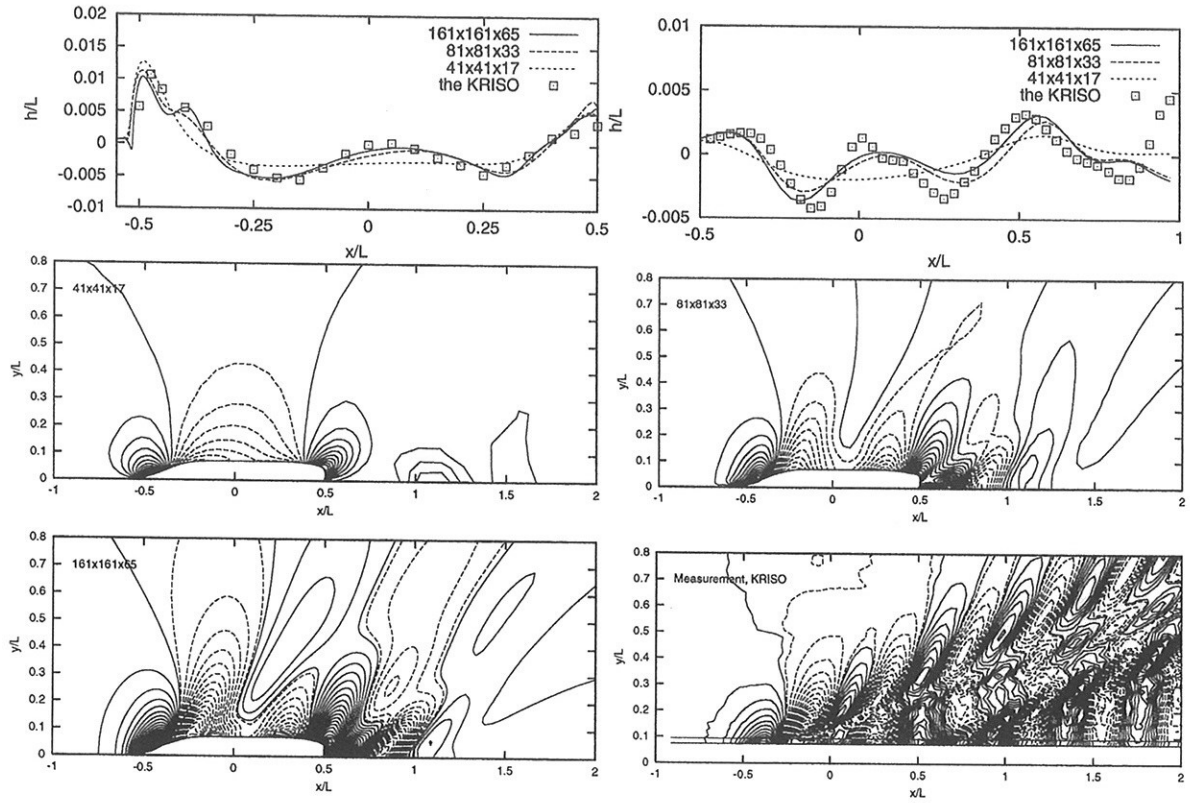

Figure 2: **Surface-wave profile, longitudinal wavecuts at y/L=0.1509 and wave contours at three grid levels, the KCS model (F_n=0.26 & R_n=1.4 $\times$ 10^7). Solid lines for crests; dashed lines for trough; levels: 0.0003.**

Li, T. and Matusiak, J., 2001, "Simulation of Modern Surface Ships with a Wetted Transom in a Viscous Flow", In Proc. 11th International Offshore and Polar Engineering Conference (Stavanger, Norway), Vol. IV, 570-576.

Li, T., 2001, "Benchmark Test Cases for Viscous Free-Surface Flows around Modern Surface Ship Models: the HTC, the KCS Model, the DTMB 5415 Model and the Tanker Model", Report, Ship Laboratory, Helsinki University of Technology, Finland.

Siikonen, T., 1998, "FINFLO User Guide, Version 2.2", Laboratory of Applied Thermodynamics, Helsinki University of Technology, Finland.

Sussman Mark, S., and Osher S., 1994," A Level Set Approach for Computing Solutions to Incompressible Two-Phase Flow", *Journal of Computational Physics*, **114**.

Vortical Structures in a 3D Unsteady Viscous Flow

Adrian Lungu[1],

1. INTRODUCTION

Whenever the turbulent flow is analysed, a strong variation of the velocity orientation and magnitude around a mean value in each point of the domain is seen. Additional frictional stresses that describe the turbulent flow determine pressure losses, which are significantly higher than those of the laminar flow. Fluid particles within the boundary layer cannot anymore follow the solid frontier contours along which the pressure shows an augmentation tendency. Due to this fact, and because the particles kinetic energy is significantly diminished through the viscous friction, the boundary layer separates. Because of the vortices placed randomly in respect with the main direction of the flow, streamlines do not remain parallel or approximately parallel as they usually are in the laminar flow. Their presence determines the genesis of the temporal and spatial streamline fluctuating topologies, which are responsible for the unsteady character of the flow. Moreover, any problem involving the 3D unsteady turbulent flow has a significant interest because of the nonlinearities that make the set-up of an analytic solution at least difficult, if not impossible. That is also the case of the backward facing step flow considered in here, for which a numerical simulation based on the integration in time of the RANS equations is proposed. The technique is based on the finite difference discretization of the partial differential equations that describe the flow [1, 2]. Turbulence is modelled by the K-ε model implemented as proposed in [3] with the modifications of Harlow and Nakayama [4, 5].

2. NUMERICAL SCHEME

The Reynolds averaged equations for continuity and momentum are solved for the primitive variables to describe the 3D turbulent flow. Closure to the turbulence is attained through the use of the K-ε model modified by Harlow and Nakayama, [4], [5]. The numerical scheme is based on the following succession of steps:

- metrics and Jacobian computation;
- boundary conditions formulation for pressure, velocities, K and ε;
- computation of the fluxes that compose the source terms of the Poisson equation for pressure and building the source terms based on the eddy viscosity already determined;
- computation of the pressure field through an iterative procedure of relaxation of the solution of the resultant Poisson equation domain within the limitations of the boundary conditions.

The convergence is attained by imposing the following criterion for the pressure residuum:

$$\text{- Res} = \sum_{i=1}^{i\max} |\Phi(i,it) - \Phi(i,it-1)| \le \varepsilon ,$$

where ε is a small quantity chosen apriori, it is the iteration counter, whereas $i_{\max}$ represents the maximum number of the grid points.

- updating the velocity field and turbulence quantities.

Euler explicit time-stepping scheme is used for the time marching procedure. The calculation proceeds through a sequence of loops each advancing the flow configuration. The output of each loop is taken as an initial condition for the next one and the computation proceeds until T_{max}. Spatial derivatives employ second-order accurate differences, while for the convective terms the third order upstream difference is used.

3. RESULTS AND DISCUSSIONS

Numerical solutions presented in the following discussions are computed for a flow regime characterised by Re=10^6. The computational domain shown in Fig.1 has a size of 5.0×1.0×1.0. The step length and height are half of the channel width. The minimum cell size and the time increment were chosen so that the Courant number computed according to the von Neumann stability criterion is less than unit everywhere in the domain. Several numerical tests performed in the present investigation have proven that T=8 is quite enough for a complete development of the flow. That is why the majority of the solutions discussed in here are computed at a non-dimensional time of T=10.

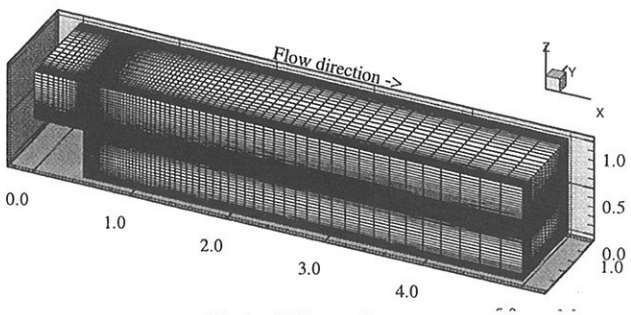

Fig.1- Grid topology.

The discussion proposed in Fig.2.a-c regards the particle paths in horizontal plane as well as the topology of the corresponding streamlines. Cross sections shown in Fig.2.a-c are made at the following z co-ordinates: z=0.01, z=0.25 and z=0.5 respectively. As it may be seen in the proposed figures, the flow is completely tridimensional, the horizontal projections of the streamlines being substantially different from a plane to the other. Thus, Fig.2.a bears the particle paths drawn in the plane of z=0.01 in the immediate vicinity of the bottom solid wall

[1] "Dunarea de Jos" University of Galati, Romania, 47 Domneasca Street, 6200 Galati, Romania, Phone: (+40) 92-362604, Email: adrian.lungu@ugal.ro

where multiple separations and reattachments can be easily identified.

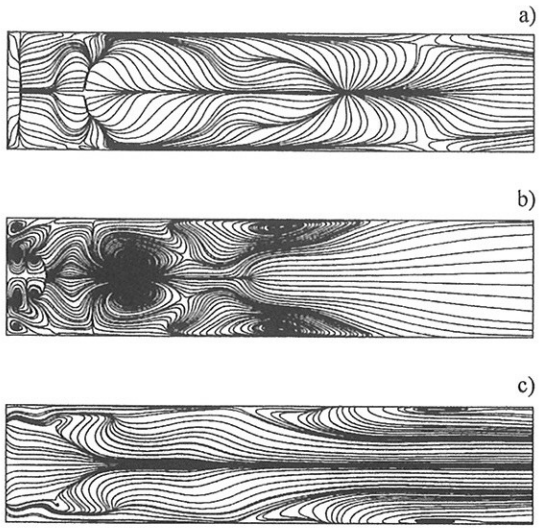

Fig.2- Streamlines in horizontal planes.

The topological structure of the streamlines inside the boundary layer is characterised by the appearance of two pairs of divergence-coalescence lines. The first divergence line is placed just behind the step at x=0.6 approximately. A nodal point of separation is placed in the symmetry plane at the same abscissae. A transversal coalescent line to which all the streamlines converge is extended over about a half of the domain width and can be observed at x=1.15 station. Apart of it, a nodal saddle point is placed at the same x- co-ordinate, in the symmetry plane. Correspondingly, a divergence line is placed between this point and the nodal point of reattachment placed at x=3.37 station.

Two coalescent lines produced by the interference between the boundary layer developed on the bottom wall with those developed on the lateral walls can be observed each side of the symmetry plane close to the vertical solid walls. They originate in the separation points (x=2.3; y=0) and (x=2.3; y=1.0) respectively, and extend towards the downstream being interrupted each side of the symmetry plane only by the pair of the saddle points at x=4.0. Although missing in Fig.2.a because of the poor graphic resolution, two more pairs of significant points occur in the horizontal plane of z=0.01. It is a pair of a saddle points placed at (x=1; y=0), and (x=1; y=1) respectively, and a pair of nodal points of reattachment placed at (x=0.5; y=0) and (x=0.5; y=1), respectively. The last one corresponds to the corner vortex shown in Fig.2.b that depicts the streamlines in z=0.25 horizontal plane. The flow topology in this plane consists on ten vortices placed symmetrically in respect with the central axis of the domain. Their number and kernel co-ordinates are identical to those reported by Noda and Miura [6, 7], thus confirming the overall accuracy of the solution. It is also worth noticing that at the x=0.6 station, four vortices are placed in the correspondence of the first divergence line depicted in Fig.2.a. Their kernels are laying each side of the symmetry plane. A saddle point placed at x=0.66 and a nodal one located at x=2.58 can also be distinguished in the symmetry plane.

Furthermore, two pairs of symmetrical saddles of separation linked by lines of coalescence-divergence, complete the topology. Co-ordinates of the separation points are x=0.95; y=0 and y=1, respectively x=2.07; y=0 and y=1. The departure from the bottom boundary layer calms down the flow activity because of the viscous dissipation. The only areas where the flow parameters still show intense action are those either just behind the step or along the sidewalls. This fact can be seen in Fig.2.c where are the streamlines drawn in the z=0.5 plane. The flow topology in this plane consists of two pairs of vortices placed symmetrically at x=0.92; y=0.17 and y=0.83, respectively x=4.14; y=0.07 and y=0.93. The streamlines structure is completed by the separation points whose co-ordinates are x=2.54; y=0 and y=1, respectively x=0.5; y=0 and y=1. The fluid particles chaotic movement shows a decrease in intensity, a trend that is more obvious in the z=0.75 and z=1.0 horizontal planes. Streamlines in the central area of the domain remain parallel to each other. On the other hand, the number of the separation points decreases while the vortex placed at x=4.14 station in Fig.2.c moves towards the upstream as the vertical co-ordinate increases.

The following discussion on the flow configuration is based on a longitudinal cut in the symmetry plane of the domain. From Fig.3.a that shows the velocity vectors one may see that although the flow is quasi 2D at the upstream, separations of the turbulent boundary layer occur immediately at the downstream. Separations determine the generation of vortical structures accompanied by wide regions of reverse flow. The velocity field modification become significant and lead to important variations of the pressure gradients, as it may be seen in Fig.3.b where the field of constant pressure lines is drawn. The dissipation introduced by the viscous friction makes these gradients decrease in intensity with the distance from the wall. The streamlines analysis proposed in Fig.3.c-e emphasises the existence of six vortices in the symmetry plane of the domain. Five of them are located below the edge of the step immediately downstream of it. It should be worth noticing that the reattachment point of the streamlines at the bottom wall is placed at x=3.37 station that represents 6.6 times the step height, as the test cases recommend [6, 7, 8]. However, it must be mentioned that because the unsteadiness, the position of the reattachment point modifies in time. Pilot computations performed by the author proved that the variations of the position around the above mentioned value occurred within a margin of ±10% of the step height.

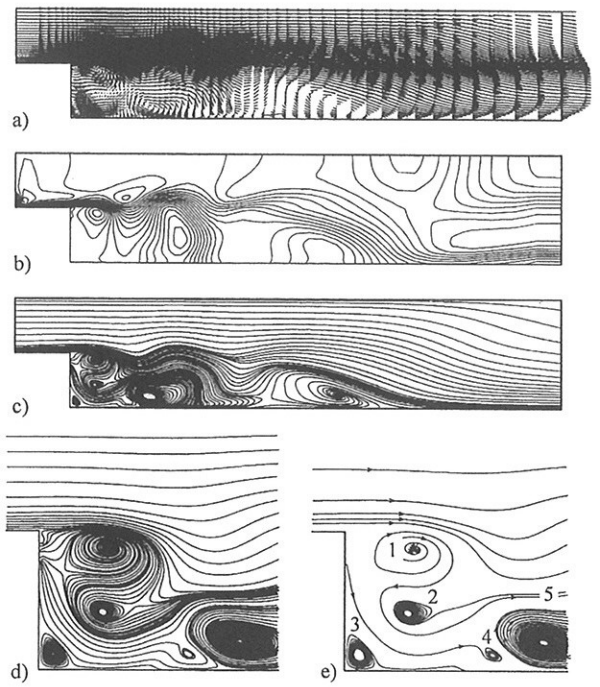

Fig.3- Physical parameters distribution in the symmetry plane: a – velocities; b – pressures; c – particle traces; d – close up view of the streamlines behind the step; e – topology of vortices behind the step.

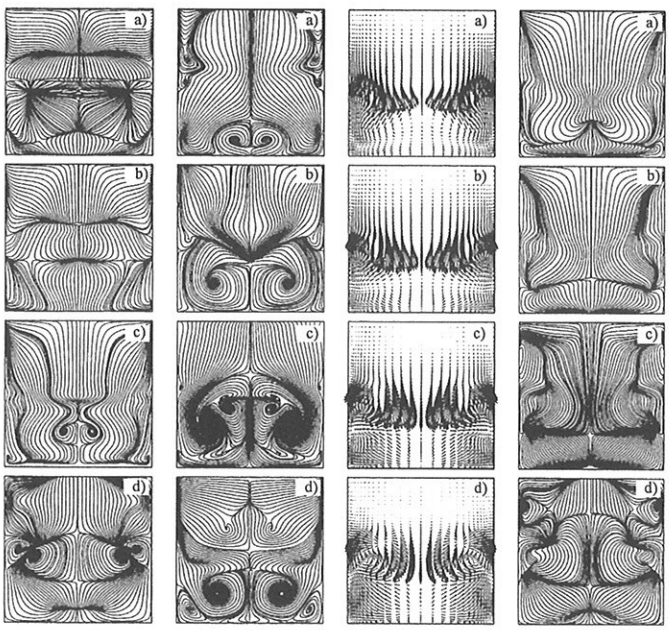

Velocity and streamlines in different cross sections

Fig.4: T=10	Fig.5: T=10	Fig.6: x=1	Fig.7: x=1
a- x=0.505;	a- x=1.250;	a- T=8.000;	a- T=8.000;
b- x=0.600;	b- x=1.500;	b- T=8.005;	b- T=8.005;
c- x=0.750;	c- x=2.000;	c- T=8.010;	c- T=8.010;
d- x=1.000	d- x=2.500.	d- T=8.015	d- T=8.015

As said above, the flow studied in this paper has a strong 3D character. To sustain this statement Figs.4-7 propose an analysis of the water particle kinematics (velocities and streamlines) in transversal cross sections. Thus, Fig.4 depicts the streamlines transversal projections in the transversal planes of abscissa: (a) x=0.505; (b) x=0.6; (c) x=0.75; (d) x=1.0. As said before, the flow has an intense fluctuating character especially in the area behind the step. Its topology in the transversal direction is characterised by separations and reattachments whose positions vary in space and time. Even though the divergence and coalescent lines remain symmetrical in respect to the vertical axis of the cross section plane, their positions and lengths are variable. Beginning with the x=0.75 station, a pair of vortices occurs and manifests till the downstream extremity. We call them main vortices in order to distinguish from the others that appear in the flowfield. Their intensities and positions vary, as Fig.5.a-d proves. Apart of them, two symmetric secondary corner vortices are captured inside the field between the x=1.25 and x=2.50 stations. The neighbourhood of the upper and lower corners of the domain is obviously responsible for their genesis.

The main vortices are weaker and relatively less extended in the regions close to the step perhaps because of the coexistent pair of secondary vortices that appear and vanish periodically since their intensity is lower. The secondary vortices development is hindered by the main vortices that determine their breakdown and shedding in the downstream. Thus, the main vortices behave exactly like the hydrodynamic conveyors. The pronounced unsteady character of the flow is proven by Figs.6.a-d and 7.a-d that show the temporal variation of the velocity and streamlines field projected on the x=1.0 transversal plane, at four different nondimensional time steps around the value of T=8. The numerical solutions considered in the figures mentioned above are plotted at equidistant time increments of T=0.005, which means that the flow monitoring was done at every 50 time steps.

The fluctuation periodicity of the velocity is a function of the physical and geometrical parameters of the computation such as the Re number, inflow velocity, step height, width of the domain. It also depends on the numerical parameters of the simulation, respectively the grid resolution, time increment, the time interval over which the Reynolds averaging is done, and so on. It is unanimously recognised that the approaches based on temporal averaging are, from the engineering point of view, more than satisfactory. However, a diminishing of the overall influence of the numerical parameters on the solution and the desire of having a more detailed information concerning the turbulence characteristics require the use of the direct numerical simulation in spite of the necessity of powerful hardware platforms and of the CPU high costs. Because it was proven before that the topological structure of the streamlines is a 3D one, any discussion based exclusively on the 2D projections of the streamlines cannot guaranty a complete insight of the flow complexity.

Keeping in with the desire of getting an overall perspective of the spatial trajectory of the fluid particles, Fig.8 shows the 3D streamlines. It has been shown that the main responsible factors for the streamlines separations and reattachments are the bottom and lateral solid walls, as well as the step edge. Because of that, the represented streamlines are started in a plane just above the step, at z=0.501 in Fig.8.a, in the near proximity of the lateral wall at y=0.001 in Fig.8.b, and on the step bottom - in Fig.8.c, respectively. The streamlines launched inside the horizontal boundary layer at the upstream of the do-

main remain approximately parallel to the solid boundary till the step edge where suddenly change the paths to describe the vortex acting downstream of the step edge. Furthermore, their trajectory reveals a second vortex extended on the entire width of the domain. This vortex denoted by 5 in Fig.3.e was also captured when the flow parameters in the symmetry plane were discussed. At the downstream of it, the fluid particles continue their way towards the outlet, reattaching later to the bottom wall. In the case of the streamlines launched on the lateral wall shown in Fig.8.b, things are seemingly simpler in a sense that, excepting the lowermost particle that behaves similarly to those described above, all the others maintain their trajectories parallel till the separation takes place. After that moment, their movement becomes chaotic.

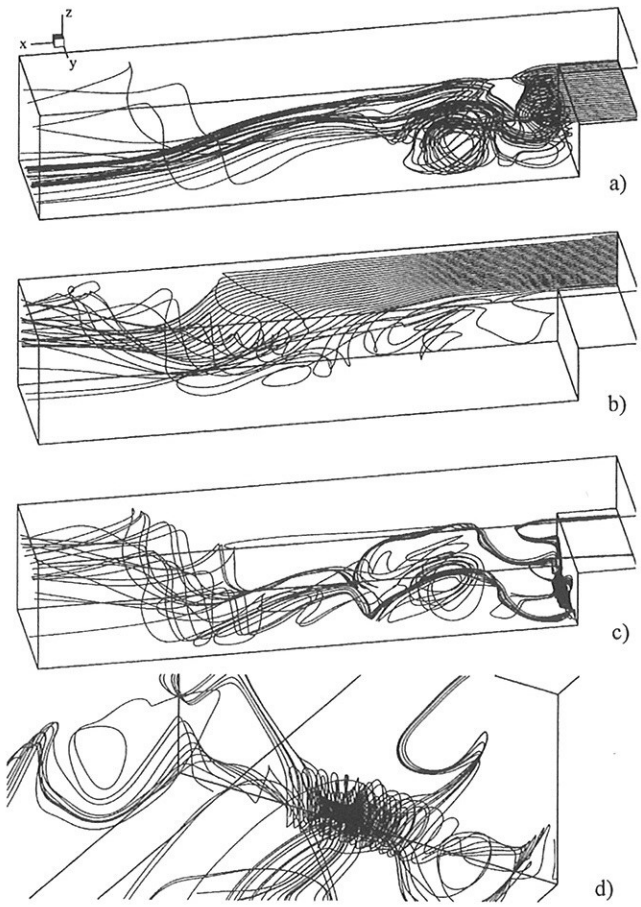

Fig.8 - 3D streamlines: a - started in the plane just over the step at z=0.501; b - started in the proximity of the lateral wall at y=0.001; c – started in the bottom corner; d – close up view of the vortex filament placed within the bottom corner.

When analysing Fig.8.c and d, one may perceive the really impressive behaviour of the streamlines launched in the closeness of the step bottom corner. The convoluted character of the flow is due to a very significant extent, to the classical vortex filament generated in the vicinity of the edge where the two solid walls intersect (see the detail). Its extension only on a limited portion of the domain width is determined by the influence of the corners, which represent the points where three boundary layers interact to each other and lead to a consequential change of the velocity field in the region.

4. CONCLUDING REMARKS

A new technique based on the use of finite differences is proposed for the numerical investigation of the unsteady 3D viscous flow over a backward facing step. The model is based on the RANS and continuity equations written for the uncompressible fluid. Turbulence is considered by means of the K- ε model. Because of the overwhelming influence on the overall accuracy of the solution, a special attention is paid to the correct formulation of the boundary conditions.

Numerical stability is assured by the imposition of the von Neumann criterion. The convergence is reached through an iterative process. The present work reveals the tridimensional vortical character of the flow. The unsteady problem comprising 128061 nodes has been solved over 10000 time steps within up to ten iterations per time step in about three hours on a Silicon Graphics machine, proving the efficiency of the algorithm as well as the code robustness

The reported research could not be possible without the generosity of the Raytheon E-Systems (Chrysler Technologies Airborne Systems) at Waco Texas USA, which is greatly acknowledged for the provided financial support.

REFERENCES

1. PATEL, V.C., SARDA, O.P., SHAHSHANAN, A., *Calculation of Ship Boundary Layers,* 4th Symposium on Turbulent Shear Flow, Karlsruhe, Paper 3.1, 1983.
2. LUNGU, A., *Numerical Analysis of the Free-Surface Flow around a Submerged Hydrofoil*, Ph.D. Thesis, Hiroshima University, 1994, pp.13 - 28.
3. LUNGU, A., P. E. RAAD, K. MORI, *Turbulent Early-Stage Breaking Wave Simulation*, ASME Fluids Engineering, Paper FEDSM97-3404, Vancouver, 1997.
4. HARLOW, F.H., NAKAYAMA, P.I., *Turbulence Transport Equations*, Physics of Fluids, 10, 1967, pp. 2323 - 2332.
5. HARLOW, F.H., NAKAYAMA, P.I., *Transport of Turbulence Energy Decay Rate*, Los Alamos Scientific Laboratory, Report LA-3854, 1968, pp.21 - 36.
6. NODA, T., NAKANISHI, Y., KAMEMOTO, K., *Numerical Simulation of Unsteady Flow behind a Backward-Facing Step by Vortex Method*, 6th Conference on CFD, Tokyo, 1992, pp.443 - 446.
7. MIURA, Y. NAKANISHI, Y., KAMEMOTO, K., *Numerical Simulation of Flow behind a Backward Facing Step by the Vortex Method*, 7th Conference on CFD, Tokyo, 1993, pp.617 - 620.
8. FERZIGER, J. H., PERIC, M., *Computational Methods for Fluid Dynamics*, Springer Verlag, Berlin Heidelberg, 1996, pp.247 - 276.

Numerical Experiments for Hull Form Improvement

Adrian Lungu[1], Gelu Alexandru[2]

1. INTRODUCTION

As free boundaries such as the water surface have recently come to be described with increasing accuracy, a series of unexpected complex physical and mathematical issues, yet often fascinating, have been revealed and put a serious challenge on the free-surface workers. The non-trivial nature of any free-surface flow problem comes mainly from the necessity of dealing with unknown boundaries on which double conditions are to be imposed. Even the neglect of surface tension and viscosity has not fully brought the simplifications the researchers have always been looking for. This is because of the rapidity with which the phenomena occur, the large amplitudes and accelerations involved and the contortions of the free surface. In spite of the progress that has been shown recently, several non-linearities such as breaking or turbulent incipient breaking, viscous interactions, strong vortical character of the flow, which sometimes coexist in the near vicinity of the water surface, sometimes lead to surprisingly poor results when such a subject is invoked. This is partly due to the fact that questions regarding physical and numerical issues still remain to get complete answers- the origin of the plunging wave in deep water continues to be unexplained, the turbulent behavior of the water around the crest still needs a model based on which to be resolved, the simulated wave crests are still vulnerable to perturbations, just to name a few. The complexity of the subject sometimes compounds with the necessity of considering a solid body either submerged or intersecting the water surface, and direct numerical simulation is often required. However, the days for the full-scale numerical stimulation are well ahead, and on that account there is greater demand on more basic studies aimed at clarifying completely the issues mentioned above. According to Hirt and Nichols there are three major problems that arise in the numerical treatment of the free boundaries:

(1) the discrete representation;
(2) the temporal evolution;
(3) the manner in which boundary conditions are imposed on them.

The capability of a certain solution procedure for the unsteady free-surface flow problem is determined to a very significant extent by the method employed for the numerical treatment of the free surface.

During the past decades several attempts have been made in simulating numerically the free surface flow problem and some significant progress has been shown. Although the methods brought up above seem apparently successful, several improper treatments are used without enough advisement. For instance, an important difference between the free-surface and unbounded flows resides in the radiation through the wave propagation. In spite of its drawbacks, the CFD analysis remains a feasible tool in the ship design process.

The total power requirement of a ship is basically derived from its total resistance, which is made up by the contribution of the bare hull resistance, the appendage resistance, machinery and shaft losses, hull fouling and environmental effects. In this respect, a complex and well-balanced approach is required for providing suitable methods to minimize the ship resistance. A balance in between numerical methods that employ complex specialized CFD codes and traditional experimental work, which provides towing tank results as benchmarks for CFD analysis has therefore to be assured in any research activity.

Recent efforts have proven a real benefit of the CFD methods well used and correctly implemented, that may become a useful tool for any flow analysis. Various techniques have been developed in order to investigate a full range of design options at the preliminary stages of the ship project. Among them, computer codes based on the use of potential flow theory remain one of the most efficient tools that are in a wide use in spite of some drawbacks that come mainly from the approximations introduced by the ideal fluid assumption.

Three different ships subjected to the hull form optimization are sequentially considered in the present paper: a twin screw ship and two container vessels.

2. HULL FORM OPTIMIZATION

The optimization has been based on both numerical and experimental investigation. A series of numerical simulations were performed at the beginning of checking the performances of each hull studied. The improvement of the overall ship hydrodynamic performances regarded:

- Modification of the aft end of the hull for a twin screw ship (see § 2.1);
- A fore bulb optimization for a container vessel (see § 2.2);
- An optimization of both ship extremities of another container vessel (see § 2.3).

2.1 A Twin Screw Ship Optimization

The numerical flow analysis doubled by experimental validation is followed by a propulsion optimization. Several hull forms have been annualized, two of them (out of a total of 10) have then carried in the towing tank in order to completely clarify the complex hydrodynamic phenomena that occur in the flow process. The most important steps taken to optimize the hull forms consist of:

- decreasing the stern angle from about 18 degrees to 13 degrees (measured at the CL);

[1] "Dunarea de Jos" University of Galati, Romania, 47 Domneasca Street, 6200 Galati, Romania, Phone: (+40) 92-362604, Email: adrian.lungu@ugal.ro
[2] Research and Design Institute for Shipbuilding - ICEPRONAV, 19A Portului Street, 6200 Galati, Romania, Phone: (+40) 36-415965, Email: icepronav@icepronav.ro

- increasing the bilge radius at the aft part of the hull;
- increasing the shaft lines height with about 3,33%;
- increasing the distance between shaft lines with 20% approximately.

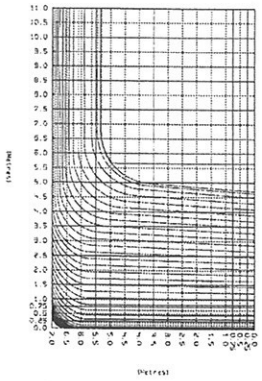

Fig. 1 Aft body lines. Initial hull version

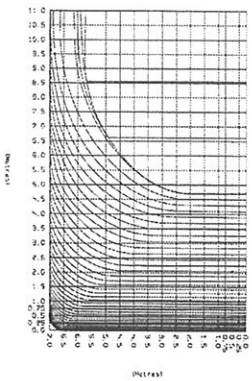

Fig. 2 Aft body lines. Final hull version

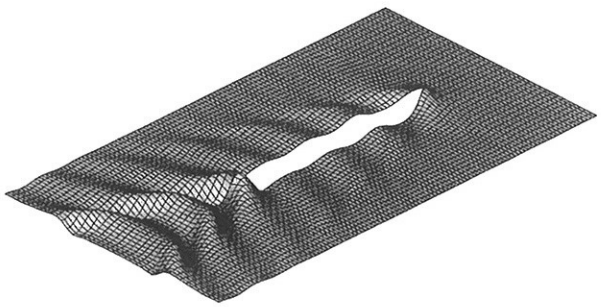

Fig. 3 Free surface elevation.
Final hull version, nonlinear computation

The computed wave resistance coefficients and the model test results are presented in Table 1 and Fig.5.

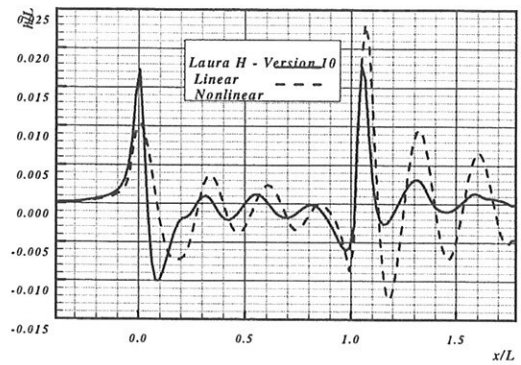

Fig. 4 Comparison between the linear and non-linear wave profiles computed for the final hull

Table 1

Hull trial	Computation (Fn=0.206)	C_w Computed	C_w Measured
Initial hull	Linear	$0.188\ 10^{-2}$	-
Final hull	Linear	$0.133\ 10^{-2}$	$0.103\ 10^{-2}$
Final hull	Non-linear	$0.125\ 10^{-2}$	$0.103\ 10^{-2}$

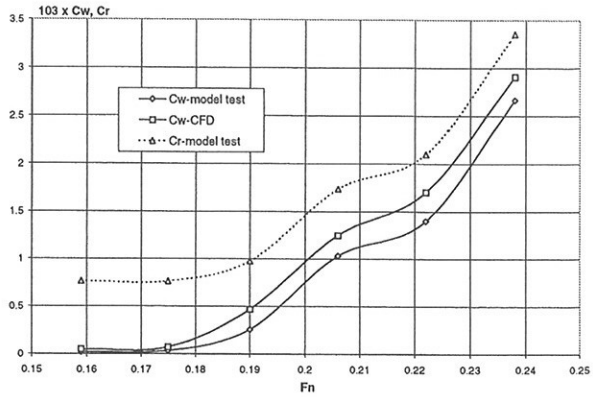

Fig. 5 Comparison between the computed and measured coefficients C_r, C_w for hull final version.

2.2 Fore Bulb Optimization

Following initial offset, eight more hull forms have been derived, out of which only three are being considered in the present paper. All of them have the overall geometry kept unchanged, except for the bow whose length has been increased by 2, 3, and 4 meters, respectively, as shown in Fig.6. Let the corresponding computational cases of the flow around those hulls be denoted by 2, 3 and 4, respectively.

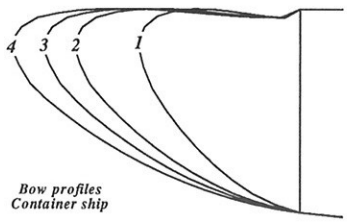

Fig. 6 Bow profiles

Both linear and non-linear computations were carried out. The wave elevations drawn upon the solution of the non-linear computation are shown in Fig.8. As depicted in both following drawings, the wave pattern computed for hull No.3 (Bow No.2 in the referred figures) seems to give the most promising shape. For the sake of accuracy, only the solutions obtained in the non-linear computations will be further discussed. Perspective views of the corresponding free-surface profiles are depicted in Fig.9.

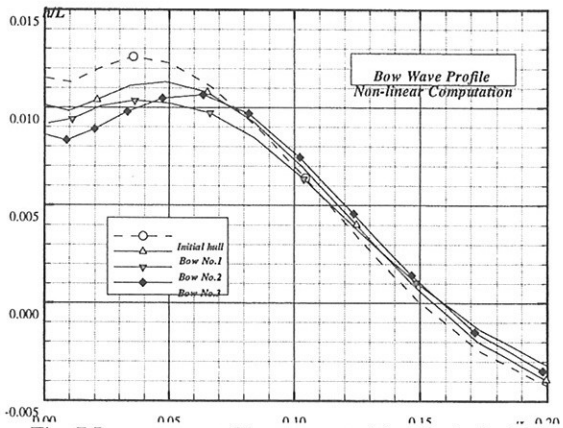

Fig. 7 Bow wave profiles computed for all the hull forms

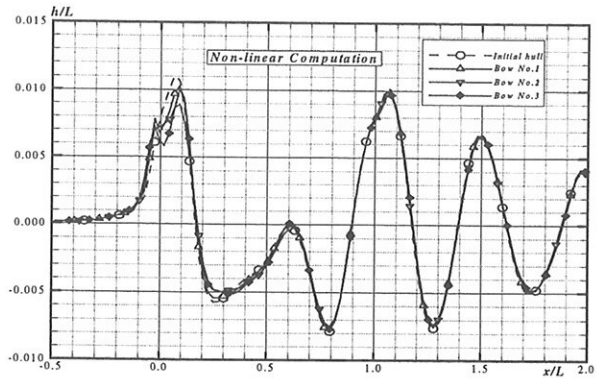

Fig. 8 Free surface profiles. Non-linear computation

For the sake of getting deeper insight into the evidence, a comparison between the solutions computed for the initial and the optimized hulls is plotted in Fig.11.

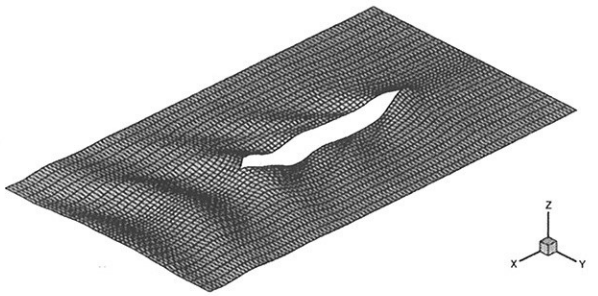

Fig. 9 Free surface elevation. Hull No.3

The computed wave resistance coefficients are tabulated in Table 2 where C_f is the total skin friction coefficient, C_{pv} the viscous pressure coefficient, C_v the viscous resistance coefficient, C_w the wave resistance coefficient, whereas C_t is the total resistance coefficient. The minimum value of the ship resistance is that corresponding to the Hull No.3. The C_t variation for all the computed hulls is shown in Fig.12. The computed wave resistance coefficients and the model test results are presented in the Table 3.

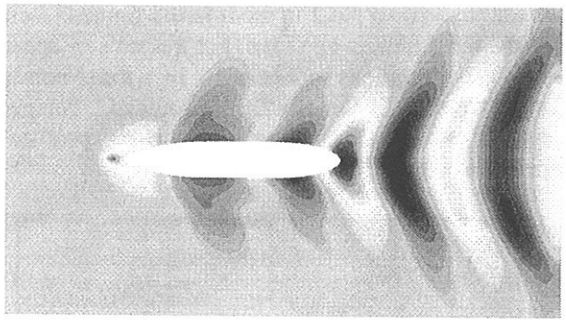

Fig.10 Free surface spectrum. Hull No.3

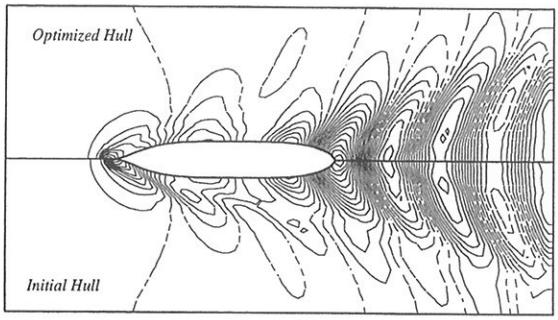

Fig. 11 Comparison between the wave profiles computed for the initial and the optimized hulls

Table 2

Hull trial	$10^3 C_f$	$10^3 C_{pv}$	$10^3 C_v$	$10^4 C_w$	$10^3 C_t$
Initial hull	1.551	2.226	1.774	5.927	2.367
Hull No.2	1.531	1.991	1.730	5.841	2.314
Hull No.3	1.532	1.986	1.731	5.742	2.304
Hull No.4	1.53	1.981	1.732	6.259	2.358

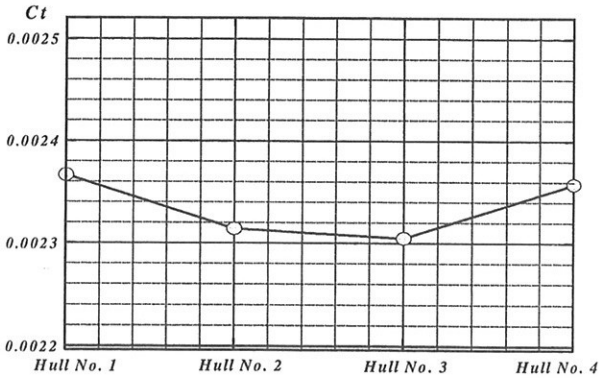

Fig. 12 - Total pressure coefficient variation for the considered hulls

Table 3

Hull trial	Computation (Fn=0.275)	C_w Computed	C_w Measured
Initial hull	Non-linear	$0.593 \cdot 10^{-3}$	$0.617 \cdot 10^{-3}$
Hull No. 3	Non-linear	$0.574\ 10^{-3}$	$0.611 \cdot 10^{-3}$

2.3 Fore and Aft End Optimization

In this case the purpose of the numerical and experimental investigation was to optimize the hull shape, in order to ensure the minimum ship resistance and to achieve the optimal pressure distribution on the aft part of the ship. Only the final version of model hull was tested in towing tank to confirm the numerical simulation results. The main results of the numerical simulation and of the model tests are tabulated in Table 4. The computed free surface and distribution of the pressure on the hull and free surface is presented in the Figs. 14÷15.

Table 4

Hull trial	$10^3\ C_w$ Computed	$10^3\ C_w$ Measured
Hull no.1 (linear calculation)	0.5078	-
Hull no. 2 (linear calculation)	0.4696	-
Hull no. 3 (linear calculation)	0.4481	-
Hull no. 3 (non-linear calculation)	0.4371	0.3908

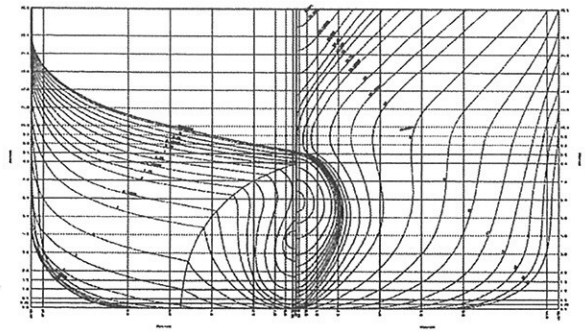

Fig. 13 - Body lines (initial hull form)

The main hull modifications consist in reducing the cross section area of the fore bulb simultaneously with a change of LCB with 0.2% in the aft.

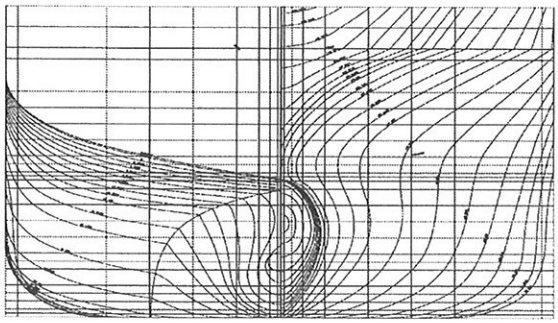

Fig. 14 - Body lines (final hull form)

Fig. 15 Free surface elevation.
Hull No.3 non-linear computation

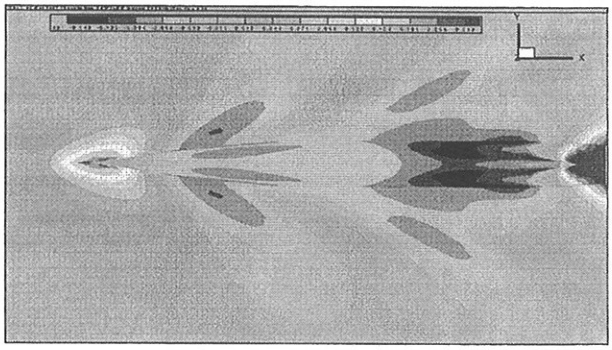

Fig.16 Free surface contours.
Hull No.3 non-linear computation

3. EXPERIMENTAL RESULTS

The experimental results show a satisfactory agreement with the solution of the numerical simulation. Based on the trial computations performed, having a grasp of understanding over the tendency of the wave resistance modification, the bodylines could be properly modified till the optimum has been achieved.

4. CONCLUSIONS

Free-surface flow around several versions of the hull forms was successively computed. Free-surface topology as well as the wave resistance were determined trough the numerical simulations. Both linear and nonlinear approaches were used to solve the flow problem. Improvement of the hull forms determined a decrease of the wave resistance in all the considered cases. As a consequence, the final version of the successively modified shapes allowed the increase of the speed performances for all the ships.

REFERENCES

JANSON, C-E., *Potential Flow Panel Methods for the Calculation of Free Surface Flows with Lift*, Ph.D. Thesis, Chalmers University of Technology, 1997.

DAWSON, C., *A Practical Computer Method for Solving Ship Wave Problems*, 2nd International Conference on Numerical Hydrodynamics, Berkley, 1977.

RAVEN, H.C., *A Solution Method for the Nonlinear Ship Wave Resistance Problem*, MARIN, Holland, Ph.D. thesis, Technical University of Delft, 1996.

JENSEN, P.S., *On the Numerical Radiation Condition in the Steady State Ship Wave Problem*, Journal of Ship Research, vol. 31, nr.1, 1987.

A model for the simulation of spilling breaking waves

R. Muscari[1], A. Di Mascio[2]

INSEAN - Italian Ship Model Basin
Via di Vallerano, 139 – 00128 Roma – Italy
tel.: +39.0650299316, fax : +39.065070619

Abstract

As well known, although flows with breaking waves frequently occur when dealing with ships' motion, very little has been done to model their effects in naval hydrodynamics codes.The present work describes a first approach to the introduction of a breaking model into an existing RANS code for the simulation of viscous flows past ship hulls.
The original idea for the model is taken from the work of Cointe and Tulin (C&T) [3] where the breaker is seen as an eddy exerting 'suitable' pressure and friction on the wave–breaker dividing streamline. To our purposes this theory has the attractive aspect that it yields some boundary conditions to model the breaker which are simple but effective and readily applicable. This characteristic of the theory has already been exploited by Rhee and Stern (R&S) [5], where promising results are obtained in the simulation of 2D spilling breaking waves by the straightforward application of the 'inviscid' part of C&T theory. In particular, R&S adopt the geometry of the breaker suggested in [3], i.e. a flat-topped breaker with the same relationship between the height of the leading wave and that of the breaker as in [3]. The velocity distribution along the wave–breaker interface is specified following the shear layer similitude. At the toe of the breaker the horizontal component of velocity (u) undergoes a discontinuity, whose intensity depends on the wave steepness. Beyond the toe, u is set according to the constant total head assumption.
The main distinguishing feature of the proposed model with respect to both [3] and [5] is the way in which the geometry of the breaking region is related to the wave height. Moreover, the breaking region is not modeled as a sharp triangle, but rather as a smoothed geometrical shape in order to mitigate the abrupt transition in the free–surface dynamic boundary condition and, hence, to enhance convergence to steady state. Finally, the kind of boundary condition enforced on the velocity field on the wave–breaker dividing streamline differs from the one used in [5]. Here, we set the normal derivative of the tangential velocity, on the basis of local equilibrium considerations and classical solutions of the mixing layer.
We tested our model against the experimental data obtained by Duncan in [1, 2] (figure 1). The pressure due to the breaker's weight damps the following wave train to a level very close to that depicted in the experimental data (figure 2). The addition of the pressure term to the RANS code does not spoil the overall robustness, that is, it neither leads to instabilities nor slows down the convergence to steady state.
The shear, arising from the tangential part of the breaker's weight, produce both a weak shifting in the phase of the wave–train and a turbulent trailing wake. In figure 3 it can be seen that the wake numerically obtained is shallower than the experimental one. Unfortunately, a tuning of the free parameters aimed to obtain a deeper wake leads to a worse convergence or even to instabilities. This behaviour probably depends on the turbulence model (the one–equation Spalart–Allmaras model [4]) which is not suited to take into account the turbulence–free-surface interaction.
Much work is still to be done to clarify this aspect and, especially, to extend the model to a more general three–dimensional case.

References

[1] J. H. Duncan, *An experimental investigation of breaking waves produced by a towed hydrofoil*, Proc. R. Soc. Lond. A, vol. 377, p. 331, 1981.

[2] J. H. Duncan, *The breaking and non-breaking wave resistance of a two-dimensional hydrofoil*, J. Fluid Mech., vol. 126, p. 507, 1983.

[3] R. Cointe, J. Tulin, *A theory of steady breakers*, J. Fluid Mech., vol. 276, p. 1, 1994.

[4] P. R. Spalart, S. R. Allmaras, *A one–equation turbulence model for aerodynamic flows*, La Recherche Aérospatiale, vol. 1, p. 5, 1994.

[5] S. H. Rhee, F. Stern, *Private communication.*

[1] e-mail: r.muscari@insean.it
[2] e-mail: a.dimascio@insean.it

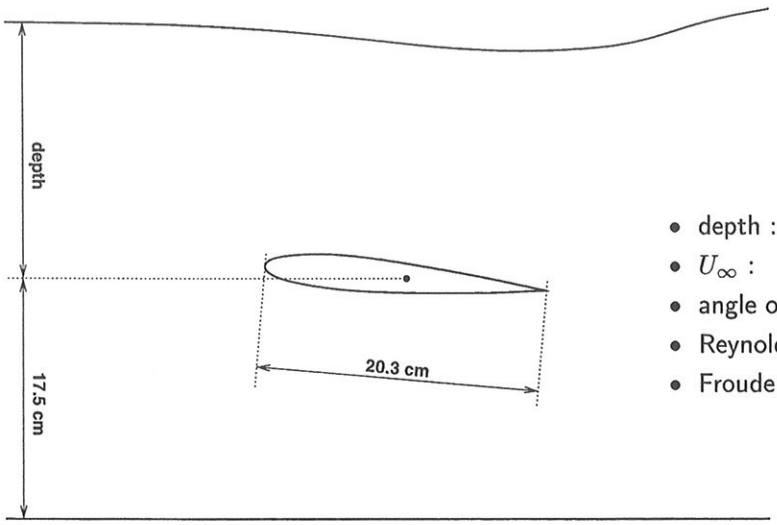

- depth : 18.5 cm
- U_∞ : 0.8 m/s
- angle of attack : 5°
- Reynolds number : 1.423×10^5
- Froude number : 0.567

Figure 1: Experimental setup

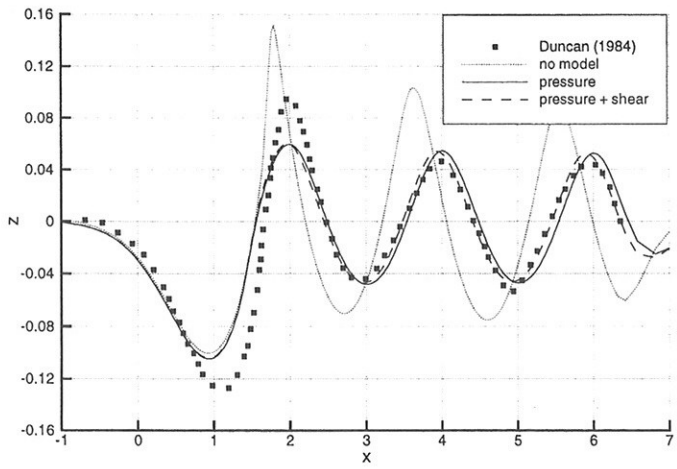

Figure 2: Numerical vs. experimental wave patterns.

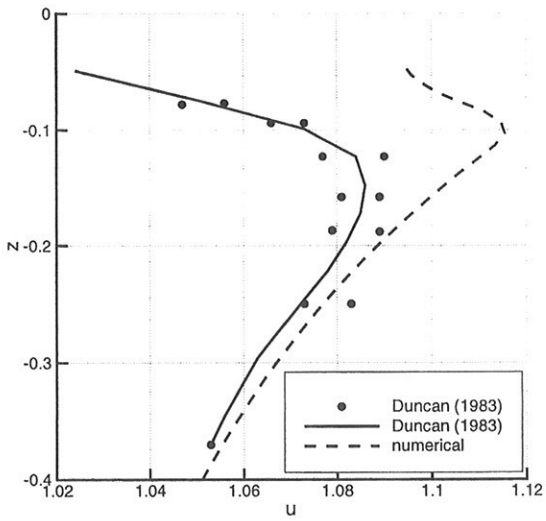

Figure 3: Horizontal flow velocity vs. depth at the second trough after the breaker. Numerical vs. experimental data.

VOF simulation of green water load problems

Kristian Bendix Nielsen*
Department of Mechanical Engineering
Studentertorvet, Bldg 101E
Technical University of Denmark
DK - 2800 Kgs. Lyngby

Stefan Mayer†
Informatics and Mathematical Modelling
Technical University of Denmark

1 Introduction

With the rising popularity of Floating Production Storage and Offloading vessels (FPSO's) and the desire to bring the FPSO's into harsher environments, the problems related to green water loads have been given increasing attention. The damage caused by green water can impose down time, or docking, which can be very costly. Therefore the prevention of green water damage is of great interest.

Green water loads occurs when a solid body of water plunges onto the deck of a moored or sailing ship. The water can cause damage to the structure on the forecastle deck, or damage equipment and deck plating in the bow region of the ship. A description of green water related problems in the Norwegian sector can be found in *Ersdal and Kvitrud* (2000). Green water loading is a complex phenomena, and consist of many contributing factors: The height and steepness of the incoming wave, the relation between incoming wave length and ship length, relative ship motion, wave diffraction at ship bow, ship bow flare, bow geometry, etc. Due to this complexity, the standard industry approach in determining green water loads has been to perform experiments.

In recent years two methods have been proposed to estimate green water loads using a combination of experimental data and numerical tools (*Buchner*, 1998; *Ogawa et al.*, 1998). Full numerical simulation of green water problems has also been reported recently: *Fekken et al.* (1999) used a Volume-Of-Fluid (VOF) type approach to solve the full Navier-Stokes equations with free surfaces. Only the final stage of the green water incident was modeled numerically, but compared well with experimental data. *Greco et al.* (2000) applied a potential flow solver on a simplified (2D) FPSO model, and on a wave run-up problem. The overall agreement between numerical and experimental data was satisfactory, but the numerical model had difficulty handling flow detachment, which occurs when a body of water is separated onto the ship deck.

This paper presents a preliminary investigation of the green water problem, using a full Navier-Stokes solver with a VOF type scheme to handle the free surfaces. The test cases include wave run-up on a solid wall, and an FPSO exposed to green water loading, in a simplified simulation.

2 Mathematical model

The basic spatial and temporal discretization implemented in the incompressible Navier-Stokes solver, NS3, follows *Mayer et al.* (1998). It uses a projection method, which is second order accurate in time, and employs a finite volume method with cell-centered variable layout on general multi block grids. The code uses a variable time step, based on a Courant (CFL) number criterion, chosen to keep the maximum CFL number below a given threshold value.

*kbn@mek.dtu.dk
†stm@imm.dtu.dk

To describe the free surfaces the Compressive Interface Capturing Scheme for Arbitrary Meshes (CICSAM, *Ubbink* (1997)) method is applied. CICSAM is a VOF type scheme, based on Normalized Variable Diagrams (*Leonard*, 1991), and switches between upwind and downwind differencing depending on the orientation of the volume fraction field gradient. It is a compressive scheme, which retains a sharp interface between void and full cells, without deforming or aligning the interface to the grid.

3 Test cases and results

3.1 Case 1

The first test case consist of wave run-up on a solid wall, simulating the initial stage of a green water incident. Wave run-up was analyzed experimentally by *Cozijn* (1996), where a wall was placed at the end of a wave flume, with a 10 cm gap from the top of the wall to the mean water surface level, with water depth $h = 1.03$ m, shown in Fig. 1. At the other end of the flume, a flap type wave maker generated waves that traveled through the flume, and hit the wall. The waves ran up and over the wall, and the location of the free surface was recorded on video. The incident wave had wave height H = 0.128 m and wave frequency was $\omega = 5$ rad/s.

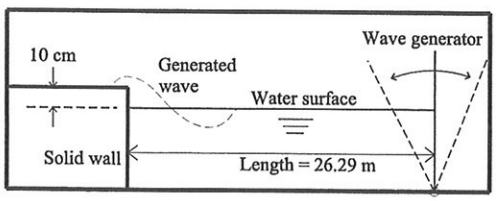

Figure 1: *Schematic of test case 1*

The numerical calculations for test case 1 are carried out in 2D, since the problem is considered to have negligible 3 dimensional effects. The computational domain consist of three blocks, and a number of different grid resolutions are tested, having between 20,000 and 200,000 grid cells. At the right boundary of the domain, a horizontal velocity profile is imposed to generate waves, using a fourier approximation of the wave profile. The threshold CFL number of the computations is set to 0.2.

A comparison between the surface contours from the numerical and experimental results is shown in Fig. 2. The surface contours at the upper edge of the solid wall are shown at 6 different time steps with 0.04 seconds between each frame. The highest grid resolution (200,000 cells) is used for the results shown in Fig. 2. The overall agreement is satisfactory, but in the phase when the wave runs over the edge of the wall (Frame 3, 4 and 5) the numerical calculations show a cavity forming at the trailing edge, which is not seen in the experiments of *Cozijn* (1996). Similar experiments as *Cozijn* (1996) were conducted by *Greco et al.* (2001), where the forming of a cavity actually was reported, which supports the current numerical simulation. However, a more detailed analysis, both numerically and experimentally, is required in order to verify the existence of the cavity.

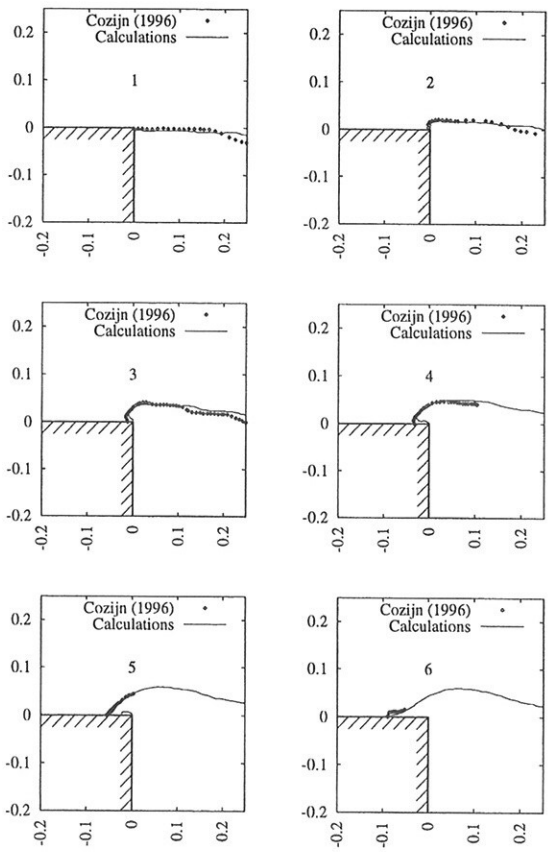

Figure 2: *Results from Case 1* ($\Delta t = 0.04$ *s*). *Comparison between computet and experimental free surface contours*

3.2 Case 2

The second test case is a green water incident on an FPSO. The experiments were conducted by *Buchner* (1995) for an FPSO with overall length of 260.34 m and depth of 17.52 m. The freeboard height is 8.88 m, and a structure is located 35.9 m from the bow. The experiments were carried out in model scale 1:60. Fig. 3 show a schematic of test case 2, where the four wave probes (P1-P4) measure the water height resulting from the shipping water.

In the numerical calculations for test case 2, the problem is greatly simplified for this preliminary investigation, i.e. calculations are carried out in 2D and the FPSO is fixed in space. However, it is still expected that this will give some information regarding the dynamics of green water incidents, show by a comparison between numerical and experimental shipped water height on deck. The computational domain used for the numerical calculations consist of five blocks, where the highest grid resolution that is tested consists of approx. 113,000 cells. Waves are generated by imposing a horizontal velocity profile at the left computational boundary, and the CFL number for these calculations is also $CFL = 0.2$.

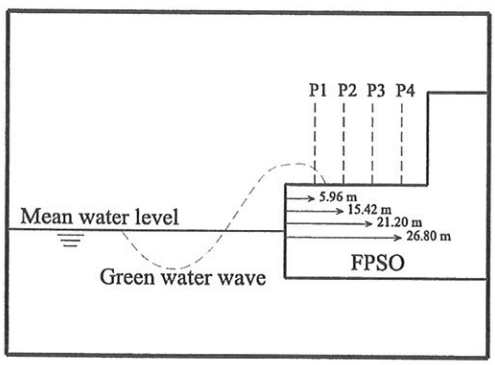

Figure 3: *Schematic of test case 2*

Results from the FPSO case are shown in Fig. 4. The figure shows a comparison between the numerical and experimental water heights on deck, measured at the water probes P1-P4, where time $t = 0$ is equal to the initiation of the green water incident. The four graphs show a time history of the measured water height on deck, where the solid lines represent the numerical calculations, and the dashed lines are from the experiments carried out by *Buchner* (1995). The incident wave has wavelength = 195.3 m, period of T = 11.2 s and wave height H = 17.57 m.

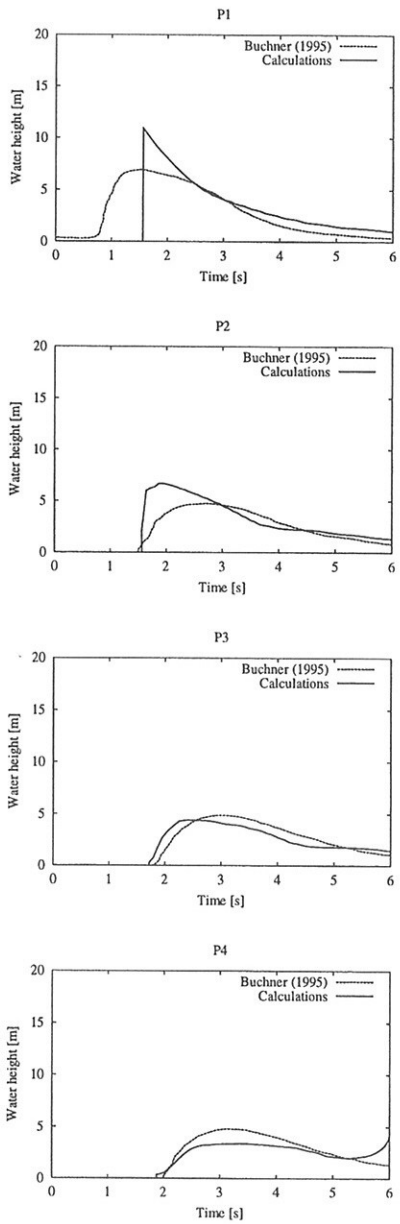

Figure 4: *Results from Case 2. Comparison between numerical and experimental water heights on deck at 4 locations along FPSO centerline.*

At probe P1 a sudden rise of water height is seen in the numerical results. This is caused by the plunging wave that forms at the edge of the deck in the initial stage of the green water incident. The calculations only registers a wave when the first cell above the deck plating is filled, so when the plunging wave hits the deck at the first probe, the full water height is registered at a single time step, which causes the sudden rise. At the remaining probes, the time history of the numerical and experimental water height on deck correspond satisfactory, except at the end of the time history for probe P4, where a second rise in water height is registered. This is caused by the reflecting wave that comes from the structure located further down the FPSO deck. This is not seen in the experiments because, in the experiments, the water can run along and around the structure normal to the ship symmetry plane.

4 Conclusion

This preliminary study has shown how simplified green water problems can be modeled by CFD techniques, and shows a satisfactory agreement between numerical end experimental results. However, two fundamental elements still need to be included in the numerical method for future studies: three dimensionality and movement of structures in the computational domain. This will enable an investigation of the more complex elements of green water loading which has been neglected here: complex 3 dimensional bow shapes (effect of ship bow flare) and relative ship motion.

References

Buchner B. (1995). *On the impact of green water loading on ship and offshore unit design.* In *The sixth International Symposium on Practical Design of Ships and Mobile Units* (PRADS, Seoul, Korea).

Buchner B. (1998). *Jip on f(p)so green water loading.* MARIN, The Netherlands (unpublished).

Cozijn J.L. (1996). *Numerical simulation of green water.* Technical report, MARIN Wageningen / Delft University of Technology, the Netherlands.

Ersdal G. and Kvitrud A. (2000). *Green water on norwegian production ships.* In *Proceedings of the Tenth (2000) International Offshore and Polar Engineering Conference.*

Fekken G., Veldman A.E.P. and Buchner B. (1999). *Simulation of green water loading using the navier-stokes equations.* In *Numerical Ship Hydrodynamics* (Nantes, France).

Greco M., Faltinsen O.M. and Landrini M. (2000). *Basic studies of water on deck.* In *Proceedings of the 23rd Symposium on Naval Hydrodynamics* (National Academic Press, Val de Reuil, Washington D.C.).

Greco M., Faltinsen O.M. and Landrini M. (2001). *Green water loading on a deck structure.* In *Proceedings of the 16th International Workshop on Water Waves and Floating Bodies*, edited by K.H. Mori and H. Iwashita (Hiroshima, Japan).

Leonard B.P. (1991). *The ultimate conservative difference scheme applied to unsteady one-dimentional advection.* Computational Methods in Applied Mechanics and Enginering, volume 88: pages 17–74.

Mayer S., Garapon A. and Sørensen L.S. (1998). *A fractional step method for unsteady free-surface flow with applications to nonlinear wave dynamics.* International Journal for Numerical Methods in Fluids, volume 28: pages 293–315.

Ogawa Y., Tagichi H. and Ishida S. (1998). *A prediction method for the shipping water height and its load on deck.* In *Practical Design of Ships and Mobile Units*, edited by M. Osterveld and S.G. Tan (Elsevier Science B.V.).

Ubbink O. (1997). *Numerical prediction of two fluid systems with sharp interfaces.* Ph.D. thesis, University of London.

Hydroelastic Simulation of Slamming Loads

by Marcos Salas
Institute of Naval and Maritime Sciences
Faculty of Engineering Sciences, University Austral of Chile
Casilla 567, Valdivia, Chile. e-mail: msalas@uach.cl

This paper investigates the main variables that govern slam occurrence and presents a numerical model for the determination of slamming and consequent impact pressures on a hull travelling in long-crested irregular seas encountered at arbitrary headings. The irregular seas, defined by a two-parameter wave energy spectrum, are generated using a random combination of a large number of regular waves. The numerical method is based on the idealisation of a prescribed slamming area, in this case the forefoot region, using four-cornered panels, referred to as slamming panels. Impact occurrence is determined by examining the relative motion and, thus, predicting the emergence and subsequent impingement of panels in the prescribed slamming area. Corresponding impact pressures are calculated taking into account the effective impact angle, dependant on relative motions and hull geometry, and relative impact velocity of the hull against the sea surface. A novelty of the numerical method presented is inclusion of roll, in addition to heave and pitch motions, when travelling in oblique irregular seas. Impingement of a slamming panel on water is detected, following an emergence, using the relative motion of the panel centre. Heave, pitch and roll motions are included when calculating the relative motion, using the three-dimensional hydroelasticity theory (Bishop, Price and Wu 1986; Price, Salas and Temarel 2001) which is briefly discussed in this paper. Evaluated impact pressures are a function of the position of the hull relative to the seaway elevation as well as operational conditions such as loading, forward speed, heading angle and seaway characteristics.

In the present paper, the concept of threshold velocity was set aside. No matter how small the vertical relative velocity is, the slamming pressure forces are evaluated on the hull. Nevertheless, it is possible to eliminate non-severe slams by a suitable selection of the slamming area. The emergence at any position (defined by the coordinates x,y,z) on the hull can be defined in terms of the relative motion of the geometric centres of the slamming panels. The relative motion can be expressed as $w_{rel}(x,y,z,t) = w(x,y,z,t) - \zeta(x,y,t)$ where w is the vertical rigid body displacement at (x,y,z) at time t and $\zeta(x,y,t)$ represents the seaway elevation which is assumed not to be affected by the presence and motions of the hull. A slam will occur whenever the relative motion is greater than the local draught $T(x,y,z)$. The relative motion at a position (i.e. slamming panel centre) on the forefoot of the hull, identifies the time instant at which slam impacts occur and the corresponding transient loading starts. The severity of a slam is dependent on two parameters, the relative velocity of the hull impacting the sea surface and the effective angle of impact. Slamming impact pressures were calculated using Stavovy and Chuang (1976) expression

$$p(x,y,z,t) = k\rho V_n^2$$

where k is a non-dimensional pressure factor and V_n is the relative normal velocity of impacting body to wave surface. To obtain V_n, the effective impact angle $\xi(x,y,z,t)$ must be known. This, itself, is a function of local deadrise, buttock and trim angles, wave slope and ship motions. Ship motions and the instantaneous effective impact angle depend on the sea surface definition. The ocean surface can be represented by the linear combination of R regular waves, where R is a suitably large number, of random height, length and if required, direction. The unidirectional or long-crested seaway can be represented by

$$\zeta(x,y,t) = \sum_{j=1}^{R} \zeta_j(x,y,t) = \sum_{j=1}^{R} a_j e^{i(\omega_j t + \varepsilon_j)}$$

where a_j is the wave amplitude of the j^{th} wave; ω_j and ε_j represent the wave frequency and phase angle respectively. The wave frequencies and amplitudes can be selected to represent a seaway described by a particular wave spectrum. In this paper, a two-parameter spectrum, defined by the significant wave height $H_{1/3}$ and characteristic wave period T_c, is used. In the numerical calculations R=350 waves were employed to simulate the irregular seaway with sufficient accuracy.

In the evaluation of the relative motions, flexible modes are considered in addition to rigid body modes. According to the hydroelasticity theory (Bishop, Price and Wu 1986) the equation of motion for a freely floating flexible structure can be written as

$$\mathbf{a}\ddot{\mathbf{p}}(t) + \mathbf{b}\dot{\mathbf{p}}(t) + \mathbf{c}\mathbf{p}(t) = \mathbf{Z}(t) \ . \qquad (1)$$

In this equation **a**, **b** and **c** are the $N \times N$ generalised mass, structural damping and stiffness matrices of the dry or in vacuo structure, with elements a_{rr}, $b_{rr} = 2\,\nu_r\,\omega_r\,a_{rr}$ and $c_{rr} = \omega_r^2\,a_{rr}$ for $r = n,\ldots,N$ respectively. n denotes the index of the first flexible mode. ω_r and ν_r denote the natural frequency of the structure in vacuo and the

structural damping factor, respectively. The part of matrix **a** corresponding to the rigid body modes contains the mass and moments and products of inertia of the structure. N is the number of degrees of freedom, associated with rigid body motions and distortions, allowed for in the analysis. $\mathbf{p}(t)$ is the $N\times1$ principal coordinate vector and $\mathbf{Z}(t)$ represents the $N\times1$ external force vector describing, in this case, the fluid actions. The equilibrium axis system xyz is placed at the calm water level with x, y and z denoting the longitudinal (+ve to bow), athwartships (+ve to port) and vertical (+ve upwards) axes respectively.

A dry or in vacuo analysis is carried out (in the absence of external forces and structural damping) to obtain the natural frequencies ω_r , r = 1,...,N and corresponding principal mode shapes as well as other modal characteristics such as modal bending moments, modal stresses, etc. associated with the distortions of the structure. For a freely vibrating structure, i.e. with no restrains in space, the first 6 principal modes obtained from a modal analysis represent the rigid body motions, namely: surge, heave sway, yaw, roll and pitch, associated with zero frequencies ($\omega_r = 0$). Having obtained the distortion mode shapes of the "dry hull", all actions can be applied as external forces, including hydrodynamic actions and structural damping, in order to perform the "wet hull" analysis. Assuming the flow is ideal, thus represented by a velocity potential, the external fluid force in regular waves contains contributions associated with the incident, diffracted and radiated wave due to the motions and distortions of the vessel, namely

$$Z_r(t) = \exp(i\omega_e t)\left[\Xi_{or} + \Xi_{dr} + \sum_{k=1}^{N}(\omega_e^2 A_{rk} - i\omega_e B_{rk} - C_{rk})p_k\right] \quad . \qquad (2)$$

Substituting eq.(2) into eq.(1) the generalised linear equations of motion for a vessel travelling in regular oblique waves is obtained, in matrix form, as

$$(\mathbf{a}+\mathbf{A})\ddot{\mathbf{p}}(t) + (\mathbf{b}+\mathbf{B})\dot{\mathbf{p}}(t) + (\mathbf{c}+\mathbf{C})\mathbf{p}(t) = \Xi\exp(i\omega_e t) \qquad (3)$$

and are solved to obtain the principal coordinates in the form $\mathbf{p}(t) = \mathbf{p}\exp(i\omega_e t)$, where $\mathbf{p}$ denotes the complex amplitude of the principal coordinate vector. In these equations the $N\times N$ matrices **A**, **B** and **C** represent the generalised added mass, hydrodynamic damping and restoring coefficients, with elements A_{rk}, B_{rk} and C_{rk}, respectively. The generalised excitation vector Ξ contains the incident (Ξ_{or}) and diffracted (Ξ_{dr}) wave contributions. $\omega_e = \omega - k\,U\cos\chi$ is the wave encounter frequency, in deep water, for waves of frequency ω, wave number $k = \omega^2/g$, encountered at heading χ (= 180°, head waves) when the vessel is proceeding with a forward speed U.

Having determined principal coordinates by solving equation (3) it is possible to evaluate hull motions or any relevant load response such as bending moments, shearing forces, twisting moments or stresses using the appropriate characteristic function of the dry structure. For example any steady state motion or load in an irregular sea is defined by

$$\bar{S}(x,y,z,t) = \sum_{j=1}^{R}\sum_{r=1}^{m} a_j\, p_r(t) S_r(x,y,z)$$

where S_r denotes any modal shape or steady state load such as bending or torsion moment, direct stress, shear stress or any known modal load. $p_r(t)$ represents the principal coordinate of the r^{th} mode and a_j represents the amplitude of the j^{th} component wave of the seaway. The corresponding modal properties of the dry structure S_r may be obtained from a Finite Element Modal Analysis. Determination of principal coordinates has been well documented in hydroelasticity papers (Bishop, Price and Wu 1986, Price, Salas and Temarel 2001, for example) and therefore will not be presented here. It is interesting to note that no contribution to the loadings arise from the rigid body modes (r =1,..,6). This is not the case when calculating relative motions, where all the modes, rigid and flexible, contribute to the total displacements.

Transient loads may be expressed as follows (Belik, Bishop and Price1983)

$$\tilde{S}(x,y,z,t) = \sum_{r=7}^{m} S_r(x,y,z)\tilde{p}_r(t) \quad .$$

The magnitudes of the transient principal coordinates $\tilde{p}_r(t)$ required in this equation are directly dependant of the slamming pressures which determines the transient excitation. The Stavovy and Chuang (1976) theory of impact slamming is a suitable way for the determination of slamming pressures as discussed previously.

Finally total loads can be obtained from addition of steady state and transient loads

$$S(x,y,z,t) = \bar{S}(x,y,z,t) + \tilde{S}(x,y,z,t) \quad .$$

Hull relative motions, including the effect of flexible modes, and impact pressure calculations were carried out for a hull with length to beam ratio L/B=4.7 and length to depth ratio L/D=9.3 (Price, Salas and Temarel 2001). All calculations were carried out for a Froude number Fn=0.31. Figure 1 shows the idealised slamming forces

acting on a hull cross section, where segments represent cuts trough panel centres. If slamming panels are defined too close to the main water surface, the number of slams will be extremely high. In the slamming simulations of the monohull the fifth row of panels (i.e. the row tangent to the mean sea surface) was discarded from the slamming area. Slamming panels selected to define the slamming area are shown in figure 2. As can be seen the slamming area is defined by 11 sections and 8 rows (4 each side of the hull centre line) making a total of 88 slamming panels. The panels are identified by section position (S_1 to S_{11}) and row position (R_1 to R_4, port and starboard). S_1 is the aftmost section of the slamming area with panel centres at x/L=0.65, x measured from AP. S_{11} is the foremost section at x/L=0.95. The rows are numbered starting from the keel with R_1; therefore, the row closest to the mean (still) waterline is R_4.

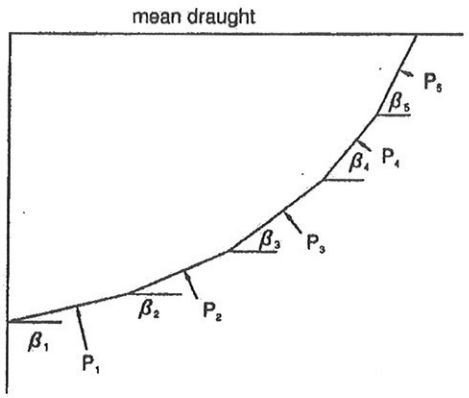

Figure 1: Slamming impact pressures on a hull. β indicates the local deadrise angle

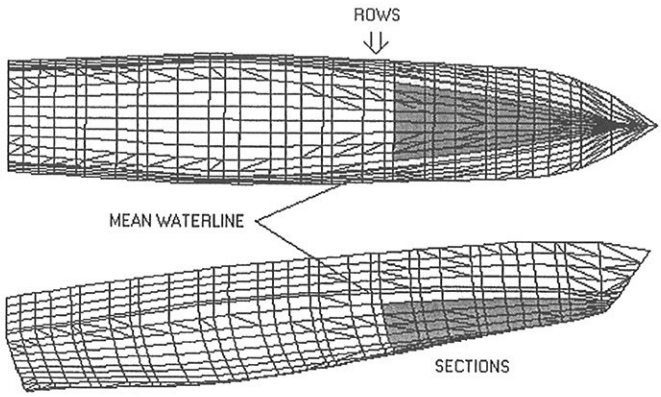

Figure 2: The slamming area defined by 11 sections and 8 rows of panels.

Relative motions and total loads calculations were carried out for several seaway conditions The numerical method takes into account heave, pitch and roll motions of the hull, which are evaluated using the three-dimensional hydroelasticity theory. 5-minute time simulations were carried out using 0.1 s time steps which is considered fine enough to adequately represent the slamming behaviour, smaller time steps could be used at the expense of increased computing time.

The hydrodynamic panel size was the same defined in the dry finite element modal analysis, this is a matter of convenience rather than a necessary condition. The FE model corresponds to the one shown in figure 2. Modal characteristics, i.e. natural frequencies and loadings such as bending and torsion moments were obtained for a finite element model using SHELL63 ANSYS elements. No bulk elements were modelled so the plate densities were manipulated in order to take into account all lump weights such as engines and onboard equipment. In determining the dynamic characteristics of the vessel it is important to obtain a mass distribution as close to the actual ship as possible.

Figure 3 shows the relative motion of starboard bottom panels at a position x/L=0.8 obtained with a heading of 135° (180°=head seas) in irregular seas described by a two-parameter wave spectrum with $H_{1/3}$=6 m and T_c=6 s. Three consecutive slams and the resulting impact pressures at slamming panels of R_1 (bottom) and R_2 rows are shown. Pressures at upper rows, R_3 and R_4, are lower due to smaller local deadrise angles. The impact pressure is not the same for panels located at similar positions but different side of the hull. This is due mainly to the effects of roll motion. The heel angle will increase the effective impact angle at one side of the hull and decrease it at the other side. Several slams were obtained for the 5-minute simulation, it was observed that any time sequence is possible. For example panels at the foremost end of the slamming area may strike the water first or last and in some cases panels in the middle of the slamming area may impact the water first. It all depends on several parameters interacting: hull motions and geometry, wave slope and angle of heading.

Figure 4 shows relative motions of the bottom at x/L=0.8 and total horizontal bending moments at x/L=0.5. The hull travels with 150° heading in a seaway described by a characteristic period 8 s and three significant wave heights $H_{1/3}$=4, 6 and 8m. It is clear that the significant wave height affects the relative contribution of the slamming to total loads. Another factor to be considered is the amount of structural damping to be incorporated in the hydroelastic equations. Unfortunately, there are not reliable methods to calculate this, therefore comparison with experimental results, not currently available, would be an appropriate way to tune structural damping.

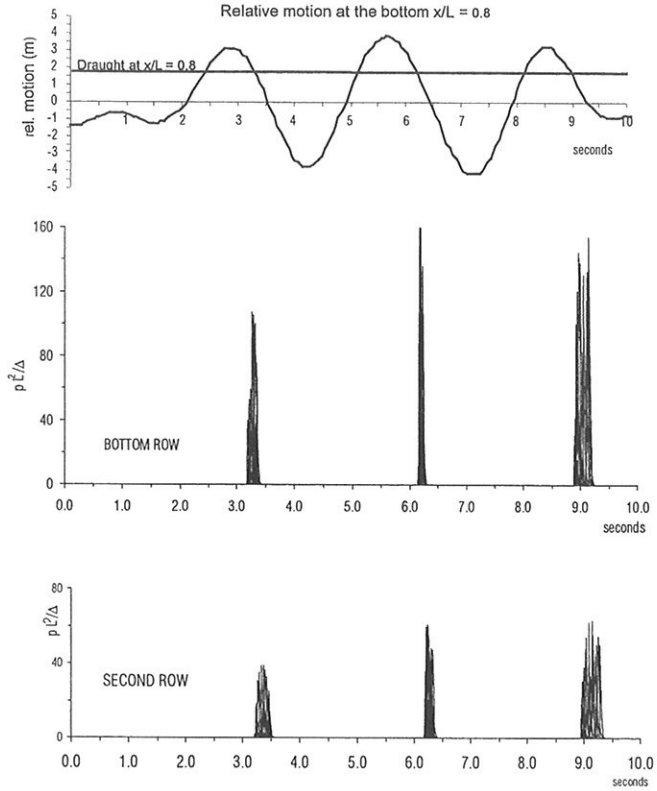

Figure 3: Relative motion at the bottom of x/L=0.8 and pressures for three consecutive slams.

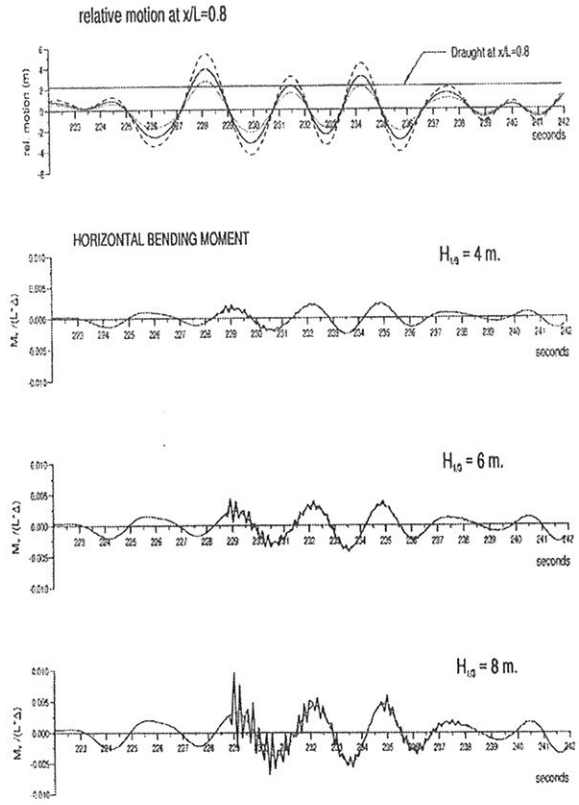

Figure 4: Total horizontal bending moment including slamming effects.

The numerical method presented is a distinct departure from slamming in head seas using two-dimensional hydroelasticity theory. The fundamental building block of the current method is the impact of at least one panel in the slamming area, which constitutes a slam. Slamming pressure is greater at bottom panels, i.e. where the deadrise angle is smaller, pressures at upper rows diminishes considerably which agrees with two-dimensional slamming practice of considering 1/10 of the draught affected by slamming loads. The number of slams in a given length of time depends on both, significant wave height and characteristic period. The number of impacts will be larger if the hull heave and pith motions (and hence the relative motions) are large. This occurs when the encounter frequency is predominantly tuned to the hull's pitch resonance.

On defining the slamming area there are no restrictions, except for CPU time considerations. Thus any region of the hull surface can be selected as slamming area if it is thought as an area prone to slamming, e.g. keel/side, flare, wetdeck for multi-hulled vessels etc. Panels within this slamming area that do not slam will not affect the evaluated impact loadings. In practice it is convenient to limit the number of panels to those which are located in hull areas prone to suffer slamming impacts, e.g. forward and bottom panels at the bow. This avoids the necessity of evaluating and monitoring the relative motions of a large number of panels.

Acknowledgements
Prof. P. Temarel, Fluid-Structures Interactions Research Group, University of Southampton, UK, support is greatly appreciated as the work presented here was developed while a member of his research group.

References

Belik, O.; Bishop, R.E.D. and Price, W.G. (1983) "A Simulation of Ship Responses Due to Slamming in Irregular Head Waves". Transactions of the Royal Institution of Naval Architects, vol. 125.

Bishop, R.E.D.; Price, W.G. and Wu, Y. (1986) "A General Linear Hydroelasticity Theory of Floating Structures Moving in a Seaway". Phil. Trans. R. Soc. Lon. 1986, A316.

Price, W.G., Salas, M. and Temarel, P. (2001) "The dynamic behaviour of a mono-hull in oblique waves using two- and three-dimensional fluid-structure interaction models". Accepted by TRINA.

Stavovy, A. and Chuang S. L. (1976) " Analytical Determination of Slamming Pressures for High-Speed Vehicles in Waves". Journal of Ship Research, vol. 20.

RANS Simulation of the Flow around a Manoeuvring Tanker

Claus D. Simonsen, John Cross-Whiter
Danish Maritime Institute, cds@dmi-online.dk

Introduction

To investigate the relatively new application of viscous CFD technology to manoeuvring calculations and to study hull, rudder and propeller interaction, DMI is currently involved in a joint project with Iowa Institute of Hydraulic Research (IIHR). The goal is to study the flow around the tanker Esso Osaka in manoeuvring situations by means of a numerical model, which includes geometrical representations of the hull and rudder and the propeller represented by a body-force field. Based on the results of the study the idea is to

- Investigate the possibility of generating a complete rudder, propeller and hull model by means of a numerical method.
- Study the rudder, propeller and hull related flow problem on both integral and field levels in order to provide information, which can hopefully help to understand the rudder, propeller and hull interaction better.
- Investigate the possibility of numerical generation of hydrodynamic forces to manoeuvring simulators.

The initial work with the numerical hull-rudder-propeller model is described in Simonsen (2000). It was found that due to the complexity of the flow problem and the size of the full numerical model it is necessary to construct the numerical model in a stepwise manner, in which the hull and rudder models are built and tested separately. This allows the performances of the hull and the rudder models to be studied individually before they are joined in the final model. The work covering a rudder in free stream and behind a body force propeller is also described in Simonsen (2000) so focus is now placed on the bare hull and the appended hull with and without propeller.

Numerical method

The computations are performed with the Reynolds Averaged Navier-Stokes (RANS) solver CFDSHIP-IOWA developed at IIHR. The code solves the RANS equations on a regular grid by means of finite differencing. For the steady state calculations performed in this context the temporal discretization is based on a first order backward Euler difference. The spatial discretization is performed by a second order upwind scheme for the convective terms, while all other first derivatives and viscous terms are discretized by a standard second order central difference scheme. The pressure and the velocities are coupled by means of the projection method, in which a pressure equation is derived by taking the divergence of the momentum equations and projecting the velocity into a divergence free field. The turbulence is modeled by the k-ω turbulence model without wall functions. Further details about the numerical method should be found in Wilson et al. (1998).

Computational grids

The code utilizes patched and overlapping structured multi block grids. The overlapping grids are used for inclusion of the rudder, and they are put together by means of the Chimera technique, which joins the grid components by means of automatic hole-cutting. The exchange of data between the boundaries of the hole is performed by tri-linear interpolation. The interpolation stencils required for the data exchange are generated in connection with the hole-cutting. The Chimera data is generated by the PEGASUS 5 code.
The current bare hull computations are performed with an O-O grid consisting of approximately 1.1 million points including both sides of the ship. When the appended hull is considered, an O-H topology, which describes the rudder, is added to the O-O system. In order to include the body-force propeller and to distribute the body-force smoothly later on, a cylindrical block is located at the propeller position. The complete grid system consists of approximately 2.2 million points distributed on 35 blocks. Figure (1) illustrates the hull and rudder grids. Finally, since no wall functions are applied, the near wall spacing of the grid on the no-slip rudder and hull surfaces satisfies $y^+ \approx 1$.

Considered ship condition

Since the Esso Osaka is considered as a benchmark test case in the manoeuvring world, it is selected for the present numerical study. The ship is considered in a condition corresponding to a full-scale speed of 7 knots. This results in a Froude number equal to 0.063. The computations are performed in model scale. Based on scaling in accordance with Froude's law and a model of scale 1:43.4783, the 7 knots correspond to model Reynolds number equal to Re=3.609 million. Due to the low Froude number wave effects are assumed to be of minor importance, so instead of modeling the free surface a mirror image is applied.

Results for bare hull

In order to study the flow problem related to the bare hull, the flow field and the corresponding hydrodynamic hull forces have been computed for a series of drift angles in the range of 0 to 12 degrees.

The calculated longitudinal and transverse forces X', Y' and the yaw moment N' are plotted in Figure (2) together with data from a Planar Motion Mechanism (PMM) test, which was conducted at DMI with a 1:43.4783 scale model of Esso Osaka earlier this year. In the figure the forces and the moment have been non-dimensionalized by the water density ρ, the ship speed U, the ship length L_{pp} and the draft T by means of the following expressions

$$X' = \frac{F_X}{0.5\rho U^2 L_{pp} T}, \quad Y' = \frac{F_Y}{0.5\rho U^2 L_{pp} T},$$

$$N' = \frac{M_Z}{0.5\rho U^2 L_{pp}^2 T}$$

A comparison between the numerical and experimental results reveals fair agreement, even though the computed transverse force Y' and yaw moment N' seem to be predicted a little lower than the experiment at the larger drift angles. As the drift angle is increased, the flow becomes more complex due to increased cross flow and vortex structures developing along the hull. As a consequence the numerical method has to deal with more pronounced separation and re-attachment, regions with high turbulence and even slight unsteadiness. These phenomena may be difficult to capture with the steady state solution and can, together with the missing free surface, explain some of the small differences between experiment and simulation.

	Calculation	Experiment
$Y'_{v'}$	0.310	0.321
$N'_{v'}$	0.132	0.133

Table (1). *Hydrodynamic derivatives.*

From the point of view of manoeuvring simulation or prediction, the hydrodynamic derivatives play an important role. In connection with the drift motion, the relevant quantities are the derivatives of the transverse force and the yaw moment with respect to the non-dimensional sway velocity $v' = v/U$. The derivatives $Y'_{v'}$ and $N'_{v'}$ are shown in Table (1) where a comparison with the experimental derivatives shows that the calculated data agrees well with the experiment.

Verification and validation are done for the forces in accordance with the guidelines presented in ITTC (1999). The numerical uncertainty is assumed to consist of a grid and an iterative component. The grid uncertainty is estimated on the basis of a grid study performed on three systematically $\sqrt{2}$ -refined grids and the iterative uncertainty on the basis of the convergence history of the forces. The verification is carried out for the four degrees drift angle case and it results in the numerical uncertainties, U_{SN} shown in Table (2). The table also shows the experimental uncertainties U_D, the comparison errors E and the validation uncertainty U_V. In the table S and D denote simulated and experimental data, respectively. It is seen that E is less than U_V for all the forces, meaning that the method is validated based on X', Y' and N'.

	X'	Y'	N'
U_{SN} % of S	4.2	8.8	1.1
U_D % of D	7.0	3.0	4.8
E % of D	0.02	5.6	1.7
U_V % of D	8.2	8.8	5.4

Table (2). *Uncertainties for β=4°.*

Results for hull with rudder

The numerical hull-rudder model has recently been generated, so only limited numerical results are available at the time of writing. However, two computations, which cover straight-ahead sailing with two different rudder angles, δ=0° and δ=-5°, have been performed.

δ	$X'_{tot} \cdot 10^2$		$Y'_{tot} \cdot 10^3$	
	Calc.	Exp.	Calc.	Exp.
0	1.786	1.764	-----	-----
-5	1.832	1.829	-0.986	-1.488

Table (3). *Global longitudinal and transverse forces.*

The non-dimensionalized forces calculated for the complete hull-rudder system are shown in Table (3) together with experimental PMM data. It is seen that the agreement between the experimental and calculated X'_{tot} data is fair and that the calculation predicts Y'_{tot} somewhat lower than the experiment. It should be noted that a closer study of the experimental data has shown that the globally measured transverse forces originating from the rudder deflection in the considered case are very small. This makes it difficult to measure them accurately with the applied gauges and may explain some of the difference between the transverse force from the experiment and the calculation.

The local rudder forces are shown in Table (4) and again both numerical and experimental data is non-dimensionalized using the expressions shown above. Taking the complexity of flow problem into account the Y-component is seen to be in relatively good agreement with the experiment.

δ	$X_R' \cdot 10^4$		$Y_R' \cdot 10^3$	
	Calc.	Exp.	Calc.	Exp.
0	2.5	1.3	-----	-----
5	2.8	1.3	0.9	1.0

Table (4). *Local lift and drag rudder forces.*

Concerning the X-component of the rudder force the agreement is less good since the computed value is approximately twice as high as the experimental value. There may be a number of different reasons for the observed behavior. First, the numerical and physical models are different, since the rudderstock is included in the experiment but not in the calculation. Second, the experimental uncertainty is relatively high since the rudder forces, and in particular the X-force, are small quantities, which are difficult to measure precisely. Third, the numerical uncertainties, originating from the grid and the iterative solution method, may influence the solution. Fourth, the turbulence model may not be able to predict the overall wake field of the hull correctly. A good prediction of the flow field behind the hull is required in order to model the correct inflow field to the rudder. Therefore, the quality of the predicted wake field may influence the calculated rudder forces. Finally, the fifth reason may be found in the turbulence modeling locally on the rudder, where transition from laminar to turbulent flow in the rudder boundary layer may have some influence on the results. Numerically the boundary layer is assumed to be fully turbulent over the whole rudder, but during the experiment some parts of the boundary layer flow may have been laminar due to the smooth rudder surface. In Simonsen (2000) this effect was found to cause the same behavior of the forces for rudders in free stream, i.e. relatively good prediction of the lift force and over prediction of the drag. One can argue that the flow in the hull wake is much more disturbed than in the free stream, and that the disturbance will trigger the turbulence in the boundary layer. But, due to the very low model speed during the test, it is possible that the turbulence was not triggered and that some part of the rudder flow therefore was laminar.

Besides providing information about the forces, the numerical results can also be used for a study of the details in the flow field as illustrated in the following example. Figures (3) and (4) show how the axial velocity, U, on a cross plane at AP, is influenced when the rudder is turned. It can be seen that the flow field overall is dominated by the presence of the hull, which gives the hook-shaped contours and that the turned rudder mainly disturbs the flow locally in a region close to the rudder. On the port side of the rudder, which is the suction side, the flow is accelerated, while it is retarded on the pressure side due to the stagnation region. The two remaining velocity components, V and W, describe the cross flow and they are shown in Figures (5) and (6). Again the hull influence is strong, since the flow is dominated by the two large bilge vortices coming from the hull. For zero rudder angle the rudder just separates the vortices, but when the rudder is turned the center of the vortex on port side moves down a little, while it moves up on starboard side. A closer look on the tip flow reveals the presence of small tip vortices, but they cannot be seen in the two figures.

The final field quantity to be considered is the pressure. Figures (7) and (8) show the pressure distribution on the port side of the hull and rudder for the two rudder angles. On the rudder it is clear that the pressure decreases when the rudder is turned, but on the hull it is a little more difficult to see the changes. However, it seems that the pressure increases slightly in the regions close to the "trailing" edge of the hull.

Future activities

Work is now progressing to address some of the issues discussed above and to quantify some of the uncertainties by verification and validation. In addition to the PMM data mentioned in this context, velocity data will also be measured in order to validate the computed velocity field in the wake. Later on the propeller will be included and parametric studies will be performed in order to study the interaction effects between hull, rudder and propeller.

Acknowledgements

This research is sponsored by The Danish Ministry of Trade and Industry and the Office of Naval Research grant N00014-00-1-0589 under the Naval International Cooperative Opportunities in Science and Technology Program (NICOP).

References

ITTC 22nd (1999)
ITTC-Quality Manual
4.9-04-01-01

Simonsen, Claus D. (2000)
Rudder, Propeller and Hull Interaction by RANS,
PhD thesis, Department of Naval Architecture and Offshore Engineering, The Technical university of Denmark, 2000.

Wilson, R., Paterson, E. and Stern F. (1998)
Unsteady RANS CFD Methods for Naval Combatants in Waves, Twenty Second Symposium on Naval Hydrodynamics, August 9-14, Preprints, Washington, D.C., 1998, pp. 198-213.

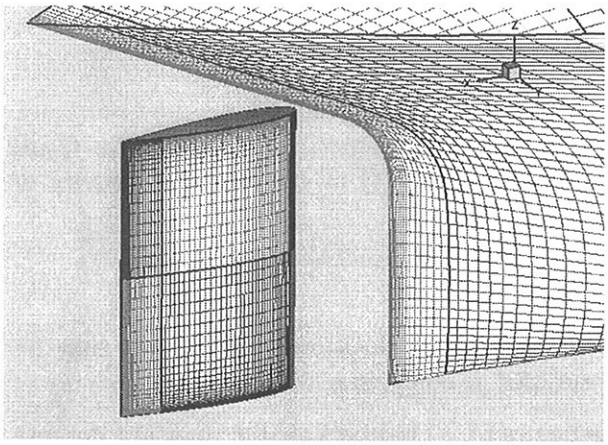

Figure 1. *Numerical hull-rudder model.*

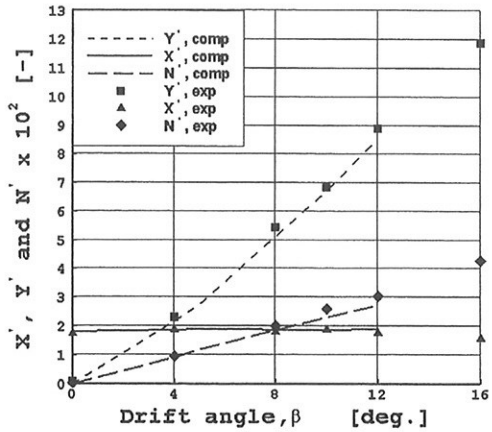

Figure 2. *Bare hull forces in pure drift.*

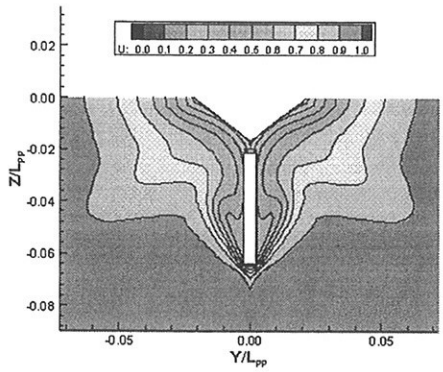

Figure 3. *Axial velocity at A.P for δ=0°*

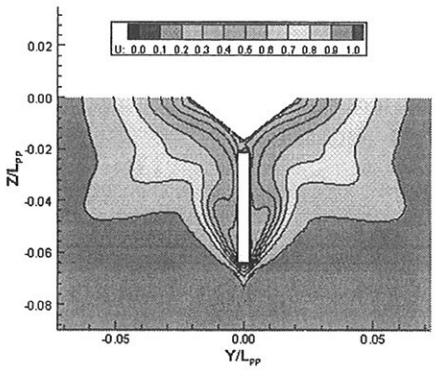

Figure 4. *Axial velocity contours at A.P for δ=-5°*

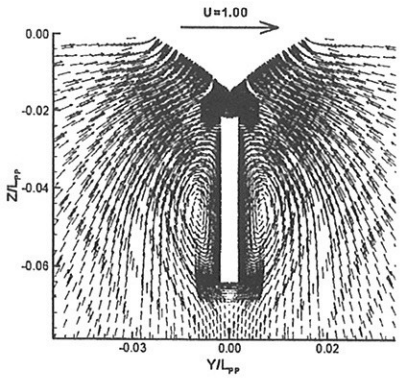

Figure 5. *Cross flow at A.P. for δ=0°*

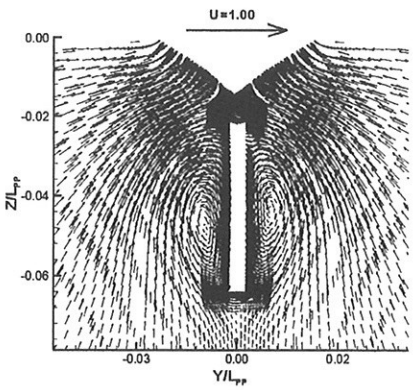

Figure 6. *Cross flow at A.P. for δ=-5°*

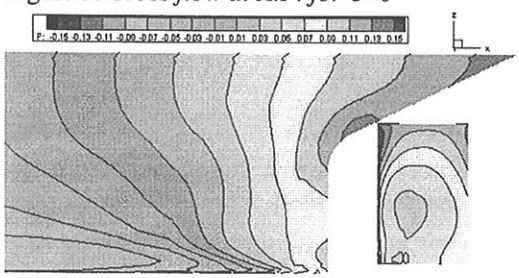

Figure 7. *Pressure on port side of ship for δ=0°*

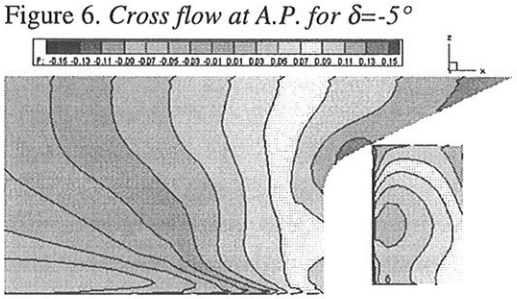

Figure 8. *Pressure on port side of ship for δ=-5°*

How to Integrate Free Motions of Solids in Fluids

Heinrich Söding, Technical University Hamburg-Harburg
h.soeding@tu-harburg.de

The free motion of a rigid body accelerated by fluid forces f_i is considered, where the f_i are produced by an incompressible Newtonian fluid. The velocity $v_j(t)$ of the center of gravity of the body is integrated from Newton's equation

$$M_{ij}\dot{v}_j = f_i \tag{1}$$

where M_{ij} is the mass matrix. (Einstein summation is implied.) Rotations of the body may be included in v_i; then, $i = 1...6$ for 3 space dimensions, and f_i comprises also moments.

Application of the usual numerical integration schemes to (1) requires that f_i does not depend on $\dot{v}_j$. This prerequisite is not satisfied for bodies in a fluid of substantial density like water. Instead there is a linear dependence of f_i on $\dot{v}_j$:

$$f_i = \bar{f}_i - A_{ij}\dot{v}_j \tag{2}$$

where A_{ij} is the added mass matrix. If A_{ij} is known, numerical integration schemes can be applied to the equation

$$(M_{ij} + A_{ij})\dot{v}_j = f_i + A_{ij}\dot{v}_j = \bar{f}_i. \tag{3}$$

However, because A_{ij} is usually unknown, it is often tried to apply numerical integration schemes directly to (1). Does this result in a stable, correct procedure?

For simplification the question is investigated first for a 1-degree-of-freedom system having mass $m = 1$ and added mass $a > 0$. One has to solve

$$\dot{v} = \bar{f} - a\dot{v}. \tag{4}$$

In the following upper indices designate time steps spaced by δt. If the explicit Euler method is used for integration, we have

$$v^{n+1} = v^n + \delta t\left(\bar{f}^n - a\frac{v^n - v^{n-1}}{\delta t}\right) = v^n + \delta t\bar{f}^n - a(v^n - v^{n-1}). \tag{5}$$

To investigate the stability, errors ϵ of v are assumed:

$$v^{n+1} + \epsilon^{n+1} = v^n + \epsilon^n + \delta t\bar{f}^n + \delta t\frac{\partial \bar{f}^n}{\partial v}\epsilon^n - a(v^n + \epsilon^n - v^{n-1} - \epsilon^{n-1}). \tag{6}$$

The difference between (6) and (5) gives the time development of the error:

$$\epsilon^{n+1} = \epsilon^n + \delta t\frac{\partial \bar{f}^n}{\partial v}\epsilon^n - a(\epsilon^n - \epsilon^{n-1}). \tag{7}$$

Even for $a = 0$ the errors can decrease with time (i.e. the integration can be stable) only if $\partial\bar{f}/\partial v \leq 0$, i.e. if there is positive or vanishing damping. In the following this is assumed to be true, and damping is neglected. We have then

$$\epsilon^{n+1} = \epsilon^n(1 - a) + a\epsilon^{n-1}. \tag{8}$$

Supposed that we have a time-independent ratio $\alpha = \epsilon^{n+1}/\epsilon^n$, then from (8) follows

$$\alpha^2 - (1 - a)\alpha - a = 0. \tag{9}$$

The equation has the solutions $\alpha = 1$ and $\alpha = -a$. That means: Any error ϵ^n consists of two parts: one remains constant ($\alpha = 1$), the other is multiplied by $-a$ at every time step. Thus the absolute value of errors increases if $|a| > 1$, i.e. the explicit Euler integration method is unstable (for arbitrary δt) if the added mass exceeds the real mass of the body. In many cases of practical interest this condition is satisfied.

For bodies with several degrees of freedom a corresponding stability investigation shows that all eigenvalues of $[M_{ij}]^{-1}[A_{ij}]$ must have absolute values ≤ 1. The Crank-Nicholsen and the fully implicit Euler integration schemes, however, are found to be neutrally stable for the case without damping irrespective of δt and a. Thus implicit schemes seem to be applicable without knowing a.

Implicit schemes, however, involve an iteration. To investigate its convergence properties, again the scalar case with mass equal 1 is considered. A naive iteration scheme for solving the motion equation $\dot{v} = f(\dot{v})$ is

$$\dot{v}^{new} = f(\dot{v}^{old}) = \bar{f} - a\dot{v}^{old}. \tag{10}$$

If $\dot{v}$ involves errors ϵ, the difference between (10) with and without errors gives the error equation

$$\epsilon^{new} = -a\epsilon^{old}. \tag{11}$$

The iteration converges only if $a < 1$. To improve the convergence limit, a relaxation factor r with $0 \leq r \leq 1$ may be introduced into (10): $v^{new} = (1 - r)\dot{v}^{old} + rf(\dot{v}^{old})$. In this case the iteration converges only if

$$r < \frac{2}{1 + a}. \tag{12}$$

Therefore, if the added mass a is unknown but may be large, the iteration converges slowly (for small r), or the method is not robust (for larger r). A robust and economic method requires to determine an approximation of the added mass matrix A_{ij} so that (3) instead of (1) can be used. If an implicit integration scheme is applied, the following equation is used for the iterations:

$$(M_{ij} + A_{ij})\dot{v}_j^{new} = f_i(\dot{v}_j^{old}) + A_{ij}\dot{v}_j^{old}. \tag{13}$$

Solving for $\dot{v}_j^{new}$ would give the exact result within one iteration step if f_i and A_{ij} were constant during the time step.

The rest of the paper deals with methods to determine an approximation for A_{ij} with small effort. At first let us assume that the flow computation is based on solving the Euler, NS or RANS equations:

$$\dot{u}_i + \frac{\partial(u_i u_j)}{\partial x_j} = -\frac{1}{\rho}\frac{\partial p}{\partial x_j} + \frac{\partial}{\partial x_j}\left[\nu\left(\frac{\partial u_i}{\partial x_j} + \frac{\partial u_j}{\partial x_i}\right)\right] + g_i \tag{14}$$

$$\frac{\partial u_i}{\partial x_i} = 0. \tag{15}$$

Imagine two flow velocity fields u_i^a and u_i^b which are identical at the considered time instant but depend differently on time due to equal velocity but different acceleration of the body. (Such flow fields can exist because neither ν nor the boundary conditions for u_i depend on acceleration or pressure.) For the difference (indicated by Δ) between u^a and u^b, (14) gives the relation

$$\Delta\dot{u}_i = \dot{u}_i^a - \dot{u}_i^b = -\frac{1}{\rho}\left(\frac{\partial p^a}{\partial x_i} - \frac{\partial p^b}{\partial x_i}\right) = -\frac{1}{\rho}\frac{\partial \Delta p}{\partial x_i} \tag{16}$$

Taking the divergence of (16) and applying (15) gives

$$\frac{\partial^2 \Delta p}{\partial x_i \partial x_i} = 0. \tag{17}$$

The boundary conditions of this Laplace equation for Δp are:
At the surface of moving bodies with normal vector n_i, the body boundary condition for translational motions, $v_i n_i = u_i n_i$, together with (16), results in the Neumann boundary condition for Δp:

$$\frac{\partial \Delta p}{\partial x_i} n_i = \rho \Delta \dot{v}_i n_i. \tag{18}$$

At non-moving impermeable free-slip or no-slip boundaries the same condition applies with $\Delta \dot{v}_i = 0$. The same holds at inlet and outlet boundaries if these are so far from the moving body that, at these boundaries, grad$p$ is nearly independent from the body acceleration.
At a free fluid surface, the pressure is constant, and a fluid particle follows the free surface. This results in

$$\frac{D}{Dt} \Delta p = \Delta \dot{p} + u_i \frac{\partial \Delta p}{\partial x_i} = 0, \tag{19}$$

which gives the following mixed inhomogeneous boundary condition at time step n:

$$\Delta p^n + \delta t \; u_i^n \frac{\partial \Delta p^n}{\partial x_i} = \Delta p^{n-1}. \tag{20}$$

Using these boundary conditions, (17) can be solved using a set (member index j) of unit body accelerations $\Delta \dot{v}_{ij} = \delta_{ij}$, where δ_{ij} is the Kroneker tensor. From the pressure distributions Δp_j for these cases the added mass matrix follows as

$$A_{ij} = \int_S \Delta p_j n_i dS \tag{21}$$

for translational motions, where S is the body surface. The extension to rotations is obvious.

The linearity of (17) and of its boundary conditions is the reason for the linear dependence of f_i on body acceleration which was assumed already in (2).

Using this method to determine A_{ij} requires to solve the Laplace equation (17) for a number of body boundary conditions which equals the number of degrees of freedom of the body. However, because of the numerically 'favorable' behavior of the Laplace equation, and because inaccuracies in A_{ij} have no effect on the final solution if the computation is stable and convergent, the computational grid may be much coarser than required for accurately solving the Euler, NS or RANS equations. For the same reason it may suffice to update A_{ij} not at every time step, but only if difficulties with stability or convergence indicate that a new approximation is appropriate.

Another possibility is to apply a panel code to determine Δp and thus A_{ij}. The panelization has to take account of the variable immersion of the body and the variable free-surface position.

Still another possibility is to estimate A_{ij}, either as constant or depending on the submergence of the body, applying approximations similarly as in vibration analysis.

For simulating ditching (landing on water) of airplanes *Shigunov et al. (2001)* use a method which requires only a small programming effort but needs substantial additional computer time: At every time step of the implicit integration procedure, the flow and the resulting fluid force f_i on the body are determined for several cases: In case 0 all accelerations are set to zero; and in case $k = 1...$ number of degrees of freedom, $\dot{v}_j = \delta_{jk}$ is used. Eq.(2) shows that this gives A_{ik}:

$$[f_i]_0 - [f_i]_k = A_{ij}(\delta_{jk} - 0) = A_{ik}. \tag{22}$$

A more economic possibility, which is recommended here, is to determine A_{ij} from the flow computations for preceding time steps and iteration steps within an implicit time integration method. If one distinguishes these different flow computations by the index k, eq.(2) becomes

$$f_{ik} = \bar{f}_{ik} - A_{ij} \dot{v}_{jk}. \tag{23}$$

I use zero acceleration for the first implicit step within each time step. By taking the difference (designated by Δ) between the fluid forces on the body determined in later and in the first implicit steps within the same time step, $\bar{f}_{ik}$ is eliminated from (23):

$$\Delta f_{ik} = -A_{ij}\dot{v}_{jk}. \tag{24}$$

For a sufficient number of k values this is an over-determined linear equation system for A_{ij}. Minimizing the sum over k of weighted squared errors of these equations, separately for each index i, one obtains the following linear equation system for A_{jk}:

$$\sum_k (g\dot{v}_l\dot{v}_j)_k A^T_{ji} = -\sum_k (g\dot{v}_l \Delta f_i)_k \tag{25}$$

where $A^T_{ji} = A_{ij}$. For 3 degrees of freedom of the body (plane motion) and 3 implicit steps per time step, it proved appropriate to use weights g_k according to the relation $g_{k-1}/g_k = 0.9$ by computing the sums in (25) recursively as

$$\sum_{k=1}^{K} (*)_k = 0.9 \sum_{k=1}^{K-1} (*)_k + (*)_K. \tag{26}$$

To de-singularize the equation system (25), which is necessary for the beginning of the simulation, the main diagonal of the coefficient matrix $\sum_k (g\dot{v}_l\dot{v}_j)_k$ is increased by a small constant times the unit matrix.

Compared to the method of *Shigunov et al. (2001)*, this procedure eliminates the flow computations with the δ_{jk} accelerations, using instead computations which are necessary anyway for the time integration. Ditching simulations of sea-planes showed that this method reduces the computing time to about one half without deteriorating the accuracy or necessitating additional implicit iterations or smaller time steps. For cases with more degrees of freedom, e.g. for 3-dimensional motion or non-rigid bodies, even larger CPU time reductions are expected.

1 Reference

Shigunov, V., Söding, H. and Zhou, Y.-Z. (2001), *Numerical simulation of emergency landing of aircraft on a plane water surface*, HIPER 2001, Hamburg

A validation study of wake-field predictions at model and full scale Reynolds numbers

Bram Starke
Maritime Research Institute Netherlands (MARIN), P. O. Box 28, 6700 AA Wageningen, the Netherlands
B.Starke@marin.nl

1 Introduction

One of the advantages of Computational Fluid Dynamics over traditional model testing is the capability to predict Reynolds-number effects on the flow field around a ship. In earlier numerical studies, successful results have been presented in computing ship stern flows from model up to full scale Reynolds number [1], with verification of numerical errors, [2] and [3]. Apart from the numerical accuracy, however, it is important to compare the predicted flow fields with experimental results. In this paper a validation study is presented of the wake field of the St. Michaelis product tanker at model and full scale Reynolds number. Experimental results obtained with laser-Doppler anemometry are available for this vessel at both Reynolds numbers from [4]. The steady double-body flow field at zero drift angle is simulated with two turbulence models. These are Menter's one-equation model [5], extended with the correction by Dacles-Mariani et al. [6], and Menter's $k-\omega$ model [7].

2 Numerical method

All computations are carried out with the computer code PARNASSOS [8], which solves the Reynolds-averaged Navier-Stokes equations on a boundary-fitted, single-block mesh. For the computations on model scale ($R_n = 8.73 \times 10^6$) the mesh consists of 145 points in the main stream direction, 81 points in wall-normal direction and 45 points in girthwise direction. For the computations on full scale ($R_n = 1.25 \times 10^9$) the number of points in wall-normal direction is increased to 121. Mesh points are strongly clustered towards the hull to capture the gradients that occur in the boundary layer. The governing equations are integrated down to the wall (no wall-functions are used) and the maximum distance of the grid points adjacent to the hull is below $y^+ = 0.3$ in all computations. The iterative solution procedure is stopped, as soon as the maximum variation of the non-dimensionalized pressure between two iterations drops below 5×10^{-5}. The computational domain extends from midship to 25% of the ship's length beyond the stern. The width and the depth of the mesh are taken approximately equal to the breadth and twice the draught of the ship, respectively. At the outer boundary of the viscous-flow domain, boundary conditions are imposed that are derived from a potential-flow calculation.

In the full-scale computations, propeller-action is simulated by axial forces only. Additional effects, such as the presence of a hub, the finite number of propeller blades and the rotation of the propeller are not taken into account. However, the blade loading has not been taken constant over the propeller-disk area, but it varies in radial direction according to

$$f_b = \frac{r}{R}\sqrt{1-\frac{r}{R}}. \tag{1}$$

Here f_b is the propeller loading, r the local radial distance to the propeller axis, and R the radius of the propeller.

3 Results

Fig. 1 and Fig. 2 compare the experimental and predicted model-scale velocity fields in a plane 0.46 R in front of the propeller plane. The propeller disk is bordered by a dashed circle. Both turbulence models reproduce the typical hook-shape in the iso-contour lines between the one and three o'-clock positions, although the magnitude of the axial velocities is slightly overpredicted in that region. In contrast, an underprediction is found for the axial velocities in the top of the propeller disk, where the one-equation model predicts $\overline{u}/V_s = 0.19$, the $k-\omega$ model $\overline{u}/V_s = 0.23$, while the experiments indicate $\overline{u}/V_s = 0.24$. Differences in the axial velocities may be related to the predicted location of the bilge vortex, which is located on a lower position in both computations compared to the experiments. A higher position of the vortex will result in an increased transport of high-momentum fluid to the top of the propeller disk (and a corresponding increase of the axial velocities) and a decreased transport towards the centre of the vortex (and a corresponding decrease of the axial velocities), which brings the computations in closer agreement with the experiments.

Fig. 3 and Fig. 4 compare the experimental and predicted axial velocity fields at full scale. The fact that the sea trials were carried out with running propeller may explain the asymmetry in the iso-contour lines around the 12 o'-clock position. This asymmetry is not modelled in the numerical simulations, but both computations show good agreement with the experiments at the starboard side of the propeller plane. Following, for instance, the 0.7 iso-contour line Menter's one-equation model is found to predict somewhat lower velocities in the top of the propeller disk, which is in closer agreement with the experiments than the prediction of Menter's $k-\omega$ model.

Summarizing it is concluded that reasonable agreement is found between the predictions and the experiments at both Reynolds numbers. Differences at model scale may be related to the predicted location of the bilge vortex, while the asymmetry in the experimental velocity field at full scale is possibly an upstream effect of the asymmetrical propeller loading, which is not modelled in the present computations. Both subjects are left for future research.

References

[1] Eça, L. and Hoekstra, M., (2000), *"Numerical prediction of scale effects in ship stern flows with eddy-viscosity turbulence models"*, In Twenty-third Symposium on Naval Hydrodynamics; applications to ship flow and hull form design, Val de Reuil, France.

[2] Hoekstra, M. and Eça, L., (1999), *"An example of error quantification of ship-related CFD results"*, In Seventh International Conference on Numerical Ship Hydrodynamics, Nantes, France.

[3] Eça, L. and Hoekstra, M., (1999), *"On the numerical verification of ship stern flow calculations"*, First MARNET workshop, Barcelona, Spain.

[4] HSVA - Bericht Nr. 1529. *"Korrelation von Nachstromaufmessungen an Modell und Grossausfuerung"*, April 1983.

[5] Menter, F.R., (1997), *"Eddy viscosity transport equations and their relation to the $k-\epsilon$ model"*, J. of Fluids Eng., Vol. 119, pp. 876-884.

[6] Dacles-Mariani, J., Zilliac, G.G., Chow, J.S. and Bradshaw, P. (1995), *Numerical / experimental study of a wingtip vortex in the near field"*, AIAA Journal, Vol. 33, pp. 1561-1568.

[7] Menter, F.R., (1994), *"Two-equation eddy-viscosity turbulence models for engineering applications"*, AIAA Journal, Vol. 32, pp. 1598-1605.

[8] Hoekstra, M. and Eça, L., (1998), *"PARNASSOS - An efficient method for ship stern flow calculation"*, In Third Osaka Colloquium on Advanced CFD Applications to Ship Flow and Hull Form Design, Osaka, Japan.

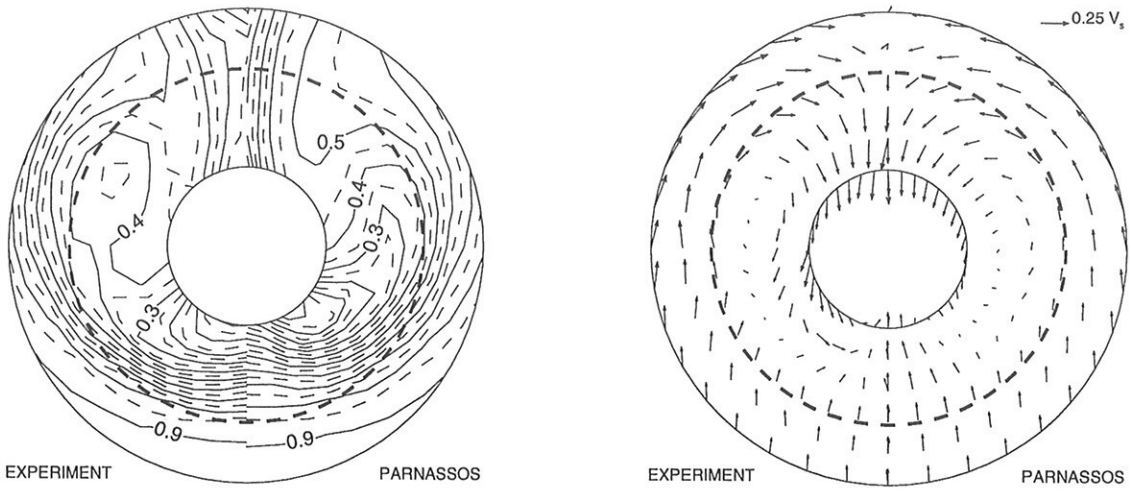

Figure 1: Comparison between the experimental and predicted velocity field 0.46 R in front of the propeller plane at model scale. Computation with Menter's one-equation model. The dashed line corresponds to the outer radius of the propeller.

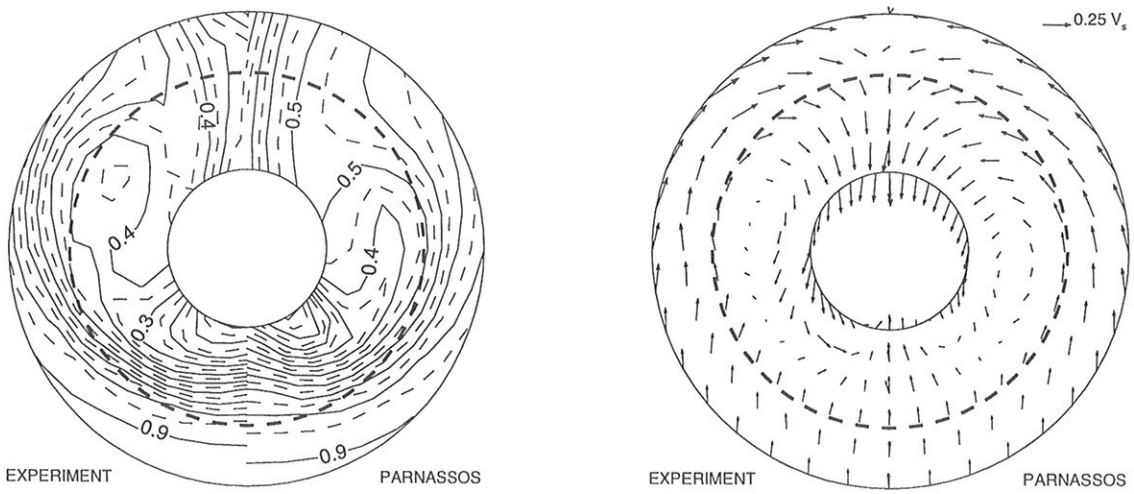

Figure 2: Comparison between the experimental and predicted velocity field 0.46 R in front of the propeller plane at model scale. Computation with Menter's k-ω model. The dashed line corresponds to the outer radius of the propeller.

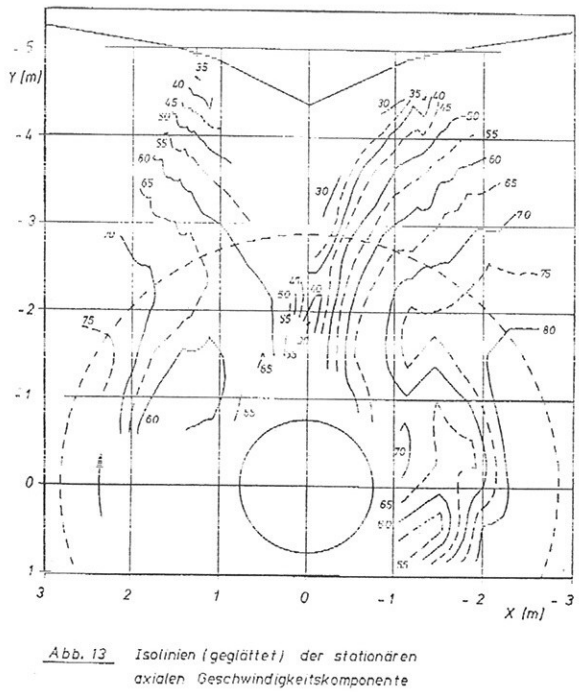

Abb. 13 Isolinien (geglättet) der stationären axialen Geschwindigkeitskomponente

Figure 3: Experimental axial velocity field 0.46 R in front of the propeller plane at full scale. The dashed line corresponds to the outer radius of the propeller.

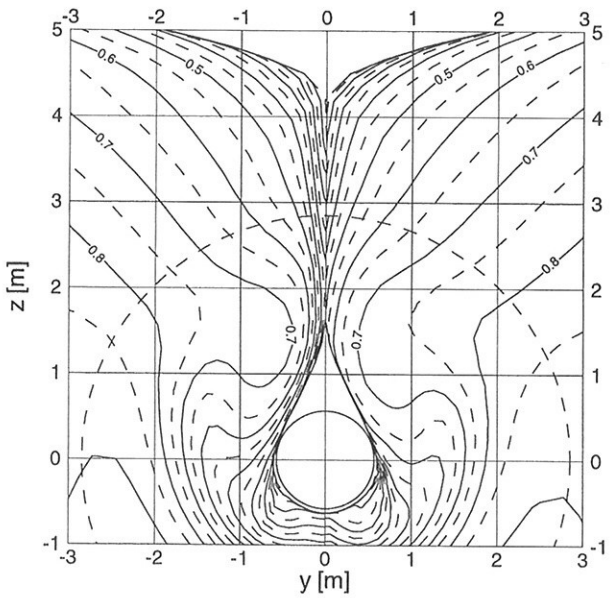

Figure 4: Predicted axial velocity field 0.46 R in front of the propeller plane at full scale. Left: Menter's one-equation model. Right: Menter's k-ω model. The dashed line corresponds to the outer radius of the propeller.

Towards RANSE Simulations for Hull, Propeller and Rudder Interaction

Heinrich Streckwall, Ould M. El Moctar

HSVA, Bramfelder Str 164, D 22305 Hamburg, Germany, elmoctar@hsva.de

By now, many RANSE simulations for ship hulls can be found in the literature. Also for propellers, there are several applications of RANSE solvers, e.g. Streckwall (1999). For hull-propeller interaction, the propeller is usually simplified in the computational model and substituted by body forces. The distribution of the body forces may be more or less sophisticated. A state-of-the-art application for numerical propulsion tests employing body-force models for the propeller is given by Chao (2001). Here we present steps towards a full modelling of ship-rudder-propeller interaction. We analyze the flow using the finite-volume RANSE solver Comet, ICCM (2000). The grid is generated using the commercial grid generation code ICEM-CFD.

El Moctar (2001a) presented rudder-propeller interaction without considering the ship, but using also geometrical modelling for both propeller and rudder. Body force models allows to simulate the flow using a steady RANSE simulation and a body-force model of rudder and propeller needs only 20% of the number of cells needed for geometric modelling of the propeller. In sum, the computational effort for a body-force model was only 1% of that for geometric propeller model.

The investigated case was a four-blade SVA propeller with a fully balanced rectangular rudder, El Moctar (2001b). The propeller-rudder study employed body forces varying only in radial direction. The body forces were distributed over the whole propeller disk. The numerical grid consisted of 450,000 cells for the body-force model and 2,200,000 cells for the grid with geometrically modelled propeller. The grid locally refined in the propeller disk area. The grid with the geometrically modelled propeller needed 220 CPU-hours on a 800Hz-Pentium processor.

The computed rudder forces were approximately 10% larger when using the body-force model, Fig.1. This difference is predominantly due to the effect of the propeller hub which is not captured by the standard approach to propeller modelling using body forces. Behind the propeller hub a dead-water region with axial velocities much lower than in the propeller slipstream is formed. The standard body-force model sets the body forces in the hub area to zero. The body-force method can be improved by setting the body forces in the hub area to force corresponding to the resistance forces on the hub taken from a first RANSE simulation with a standard body-force model. Then the forces on the rudder differ only by 4% from those for the geometrically modelled propeller grid, Fig.1. This accuracy appears quite acceptable considering other inaccuracy in the model. The conclusion of this analysis is that for practical purposes in rudder design, body-force models are a good compromise between accuracy and effort.

With the progress in grid generation capabilities and available hardware, we can now take the next step and consider hull, propeller, and rudder in one model. Successful simulations of such complete models would be a major step forward towards the numerical towing tank. The topic of propeller-ship interaction is complex and the standard experimental approach of separating propulsion and resistance not completely satisfactory. CFD may here help to understand the physics and to support more reliable procedures for full-scale prediction. Complete model simulation will also give insight how good body-force models are for standard RANSE propulsion test simulations. We expect that we will continue with body-force models as best practical compromise, but we can now quantify the difference at last.

A major complication is the geometrically modelled propeller. The propeller is complex in geometry and for most modern propellers with high-skew generation of a good grid avoiding highly skewed cells is a difficult task. For the analysis of just the propeller, this task is simplified as the domain around the propeller can be chosen at one's convenience. For the propeller behind the ship, the

constraining near hull with free-form shape poses some additional problems. Unstructured grids could comfortably cope with the complex geometries, similarly as proven for propeller-rudder interaction or for our aerodynamic analyses. However, the cell count rises considerably with unstructured, tetraeder grids and ship-hull-rudder application require already very high cell numbers even if employing hexaeder grids. We are therefore limited in practice to block-structured hexaeder grids.

Block-structured grids are needed anyhow as the block containing the propeller is sliding versus the rest of the blocks while the propeller turns. This modelling requires sliding block interfaces with non-matching block-boundaries, a feature supported by Comet. The analysis is then performed as unsteady RANSE simulation with time-steps corresponding to 1° turn of the propeller. This value was found to be a good compromise between accuracy and computational requirements for the propeller-rudder analyses of El Moctar (2001a,b). We neglect the free-surface in the computational model to avoid further complications of an already ambitious task.

We selected a ship which we had previously analyzed without geometrically modelled propeller, namely the C-Box of FSG, El Moctar (2001a,b). The grid including rudder, propeller and ship consisted of 30 blocks using in total approximately 2,000,000 cells. The analysis is conducted on a parallel PC cluster (beowulf configuration) consisting of 8x2 Pentium 600MHz processors and 10x2 Pentium 800 MHz processors.

At the time of abstract submission, we had just started our first trial computations for the complete ship-propeller-rudder simulation. We hope to be able to show preliminary results at the symposium.

CHAO, K.Y. (2001), *Numerical propulsion tests*, Ship Technology Research 48/2, pp.49-96

EL MOCTAR, O.M. (1999), *Numerical investigation of propeller-rudder interaction*, NuTTS'99, Rome

EL MOCTAR, O.M. (2001), Numerische Berechnung von Strömungskräften beim Manövrieren von Schiffen, PhD Thesis, TU Hamburg-Harburg

EL MOCTAR, O.M. (2001), *Numerical computations of flow forces in ship manoeuvring*, Ship Technology Research 48/3, pp.98-123

HAFERMANN, D.; STEBERL, R. (2001), *Efficient grid generation for maritime RANSE simulations*, NuTTS'01, Hamburg

ICCM (2000), *User Manual Comet Version 1.045*, Institute of Computational Continuum Mechanics, Hamburg

STRECKWALL, H. (1999), *Numerical prediction of viscous propeller flows*, Ship Technology Research 46/1, pp.35-42

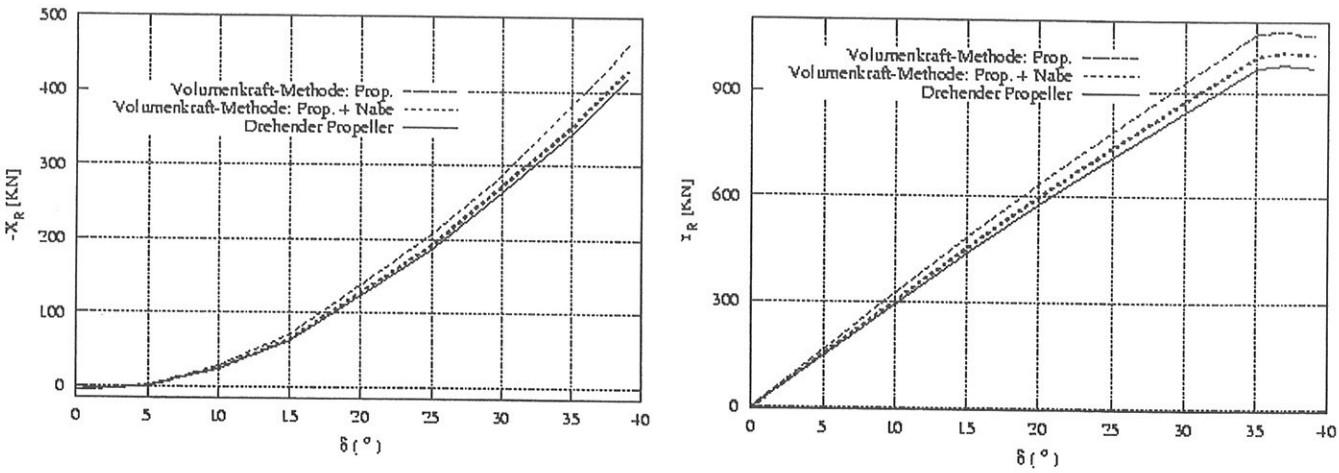

Fig.1: Rudder forces in x (left) and y (right) direction using a body force method
"Volumenkraft-Methode: Prop.": body force method for propeller
"Volumenkraft-Methode: Prop.+Nabe": body force method for propeller and hub
"Drehender Propeller": geometrically modelled propeller

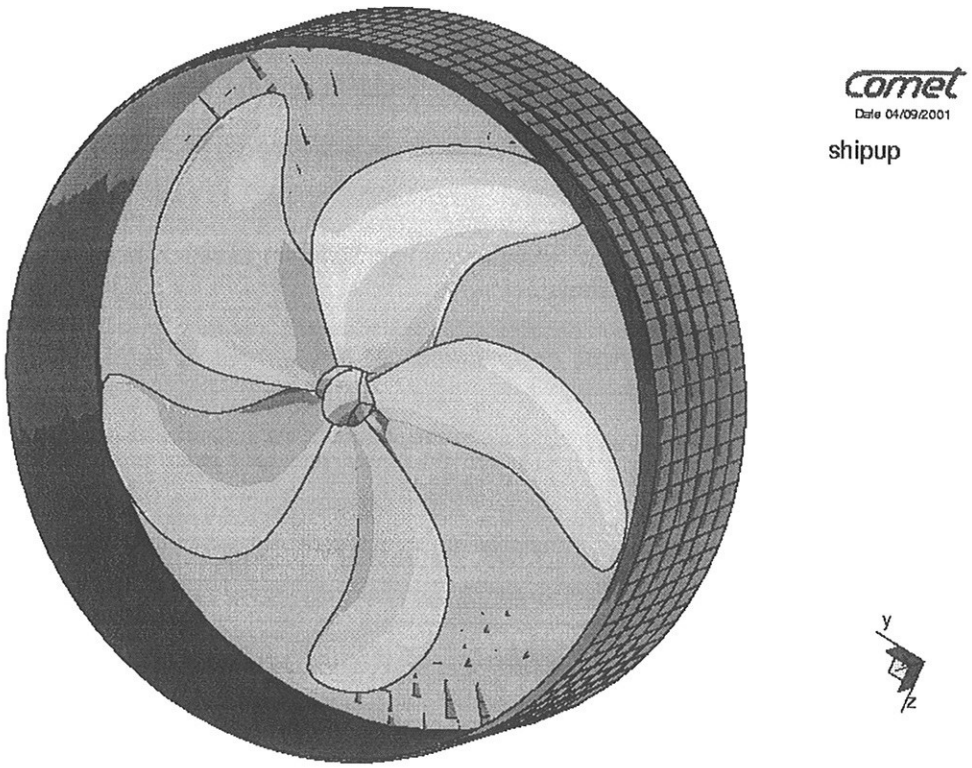

Fig.2: Method: Rotating propeller cylinder block is sliding on an outer cylinder that is part of a cell system fixed to the ship

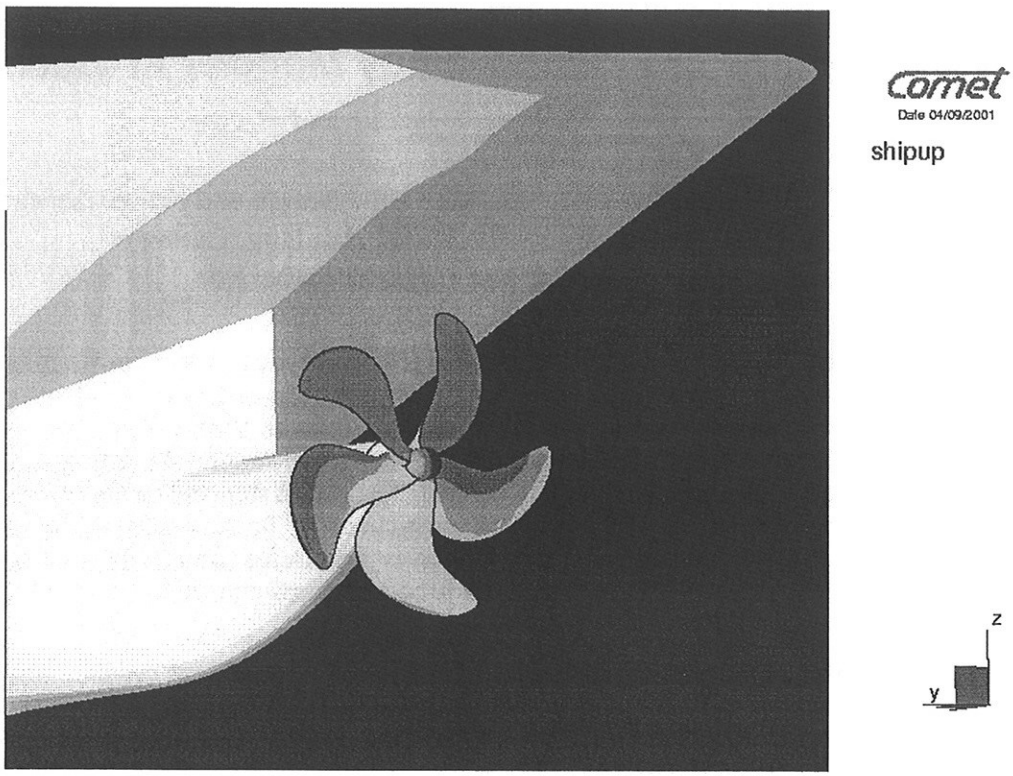

Fig.3: Propeller behind hull for a specific time step

Predictions of Floating–Body Motions in Viscous Flow

Y. Xing, I. Hadzic and M. Peric

TU Hamburg–Harburg, AB Fluiddynamik und Schiffstheorie
Laemmersieth 90, 22305 Hamburg, Germany
Email: yan.xing@tu–harburg.de

Introduction

The techniques of Computational Fluid Dynamics (CFD) are applied to simulate floating–body motions in free–surface flow (e.g. waves). It is demonstrated that a wide variety of problems associated with the coupled analysis of flow and flow–induced body motions can be dealt with by a single computer code, which solves the Navier–Stokes equations and the equations of motion for a floating body in a coupled manner. The method is relevant to a wide range of applications in ship and ocean engineering, such as ship seakeeping and maneuvering etc. In this paper, predictions of floating–body motions in large incident waves as well as Wigley's ship motions in head waves are discussed and numerical results on floating–body motions under large wave packages are compared with measurements.

Numerical Methods

In the present study, the finite volume method has been used, which can accommodate any type of grid, and is therefore applicable to complex geometry problems. SIMPLE algorithm [1] has been taken to couple the pressure field properly to the velocity field. HRIC (High–Resolution Interface Capturing) scheme [2] has been used to simulate the free surface and to achieve the sharpness of the interface between water and air.

For predicting the body movements, floating–body dynamics has been implemented into the program Comet [3] via user–coding, a fully–implicit predictor–corrector procedure has been employed to implement the motions of the body, taking the advantage of the iterative nature of the fluid–flow solver.

For simulating the body movements, there are two possible approaches:

1. Within a body–fixed coordinate/grid system, the motion of the body is treated as body forces introduced into external force term of the Navier–Stokes equations;

2. By the use of moving grid strategies, the motions of the bodies are represented by the displaced and adapted grid system fitted to the bodies' surfaces. The body movements are calculated according to the forces obtained by integrating pressure and shear stress over body surfaces.

In this study, the latter technique is used to capture the general nature of this problem.

Numerical Tank

Our numerical tank consists of a fluid domain with two phases (water and air) bounded by a layer of air on top, a bottom surface in water and four vertical boundaries. All boundaries can be physical ones if the fluid is really bounded, but otherwise they are imaginary ones. For wave generation, either the movements of a flapping wave–maker are simulated by moving the boundary grids, or inlet velocities are specified at the corresponding section. Numerical beaches are incorporated near other imaginary boundaries so that no waves are reflected. At solid walls, no–slip conditions are applied.

Moving grids are used to simulate the body movements. For large body rotations, the sliding interface is used between a block attached to the body and the rest of the computational domain; the surrounding grids can be extended or compressed to allow the translation movement. For small body motions, grids in the vicinity of the body are adapted and smoothed due to the body movements to retain the grid quality; the rest of the grids, which are far from the body (e.g. grids near wave–maker or grids in the numerical beach), remain the same so that the waves can travel smoothly into or out of the near–body region.

As mentioned before, waves are generated by two ways:

a. Simulating the exact physical movements of the wave–maker in experiment by moving the corresponding boundary with the moving–grid method. The velocity distributions at the moving boundary are specified according to the velocities of the wave–maker.

b. Imposing the boundary condition as inlet velocity boundary. Velocities are given by appropriate values according to linear wave theory, more detail can be found in Newman [4].

Results and Discussion

After first confirming the present numerical method can predict the floating–body motions in small regular waves to reasonable accuracy [5], investigations on 2D floating–body motions in large waves are carried out, where the nonlinear motions and viscous effects are more important. Results from the free–floating body motions under the large wave packages are presented and compared with the measurements in this paper.

The 2D experiment was set up in a small towing tank of Technical University of Berlin, which has the dimensions of 30 cm width, 1200 cm length and 40 cm water depth. The model is rectangular prism with 10 cm width, 5 cm height and 29 cm length, and the density of the body is 0.68 g/cm^3. Several wave packages have been generated by specifying the flapping–motions of the wave–maker to investigate the behavior of the body under the large impact–wave loads. Wave packages were generated first without placing the body in the tank, as it can be observed, the wave packages have been generated successfully to concentrate at the place where the body was supposed to be located. The body was then located at $x = 2.11$ m away from the wave–maker and two probes were set before and behind the body at $x = 1.16$ m and $x = 2.66$ m respectively, to measure the water surface elevation in time domain. The free–floating body motions were obtained from the continual pictures taken by a digital camera.

The numerical towing tank has been set up with 40 cm water at the bottom and 200 cm air–layer on the top of the water to minimize the air flow's influence on the water surface. One vertical boundary has been simulated as wave–maker with flapping motions by moving grids. The effective numerical towing tank has been set 300 cm long with 500 cm numerical beach to prevent wave–reflection. To capture the flow separation, finer grid has been applied to free surface zone and near–body region. No–slip conditions have been employed at the body surfaces and the solid walls of the water tank.

The comparisons between the experimental and numerical results on the time history of the free surface elevations measured by the two probes before and behind the body are shown in Figure 1 a and b respectively. The agreement is rather good, given that the probes' locations in numerical tank are slightly different from the ones in the experiment due to the limit of grid nodes in numerical tank. Three degrees' motions of the rigid–body under the wave package loads are compared in Fig. 2. The experimental data are obtained by a digital camera, errors are approximately 1.5%, 5.1% and 9.1% in horizontal, vertical and angular motions respectively, also certain phase error due to camera frequency should be taken into account. As shown in Fig. 2, the agreements with all three degrees of body motions are reasonably good. The body has been driven to a large rotation angle as ± 20 degree and the simultaneous heave motion has reached the amplitude as 80 percent of the body height. Fig. 3 shows the free surface deformation, the body position and fluid velocity vectors from the numerical tank at $t = 7.2$ s; the experimental picture are also taken at the same time for comparison. As can be observed, a great similarity exists (although the experiment seems to have slightly 3D effect) and the waves are nonlinear and partially broken around the body and the body has been driven to a large angular movement by the impact of the wave packages. For this case, the nonlinear and viscous effects become very important and should not be ignored.

After verifying and validating the present method for two dimensional cases, the method has been expanded to the analysis of three dimensional problems. Investigation on motions of ships advancing in head waves has been first carried out, where Wigley's mathematical model has been used.

Calculations are first set up for Wigley's ship advancing at Froude number 0.3 in head waves on a coarse grid with 44880 cells (only half of the ship has been taken in the calculation). The pitching and heaving motions are free and other motions are not permitted. The waves are generated by specifying the inlet flow according to the linear wave theory. The wavelength is set to be equal to the ship length, and the ratio of wave height and the wavelength is 0.05. Fig. 4 shows the computed water elevation at the position of 1.8L (ship length) right before the ship. The time history of Ships heaving and pitching motions are shown in Fig. 5. a. and b. respectively. Large motions can be observed at the beginning directly after being released at 2nd second in both heave and pitch motions, which indicates ship is initially not at its balanced status due to the initial constant velocity specified in flow and needs some time to find its balancing position. The moving grids and adaptation of the grids have been used to implement ship motions. Figure 6 a. and b. shows ship positions and wave contours (created or influenced by ship movements) at different instants. As a first step, very coarse grid has been taken, therefore free surface is smeared and the wave patterns can not be captured exactly. For the next step, finer grid will be generated for further investigation.

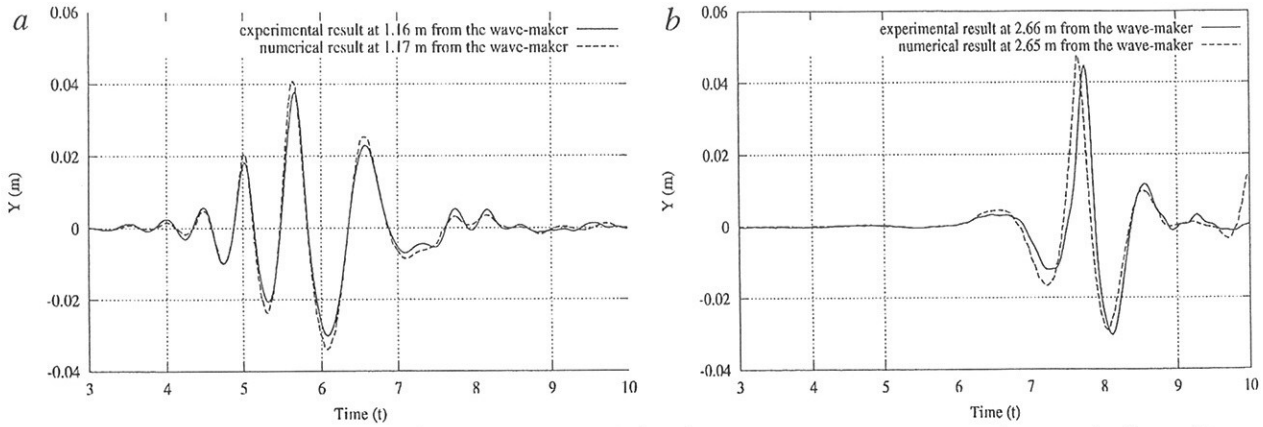

Fig. 1. Comparison on water elevation at two probes between measurements and numerical results

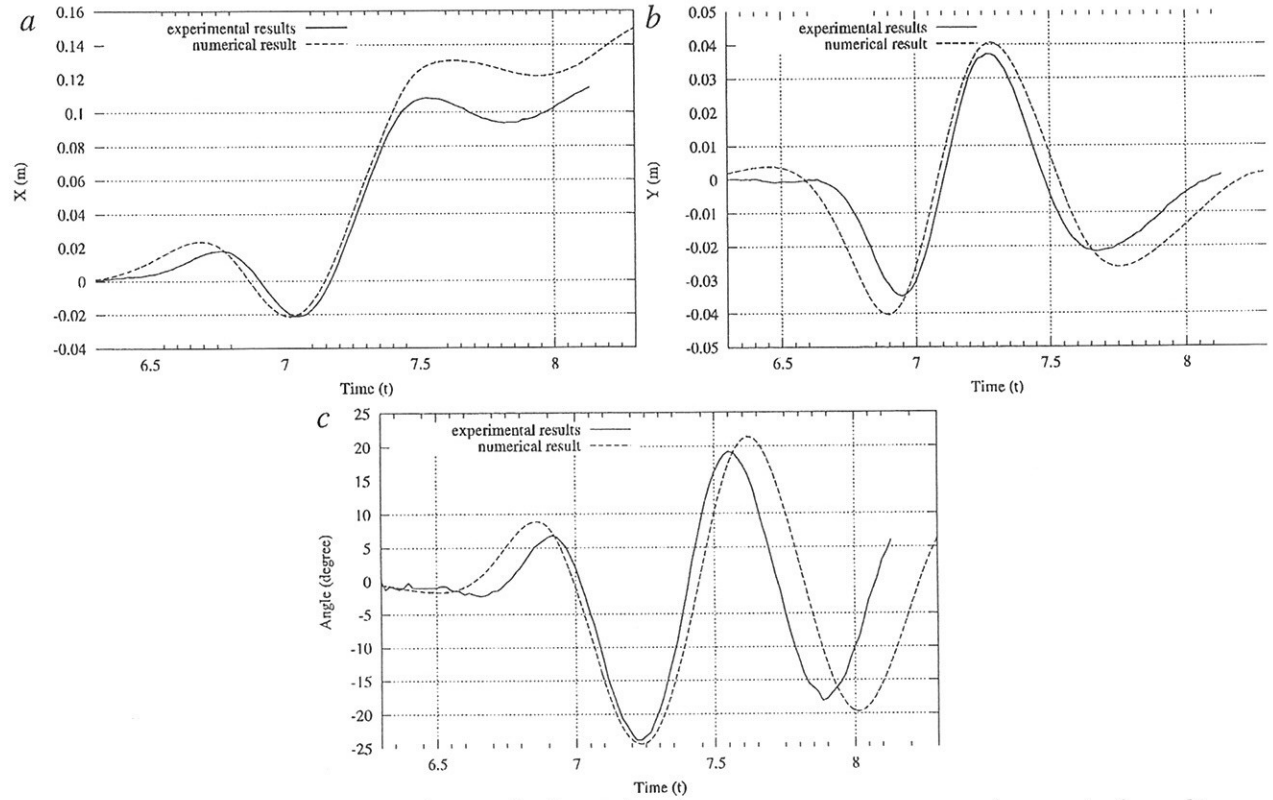

Fig. 2. Comparison on free–floating body motions between measurements and numerical results (a. horizontal motions; b. vertical motions; c. rotation motions)

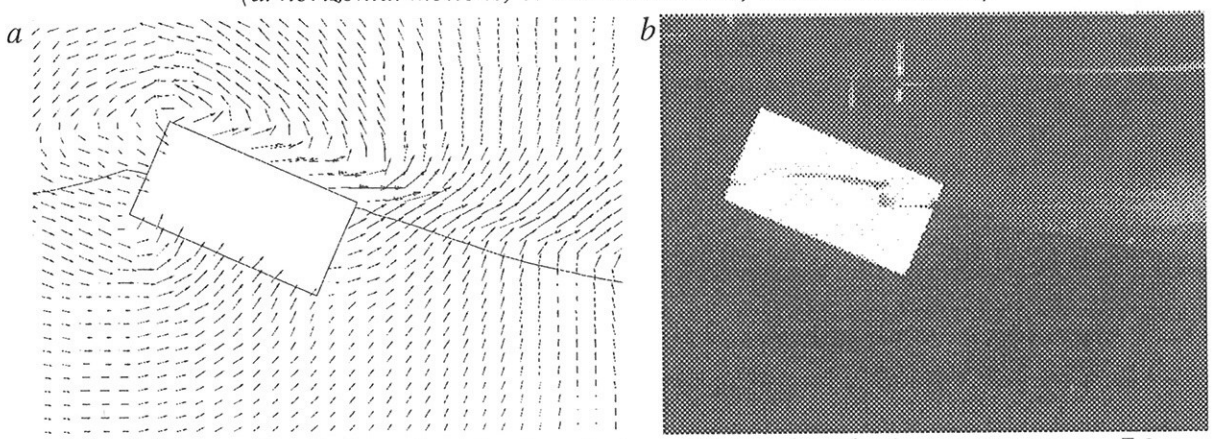

Fig. 3. Free surface deformation, floating–body position and fluid velocity vector at t = 7.2 s (a. numerical results; b. experimental picture)

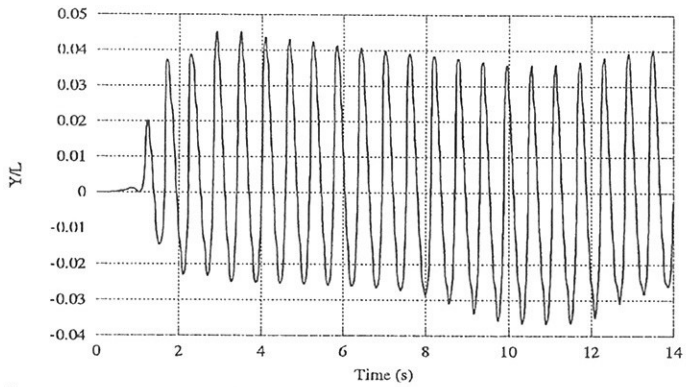

Fig. 4 Computed time history of water elevation at the position x=1.8L (ship length) before ship

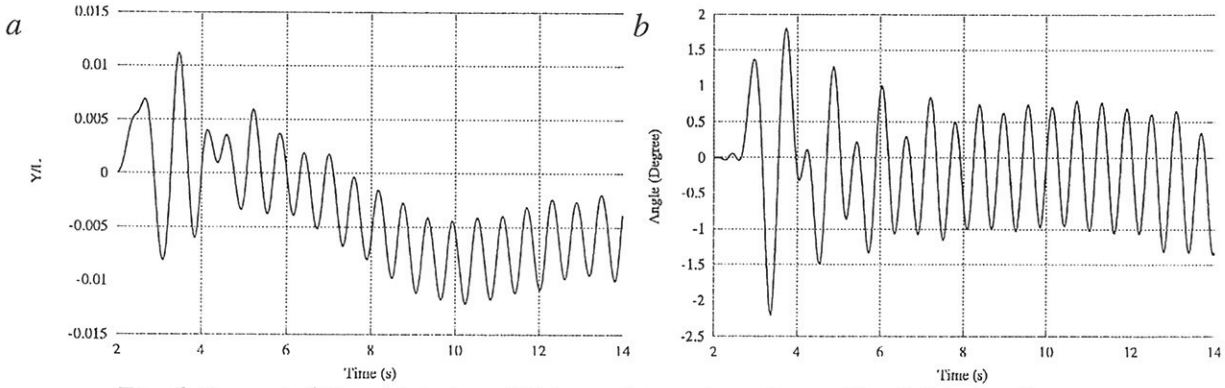

Fig. 5 Computed time histories of Ship motions advancing at Fn=0.3 in head waves (a. heaving motions; b. pitching motions)

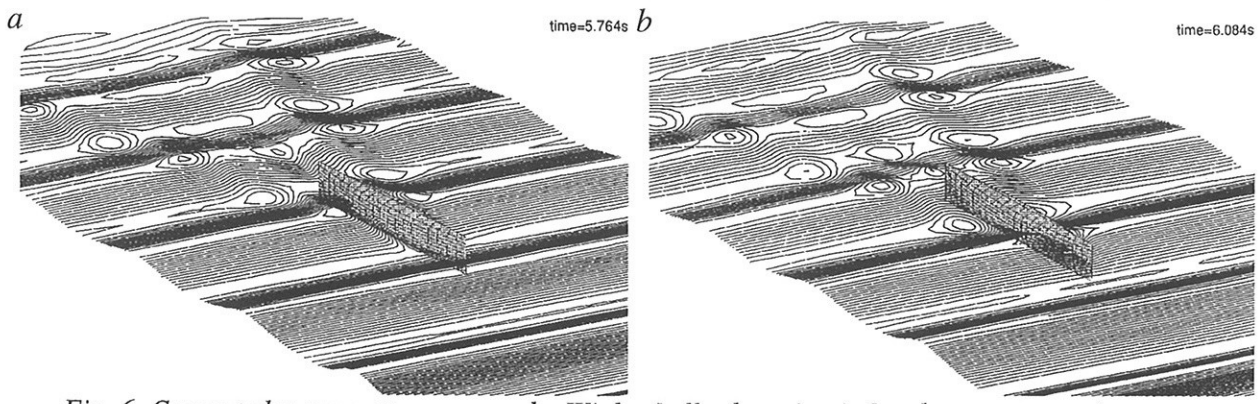

Fig. 6 Computed wave patterns around a Wigley hull advancing in head waves at two instants

References:

1. S. V. Patankar and D. B. Spalding: A calculation procedure for heat, mass and momentum transfer in three–dimensional parabolic flows. Int. J. Heat and Mass Transfer, 15:1787–1806, 1972.
2. S. Muzaferija and M. Peric: Computation of Free Surface Flow Using Interface–Tracking and Interface–Capturing Methods, chap. 2 in O. Mahrenholtz and M. Markiewicz (eds.), Nonlinear Water Wave Interaction, pp. 59–100, WIT Press, Southampton, 1999.
3. Comet user manual, ICCM (Institute of Computational Continuum Mechanics GmbH), Hamburg, 2000.
4. J. N. Newman: Marine Hydrodynamics, MIT Press, England, 1978.
5. I. Hadzic, S. Muzaferija, M. Peric, Y. Xing and P. Kaeding: Predictions of Flow–Induced Motions of Floating Bodies, Proc. 3rd Numerical Towing Tank Symp., Tjaernoe/ Sweden, 2000.

5th Numerical Towing Tank Symposium (NuTTS'02)

Nantes, France, 29 September - 1 October 2002

Topics:

- Nonlinear flows around marine structures (LES, RANSE, Euler with or w/o free surface)
- Free-surface flows around marine structures (3-d ship seakeeping, free-surface viscous flows)
- Related topics (validation experiments, numerical techniques, grid generation, etc)

Deadlines:	Early feedback:	15 July 2002
	Abstracts received:	**15 August 2002**
	Notification of acceptance:	22 August 2002
	Last possible update:	15 September 2002

You are invited to participate in the above event. The objective of the event is to provide a forum for informal discussions among experts in the field and to disseminate latest results. Younger workers and Ph.D. students are especially encouraged to participate. The event will be held at a small seaside resort near Nantes. All participants stay and have meals together to maximize interaction and discussion.

The abstracts of the proposed talk will be directly reproduced in the proceedings. There will be no final full papers. Rather, the symposium is intended to give 'sneak previews' to full papers. Work in progress, encountered problems, etc. should be discussed in an open, informal atmosphere among colleagues. The first page of the extended abstract should be headed with the title and authors' names and address (incl. email) in a compact form to economise on space. Extended abstracts should be limited to 6 pages in a field 17cm by 25cm per page. Copies of the extended abstract should be sent in good quality to the host.

An early reply will help us in organising the event better. For the early feedback, a tentative title or topic will suffice.

Following the tradition of previous NuTTS events, the fees will be kept low to allow a maximum number of scientists to attend. The fees including accommodation and meals during the symposium will be:

400/300/200 EUR	for regular participants/for authors/for students incl. PhD candidates
150/100/50 EUR	same as above, but excluding accommodation, breakfast and dinner

Gerard Delhommeau, Gerard.Delhommeau@ec-nantes.fr

Michel Visonneau, Michel.Visonneau@ec-nantes.fr

Volker Bertram, bertram@waves.insean.it